REFINING TERRESTRIAL BIOSPHERE FEEDBACKS TO CLIMATE CHANGE THROUGH PRECISE CHARACTERIZATION OF TERRESTRIAL VEGETATION

by © Lynsay Spafford A Thesis submitted
to the School of Graduate Studies in partial fulfillment of the
requirements for the degree of

Doctorate of Philosophy
Environmental Sciences
Memorial University of Newfoundland

May 2023
St. John's, Newfoundland and Labrador, Canada

Abstract

Climate change is primarily driven by the human activities of fossil fuel combustion and land use change, which together result in the emissions of greenhouse gases such as carbon dioxide (CO_2). The terrestrial biosphere currently absorbs about a third of total anthropogenic CO_2 emissions, mostly through primary production by vegetation. The continued function of vegetation as a CO_2 sink is uncertain, as climate change has the potential to enhance or restrict the carbon uptake capacity of vegetation. Uncertainty in terrestrial vegetation function in the context of climate change, due in part to a lack of precise observations of leaf biochemistry and function with which to develop models, therefore limits the confidence of climate change projections. In its entirety, this thesis examines the potential for more precise observations of leaf function and their integration across a variety of models and observational scales. The first chapter provides an introductory overview of the subsequent four chapters and how each compliments the other. The second chapter demonstrates the role of the terrestrial biosphere in influencing the relationship between temperature change and cumulative CO_2 emissions. The third chapter provides adaptations to current radiative transfer modelling approaches to improve estimations of leaf biochemical constituents. The fourth chapter applies high spatiotemporal resolution observations of leaf phenology, the timing of leaf emergence and senescence, across North America to predict species-specific leaf phenology patterns under various emissions scenarios throughout the 21st century. The fifth chapter provides an approach to detect declines in ecosystem processes such as carbon uptake using observational leaf phenology networks. These chapter results indicate that 1) uncertainty in the land-borne fraction of carbon emissions contributes largely to uncertainty in the relationship between temperature change and emissions, 2) spectral subdomains and prior estimation of leaf structure improves leaf biochemistry estimations, 3) leaf senescence timing may diverge between boreal and temperate species under a high emissions scenario, and 4) declines in vegetational carbon uptake can be accurately detected using quantitative phenocam-based indicators. The fundamental and technical insights provided through this thesis will facilitate more reliable and functionally resolved projections of terrestrial biosphere feedbacks to climate change.

Acknowledgments

Firstly, I would like to thank my supervisor Dr. Andrew H. MacDougall who has been an outstanding supervisor and mentor. Throughout my PhD studies, Andrew has inspired me to pursue the highest standards. His constant dedication and timely support have allowed me to thrive as a student and have contributed enormously to the foundation and motivation of my academic career. I would also like to thank my other committee members Dr. Joel Finnis, Dr. Carissa Brown, and Dr. Lisa Kellman for their support, patience, and guidance over the years. I am eternally grateful for the collaborative support of Dr. James Steenberg from the Nova Scotia Department of Natural Resources and Renewables, who helped to make the Acadian Phenocam Network possible and provided me with so many rewarding connections. In addition, I would like to thank my fellow student colleague Makcim De Sisto for making time in the office enjoyable and fostering a delightful sense of camaraderie.

Beyond the academic realm I would like to thank my partner Malcolm for his unwavering support and companionship throughout my degree. Thank you for your boundless patience in teaching me how to assemble and install each of my aluminum research stations. I would also like to thank my family for their encouragement and provision of an outlet from work via beach walks and farm chores. A special thank you is due to my father for gifting me with a fascination in the natural sciences after spending much of my youth in the great outdoors and to my mother for teaching me the value of hard work. Thank you to my brother for the long talks about research, study music recommendations, and the reminder to think on the big picture. Thank you to my friends, fiddle, and felines for the refreshing diversions from work.

Chapters 2, 3, 5, and appendix I have been published, while Chapter 4 is currently under review for publications. Chapters 2, 3, 4, and 5 as well as Appendix I in this thesis are freely

available under a Creative Commons License, which allows users to copy, distribute, transmit, and adapt an article. Thank you to anonymous reviewers in the published version of these chapters as well as Appendix I for their insightful comments.

The research in this thesis was financially supported by the Natural Sciences and Engineering Research Council of Canada (NSERC) Discovery Grant Program. I am grateful for support from a NSERC Canada Graduate Scholarships – Doctoral Program Scholarship and a Dean's Excellence Award from Memorial University. The research in this thesis was enabled in part by support provided by Compute Canada (www.computecanada.ca). Advanced computing resources are provided by the Digital Research Alliance of Canada, the organization responsible for digital research infrastructure in Canada, and ACENET.

For the data used within chapter 3, I warmly thank Luc Bidel, Christophe François and Gabriel Pavan who collected the ANGERS dataset. The HYYTIALA dataset was collected through the International Network for Terrestrial Research and Monitoring in the Arctic (INTERACT) (FLUO-SYNTHESIS project); the Brazilian Coordination for the Improvement of Higher Education Personnel (CAPES). ITATINGA genotype test is funded in part by the EUCFLUX project of Forestry Science and Research Institute (IPEF) and in part by SOERE F-ORE-T, which is supported annually by Ecofor, Allenvi, and the ANAEE-F. I also thank Valentine Alt, Samuel Counil, and Philippe Gaucher for tree climbing and data collection, as well as Anna Grandchamp for her help during data collection at the Nouragues field station.

The Nova Scotia Department of Natural Resources and Renewables provided assistance in locating the Nova Scotia Acadian Phenocam Network phenocam locations included in chapter 4 based on analysis of local climate and forest conditions and assisted in the installation of phenocams in 2019. I wish to thank ClimateData.ca for providing the climate information used in chapter 4. ClimateData.ca was created through a collaboration between the Pacific Climate Impacts Consortium (PCIC), Ouranos Inc., the Prairie Climate Centre (PCC), Environment and Climate Change Canada (ECCC) Centre de Recherche Informatique de Montréal (CRIM) and Habitat7.

Well not directly included in this thesis, I would like to acknowledge the valuable in-kind contributions made by Parks Canada, including permission to conduct research within Kejimkujik National Park and National Historic Site, Cape Breton Highlands National Park, Prince Edward Island National Park, and Fundy National Park, as well as field support provided by Donna Crossland, Gavin Carpenter, Friedrich Meyer, Kyle Rowter, Troy Pretzlaw, Jared Tomie, Clayton D'Orsay, Megan Blaxley, Alain Caissie, Neil Vinson, Garrett Mombourquette, Louis Charron, and Travis James. I thank the collaborators, including site PIs and technicians, for their efforts in support of PhenoCam, whose data I used in chapters 4 and 5. The development of PhenoCam has been funded by the Northeastern States Research Cooperative and NSF's Macrosystems Biology program (awards EF-1065029 and EF-1702697).

I wish to thank Drs. Susan Ziegler, Hugo Beltrami, Entcho Demirov, Joel Finnis, and Evan Edinger for their insightful comments on an early draft of the manuscript in Appendix I.

I acknowledge that the lands on which Memorial University's campuses are situated are in the traditional territories of diverse Indigenous groups, and I acknowledge with respect the diverse histories and cultures of the Beothuk, Mi'kmaq, Innu, and Inuit of the province of Newfoundland and Labrador. I acknowledge that St Francis Xavier University is located on the unceded and traditional territory of the Mi'kmaw, who have maintained a connection to this land.

Table of Contents

List of Figures

List of Tables

List of Abbreviations

ACCESS-ESM1.5	Australian Community Climate and Earth System Simulator
ANGERS	dataset of leaf optical measurements and biochemistry collected in Angers, France
AR	autotrophic respiration
AR5	Fifth Assessment Report
AR6	Sixth Assessment Report
AT	alternating leaf emergence model
AVHRR	Advanced Very High-Resolution Radiometer
BA	burned area
BCC	Beijing Climate Centre
BCCAQv2	Bias Correction/ Constructed Analogues with Quantile delta mapping reordering method
BCC-CSM2-MR	BCC Climate System Model version 2 with medium resolution
BNF	biological nitrogen fixation
Cab	chlorophyll a and b content ($\mu g \cdot cm^{-2}$)
CABLE	Community Atmosphere Biosphere Land Exchange model
CANESM5	Canadian Centre for Climate Modelling and Analysis fifth generation Earth System model
CCCma	Canadian Centre for Climate Modelling and Analysis
CERFACS	Centre Européen de Recherche et de Formation Avancée en Calcul Scientifique
CESM2	Community Earth System Model version 2

CH_4	methane
CLM5	Community Land Model version 5
CLM5BGC	Community Land Model version 5 with prognostic phenology
CLM5BGC	Community Land Model version 5 with perscribed phenology
CMIP	Coupled Model Intercomparison Project
CMIP5	Fifth Phase of the Coupled Model Intercomparison Project
CMIP6	Sixth Phase of the Coupled Model Intercomparison Project
CMIP7	Seventh Phase of the Coupled Model Intercomparison Project
CNRM	Centre National de Recherches Météorologiques
CNRM-ESM2-1	earth system model by Centre National de Recherches Météorologiques and Centre Européen de Recherche et de Formation Avancée en Calcul Scientifique
CO_2	carbon dioxide
COSINE	ClOse-range Spectral ImagiNg of lEaves model
CRS	coordinate reference system
CRUNCEPv7	Atmospheric Forcing Dataset version 7 for the Community Land Model
CSIRO	Australian modelling group Commonwealth Scientific and Industrial Research Organization
CTEM	Canadian Terrestrial Ecosystem Model
CUE	carbon use efficiency
CWC	cumulative warming commitment
Cxc	carotenoid content ($\mu g \cdot cm^{-2}$)
DART	Discrete anisotropic radiative transfer

DB	deciduous broadleaf
DECK	Diagnosis, Validation, and Characterization of Klima
DM	Delpierre leaf senescence model
DOGWOOD-1	dataset of leaf optical measurements and biochemistry collected in Moscow, Russia
DOY	day of year
DMs	Delpierre with preceding spring leaf emergence leaf senescence model
DP	Dormphot leaf emergence model
DPDI	Dormphot with just dormancy induction leaf senescence model
DPDIs	Dormphot dormancy induction with preceding spring leaf emergence leaf senescence model
ECS	equilibrium climate sensitivity
ECT	ecosystem carbon turnover
ECV	essential climate variable
Eg	exagram of carbon
EMIC	earth system model of intermediate complexity
EN	evergreen needleleaf
EnMAP	German Environmental Mapping and Analysis Program
EOS	end of season or leaf senescence
ER	ecosystem respiration
ESM	earth system model
ESMValToolv2.0	Earth System Model Evaluation Tool version 2
EWT	equivalent water thickness or leaf water content ($g \cdot cm^{-2}$)

FACE	free-air CO2 enrichment experiment
FAO	Food and Agriculture Organization of the United Nations
GBAF	Global Bio-Atmosphere Flux
GCC	green chromatic coordinate
GCP	Global Carbon Project
GFDL	American National Oceanic and Atmospheric Administration Geophysical Fluid Dynamics Laboratory
GFDL-ESM4.1	American National Oceanic and Atmospheric Administration Geophysical Fluid Dynamics Laboratory Earth System Model version 4.1
GLCS	global land carbon sink
GPP	gross primary production
GSWP3v1	forcing dataset used in the Land Surface, Snow and Soil Moisture Model Intercomparison Project
GtC	gigatonnes of carbon, equivalent to petagrams of carbon (10^{15} g)
HAZEL	dataset of leaf optical measurements and biochemistry collected in Moscow, Russia
H_2O	water
HR	heterotrophic respiration
HWSD	Harmonized World Soil Database
IGBP	International Geosphere-Biosphere Programme
ILAMB	International Land Model Benchmarking package
IPCC	Intergovernmental Panel on Climate Change
IPSL	Institut Pierre Simon Laplace

IPSL-CM6A-LR	Institut Pierre Simon Laplace earth system model
IR	infrared portion of the electromagnetic spectrum (750 nm – 1,000 μm)
ISBA-CTRIP	Interaction Soil-Biosphere-Atmosphere with Total Runoff Integrating Pathways with carbon cycling
ITATINGA	dataset of leaf optical measurements and biochemistry collected in Itatinga, Brazil
JAMSTEC	Japanese Agency for Marine-Earth Science and Technology
JM	Jeong leaf senescence model
JSBACH3.2	land surface model of the Max Planck Institute for Meteorology Earth System Model version 1.2 Low Resolution
JULES	Joint UK Land Environment Simulator
LACF	land-atmosphere CO_2 flux
LAI	leaf area index
LC	land cover
LM4.1	American National Oceanic and Atmospheric Administration Geophysical Fluid Dynamics Laboratory Land Model version 4.1
LMA	leaf mass per unit area or leaf dry matter content ($g \cdot cm^{-2}$)
LOESS	locally estimated scatterplot smoothing
LOPEX	Leaf Optical Properties Experiment database collected at Ispra, Italy
LOS	length of season
LSM	land surface model
LUT	look up table
MIP	model intercomparison project

MIROC-ES2L	Model for Interdisciplinary Research on Climate Earth System version 2 for Long-term simulations
MODIS	Moderate Resolution Imaging Spectroradiometer
MP	megapixel
MPI	Max Planck Institute
MPI-ESM1.2-LR	Max Planck Institute for Meteorology Earth System Model version 1.2 Low Resolution
MTE	model tree ensemble
N_2	nitrogen gas
NBP	net biome production
NCAR	Climate and Global Dynamics Laboratory at the American National Centre for Atmospheric Research
NCC	Norwegian Climate Consortium
NCSDV2	Northern Circumpolar Soil Carbon Database version 2
NDVI	normalized difference vegetation index
NECB	net ecosystem carbon balance
NEE	net ecosystem exchange
NEON	NEON.D07.GRSM.DP1.00033 phenocam
NEP	net ecosystem production
NERC	United Kingdom Natural Environmental Research Council
Net	network
NH_3	ammonia
NH_4^+	ammonium

NIR	near infrared region of the electromagnetic spectrum (750 – 1,400 nm)
nm	nanometer
N_2O	nitrous oxide
NO_2	nitrogen dioxide
NORESM2	Norwegian Earth System Model version 2
NOURAGUES	dataset of leaf optical measurements and biochemistry collected at the CNRS Nouragues experimental research station, French Guiana
NPP	net primary productivity
NRMSE	normalized root mean squared error
NULL	null model
Obs4MIP	Observations for Model Intercomparison Project
ORCHIDEE	Organising Carbon and Hydrology In Dynamic Ecosystems land surface model
PDF	probability density function or probability distribution function with a continuous variable
PFT	plant functional type
PgC	petagrams of carbon, equivalent to gigatonnes of carbon (10^{15} g)
phenocam	phenology camera
PLSR	partial least square regression
ppmv	parts per million by volume
PROCWT	continuous wavelet transformation combined with the PROSPECT model
PROSPECT	leaf optical properties model
PTT	photo-thermal time leaf emergence model

PTTs	photo-thermal time with sigmoidal temperature response leaf emergence model
RCP	representative concentration pathway
RMS	root mean square
RMSD	root mean square deviation
RMSE	root mean squared error
ROI	region of interest
RTM	radiative transfer model
SIMUL-N	simulated dataset of PROSPECT model parameters, reflectance, and transmittance
SAC	spectral specific absorption coefficient
SAIL	Scattering by Arbitrarily Inclined Leaves model
SC	soil carbon
SLA	specific leaf area
SOS	start of season or leaf emergence
SQ	sequential leaf emergence model
SR1.5	Intergovernmental Panel on Climate Change Special Report on the impacts of global warming of 1.5 °C
SRMSE	standardized root mean squared error
Surf[CO2]	surface CO_2 concentrations
SWIR	shortwave infrared region of the electromagnetic spectrum (various definitions, herein 1,400 – 3,000 nm)
TB	total biomass

TCR	transient climate response
TCRE	transient climate response to cumulative CO_2 emissions (K EgC^{-1})
TT	thermal time leaf emergence model
TTs	thermal time with sigmoidal temperature response leaf emergence model
UKESM1-0-LL	United Kingdom Community Earth System Model
VIRGINIA	dataset of leaf optical measurements and biochemistry collected in Moscow, Russia
VB	vegetation biomass
VC	vegetation carbon
VIS	visible region of the electromagnetic spectrum (400 – 750 nm)
VISIT-e	Vegetation Integrative Simulator for Trace gases model
WATCH	Water and Global Change forcing dataset
WCRP	World Climate Research Programme
WFDEI	Water and Global Change forcing dataset Methodology Applied to ERA-Interim data
WISE30Sec	harmonized soil property values for broad-scale modelling
WM	White leaf senescence model
yr	year
ZD^2OM	Zero Dimensional Diffusive Ocean heat and carbon uptake Model

List of Symbols

a	response parameter in leaf phenology model
A	the rising portion of the greenness curve between the onset of leaf growth and the seasonal peak in greenness (10-90% amplitude)
$a1$	dormancy induction sensitivity parameter in leaf phenology model
$a2$	threshold modification parameter in leaf phenology model
b	response parameter in leaf phenology model
B	the plateau portion of the greenness curve following the seasonal peak in greenness (95-50% amplitude)
β	rate of atmospheric CO_2 change
$b2$	threshold modification parameter in leaf phenology model
B_B	intensity of the blue colour channel
B_G	intensity of the green colour channel
B_R	intensity of the red colour channel
Bo	unit conversion for carbon (m^2 Pg mol^{-1})
c	response parameter in leaf phenology model
C	the entire leaf-on period of the greenness curve (50-50% amplitude)
°C	degrees Celsius
C_A	atmospheric carbon pool
C_{AO}	original atmospheric carbon pool
C_i	biochemical constituent content per unit of leaf surface for constituent i
C_{req}	threshold for forcing accumulation in leaf phenology model
d	rate of chilling accumulation parameter in leaf phenology model

D_{crit}	threshold for dormancy induction or senescence in leaf phenology model
df	forcing accumulation parameter
DR_p	rate of dormancy induction accumulation based on photoperiod
DR_t	rate of dormancy induction accumulation based on temperature
ε	ratio of sea surface temperature change to global temperature change
$\overline{EOS_o}$	mean leaf senescence date from all observations
F_{crit}	critical threshold for leaf emergence or senescence
f_o	fraction of the Earth covered by ocean
G_{CC}	green chromatic coordinate
gT	daylength sensitivity parameter
h_L	forcing sensitivity parameter in leaf phenology model
k	response parameter in leaf phenology model
k	number of sample groups used in k-fold cross validation
K	degrees Kelvin
l	land-borne fraction of carbon
L_{crit}	threshold for daylength accumulation for dormancy induction in leaf phenology model
L_i	daylength in leaf phenology model
M	merit function for the inversion of the PROSPECT model
N	number of uniform compact layers within leaves in the PROSPECT model
N	ocean heat uptake in the ZD^{2}OM model
$N_{SWIR,R}$	linear model for estimating the N parameter in the PROSPECT model with the full spectral range of reflectance

$N_{SWIR,T}$	linear model for estimating the N parameter in the PROSPECT model with the full spectral range of transmittance
$N_{VNIR,R}$	linear model for estimating the N parameter in the PROSPECT model with the availability of VIS and NIR spectral reflectance
$N_{VNIR,T}$	linear model for estimating the N parameter in the PROSPECT model with the availability of VIS and NIR spectral transmittance
p	number of biochemical constituents to be retrieved in the PROSPECT model model
ρC_p	specific heat capacity of water
r	Pearson correlation coefficient
R	radiative forcing from an e-fold increase in atmospheric CO_2 concentration (W m^{-2})
R_λ	measured reflectance
$\widehat{R_\lambda}$	simulated reflectance
R^2	coefficient of determination
R_{800}	reflectance at the wavelength 800 nm
R_{1131}	reflectance at the wavelength 1,131 nm
R_{Amin}	reflectance measured at the wavelength of minimum absorption
R_{chl}	rate of chilling in leaf phenology model
R_{frc}	rate of forcing in leaf phenology model
R_p	rate of photoperiod reducing in leaf phenology model
R_t	rate of temperature cooling in leaf phenology model

R_{tp}	rate of temperature cooling and photoperiod reducing in leaf phenology model
S_a	threshold modification parameter of anomaly in leaf emergence in the preceding spring relative to the 30-year average
S_{chl}	state of chilling in leaf phenology model
S_{frc}	state of forcing in leaf phenology model
S_{DR}	state of dormancy induction accumulation in leaf phenology model
$\overline{SOS}_o$	mean leaf emergence date from all observations
S_p	state of accumulated photoperiod reducing in leaf phenology model
S_t	state of accumulated temperature cooling in leaf phenology model
S_{tp}	state of accumulated temperature cooling and photoperiod reducing in leaf phenology model
τ	unit conversion for heat (s a^{-1})
t	time
T_λ	measured transmittance
$\widehat{T}_\lambda$	simulated transmittance
T_{800}	transmittance at the wavelength 800 nm
T_{1121}	transmittance at the wavelength 1,121 nm
T_{Amin}	transmittance measured at the wavelength of minimum absorption
T_b	base temperature for accumulation in leaf phenology model
T_{b1}	temperature for combined temperature daylength senescence trigger in leaf phenology model

T_{b2}	temperature for singular temperature senescence trigger in leaf phenology model
T_i	daily mean temperature in leaf phenology model
T_{max}	maximum temperature for chilling accumulation in leaf phenology model
T_{min}	minimum temperature for chilling accumulation in leaf phenology model
To	change in sea surface temperature
t_0	starting date in leaf phenology model
t_{0c}	starting date for chilling in leaf phenology model
t_{0f}	starting date for forcing in leaf phenology model
T_{opt}	optimum temperature for chilling accumulation in leaf phenology model
μ	effective ocean diffusivity (m^2 a^{-1})
$\mathrm{V}_{\mathrm{cmax25}}$	maximum rubisco carboxylation rate at 25°C and high irradiance per unit leaf area in $\mu mol \cdot m^{-2} \cdot s^{-1}$
Vq	ocean heat removal velocity
$W_{R,\lambda}$	weight applied to squared residuals between measured and simulated reflectance
$W_{R,\lambda}$	weight applied to squared residuals between measured and simulated transmittance
x	exponential weight parameter for temperature importance in leaf phenology model
y	exponential weight parameter for daylength importance in leaf phenology model
λ	climate feedback parameter (W m^{-2} °C^{-1})

λ_1	the first wavelength included in a PROSPECT model inversion
λ_n	the final wavelength included in a PROSPECT model inversion
Γ	ocean surface dissolved inorganic carbon change from e-fold change in atmospheric CO_2

List of Appendices

Chapter 1. Introduction and overview

1.1 Overview and objectives

1.1.1 Overview

Greenhouse gas emissions from land use change, agriculture, and industrialization have led to an energy imbalance at the top of Earth's atmosphere, trapping heat which would otherwise radiate to space. The most abundant non-condensing greenhouse gas emitted through human activities in Earth's atmosphere is carbon dioxide (CO_2), followed by methane (CH_4) and nitrous oxide (N_2O). Since the dawn of the Industrial era (~1750 CE) until 2022, atmospheric CO_2 has risen in concentration from about 278 parts per million by volume (ppmv) to about 415 ppmv, amounting to a 50% increase (Friedlingstein et al., 2022). Vegetation within the terrestrial biosphere reduces this rise in atmospheric CO_2 concentration through the process of photosynthesis within leaf tissues which translates atmospheric CO_2 into carbohydrates and biomass. Carbon uptake by vegetation removes about a third of anthropogenic CO_2 emissions from the atmosphere, for example 3.5 gigatonnes of carbon (GtC) of the 10.9 GtC total anthropogenic emissions emitted in 2021, substantially reducing the warming impact of emissions (Friedlingstein et al., 2022).

The capacity for vegetation to continue to uptake this portion of anthropogenic emissions is uncertain (Fatichi et al., 2019; Krause et al., 2018; Friedlingstein, 2015). Climate-driven changes in growing conditions including gradual and abrupt alteration of temperature and moisture regimes that have the potential to both promote and inhibit vegetational carbon uptake. The proximate driver of climate change, elevated atmospheric CO_2 concentrations, also has the potential to promote, not affect, or even inhibit vegetational carbon uptake. For example, elevated atmospheric CO_2 concentrations lead to increased photosynthetic substrate availability or the ‘CO_2 fertilization effect’ for C3 plants and may promote increased vegetational carbon uptake as well as increased light-use and water-use efficiency (Ainsworth and Long, 2005). On the other hand, nutrient constraints, limited moisture, and photosynthetic acclimation in the context of elevated CO_2 may prevent increases in vegetational carbon uptake despite elevated CO_2 concentrations (Bäurle et al., 2023). Elevated atmospheric CO_2 may even lead to declines in nutrient acquisition within plants, which could culminate in vegetation carbon losses (Gojon et al., 2022). Plant phenology, the timing of recurrent plant biological events such as leaf emergence and leaf senescence, is influenced by temperature, daylength, moisture, and other variables (Lieth, 1974). In the extratropics, warming leads to a climatically lengthened growing season, promoting increased carbon uptake (Sakalli et al., 2017; Arora and Boer, 2014). Over recent decades across the northern high latitudes, the winter seasons have been exhibiting greater warming than the summer season (Gong et al., 2017; Graham et al., 2017). With sufficient winter warming, the timing or even occurrence of some plant phenological phases could be altered. For example, some phases require a certain duration and intensity of chilling to proceed and warming during the winter could delay the meeting of these requirements or lead to mortality through a premature loss of cold hardiness (Caffarra et al., 2011; Bokhorst et al., 2009). Another important consideration is that warming increases the rate of cellular respiration leading to more CO_2 emissions to the atmosphere. This counteracts the warming-enhanced carbon uptake in vegetation, though the magnitude of this counteraction is uncertain (Watts et al., 2021; Liu et al., 2020; Dusenge et al., 2019; Fatichi et al., 2019; Bronson and Gower, 2010).

In addition to seasonal changes, extreme weather in the form of frost events, heat waves, ice storms, windstorms, and hurricanes associated with enhanced climate variability interrupt vegetational carbon uptake and can lead to sustained carbon losses (Gong et al., 2021;

Richardson et al., 2018). Together these climate-driven phenomena lead to reduced carbon uptake, counteracting the growing season warming benefit. To formulate confident predictions of climate change and consequent climate policy, more research and model development is needed to understand the combined implications of extended growing seasons, changing growing season conditions, extreme weather for vegetation functioning, and different responses between species (IPCC, 2021; Arora and Boer, 2014; Jeong et al., 2012). Observations of vegetation function with improved spatial and temporal resolution are needed to address these uncertainties and fine-tune models at the intra-seasonal and individual tree functional scale (Spafford and MacDougall, 2021[1]; Fatichi et al., 2019).

1.1.2 Objectives

Through my thesis, I aim to reduce uncertainty surrounding the feedback of terrestrial vegetation to global change. I incorporate modelling and observational approaches to promote the integration of more finely resolved observational platforms into terrestrial vegetation climate change feedback research. With a broad scale approach, I examine the role of the terrestrial carbon exchange among other variables in influencing the relationship between the driving force of climate change, anthropogenic CO_2 emissions, and global temperature change. Through alterations to a commonly used model, I provide a means to improve the success and accessibility of leaf biochemical constituent estimations. This elucidation of leaf-scale characteristics and function translates into an improved understanding of canopy and global scale processes. I also apply a cost-effective high fidelity observational technique to reveal important environmental constraints on leaf phenology and a means to detect interruptions to vegetation carbon uptake. Together the insights from this technique provide critical background on global

---

[1] This paper was adapted from the written component of my comprehensive examination and is included in Appendix I.

scale implications of plant processes for the carbon cycle and ecological integrity. My thesis is composed of the following themes: the relationship between cumulative CO_2 emissions and global temperature change (chapter 2), how techniques of observing vegetation function can be improved through hyperspectral observations at the leaf-scale (chapter 3), calibrating species specific predictive models with timelapse canopy scale imagery to examine leaf phenology under a range of emissions scenarios (chapter 4), and a novel ecological indicator for the fine-scale detection of climate-driven interruptions to carbon uptake by vegetation (chapter 5).

1.1.3 Transient Climate Response to Cumulative CO_2 Emissions

The Transient Climate Response to Cumulative CO_2 Emissions (TCRE) is the near-linear relationship between total anthropogenic CO_2 emissions and global temperature change. This near linearity arises due to two phenomena which occur simultaneously: the reduction in radiative forcing per unit CO_2 emissions as atmospheric CO_2 concentration increases (sometimes mistakenly called the saturation effect), and a reduction in the heat and carbon uptake efficiency of the ocean with increased CO_2 emissions (Figure 1-1; MacDougall, 2017; MacDougall and Friedlingstein, 2015; Allen et al., 2009; Matthews et al., 2009). In simple terms, this leads to less warming per unit atmospheric CO_2 in junction with more carbon and heat staying in the atmosphere as emissions accumulate and global temperatures increase.

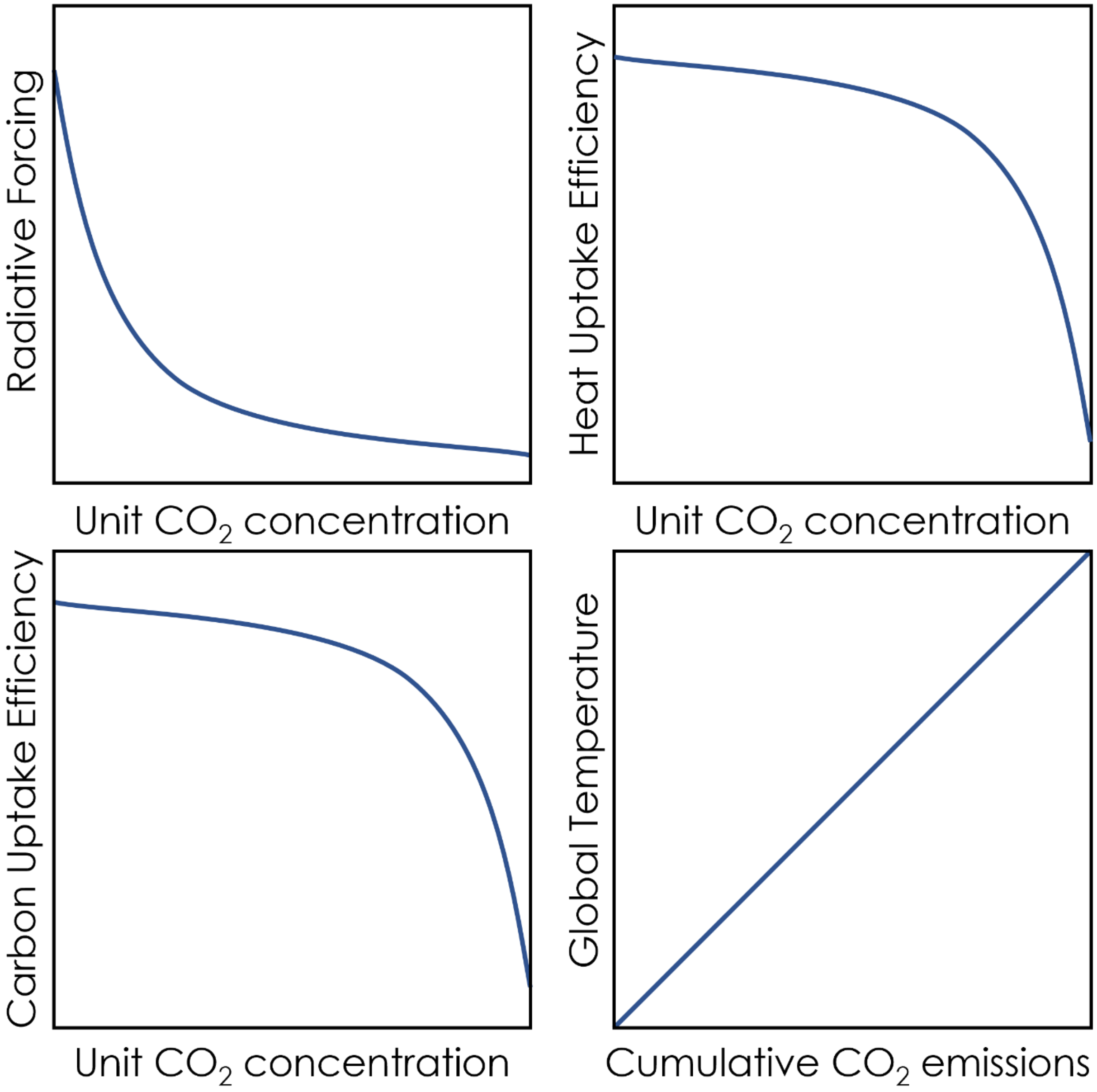

Figure 1-1*. An idealized representation of radiative forcing (left top), heat uptake efficiency by the ocean (top right), and carbon uptake efficiency by the ocean (bottom left) per unit* CO_2 *concentration as* CO_2 *concentrations increase. In combination, these phenomena result in the near-linear relationship between global temperature and* CO_2 *emissions which is the foundation for the concept of the TCRE (right).*

The TCRE is conveyed in units of temperature change per unit carbon of CO_2 emissions, such as Kelvin or degrees Celsius per exagram (10^{18} g) of carbon emissions (EgC) denoted as 'K

EgC^{-1}' or rarely '°C EgC^{-1}' (due to the Celsius, carbon confusion). Carbon uptake by the terrestrial biosphere along with other Earth System processes influence the TCRE in unique ways (e.g., MacDougall and Friedlingstein, 2015). This relationship between CO_2 emissions and global temperature change largely determines the severity of climate change resulting from human activities, and therefore in turn exerts an interactive influence upon the terrestrial biosphere. The TCRE is one of the most useful metrics for climate change policy and mitigation. It conveys the explicit relationship between CO_2 emissions and warming, allowing the designation of carbon budgets compatible with avoiding a particular threshold in global temperature change. Additionally, given the near linearity of the relationship between cumulative CO_2 emissions and global temperature change conveyed by the TCRE, carbon budgets can be meaningful climate change communication tools which do not vary much between divergent complex emissions scenario pathways. Dissecting the combined driving influences on the TCRE is crucial to understanding the role of terrestrial vegetation in dampening or exacerbating future climate change, and in turn the potential severity of climate change affecting terrestrial vegetation due to anthropogenic CO_2 emissions.

The concept of the TCRE arose in the early 21st century when researchers found that Earth System Model simulations displayed a near-linearity between cumulative CO_2 emissions and global temperature change (MacDougall, 2016; Eby et al., 2013; Gillett et al., 2013; Matthews et al., 2009; Gregory et al., 2009). A metric closely related to the TCRE and commonly used in Earth System Model studies is the transient climate response (TCR) which conveys the temperature change corresponding to a doubling in atmospheric CO_2 concentration relative to the pre-industrial era under idealized conditions (Nijsse et al., 2020). Unlike the TCR, the TCRE incorporates the uncertainty from not only the relationship between atmospheric CO_2

concentrations and global temperature change, but also the relationship between CO_2 emissions and atmospheric CO_2 concentrations.

There are two main approaches to estimate the TCRE, using observations or models. Observational studies usually involve observationally constrained simulations or detection and attribution analyses. A range of estimated TCRE values have arisen from observational studies, with best estimates ranging from about 1.3-1.9 K EgC^{-1} (Jenkins et al., 2021; Millar and Friedlingstein, 2018; Gillett et al., 2013; Allen et al., 2009). Attributing the portion of observed warming since the pre-Industrial era due only to CO_2 emissions is particularly challenging, due to uncertainty in observational records as well as climate variability affecting land and ocean carbon uptake (Spring et al., 2020; Matthews et al., 2014). Alternatively, model-based studies typically involve the use of simple (MacDougall, 2017; Raupach et al., 2011; Katavouta et al., 2019), intermediate (Herrington and Zickfeld, 2014; Williams et al., 2016; Goodwin et al., 2015; Eby et al., 2013), or full-complexity (Arora et al., 2020; Tachiiri et al., 2019; Tokarska et al., 2016; Williams et al., 2017) Earth System Models. As with observational studies, a range of estimated TCRE values have arisen from model-based studies, with best estimates ranging from about 1.1-2.2 K EgC^{-1}. (Tachiiri et al., 2019; Goodwin et al., 2015). While there is no clear trend in reported values of the TCRE from observational and model-based studies over the last two decades, successive Intergovernmental Panel on Climate Change reports have shown a reduction in the uncertainty of carbon budgets developed from the TCRE over time. The Sixth Assessment Report estimated the likely range for the TCRE as between 1.0-2.3 K EgC^{-1} while the previous Fifth Assessment Report estimated this range as 0.8-2.5 K EgC^{-1} (IPCC 2021; IPCC 2013).

In chapter 2 of this thesis, I provide evidence that the probability distribution function of the TCRE is best characterized as log-normal rather than normal as is commonly assumed. In

Chapter 2 I also demonstrate that climate sensitivity along with the portion of land-borne carbon, that is the portion of excess carbon emissions which remains in the terrestrial biosphere rather than the atmosphere or ocean, exerts a predominant influence on the TCRE relative to other parameters. Other studies have found these two parameters to exert an important influence on the TCRE using a variety of observational and model-based approaches (IPCC, 2021; Arora et al., 2020; Jones and Friedlingstein, 2020; Katavouta et al., 2019; Gillett et al., 2013; Ehlert et al., 2017; MacDougall et al., 2017; Williams et al., 2017, 2020; Matthews et al., 2009). The value of the TCRE directly conveys the severity of global temperature change corresponding to a given quantity of anthropogenic CO_2 emissions. A higher TCRE value means a hotter climate future, affecting not only the health and vigour of the terrestrial biosphere though also the potential for the terrestrial biosphere to continue to ameliorate future emissions. The fraction of carbon cycled through the terrestrial biosphere is uncertain and has an important influence of the TCRE (Arora et al., 2020; Lovenduski and Bonan, 2017). For example, if excess carbon absorbed by vegetation is increasingly cycled through fast turnover pools such as through fine roots and respiration before quickly returning to the atmosphere rather than being cycled through long turnover pools such as woody biomass, this leads to a greater TCRE value. Chapter 2 demonstrates that uncertainty in our understanding of how carbon is cycled through the terrestrial biosphere is the second largest contributor to uncertainty in the TCRE. In order to more confidently estimate the TCRE and thus the severity of climate change resulting from human activities, an improved understanding of terrestrial carbon uptake through vegetation function is paramount.

1.1.4 Hyperspectral estimation of leaf biochemistry

Knowledge of how warming growing seasons and excess carbon will influence terrestrial carbon uptake is still quite limited due to a lack of fine-scale observations (Dow et al., 2022; Liu et al., 2020; Piao et al., 2008). Spafford and MacDougall (2021; Appendix I) and Lovenduski and Bonan, (2017) show that to better understand the feedback implications of terrestrial biosphere function, we need more spatiotemporally resolved observations of leaf development in response to gradual change, such as warming at atmospheric CO_2 accumulation over decadal scales, and in response to abrupt environmental changes, such as extreme weather and persistent climate anomalies. One promising pathway to filling this observational gap is through improving the accessibility of leaf biochemistry and canopy function observational technologies.

Biochemical and structural traits in leaves, such as pigments, water content, and dry matter content, enable essential physiological and biological functions such as photosynthesis and natural defence mechanisms (Wang et al., 2022; Féret et al., 2019; Croft et al., 2017; Usha Rani and Jyothsna, 2010). These constituents are therefore crucial to the continuation of vegetational carbon uptake in the context of global change. A variety of internal and external cues trigger the production, degradation, or mobilization of these constituents, such as temperature, soil moisture availability, and photoperiod, among others. Changes in moisture and temperature regimes have the potential to alter the quantity of these constituents in leaf tissues over seasonal to interannual timescales. These constituents also serve as indicators of physiological health, such as leaf equivalent water thickness in the context of dry growing conditions (Watt et al., 2021; Cao et al., 2015). In order to understand how global change might affect plant physiology and consequently vegetation carbon uptake, these constituents must be monitored over time in a variety of species and growing contexts.

Four trait constituents are predominantly monitored in leaf tissues: chlorophylls, carotenoids, equivalent water thickness (EWT), and leaf dry matter content (LMA). The chlorophyll a and b pigments are arguably the most commonly monitored constituents in leaves, as these pigments perform the majority of light energy harvesting in photosynthesis, are important indicators of nutritional status for precision agriculture, and are responsible for the typically green colour of vegetation (Zhu et al., 2020). Carotenoids are multi-purpose pigments that protect leaf tissues from harmful short wavelength radiation, support acclimation to heat stress, and also contribute to light energy harvesting in photosynthesis (Dhami and Cazzonelli, 2020). Leaf EWT, the quantity of water per unit area of leaves, expresses the drought resiliency status of vegetation, and can even reflect regional water resource availability (Li et al., 2021; Kattenborn et al., 2017). Leaf dry matter content is an important characterizing feature as it covaries with particular trait assemblages along the leaf economic spectrum and enables conversion between area and weight-based constituent quantities (Buraczyk et al., 2022; Lei et al., 2022). Together, LMA and EWT constitute a metric of fire risk through fuel moisture content (Féret et al., 2019). Chlorophyll a and b along with carotenoid pigments are expressed in units of $\mu g \cdot cm^{-2}$, while EWT and LMA are expressed in units of $g \cdot cm^{-2}$.

Each of these constituents reflect, absorb, and transmit light in unique ways. The concentration of biochemical constituents within leaf tissues can therefore be approximated by examining the pathway of light through leaf tissues. This can be performed with destructive or non-destructive techniques. Destructive techniques typically involve wet chemistry or drying processes (Lichtenthaler, 1987). Non-destructive techniques, such as hyperspectral monitoring, involve subjecting plant tissues to a light source and quantifying reflectance and transmittance across the visible and infrared wavelength spectra. There are a variety of techniques used for hyperspectral monitoring, though a commonly used technique is field-based spectroscopy, which allows for rapid, repeat, non-destructive measurements over time. Field-based spectroscopy involves the use of a spectroradiometer to measure hyperspectral reflectance and transmittance with a variety of measurement geometries (Figure 1-2). Light absorptance can then be calculated as the remaining portion of light unaccounted for as light is partitioned between reflectance, transmittance, and absorptance. This technique of measuring leaf biochemistry offers some advantages in being rapid, cost-effective, and non-destructive relative to laboratory-based wet chemistry or drying techniques which require sample preservation and transport to a laboratory.

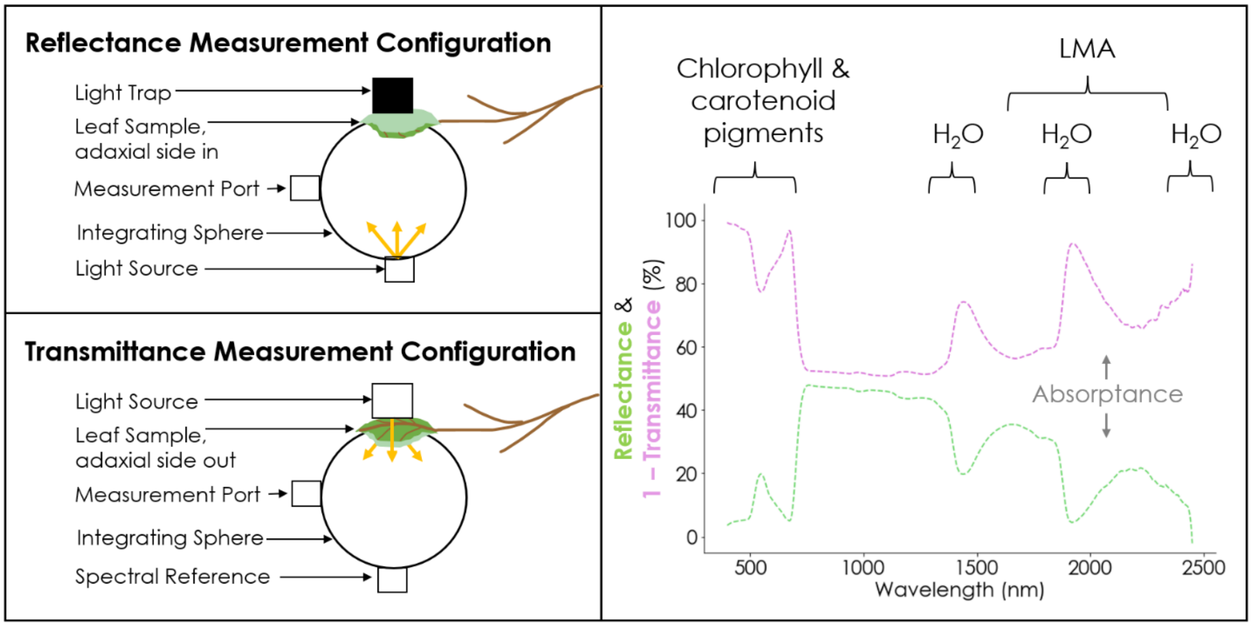

Figure 1-2. *On the left is shown an example measurement configuration of directional-hemispherical hyperspectral leaf reflectance (left top) and transmittance (left bottom) with an integrating sphere. Note measurement configurations vary among instruments and though typically include the use of a Spectralon reference standard and calibration or control measurements without the leaf sample. On the right is shown the regions of influence across the visible, shortwave infrared, and near infrared spectra by leaf biochemical constituents. Leaf mass per unit area (LMA) and water (H_2O) influence optical responses in the short wave and near infrared regions.*

Following field measurements, leaf biochemistry is estimated through one of three model-based approaches: statistical, physical, or a hybrid combination. Statistical models used to estimate leaf constituents typically involve regression models, spectral indices, or machine learning, and can produce highly accurate estimates of constituents following training (Féret et al., 2019; Hill et al., 2019; Kovar et al., 2019; Martin et al., 2018; Chavana-Bryant et al., 2017; Le Maire et al., 2004). A caveat to this approach is the requirement of an extensive training dataset which limits applicability to leaves collected from other species, growing contexts, and different leaf ages. This being said, novel statistical approaches have shown promise with independent validation and improved transferability (Furbank et al., 2021; Fu et al., 2019; Serbin et al., 2019). Contrary to statistical models, physical models simulate the fundamental relationship between light, leaf tissues, and leaf traits, and are therefore widely applicable without local calibration.

One of the most widely used physical models is the model of leaf optical properties spectra known as PROSPECT (Jacquemod et al., 2016; Jacquemoud and Baret, 1990). PROSPECT is a radiative transfer model, which treats leaves as a series of layered plates and reproduces the optical properties of leaves across the visible, shortwave, and near infrared domains, from 400 to 2500 nanometers (nm), based upon well-validated optical equations. The plate model PROSPECT is based upon was developed by Allen et al. (1969) and assumes leaves are composed of a series of superimposed plates, each plate having a particular reflectance and diffuse transmittance factor. Optical refraction and absorption through and within plates is modelled with the Stokes system of equations, dating back to the mid-19th century (Stokes, 1862). In forward mode, PROSPECT estimates directional-hemispherical reflectance and transmittance from leaf biochemical and structural traits including chlorophyll a and b, carotenoids, EWT, and LMA, the N number of hypothetical leaf plates, and other foliar constituents such as proteins (Féret et al., 2020; 2019; 2017). In inverse mode, PROSPECT provides estimates of these biochemical and structural traits from directional-hemispherical reflectance and transmittance measured with an integrating sphere (Schaepman-Strub et al., 2006; Figure 1-2). While PROSPECT has provided reliable estimates of these constituents for decades (Jiang et al., 2018; Féret et al., 2008; Le Maire et al., 2004; Jacquemoud et al., 1996), its integration into the research community is challenged by the strictness of the measurement requirements. For example, the physical assumptions of PROSPECT require the use of a directional-hemispherical integrating sphere rather than the more affordable and convenient leaf clip which can be used to measure bidirectional reflectance and estimate transmittance, though some researchers have directly applied PROSPECT to bidirectional leaf optical measurements (Hill et al., 2019; Kattenborn et al., 2019; Lassalle et al., 2019; Lu et al., 2018; Sonobe et al., 2018; Arellano et al., 2017; Shiklomanov et al., 2016; Buddenbaum et al., 2012). Chapter 3 of this thesis provides a means to better integrate stand alone reflectance or transmittance measurements for the purposes of extracting foliar constituents, which helps to bridge the applicability gap between PROSPECT and leaf clip measurements. Chapter 3 also shows that we can make substantial improvements to monitoring leaf-level leaf traits overall by accounting for leaf structure. With these techniques, the field-based measurement of leaf traits can become increasingly affordable and convenient, leading to more replicated measurements per unit effort.

Precise non-destructive measurements of leaf biochemical and structural traits improve the efficiency and success of precision agriculture, which will aid in meeting global agricultural, mitigation, and adaptation challenges in the context of climate change. For example, improved monitoring of chlorophyll pigments and EWT can reduce instances of excessive application of fertilizer and conserve water resources, helping to conserve resources and reduce the greenhouse footprint of agriculture (Zhu et al., 2020). The use of techniques included in chapter 3 of this thesis will improve the ease of application for hyperspectral measurements of leaf reflectance and transmittance, facilitating studies with greater replication in a variety of field conditions, such as remote locations in the tropics and high latitudes (Serbin et al., 2019; Asner et al., 2015). More replicated and temporally extensive datasets of foliar traits achieved through the adaptations presented in Chapter 3 are needed to realize inherent variation in leaf level traits not only at the global level though also at the community level (Nunes et al., 2017; Wright et al., 2004). With a better understanding of variation in these traits, more confident predictions of the potential responses of vegetation to global change can be formulated.

The widely applicable physical model basis of the PROSPECT model included in chapter 3 also improves the potential for estimating leaf structural and biochemical traits for species and in regions with limited sampling records available. The information provided through hemispherical monitoring contributes crucial insight into how vegetation will respond to climate change in terms of leaf biochemistry and structure, and whether vegetation will continue to sequester as much as one third of anthropogenic CO_2 emissions. For example, monitoring chlorophyll content in the context of warming and CO_2 elevation experiments with hemispherical spectroscopy can provide a direct indication of how these changes may influence vegetational carbon uptake through photosynthesis, as chlorophyll content is directly proportional to photosynthetic capacity (Croft et al., 2017). Another important gap in knowledge surrounding vegetation function in the context of climate change is how gradual and abrupt environmental changes might influence leaf function over time, especially with regards to pigments on sub-seasonal and interannual scales. To address this knowledge gap, while hyperspectral monitoring can provide high fidelity insight into pigment dynamics within leaf tissues (Yang et al., 2014), spatiotemporally resolved observations of leaf function at the canopy scale are also needed. A promising monitoring technique known as a phenocam in the form of a stationary timelapse camera monitoring at the canopy-scale is gaining momentum for this purpose (Richardson, 2019).

1.1.5 Global Change Implications of Climate-Driven Shifts in Leaf Phenology

Phenology, the study of the timing of recurrent biological phenomena in relation to climate, is often observed through plants, though other examples include insect emergence from diapause, animal reproduction, and animal migrations (Pureswaran et al., 2019; Renner and Zohner 2018; Lieth, 1974). Leaf phenology, the timing of leaf life cycle events, is a vital feature of the terrestrial biosphere, influencing structural and biochemical leaf traits and photosynthetic potential (Boren et al., 2019, Liu et al., 2019; Funk et al., 2017; Bonan et al., 2003). Leaf phenology has long been recognized as an ecologically important phenomenon related to both carbon cycling and ecological interactions (Piao et al., 2019; MacKay 1903). Common leaf phenology phases or phenophases studied include leaf emergence and leaf senescence (Figure 1-3).

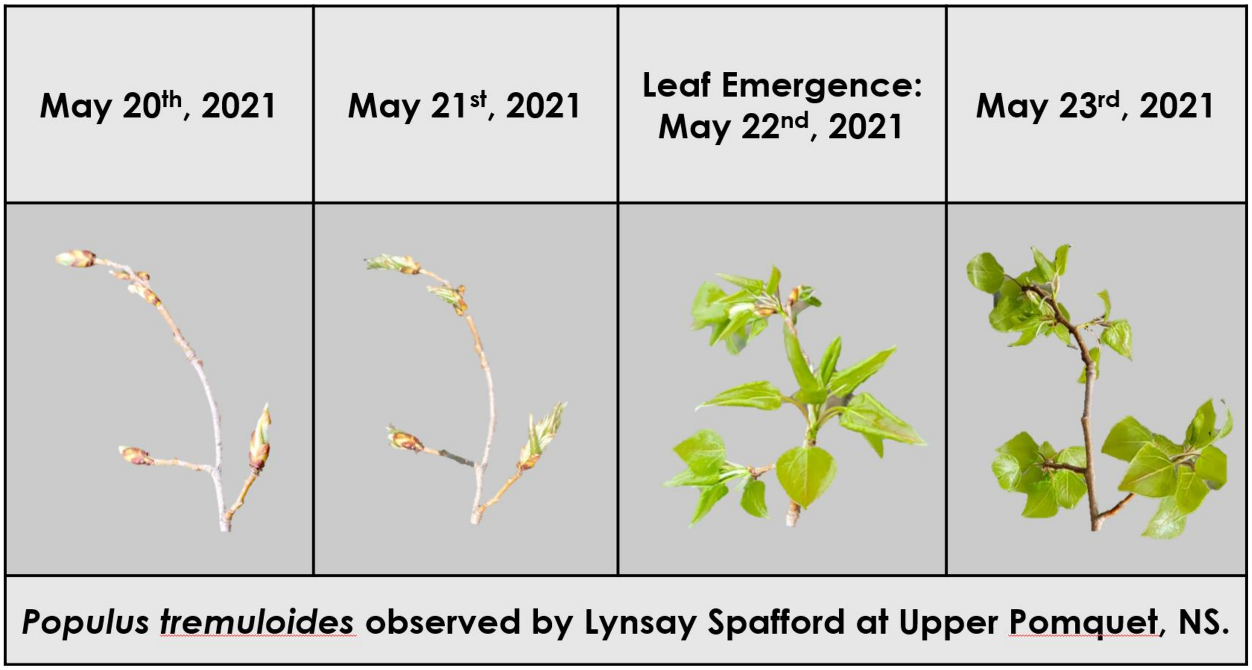

Figure 1-3. *An example photographed observation of the leaf emergence of Populus tremuloides.*

The timing of leaf emergence and leaf senescence varies within and among species (Reich et al., 1992), and both serve as sensitive indicators of the biological and ecological effects of climate change (Klosterman et al., 2014; Sonnentag et al., 2012; Morin et al., 2009). Warming has advanced leaf emergence over the last five decades (Piao et al., 2019; Estiarte and Peñuelas 2015; Peñuelas and Filella 2009; Menzel et al., 2006) and delayed leaf senescence (Xie et al., 2018b; Estiarte and Peñuelas 2015; Peñuelas et al., 2002; Menzel and Fabian 1999). Nevertheless, due to variation in evolved phenological cues between tree species, climate change has the potential to both advance and delay the timing of leaf emergence and senescence (Chen et al., 2019; Piao et al., 2019; Renner and Zohner 2018; Xie et al., 2018a; Keenan and Richardson 2015; Migliavacca et al., 2012; Tanino et al., 2010; Morin et al., 2009; Vitasse et al., 2009). For example, warm winters can delay leaf emergence due to reduced chilling accumulation required for the release from wintertime endodormancy for some species, and warming can also lead to early leaf senescence during the growing season due to heat stress (Xie et al., 2018b; Delpierre et al., 2016).

During the growing season of leaves, if climate-induced shifts in the timing of leaf emergence are not offset by shifts in the timing of leaf senescence, the lifespan of leaves will be altered (Keenan and Richardson 2015; Vitasse et al., 2011; Peñuelas and Filella 2009; Vitasse et al., 2009; Menzel et al., 2006; Matsumoto et al., 2003; Peñuelas and Filella 2001), with implications for the carbon cycle (Piao et al., 2019; Brown et al., 2016; Buitenwerf et al., 2015; Migliavacca et al., 2012), nutrient exchanges (Estiarte and Peñuelas 2015; Richardson et al., 2013; Fridley 2012; Vitasse et al., 2011; Niinemets 2010), and ecology (Renner and Zohner 2018; Xie et al., 2018b; Ellwood et al., 2015; Hufkens et al., 2012b). For example, if leaf emergence occurs earlier and leaf senescence occurs later, this could lead to an extension in the lifespan of leaves, and potentially increased carbon uptake (Sakalli et al., 2017; Piao et al., 2007). Conversely, extreme weather in the context of climate change such as late spring frost events, dry conditions, and hurricanes could result in damage or premature removal of leaf tissues. These phenomena consequently lead to carbon losses to the atmosphere on seasonal to interannual timescales due to depressed carbon uptake by vegetation within the season, nutrient losses, impediments to reproduction, or vegetation mortality (Richardson et al., 2018c). This uncertainty in the potential direction and magnitude of vegetational carbon uptake in response to climate change is compounded by the sparsity of studies examining how responses to climate change differ within and among species (Delpierre et al., 2020; Jeong et al., 2012). In combination, the potential for both lengthened and abbreviated leafing periods and the lack of species-specific perceptions challenges the certainty of predictions of vegetational carbon uptake in the context of climate change.

Plant phenology has a lengthy observational history, with some records dating to 1,000 BCE (Piao et al., 2019; Chen, 2013; Chuine et al., 2004; Ge et al., 2003; Lauscher, 1978; Chu, 1921). The longest near-continuous record of phenology observations is that of cherry (*Prunus jamasakura*) flowering in Kyoto, Japan, which has been recorded in diaries, chronicles, and newspapers for more than 600 years from 801 CE to the 21st century (Aono and Kazui, 2008). In western Canada, there is evidence of indigenous peoples recording phenophases to track the timing of available plant and animal resources (Beaubien and Hall-Beyer, 2003; Lantz and Turner, 2003). A transition in the motivation for recording leaf phenology came about in the 18th century, with the Marsham family phenological records and early forms of process-based models describing the influence of temperature on leaf emergence known as growing degree days (Sparks and Carey, 1995; Linnaeus, 1751; Réaumur, 1735). In this era, phenology became an area of scientific interest for geographers and natural historians, with experiments and observational networks established across Europe (Piao et al., 2019). This scientific interest in leaf phenology has continued for centuries, and in the early 20th century in the Canadian province of Nova Scotia, Dr. Alexander MacKay promoted the pastime of plant phenology observations among school children (MacKay et al., 1903).

In recent decades leaf phenology has garnered interest as a monitoring tool in the context of climate change (Schwartz et al., 2006). During this time a variety of approaches have been utilized for leaf phenology monitoring, with variable spatial and temporal resolution, each with distinct advantages and disadvantages (Liu et al., 2017; Morisette et al., 2009). As with previous eras of leaf phenology observations, manual observations of leaf phenology have been ongoing, providing high spatial resolution observations of leaf phenology at the individual or sub-individual scale (Holland et al., 2015). A disadvantage of this approach is the challenge of reconciling observer bias, as two different observers may quantify a phenophase stage differently. For example, one observer may score an individual tree as having 40% of leaves exhibiting fall colours, while another may score the same tree as having 60% of leaves coloured, and some observers may misidentify species or erroneously record phenomena (Liu et al., 2021; Sparks and Carey, 1995). In addition, these datasets are prone to observational gaps or having coarse temporal resolution due to their being laborious and costly in terms of fieldwork being required for each observation.

In contrast, since the 1970's, satellite-based observations have provided a broad scale perspective of land surface phenology, capturing objective quantifications of land surface features based upon remote sensing (Xiao et al., 2019). This technique of observation is not susceptible to observer bias, as remote sensing instruments are capable of quantitative rather than qualitative measurements. A drawback of this approach however is the coarse spatial and temporal resolution of satellite-based observations necessary to accommodate such broad extents. Additionally, while not susceptible to observer bias, quality control and post-processing measures are still required to rectify sun-sensor geometry, variable viewing angles, and atmospheric interference inherent in remote-sensing based observations (Lopes et al., 2016; Spanner et al., 1990). The spatiotemporal resolutions of satellite missions are continuously improving. In the late 20th century, the finest spatial resolution of observation technologies aboard satellite missions for the purpose of land surface phenology monitoring, such as Moderate Resolution Imaging Spectroradiometer (MODIS), ranged from 250 m to more than 5 km (Caparros-Santiago et al., 2021). In contrast, the recent Sentinel-2A twin satellite mission launched in June 2015 can collect observations every 5 days under cloud-free conditions with spatial resolutions of 10 m for some sampling bands (Brown et al., 2019; Grabska et al., 2019;

Vaduva et al., 2019). To precisely characterize leaf phenology patterns within and between species, quantitative observations are needed at the individual-tree scale at a daily or sub-daily frequency (Alberton et al., 2017; Klosterman et al., 2014).

Near-remote sensing through a time-lapse camera at the canopy level, or phenocam, provides a strategic bridge between the objective yet coarse spatiotemporal resolution of remote satellite observations and individually resolved yet potentially subjective nature of manual observations (Moon et al., 2021b; Browning et al., 2017). Since the early 2000's, phenocams have facilitated the ground truthing of satellite-based studies and high-fidelity analysis of processes spanning the individual to canopy scale and through networked phenocams the intercontinental scale (Richardson, 2019; Richardson et al., 2017; Brown et al., 2016). Most studies to date employing phenocams however do not consider the phenology of individual trees within the camera field of view, and instead often examine the average leafing dynamics amalgamated across the observed canopy (Richardson et al., 2018a). While this approach allows for efficient analysis of numerous canopies across extensive climate gradients, it obscures variability in intraspecific and interspecific responses to climate change. Studies which have considered species-level leaf phenology have shown the potential for unique species-specific responses to climate change (Denéchère et al., 2021; Delpierre et al., 2020; Peltoniemi et al., 2018; Delpierre et al., 2017; Nakaji et al., 2011).

Divergent species-specific responses to climate change connotate important ecological implications. Examples include a change in the success of native versus non-native species during the brief yet crucial period of acquiring resources for leaf emergence, and altered interactions within and across trophic levels due to phenological asynchrony (Pureswaran et al., 2019; Renner and Zohner, 2018; Wolkovich and Cleland, 2011). These ecological implications of divergent phenological changes translate into biogeochemical implications, as carbon uptake is an aggregate ecosystem process reflecting the activity of all producers. For example, the climate-driven proliferation of tropical lianas, which have adaptive traits and growing strategies that allow them to better capitalize on changing conditions in the context of climate change relative to slow growing species, could result in reduced carbon uptake across tropical forest ecosystems (van der Heijen et al., 2015). Consequently, observational techniques capable of observations at the individual scale are crucial to develop and train models of vegetation function which will accurately characterize feedbacks of terrestrial vegetation to climate change in terms of both biogeochemistry and ecology.

Phenocam studies have provided key insights into both ecological and biogeochemical implications of transitions in leaf phenology patterns and have informed mechanistic understandings of the processes of leaf emergence and senescence. Delpierre et al. (2020) applied phenocams at the individual tree scale at two sites in France and found that relatively cold springs promote a greater diversity in the timing of leaf emergence within a population relative to warm springs. This suggests that in a warmer climate, leaf emergence could be more synchronized within populations for some species. The alternative is also possible, that colder springs could lead to a greater range in the timing of leaf emergence within and between species due to chilling and daylength constraints. In addition, Delpierre et al. also reported extensive interannual variability in the timing of leaf emergence at each phenocam site by more than two weeks. This indicates that leaf phenology studies should ideally be performed over more than a single growing season in order to capture the influence of interannual variability in seasonal conditions on leaf phenology. With 12 phenocam sites monitoring birch trees across Finland, Peltoniemi et al. (2018) revealed the aptitude of phenocams to track leaf emergence and senescence of individual trees which represent a small portion of the image field of view. With replication across latitudes and years, Peltoniemi et al. also demonstrated a latitudinal gradient in the timings of leaf emergence and leaf senescence, and thus overall growing season length, which was conserved across all three years of the study. This suggests that individuals of a species may exhibit similar magnitudes of leaf phenology responses to climate change despite being located at disparate points within a region. Richardson et al. (2018c) applied phenocams to collect high temporal resolution observations of leaf phenology for an ecosystem warming experiment, revealing species-specific differences in susceptibility to gradual and abrupt changes in growing conditions. Interestingly, Richardson et al. (2018c) found that photoperiod did not constrain the timing of leaf emergence for spruce trees subject to as much as +9°C warming beyond ambient temperatures. Together these studies reveal the potential and value of phenocams for monitoring species-specific leaf phenology patterns and using these observations to predict leaf phenology patterns in the context of climate change.

Despite this wealth in knowledge generation, disagreements have also arisen as to prominent constraints on the timing of leaf emergence and leaf senescence. For example, Keenan and Richardson (2015) found that the timing of leaf senescence in the autumn is likely influenced by leaf emergence, implying a fixed growing season length or seasonal photosynthetic production limit which would constrain the leafing period in the context of climate change, which corroborates with other later works (Zani et al., 2020). Conversely, with a multi-faceted observation approach, Lu and Keenan (2021) found evidence that the timing of leaf senescence is not directly linked to the timing of leaf emergence based on a seasonal photosynthetic production limit. Across phenocam, field-based, and satellite-based studies, autumn leaf phenophases such as leaf colouration and senescence are understudied with respect to leaf emergence, and understandings of the mechanisms controlling the timing of leaf senescence are limited (Jiang et al., 2022; Gallinat et al., 2015). More phenocam studies including both leaf senescence and leaf emergence observations over interannual timescales and across multiple sites are needed to clearly identify the mechanisms of leaf emergence and senescence and predict their response to climate change.

With phenocam observations of both leaf emergence and leaf senescence over several growing seasons, in chapter 4 of this thesis I apply species-specific process-based modelling to reveal differences in the responses of temperate and boreal tree species to warming throughout the 21st century. I found that models which include the influence of photoperiod, preceding dormancy induction, and chilling exposure over the dormant period perform well in predicting the timing of leaf emergence for a variety of species across North America, agreeing with other studies that have found such components are influential in a variety of regions (Baumgarten et al., 2021; Beil et al., 2021; Caffarra et al., 2011). Chapter 4 also shows that the relationship between leaf senescence and seasonal temperatures is distinct from the relationship between leaf emergence and seasonal temperatures across a variety of growing season contexts. Despite the distinction between environmental cues for leaf emergence and senescence, the mathematical parameterizations of commonly used leaf senescence models are similar to that of leaf emergence models. Therefore a promising avenue for improved simulations of leaf senescence is the development of mathematically novel leaf senescence model equations.

In addition to uncertainty regarding how leaf phenology responds to environmental changes over seasonal timescales, another prominent research question is how leaf phenology responds to abrupt changes, such as abiotic disturbance, and how this in turn affects ecosystem ecology. Recent abiotic disturbances, such as Hurricane Dorian (Taylor et al., 2020), and

Hurricane Fiona (The Canadian Press, 2022), the latter of which exceeded previous weather and economic cost records in Canada, occurred during the short time period in which the research component of this thesis was conducted. Abiotic disturbances like these will become more frequent and intense as a consequence of climate change (IPCC, 2021). Despite its influence on a myriad of ecosystem processes, little work has been done to apply leaf phenology as an ecological indicator. Ecological indicators are useful metrics which convey the integrity of ecosystem processes such as carbon cycling over time. The novelty of leaf phenology as an ecological indicator due in part to the challenge of identifying leaf phenological changes which clearly correspond to disruptions in ecosystem processes. In chapter 5 of this thesis, I demonstrate a promising technique to detecting interruptions to leaf function and consequently carbon uptake due to extreme weather in the form of hurricanes, late spring frost events, drought, and more. Applying the insights shared in both chapters 4 and 5 will elucidate terrestrial vegetation feedbacks to climate change through both gradual phenological shifts and abrupt declines in carbon uptake due to extreme weather associated with climate change. Along with the techniques for precise characterization of leaf biochemistry provided in chapter 3, the role of terrestrial vegetation in influencing the linkage between global temperature change and cumulative anthropogenic CO_2 emissions, discussed in chapter 2, can be better resolved through the combination of insights afforded through these thesis chapters. In combination, the chapters of this thesis contribute fundamental insight and promising technical advancements to refine the feedback of terrestrial vegetation to global change.

1.2 Thesis outline

In addition to the introductory chapter, this thesis includes the following:

Chapter 2: Quantifying the probability distribution function of the transient climate response to cumulative CO_2 emissions. This chapter was published in Environmental Research Letters, 15(3), 034044, https://iopscience.iop.org/article/10.1088/1748-9326/ab6d7b/meta.

Chapter 3: Spectral subdomains and prior estimation of leaf structure improves PROSPECT inversion on reflectance or transmittance alone. This chapter was published in Remote Sensing of Environment, 252, 112176, https://doi.org/10.1016/j.rse.2020.112176.

Chapter 4: Climate-driven shifts in leaf senescence are greater for boreal species than temperate species in the Acadian Forest Region. This chapter is under review for publication in Ecology and Evolution (submitted on December 19th, 2022).

Chapter 5: Leaf phenology as an indicator of ecological integrity. This chapter was accepted for publication in Ecosphere on January 17th, 2023, Manuscript ID: ECS22-0592.

Appendix I: Validation of Terrestrial Biogeochemistry in CMIP6 Earth System Models: A Review. This paper was published in Geoscientific Model Development, 14(9), 5863-5889, https://doi.org/10.5194/gmd-14-5863-2021. This paper was adapted from the written component of my comprehensive examination.

Co-authorship statement

Within this thesis, chapters 2-5 and Appendix I were completed in collaboration with co-authors. I contributed the most of all co-authors to the completion of these manuscript chapters. For manuscript #1 (chapter 2) – “Quantifying the probability distribution function of the transient climate response to cumulative CO_2 emissions” by Lynsay Spafford and Andrew MacDougall (AM), I am the first author who analyzed the data and wrote the original manuscript. AM provided funding for this study. Both authors contributed to the revision process.

For manuscript #2 (chapter 3) – "Spectral subdomains and prior estimation of leaf structure improves PROSPECT inversion on reflectance or transmittance alone" by Lynsay Spafford, Guerric le Maire, Andrew H. MacDougall, Florian de Boissieu, and Jean-Baptiste Féret, I am the first author who wrote the original manuscript. I collaborated with JF and GM to conceive the study. I collaborated with JF to analyze the data and design the study. AM provided funding for this study. All authors contributed to the revision process.

For manuscript #3 (chapter 4) – "Climate-driven shifts in leaf senescence are greater for boreal species than temperate species in the Acadian Forest Region" by Lynsay Spafford, Andrew H. MacDougall, and James Steenberg, I am the first author who analyzed the data and wrote the original manuscript. I also conceived and designed the study. AM provided funding for this study. All authors contributed to the revision process.

For manuscript #4 (chapter 5) – "Leaf phenology as an indicator of ecological integrity" by Lynsay Spafford, Andrew H. MacDougall, Yann Vitasse, Gianluca Filippa, Andrew Richardson, James Steenberg, and Jelle Lever, I am the first author who analyzed the data and wrote the original manuscript. I also conceived and designed this study. AM provided funding for this study. All authors contributed to the revision process.

For manuscript #5 (Appendix I) – "Validation of Terrestrial Biogeochemistry in CMIP6 Earth System Models: A Review" by Lynsay Spafford and Andrew H. MacDougall, I am the first author who analyzed the data and wrote the original manuscript. I also conceived and designed this study. AM provided funding for this study. Both authors contributed to the revision process.

Chapter 2. Quantifying the probability distribution function of the Transient Climate Response to Cumulative CO_2 Emissions

This chapter was published in Environmental Research Letters, 15(3), 034044, https://iopscience.iop.org/article/10.1088/1748-9326/ab6d7b/meta.

2.1 Introduction

To avoid the most severe impacts of climate change the Paris Agreement aims to limit global warming to well below 2 °C relative to pre-industrial temperatures, and to pursue efforts to limit the warming to 1.5 °C (Falkner, 2016; Matthews et al., 2018; Mengis et al., 2018; Rogelj et al., 2016). Carbon dioxide is the principal driver of anthropogenic climate change due to its longevity (Eby et al., 2009; Knutti and Rogelj, 2015; Millar et al., 2017a) and the quantity of anthropogenic emissions of this gas (Matthews et al., 2018; Goodwin et al., 2018; Hofmann et al., 2006; MacDougall, 2015; MacDougall et al., 2015; Patarasuk et al., 2016; Randerson et al., 2015). Due to the saturation effect the radiative forcing per unit change in atmospheric CO_2 concentration decreases with increased atmospheric CO_2 concentrations. Simultaneously the heat and carbon uptake efficiency of the ocean decreases with increased radiative imbalance and atmospheric CO_2 concentrations. The combined effect of these complex nonlinear processes is a near linear increase in global surface air temperature with increased cumulative CO_2 emissions, known as the as the Transient Climate Response to Cumulative CO_2 Emissions (TCRE; Matthews et al., 2018; Mengis et al., 2018; Knutti and Rogelj, 2015; MacDougall, 2015; Gillett et al., 2013; MacDougall and Friedlingstein, 2015; Matthews et al., 2009). The finding of a linear relationship between CO_2 emissions and global mean temperature change has climate policy significance, suggesting that any given warming target is associated with a cumulative quantity of CO_2 emissions, regardless of the emission scenario followed (MacDougall, 2015; MacDougall et al., 2015; Gillett et al., 2013; Matthews et al., 2009; Krasting et al., 2014; MacDougall, 2017; Rogelj et al., 2019). The TCRE allows the development of a ‘carbon budget’, which conveys the total allowable quantity of CO_2 emissions consistent with not exceeding a certain temperature change limit (Matthews et al., 2018; Rogelj et al., 2016; Knutti and Rogelj, 2015; MacDougall et al., 2015; Rogelj et al., 2019; Allen et al., 2009; Herrington and Zickfeld, 2014; Zickfield et al., 2012).

Carbon budgets are effective climate policy tools (Falkner, 2016; Knutti and Rogelj, 2015; MacDougall, 2015; Allen et al., 2009; Zickfield et al., 2012; Messner et al., 2013; Rogelj et al., 2018), yet their application is challenged by scientific uncertainty in the TCRE, translating into an extensive breadth of estimated allowable CO_2 emissions compatible with a given temperature target (Matthews et al., 2018; Goodwin et al., 2018; Patarasuk et al., 2016; Rogelj et al., 2019; Rogelj et al., 2018; Matthews et al., 2017; Millar and Friedlingstein, 2018; Peters, 2018). While total carbon budgets reflect the amount of CO_2 emissions that can be released from the preindustrial period on, including past, present, and future CO_2 emissions, remaining carbon budgets are estimates of the amount of CO_2 emissions that can be released in the future without surpassing a given global warming temperature change limit (Rogelj et al., 2019). The remaining carbon budget must also account for non-CO_2 forcing, which reduces allowable CO_2 emissions, and thus makes the policy relevance of the metric more complex (Rogelj et al., 2018). CO_2-only total carbon budgets can be estimated by dividing a warming target by the TCRE, and remaining CO_2-only carbon budgets can be estimated by either dividing the remaining allowable warming with the TCRE or computing the total CO_2-only carbon budget and subtracting emissions to date (Rogelj et al., 2019; Rogelj et al., 2018). However remaining carbon budgets estimated this way assume a linearity in the TCRE which may not fully hold under constant, declining, or zero emissions (Matthews et al., 2018; Tachiiri et al., 2019).

The Intergovernmental Panel on Climate Change (IPCC) Special Report on the impacts of global warming of 1.5 °C (SR1.5) suggested a median 2 °C carbon budget from 2018 onwards of about 410 PgC (rounded to the nearest 5 PgC) corresponding to the 50th percentile of the TCRE distribution. The 67th to 33rd TCRE percentile range by the SR1.5 corresponds to a 2 °C remaining carbon budget range of 320–550 PgC (Rogelj et al., 2018), equivalent to about 37, and 29–50 years of emissions at current emission rates of 11 PgC yr^{-1}, respectively. While CO_2-only budgets constructed from TCRE inversion assume CO_2 is the sole climate forcing agent, in reality non-CO_2 greenhouse gases and aerosols influence temperature change (MacDougall et al., 2015; Gillett et al., 2013; MacDougall and Friedlingstein, 2015; Rogelj et al., 2019; Rogelj et al., 2018, Tokarska et al., 2018). The IPCC SR1.5 report indicates uncertainty due to non-CO_2 forcing may reduce the remaining median carbon budget for 1.5° C warming by 177 PgC or increase the budget by 123 PgC, due largely to the asymmetric influence associated with future declining sulfate aerosol emissions and uncertainty due to non-CO_2 scenario variation (Rogelj et al., 2018). With this caveat in mind, the TCRE can still be useful in prescribing allowable cumulative CO_2 emissions.

The probability density function (PDF) of the TCRE is often assumed to be a normal distribution (Millar et al., 2017a; Gillett et al., 2013; Matthews et al., 2009; Collins et al., 2013). However, there is little evidence to support the assumption of a normally distributed TCRE (Rogelj et al., 2019), and this assumption may have been an artefact inherited from the ensemble of opportunity within CMIP5 models. The Fifth Assessment Report of the IPCC (AR5) did not assess the PDF shape compatible with the proposed likelihood range for the TCRE, though the SR1.5

acknowledged the TCRE may have a normal or log-normal PDF, while not suggesting one as more likely than the other.

The SR1.5 chose to represent the influence of imprecise TCRE distribution uncertainty as +27 to +54 PgC for the 1.5 °C remaining carbon budget (Rogelj et al., 2018) showing the influence of an assumed log-normal rather than normal distribution. Previous studies show that climate sensitivity has a strong influence on estimates of the TCRE (MacDougall et al., 2017; Raupach et al., 2011). MacDougall et al. (2017) observed a small positive skew in a histogram of TCRE values produced through 150 perturbed physics ensemble simulations conducted with an Earth System Model (ESM) of intermediate complexity and suggested the positive skew of the TCRE is due to the long tail of the climate sensitivity PDF. Climate sensitivity is generally represented with a positively skewed distribution (Goodwin et al., 2018; Knutti et al., 2017; Olson et al., 2012; Pueyo, 2012), which may translate into the TCRE distribution (Rogelj et al., 2019; Collins et al., 2013). Pueyo (2012) provides arguments for the assumption of a log-normal PDF for prior distributions of the climate sensitivity parameter, their arguments also apply to the TCRE.

The uncertainty in the TCRE is primarily the result of uncertainty in climate sensitivity (Krasting et al., 2014; Knutti et al., 2017) followed by uncertainty in the carbon cycle response to CO_2 emissions (Matthews et al., 2018; 10]. The transient climate response (TCR) represents the transient warming response to a doubled atmospheric CO_2 concentration relative to pre-industrial levels (Knutti et al., 2017). Equilibrium climate sensitivity (ECS) is defined as the warming response to a doubled atmospheric CO_2 concentration relative to pre-industrial levels after the climate has fully equilibrated (Knutti et al., 2017). While the timescale of transient rather than equilibrium climate response is of more relevance to the TCRE, the uncertainty associated with climate sensitivity is primarily inferred from ECS, as the transient climate response is a less applicable model metric highly dependent upon emission pathway. The IPCC AR5 evaluated the ECS lies between 1.5 °C and 4.5 °C (66% confidence; Krasting et al., 2014; Knutti et al., 2017; Stocker, 2014). Equilibrium climate sensitivity is typically represented with a positively skewed distribution due to the nonlinear relationship between forcings and feedbacks (Randerson et al., 2015; Knutti et al., 2017). While ECS is an effective model inter-comparison tool, it does not encompass the uncertainty arising from how CO_2 emissions influence atmospheric CO_2 concentrations (MacDougall, 2015; Knutti et al., 2017), and therefore cannot be used to directly quantify the warming from CO_2 emissions.

How the carbon cycle responds to CO_2 emissions constitutes another major source of uncertainty for TCRE and carbon budget calculations after climate sensitivity (Matthews et al., 2018; Rogelj et al., 2019). Atmospheric CO_2 concentrations evolve from the combined influence of CO_2 emissions from land use change, and fossil fuel combustion, as well as CO_2 uptake by the ocean and terrestrial biosphere (Friedlingstein et al., 2014). The rate of ocean carbon uptake is predicted to decline initially in response to emissions due to the limited ocean alkalinity shifting the dissolved inorganic carbon equilibrium towards CO_2, the reduced solubility of dissolved CO_2 with increased ocean temperature (Randerson et al., 2015; Herrington and Zickfeld, 2014; Williams et al., 2016), and increased stratification (Ridgwell and Hargreaves, 2007). Processes contributing to an increased land carbon uptake include CO_2 fertilization, nitrogen deposition, aforestation, and a lengthening growing season, while conversely drought, deforestation, enhanced decomposition, nitrogen and phosphorus limitations reduce land carbon uptake, and these carbon losses are predicted to dominate future carbon-climate feedbacks (Randerson et al., 2015; MacDougall and Friedlingstein, 2015; Herrington and Zickfeld, 2014; Cox et al., 2013; Huntzinger et al., 2017; Jones et al., 2013; Shevliakova et al., 2013).

Rather than separately conceptualizing the uncertainty of two nonlinear, emission rate-dependent processes, the TCRE encompasses uncertainty from both climate sensitivity and carbon cycle feedbacks into a single metric largely robust to varying emission rates (Matthews et al., 2018; Rogelj et al., 2016; MacDougall, 2015; MacDougall et al., 2015; Krasting et al., 2014; MacDougall, 2017; Allen et al., 2009; Goodwin et al., 2015; Tokarska et al., 2016). Several approaches have been explored to estimate the TCRE, which can be classified as observational or simulation based, with the comprehensive IPCC AR5 best estimate ranging from 0.8 to 2.5 K EgC^{-1} (MacDougall, 2015; Collins et al., 2013).

Allen et al. (2009) employed observationally and comprehensively constrained simulations to estimate the TCRE at 2 K EgC^{-1}, with a 5%–95% confidence interval of 1.3–3.9 K EgC^{-1}. Gillett et al. (2013) used a detection and attribution analysis based on 150 years of observations, proposing a lower range of TCRE values from 0.7 to 2.0 K EgC^{-1} at 5%–95% confidence, with a best estimate of 1.35 K EgC^{-1}. Recently, using a standard detection and attribution technique, Millar and Friedlingstein (2018) estimated the TCRE to be 0.88–2.60 K EgC^{-1} (5%–95% confidence), with a best estimate of 1.31 K EgC^{-1}. Observational estimations of the TCRE have varied over the past decade, with no clear trend in mean or median values and confidence interval limits.

ESMs of simple (MacDougall, 2017; Raupach et al., 2011; Katavouta et al., 2019), intermediate (Herrington and Zickfeld, 2014; Williams et al., 2016; Goodwin et al., 2015; Eby et al., 2013), and full-complexity (Gillett et al., 2013; Tachiiri et al., 2019; Tokarska et al., 2016; Williams et al., 2017) have been used to study the TCRE and to establish a physical basis for the path independence of the TCRE (Matthews et al., 2009; MacDougall, 2017; Herrington and Zickfeld, 2014; Johns et al., 2011). Williams et al. (2016) used a set of full-complexity CMIP5 ESMs to diagnose the relative importance of thermal and carbon responses to CO_2 emissions, as well as the importance of non-CO_2 forcing. The full-complexity ESMs used in IPCC AR5 produced TCRE estimates of 0.8–2.4 K EgC^{-1}, with a median value of 1.6 K EgC^{-1} (Collins et al., 2013). Using the temperature outputs from 23 models of the CMIP5, and a perturbed physics approach within the University of Victoria Earth System Climate Model, MacDougall et al. (2017) found a mean TCRE of 1.72 K EgC^{-1}, and a 5%–95% confidence interval of 0.88–2.52 K EgC^{-1}, consistent with the CMIP5 range of 0.8–2.5 K EgC^{-1}. Generally, the estimated TCRE ranges from simulation-based approaches are more broad than those of observational based approaches (Matthews et al., 2018; Millar and Friedlingstein, 2018).

Here we calculate the TCRE based upon current understandings of the interactions between climate and carbon processes, examine the uncertainty distribution of the TCRE using a Monte-Carlo error propagation, explore the sensitivity of the TCRE to various Earth system parameters, and compute the CO_2-only carbon budget consistent with 2°C warming.

2.2 Methods

To calculate the TCRE, we used the Zero Dimensional Diffusive Ocean heat and carbon uptake Model (ZD^2OM) derived by MacDougall, (2017). The analytical model is based upon the mathematical definition of the TCRE by Matthews et al. (2009), the forcing response equation developed by Wigley and Schlesinger (1985) and a relationship for cumulative CO_2 emissions, summarized as follows:

$$\Lambda = \left(\frac{R(1-l)}{\lambda}\right)\left(\frac{\ln\left(\frac{C_A}{C_{AO}}\right)}{1+\frac{f_O \rho C_p \tau \varepsilon \sqrt{\beta}}{\sqrt{\mu \lambda^2 \ln\left(\frac{C_A}{C_{AO}}\right)}}}\right)\left(\frac{1}{C_A - C_{AO} + \frac{2 B_O \Gamma \ln\left(\frac{C_A}{C_{AO}}\right)^{\frac{3}{2}}}{3\sqrt{\mu \beta}}}\right) \quad 1\text{-}1$$

where Λ is the TCRE, R is radiative forcing from an e-fold increase in atmospheric CO_2, l is the land-borne fraction of carbon, λ is the climate feedback parameter, C_A is the size of the atmospheric carbon pool, C_{AO} is the original size of the atmospheric carbon pool, f_o is the fraction of the Earth covered by ocean, ρC_p is the specific heat capacity of water, τ is a unit conversion for heat in units of s a^{-1}, ε is the ratio of sea surface temperature change to global temperature change, μ is effective ocean diffusivity, β is the change rate of atmospheric CO_2, B_o is the unit conversion constant for carbon in m^2 Pg mol^{-1}, Γ is the ocean surface dissolved inorganic carbon change from e-fold change in atmospheric CO_2. We assumed a present-day CO_2 concentration of 400 ppmv, corresponding to a C_A of 852 PgC. We assumed C_{AO} to be constant at 596.4 PgC. For the complete derivation of Equation 1-1, see MacDougall, (2017; https://static-content.springer.com/esm/art%3A10.1038%2Fs41598-017-10557-x/MediaObjects /41598_2017_10557_MOESM1_ESM.pdf).

To examine the PDF for the TCRE, we calculated the TCRE using a Monte-Carlo error propagation (n = 10,000,000) drawing parameter values from PDFs of the climate feedback parameter (λ) (W m^{-2} $°C^{-1}$), radiative forcing from an e-fold increase in atmospheric CO_2 (R) (W m^{-2}), effective ocean diffusivity (μ) (m^2 a^{-1}), the land-borne fraction of carbon (l), and the ratio between sea surface and global temperature change (ε) (Figure 2-1). To explore the sensitivity of the TCRE to these parameters and their distributions, we conducted a sensitivity analysis assuming normal distributions, and another assuming uniform distributions between the minimum and maximum plausible values for each input parameter PDF (Appendix II: Figures A2-1, A2-2, and Table A2-1). These sensitivity tests explore the important influence of prior distribution assumptions in computing uncertain parameters such as the TCRE (Pueyo, 2012).

The correlations between the TCRE and each parameter value for each iteration were also computed to understand the portion of variation in the TCRE explained by each parameter.

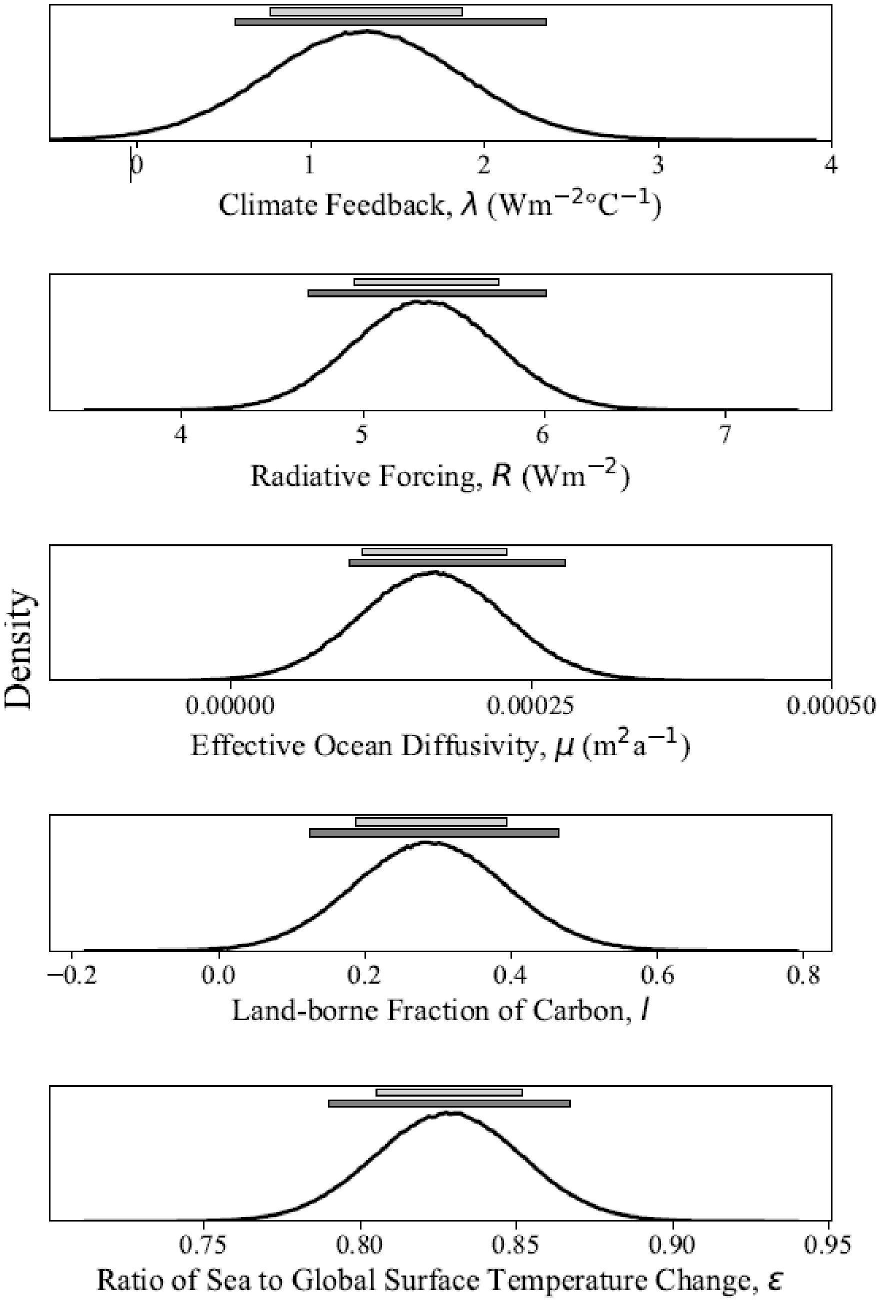

Figure 2-1. *Probability density functions (PDFs) of parameters used in the calculation of the TCRE. The light grey bar designates a 16%– 84% confidence interval, and the dark grey bar designates a 5%–95% confidence interval.*

To develop the PDF for λ (climate feedback), we first computed the PDF for climate sensitivity, from the combination of two normal inverse gaussian distributions following Olson et al. (2012). We designated the median value of the climate sensitivity PDF as 3.0 °C W m^{-2}, to reflect the combined likely PDF suggested by Knutti et al. (2017) developed from historical warming, climatological constraints on full complexity models, and paleoclimate data, including Rohling et al. (2012). To convert climate sensitivity values to λ values, we divided 3.71 W m^{-2}, the radiative forcing for a doubling of CO_2 (Knutti et al., 2017; Myhre et al., 1998), by the climate sensitivity PDF values. We conducted a sensitivity analysis to examine the effect of varying or holding constant the climate forcing associated with a doubling of CO_2, in constructing the λ PDF and subsequently calculating the TCRE, shown in Appendix II: Figure A2-5 of the supplementary material. The median and mean values of the λ PDF were 1.24 and 1.32 W m^{-2} $°C^{-1}$, corresponding to equilibrium climate sensitivity values of 3.0 and 2.8 °C W m^{-2}.

To develop the PDF for R (radiative forcing from an e-fold increase in atmospheric CO_2), we assumed a normal distribution around a mean value of 5.35 W m^{-2}, calculated from the radiative forcing corresponding to a doubling of CO_2, 3.71 W m^{-2} (MacDougall et al., 2017; Knutti et al., 2017; Myhre et al., 1998) with a standard deviation of 0.4 W m^{-2} based upon the mean variability of three methods of CO_2 radiative forcing estimation (MacDougall et al., 2017; Andrews et al., 2012; Vial et al., 2013; Zhang and Huang, 2014). While there is an inverse correlative structure between R and λ (Ringer et al., 2014), we chose to vary these parameters independently to assess the influence of each parameter on the TCRE. The R parameter is relatively well constrained, though the λ is less well constrained, and could vary independently of radiative forcing from CO_2 due to the influence of forcing from aerosol and non-CO_2

greenhouse gas emissions, as well as unforced climate variability (Knutti et al., 2017; Gregory and Andrews, 2016; Paynter and Frölicher, 2015). However to explore the influence of the correlative structure between R and λ we conducted an additional Monte Carlo simulation to calculate the PDF of the TCRE while varying these parameters with dependent probabilities (see Appendix II: Figure A2-3).

We generated the PDF for μ (effective ocean diffusivity) using the relationship for ocean heat removal velocity (V_q) in a diffusive half-space, which is inversely proportional to the root of the product of μ and time (MacDougall, 2017):

$$V_q = \frac{1}{\sqrt{\mu t}},$$

where t is time. We used t values selected from a uniform distribution ranging from 75 to 100 years, corresponding to a stability in the fit between ocean heat removal velocity values and diffusive approximations within the ZD^2OM (MacDougall, 2017). We obtained V_q from ocean heat uptake as follows (MacDougall, 2017):

$$V_q = \frac{N}{\rho C_p T_o},$$

where T_o is the change in sea surface temperature and N is the ocean heat uptake. We represented the uncertainty in *N* using a normal distribution centered on 0.71 W m^{-2} with a standard deviation of 0.11 W m^{-2} corresponding to the 2005.5–2015.5 period by Johnson et al. (2016), with a corresponding change in sea surface temperature since the preindustrial era (1850) until the midpoint of the 2005.5–2015.5 period (2011) of 0.63 °C (Zhang et al., 2019). We then generated the PDF for μ from V_q, in units of m^2 a^{-1}. The PDF for μ had a mean value of 1.69 ×

10^{-4} m^2 a^{-1} and a median value of 1.57×10^{-4} m^2 a^{-1}. In representing the ocean in a diffusive manner, we are approximating in a simplified way the advection dominated ocean ventilation processes which control ocean heat and carbon uptake in the natural ocean. On annual to centennial timescales, ocean heat and carbon removal at the global scale in ESMs have been shown to mimic that of a diffusive process (MacDougall, 2017). Thus our approximation, though simple, is consistent with processes simulated in complex models, for our timeframe of interest. However this simplification of ocean ventilation processes may negatively bias the TCRE, as it omits the surface warming effect of reduced ocean heat uptake with weakened overturning circulation which occurs in the natural ocean.

We generated the PDF for ε (ratio between sea surface and global temperature change) using a normal distribution constructed from the ratio of decadal mean sea to global surface temperature anomalies from 1950 to 2010, relative to the 1880–1910 normal (MacDougall, 2017; Zhang et al., 2019), with a mean ratio of 0.83 and standard deviation of 0.02.

We generated the PDF for l (land-borne fraction of carbon) based upon land-borne CO_2 emissions and net CO_2 emissions from 1750 to 2011 estimated by the IPCC AR5 (Collins et al., 2013). We generated two normal distributions, one for land-borne CO_2 emissions and one for net CO_2 emissions, with mean values of 160 and 550 PgC and standard deviations of 55 and 52 PgC. We then generated the PDF for l by calculating the ratio of land-borne CO_2 emissions PDF values to the net CO_2 emissions PDF values using 10,000,000 randomly chosen values from each PDF. The PDF for l had a mean value of 0.29 and standard deviation of 0.10.

2.3 Results and Discussion

Figure 2-2 shows the PDF for the TCRE as calculated using our method. The TCRE has a positively skewed PDF ranging from 1.1 to 2.9 K EgC^{-1} (5%–95% confidence), with mean and median values of 1.9 K EgC^{-1} and 1.8 K EgC^{-1}, respectively. This is comparable to previous estimates (Table 2-1), though with a positively shifted range of values relative to the IPCC AR5 expert judgement range of 0.8–2.5 K EgC^{-1} (Collins et al., 2013). While our lower limit of the 5%–95% confidence interval is slightly greater than previous estimates (Millar and Friedlingstein, 2018; MacDougall et al., 2017; Smith et al., 2018), our upper limit is considerably higher than previously reported upper limits (Matthews et al., 2018; Gillett et al., 2013; Herrington and Zickfeld, 2014; MacDougall et al., 2017; Goodwin et al., 2015; Frölicher and Paynter, 2015; Katavouta et al., 2018). Our mean and median values are similar to previous estimates (MacDougall and Friedlingstein, 2015; Allen et al., 2009; Herrington and Zickfeld, 2014; Tachiiri et al., 2019; Frölicher and Paynter, 2015; Katavouta et al., 2018; Cherubini et al., 2014; Partanen et al., 2017; Steinacher and Joos, 2016; Zickfeld et al., 2013). The agreement we observed between our TCRE estimates and previous estimates in terms of lower limits, mean, and median values, in contrast to the relatively high upper limit we found suggests that the TCRE may exhibit a more positively skewed distribution than previously thought, though this observation may be sensitive to assumed prior distributions. Allen et al. (2009) and Matthews et al. (2018) also reported asymmetry in the range of Cumulative Warming Commitment or TCRE values observed from simple, intermediate, or full complexity ESMs. The Cumulative Warming Commitment is the peak warming associated with a quantity of cumulative CO_2 emissions, and therefore equivalent to the TCRE assuming a negligible zero-emissions commitment, or the amount of unavoidable warming following cessation of CO_2 emissions. However Allen et al. (2009) suggested the asymmetry in the distribution of the Cumulative Warming Commitment is due to the possibility of a substantial zero-emissions commitment.

Table 2-1. *The interval, best estimate, and median values of the TCRE estimated by this study and previous studies.*

TCRE Inteval (K EgC^{-1})	**Range**	**Best Estimate (K EgC^{-1})**	**Median (K EgC^{-1})**	**Reference**
1.0–2.7	5%–95% Confidence	1.9	1.8	This study
1.14–1.26	Inter-simulation range	-	-	Katavouta et al., 2019
2.08–2.37	Inter-simulation range	2.2	-	Tachiiri et al., 2019
1.1–2.4	5%–95% Confidence	1.8	1.7	Katavouta et al., 2018
0.88–2.60	5%–95% Confidence	1.3	-	Millar and Friedlingstein, 2018
0.96–2.23	5%–95% Confidence	-	1.4	Smith et al., 2018
~0.9–2.1	5%–95% Confidence	~1.6	-	Wang et al., 2018
1.1–2.1	Inter-model range	-	-	Ehlert et al., 2017
0.88–2.52	5%–95% Confidence	1.72	-	MacDougall et al., 2017
0.65–2.28	17%–83% Confidence	-	1.29	Millar et al., 2017a
1.0–2.4	5%–95% Confidence	1.5	-	Millar et al., 2017b
1.63–1.73	Seasonal range	1.68	-	Partanen et al., 2017
1.39–2.21	2 standard deviations	1.8	-	Williams et al., 2017
1.25–1.54	Inter-scenario range	-	-	Hansen et al., 2016
1.3–2.1	2 standard deviations	1.7	-	Leduc et al., 2016
1.93–1.98	Inter-simulation range	1.95	-	Liddicoat et al., 2016
-	-	1.72	-	Simmons and Matthews, 2016

1.3–2.7	17%–83% Confidence	1.9	-	Steinacher and Joos, 2016
1.28–1.9	Inter-model range	1.64	-	Tokarska et al., 2016
2.31–2.67	Inter-simulation range	1.69	-	Williams et al., 2016
1.21–1.80	Inter-simulation range	-	-	Zickfield et al., 2016
1.1–2	2 standard deviations	1.4	-	Frölicher and Paynter, 2015
0.6–1.6	5%–95% Confidence	1.1	-	Goodwin et al., 2015
1.61–1.71	Inter-scenario range	1.66	-	Leduc et al., 2015
-	-	2.2	-	MacDougall and Friedlingstein, 2015
1.57–1.79	Inter-simulation range	-	-	MacDougall et al., 2015
1.8–2.4	Inter-scenario range	2.2	-	Nohara et al., 2015
1.4–3.1	Inter-simulation range	-	-	Randerson et al., 2015
1.1–1.7	5%–95% Confidence	-	-	Tachiiri et al., 2015
1.6–2.3	2 standard deviations	1.95	-	Cherubini et al., 2014
1.9–2.4	5%–95% Confidence	-	2.1	Friedlingstein et al., 2014
1.7–1.9	Inter-scenario range	1.8	-	Herrington and Zickfield, 2014
0.76–1.04	Inter-scenario range	-	-	Krasting et al., 2014
1.07–2.12	Inter-model range	1.57	-	Eby et al., 2013
0.8–2.5	66% Confidence	-	-	IPPC AR5 – Collins et al., 2013 & SR1.5 – Rogelj et al., 2018

0.7–2.0	5%–95% Confidence	1.3	-	Gillett et al., 2013
1.4–2.5	5%–95% Confidence	1.9	-	Zickfield et al., 2013
1–2.5	5%–95% Confidence	1.8	-	Matthews et al., 2012
1–2	5%–95% Confidence	-	-	Rogelj et al., 2012
0.8–1.9	Inter-simulation range	-	-	Williams et al., 2012
1.3–1.52	5%–95% Confidence	1.4	-	Zickfield et al., 2012
1.0–4.0	Inter-model range	-	-	Johns et al., 2011
-	-	-	2	Raupach et al., 2011
1.4–2.5	5%–95% Confidence	1.9	-	Allen et al., 2009
1.0–2.0	5%–95% Confidence	1.6	-	Matthews et al., 2009
1.1–2.7	5%–95% Confidence	-	-	Meinshausen et al., 2009
-	-	1.5	-	Zickfield et al., 2009

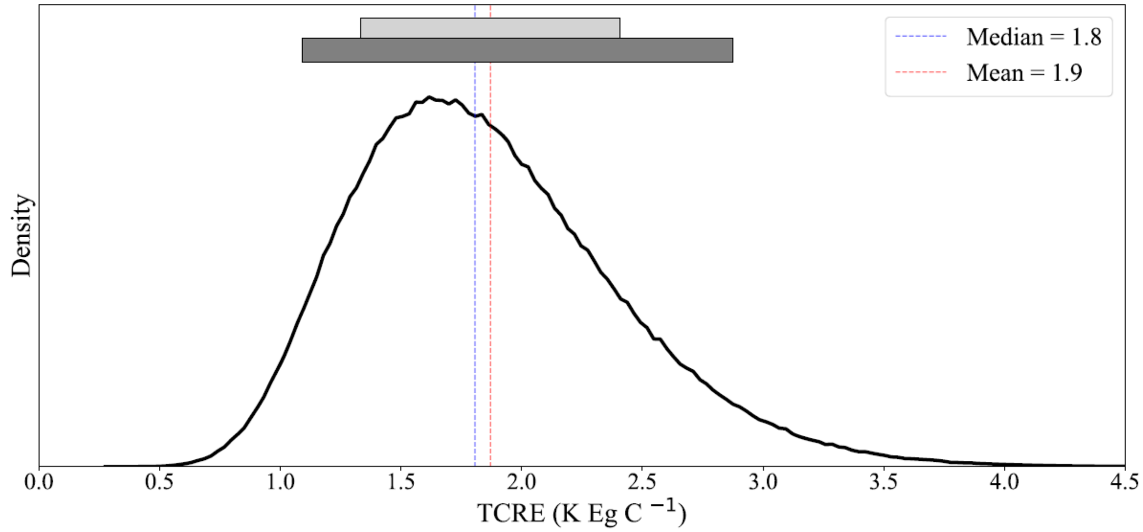

Figure 2-2. *Probability density function of calculated TCRE values. The light grey bar designates a 16%–84% confidence interval, and the dark grey bar designates a 5%–95% confidence interval.*

The results of our sensitivity analyses revealed that the form of the TCRE we observed is robust to the distribution of the underlying parameters, when all parameters are assigned normal distributions, the TCRE still is best approximated with a log-normal distribution PDF (see Appendix II: Figures A2-1 and A2-2), therefore it can be concluded that the positive skew of the TCRE is likely not inherited directly from the skewed distribution of the climate feedback parameter, though it may similarly be the result of mathematically combining two varying uncertain parameters to calculate the TCRE.

The transient climate response, the warming expected at the time of atmospheric CO_2 concentration doubling relative to the pre-industrial period under an idealized 1% yr^{-1} CO_2 increase experiment, also follows a positively skewed PDF (Knutti et al., 2017; Millar et al., 2017b). The commonality of the application of physical climate parameters for the equation of the TCRE with that of the transient climate response may provide another explanation for the shape of the TCRE PDF we observed. The transient climate response is determined by the ratio of observed warming to radiative forcing under a doubled atmospheric CO_2 concentration and has a positively skewed distribution due to the assumption of non-stationary feedbacks within the climate system in response to radiative forcing. Therefore the form of the TCRE we observed may be the result of the assumption of non-stationary feedbacks.

Given the difference between the median and mean value we observed was small, <0.1 K EgC^{-1}, the implications of this asymmetry for allowable carbon budgets may be negligible assuming the true value of the TCRE lies near the centre of this PDF. However, if the true value of the TCRE is actually within either tail of the PDF, though unlikely, assuming a normally distributed TCRE PDF rather than a log-normally distributed PDF may overestimate allowable carbon budgets. While the use of median values rather than mean values in describing the central tendency of an uncertain parameter is more robust to outliers (Kokoska and Zwillinger, 2000), it may be important to consider the implications of the difference between the median and mean value for a log-normally distributed variable such as the TCRE. We recommend where possible for future studies of the TCRE to report both a mean and median value, and that the mean value is used for the basis of carbon budgets to avoid overestimation of allowable carbon budgets.

Figure 2-3 shows the correlations between input parameters and TCRE values for each iteration. The most important parameter to the TCRE is the climate feedback parameter, followed by the land-borne fraction of carbon, radiative forcing, effective ocean diffusivity, and lastly the ratio of sea to global surface temperature change. Our observed hierarchy in importance is similar to that observed by MacDougall et al. (2017), who found a $r = 0.86$ between climate sensitivity and the TCRE, −0.39 with ocean heat uptake, and 0.17 with radiative forcing for a doubling of CO_2. As climate sensitivity is inversely proportional to climate feedback, ocean heat uptake is inversely proportional to effective ocean diffusivity, and radiative forcing for a doubling of CO_2 is directly proportional to radiative forcing for an e-fold increase in CO_2, our results for the relative importance of climate feedback, effective ocean diffusivity, and radiative forcing are in agreement with MacDougall et al. (2017).

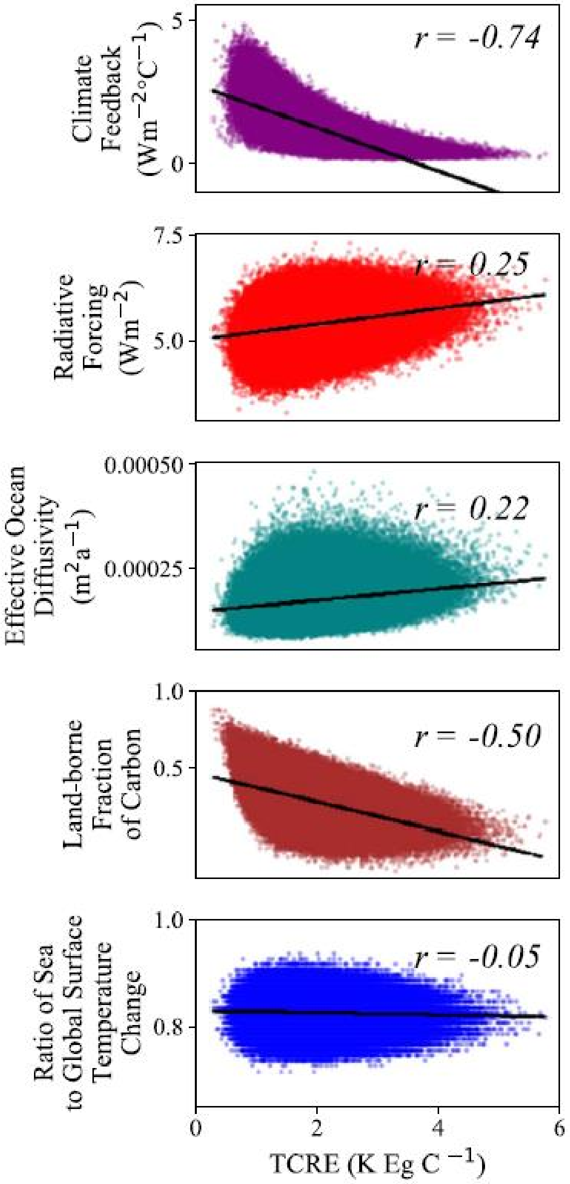

Figure 2-3. *Input parameter values versus TCRE values computed for each iteration (n=10,000,000). The line denotes the line of best fit between the values of a given parameter and the associated calculated TCRE values.*

The ocean plays a predominant role in the global uptake of excess energy at the surface, and an important role in modulating the airborne fraction of CO_2 emissions, and thus modulates the TCRE (Williams et al., 2016; Goodwin et al., 2015; Katavouta et al., 2019; Williams et al., 2017; Katavouta et al., 2018; Ehlert et al., 2017). Heat and CO_2 are taken up by the mixed layer of the ocean and transported through depth primarily via advective meridional circulation (Katavouta et al., 2019). This mechanism is expected to vary substantially with a changing temperature stratification regime within the ocean (Williams et al., 2016; Williams et al., 2017), though a recent study, Ehlert et al. (2017) suggests the processes of ocean heat and carbon flux scale linearly with changes in vertical mixing. We have chosen to represent ocean heat and CO_2 uptake using a diffusive approximation for simplicity, and as at a global scale ocean uptake of heat and CO_2 mimics that of a diffusive process, as previously shown in intermediate and full-complexity ESMs (MacDougall, 2017). This simplifying assumption may over-estimate heat uptake by the ocean, by omitting the important influence of a changing ocean ventilation in response to isopycnal heave associated with increased stratification weakening ocean meridional circulation (Purkey and Johnson, 2013). Katavouta et al. (2018), Ehlert et al. (2017), Williams et al. (2016), and Goodwin et al. (2015) suggest processes of ocean heat and carbon compensate one another in affecting the linearity between surface warming and cumulative CO_2 emissions. Williams et al. (2016) further advise that the warming effect of decreased ocean heat uptake may exceed the cooling effect by ocean uptake of CO_2, and Goodwin et al. (2015) show that a predicted drift in the Atlantic meridional overturning uptake alters thermal uptake more than carbon uptake, while Ehlert et al. (2017) show that variations in vertical ocean mixing have a greater influence on the TCRE than changes in mixing along isopycnals. Thus caution is warranted when extending our results beyond decadal to centennial time-scales at which the diffusive approximation works well (MacDougall, 2017).

To examine how our calculated TCRE differs from a normally distributed TCRE PDF, we generated a normally distributed TCRE PDF with an identical mean and standard deviation to that of our calculated TCRE PDF, as well as a log-normally distributed PDF, shown in Figure 2-4. Note that a PDF generated this way can have non-physical values corresponding to continuous prescribed probabilities rather than sampled TCRE estimates. A normally distributed TCRE has a negatively shifted 5%–95% confidence range relative to the calculated TCRE, 1.0–2.8 K EgC^{-1} and 1.1– 2.9 K EgC^{-1}, respectively. Previous studies which construct a PDF for the TCRE assuming a normal distribution using standard deviation and mean TCRE estimates may negatively bias confidence intervals for the TCRE, even if reported mean values and standard deviations are representative.

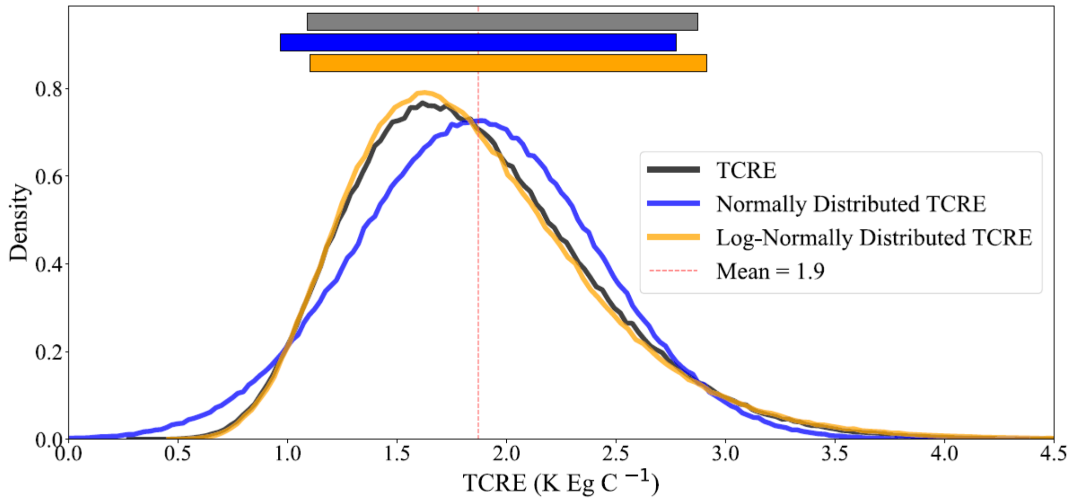

Figure 2-4. *Probability density function (PDF) of calculated TCRE values, a normally distributed TCRE PDF, and a log-normally distributed TCRE PDF, the latter two based upon the mean and standard deviation of calculated TCRE values. Each bar designates a 5%–95% confidence interval, the grey bar corresponding to the calculated TCRE, the blue bar corresponding to a normally distributed TCRE and the orange bar corresponding to a log-normally distributed TCRE.*

To limit global warming to 2 °C relative to pre-industrial temperatures, the CO_2-only cumulative carbon budget is between 700 and 1,800 PgC (5%–95% confidence), with a best estimate value of 1,100 PgC (rounded to the nearest 100 PgC). Figure 2-5 shows the consequences of a calculated TCRE PDF relative to a normally distributed TCRE PDF with regards to a CO_2-only carbon budget. A calculated TCRE reduces the upper confidence limit of the CO_2-only carbon budget. While both share a mean projected carbon budget of 1,100 PgC, a normally distributed TCRE produces a greater upper limit of emissions allowance than the calculated TCRE, 2,100 and 1,800 PgC, respectively. At annual emissions of 11 PgC yr^{-1}, the difference between these upper limits is equivalent to about 27 years of emissions.

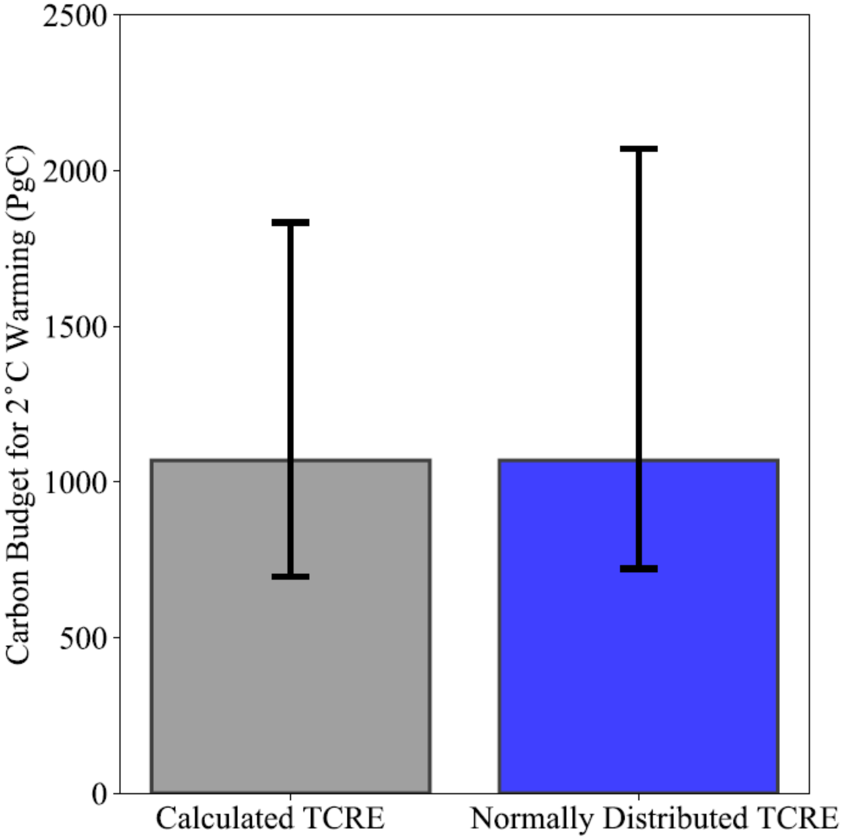

Figure 2-5. *The quantity of CO_2 emissions consistent with not exceeding 2°C in warming according to the calculated TCRE (grey) and a normally distributed TCRE (blue). Error bars designate 5%–95% confidence intervals.*

While the TCRE and proposed CO_2-only carbon budgets relate the primary driver of anthropogenic climate change, CO_2 emissions, to global warming, these do not take into account the influence of non-CO_2 greenhouse gas and aerosol emissions (MacDougall and Friedlingstein, 2015). Caution is warranted in the interpretation and application of CO_2-only carbon budgets associated with the TCRE, as these overestimate emissions compatible with a given temperature target by not encompassing non-CO_2 forcing (Rogelj et al., 2018).

2.4 Conclusions

Here we have examined the uncertainty distribution of the Transient Climate Response to Cumulative Emissions (TCRE) using a Monte-Carlo error propagation and found the TCRE to have a positively skewed PDF best approximated as a log-normal distribution rather than a normal distribution as is commonly assumed (Rogelj et al., 2018; Collins et al., 2013). The TCRE ranges from 1.1 to 2.9 K EgC^{-1} at 5%–95% confidence, with a mean and median value of 1.9 and 1.8 K EgC^{-1}. While our lower limit and mean estimate of the TCRE is consistent with previous estimates, our upper limit is greater than previous estimates. We explored the relative influence of sources of uncertainty for the TCRE and found that climate feedback is the most influential parameter, followed by the land-borne fraction of carbon, radiative forcing, effective ocean diffusivity, and lastly the ratio of sea to global surface temperature change. A positively skewed TCRE reduces the upper limit on CO_2-only carbon budgets, producing a CO_2-only carbon budget for 2° C warming of 700–1800 PgC at 5%–95% confidence, while a normally distributed TCRE produces a budget of 700–2100 PgC at 5%–95% confidence. The difference in the upper limit estimates on carbon budgets corresponds to about 27 years of emissions at 11 PgC yr^{-1}. The uncertainty in the TCRE and associated carbon budgets is substantial. However the representation of the TCRE as a log-normal PDF improves estimations of the TCRE and associated carbon budgets. Given the large roles of climate sensitivity and the land-borne fraction of carbon, improved estimates of these variables may contribute to reducing uncertainty in the TCRE and carbon budgets.

Chapter 3. Spectral subdomains and prior estimation of leaf structure improves PROSPECT inversion on reflectance or transmittance alone

This chapter was published in Remote Sensing of Environment, 252, 112176, https://doi.org/10.1016/j.rse.2020.112176.

3.1 Introduction

Climate change may alter the fitness and interactions of global plant functional types due to changes in temperature (Ciais et al., 2005; Euskirchen et al., 2009; Gray and Brady, 2016), moisture (Allen et al., 2010; Zandalinas et al., 2018; Breshears et al., 2013), and nutrient (Sardans and Peñuelas, 2015; Yuan and Chen, 2015; Bardgett et al., 2013) regimes. Leaf biochemical and structural traits are physiological indicators of leaf functioning, fundamental to multiple fields including environmental monitoring (Ali et al., 2016; Luyssaert et al., 2007), agriculture (Faucon et al., 2017; Martin and Isaac, 2015; Le Maire et al., 2011), land-use management (Murray et al., 2013; Yebra et al., 2008; Gross et al., 2007), ecology (Shipley et al., 2016; Maire et al., 2015; Levine, 2016; Le Maire et al., 2013), and modelling (Le Maire et al., 2008; Nouvellon et al., 2010).

Photosynthetic pigments are primarily studied in the forms of chlorophyll a and b, and carotenoids (including xanthophylls and carotenes). These pigments dominate light absorption in the visible region of the electromagnetic spectrum, from 400 nm to 750 nm (VIS). Chlorophylls are key molecules for photosynthesis as they absorb light energy and contribute to its conversion into chemical energy. Carotenoids are accessory pigments participating in light energy harvesting, and performing photoprotection from harmful radiation (Zarco-Tejada et al., 2013; Hernández-Clemente et al., 2012). The ratio of chlorophyll a and b to carotenoid content provides information on leaf function, as chlorophyll content (Cab, expressed in mass per leaf surface unit) is dynamic throughout a leaf life cycle or under conditions of environmental stress (Féret et al., 2008; Gitelson et al., 2017), while carotenoid content (Cxc, expressed in mass per leaf surface unit) content is relatively stable until an advanced stage of senescence (Féret et al., 2017; Chavana-Bryant et al., 2017; Coussement et al., 2018).

Leaf water content, known as equivalent water thickness (EWT, expressed in mass per leaf surface unit), and leaf dry matter content, known as leaf dry mass per unit area (LMA, expressed in mass per leaf surface unit), the inverse of specific leaf area (SLA), are two important leaf traits related to tissue density which in turn influence other leaf functional traits. EWT, the difference between fresh mass and dry mass per unit area, influences dehydration resiliency (Kattenborn et al., 2017). Due to the biophysical constraints imposed by the leaf economic spectrum, LMA is systematically correlated with assemblages of other plant traits as it represents the compromise between the cost of leaf construction and the resultant light interception area (Asner et al., 2014). LMA is related to leaf life-span, and inversely related to individual plant water conductance, photosynthetic capacity, root system, nutrient uptake, turnover and growth rate (Gara et al., 2019; Reich et al., 1997; Maréchaux et al., 2016). LMA can thus capture a large portion of functional variation in ecosystems. LMA also allows conversion between mass-based and area-based constituent quantities, bridging the gap between different modelling approaches. The ratio of EWT to LMA is used to calculate fuel moisture content for fires, as both together influence fire ignition and propagation (Qi et al., 2014; Riano et al., 2005).

Several techniques can be used to measure leaf traits, which are either destructive or non-destructive. Destructive measurements require the collection and transportation of leaf samples, followed by empirical analysis of leaf sample constituents using wet chemistry techniques or drying processes (Jacquemoud and Baret, 1990; Lichtenthaler, 1987). Destructive techniques are thus time consuming, expensive, and in the case of remote sites logistically restricting due to the light and heat-sensitive nature of pigment and moisture analyses (Asner et al., 2015). Alternatively, non-destructive techniques based upon leaf spectroscopy, have been successful in retrieving leaf traits. Leaf spectroscopy is relatively cost-effective, with the benefit of repeatability, and remote application, and has been adopted as a common approach to the study of leaf traits (Hill et al., 2019; Féret et al., 2019; Féret et al., 2017; Chavana-Bryant et al., 2017; Sun et al., 2018; Nunes et al., 2017; Le Maire et al., 2004, 2008). Leaf spectroscopy takes advantage of the relationship between leaf optical properties (including reflectance, transmittance and absorptance) and their structural and biochemical properties.

A variety of approaches have been developed to estimate Cab, Cxc, EWT, and LMA from leaf optical properties (Hill et al., 2019; Sun et al., 2018; Cheng et al., 2014; Le Maire et al., 2008; Goetz et al., 1990). These approaches can be largely grouped into three categories: statistical, physical, and hybrid approaches (Verrelst et al., 2015; 2012). Statistical approaches involve the collection of a calibration dataset of leaf constituents concurrent with optical measurements from which regression models are established to estimate leaf constituents from reflectance and/or transmittance spectra. The most direct models correspond to spectral indices involving combinations of optical properties at a reduced number of relevant wavelengths. For example, Cab can be estimated from leaf reflectance data with various spectral indices (Chavana-Bryant et al., 2017; Le Maire et al., 2004). Partial least square regression (PLSR) and machine learning algorithms have also been employed to estimate quantities of biochemical constituents (Féret et al., 2019; Hill et al., 2019; Martin et al., 2018). Statistical approaches are computationally very efficient and have been successful in the retrieval of a large number of leaf traits based on spectral data at both leaf and canopy scale. The two main disadvantages of statistical and machine learning approaches however are the need for comprehensive training datasets, and the lack of generalization ability, leading to limited applicability to the retrieval of leaf traits from different sites and species (Féret et al., 2019; Jiang et al., 2018; Sun et al., 2018; Wang et al., 2015). However recent studies have shown that improvements in instrumental design, data calibration, methods and algorithms now enable more robust data driven predictive models applicable to larger and more diverse areas and vegetation types (Hill et al., 2019, Serbin et al., 2019).

Physical approaches based on radiative transfer models (RTMs) such as the PROSPECT model at the leaf scale (Jacquemoud and Baret, 1990) are theoretically robust, as they are built upon fundamental relationships between light and vegetation tissues, relying on well-defined equations of optics involving scattering and absorption interactions which are site and species-independent (Jacquemoud and Baret, 1990; Féret et al., 2008). PROSPECT assumes a relatively simplistic representation of leaves and simulates them based upon a generalized plate model. The plate model, first developed by Allen et al. (1969), defines the diffuse reflectance and transmittance of a typical compact leaf based upon indices of optical refraction and absorption using the Stokes system of equations (Stokes, 1862). The generalization of the plate model (Allen et al., 1970; Breece and Holmes, 1971; Stokes, 1862) is based on the solution of the system of equations corresponding to N uniform compact layers separated by N-1 air spaces, in order to obtain reflectance and transmittance of the series of layers. The PROSPECT model is based on this generalized plate model for continuous values of N, and this number of layers N is defined as the structure parameter, allowing representation of leaf internal structure for dicotyledon species. In forward mode PROSPECT simulates leaf directional-hemispherical reflectance and transmittance from 400 nm to 2500 nm (Schaepman-Strub et al., 2006) based upon a limited number of input biochemical and structural components (Jacquemoud and Baret, 1990). Several versions of PROSPECT have included progressively more constituents (Féret et al., 2008), the latest version, PROSPECT-D, including Cab, Cxc, anthocyanins, brown pigments, EWT, LMA, and the N structure parameter, allowing accurate simulation of leaf optical properties for a broad range of leaf morphologies and development stages (Coussement et al., 2018; Jiang et al., 2018; Féret et al., 2017). The inversion of PROSPECT alternatively allows the retrieval of biochemical constituents from leaf directional-hemispherical reflectance and transmittance data by computing the model parameters which allow the best fit between simulated and measured spectra. Several algorithms have been used in literature to perform this inversion, including look-up-table (LUT) methods (Ali et al., 2016) and iterative optimization based on minimization algorithms (Jacquemoud et al., 1996). Finally, hybrid approaches combine statistical and physical approaches, such as the establishment of spectral indices or machine learning regression models based on simulated optical data generated with RTMs in forward mode (Brown et al., 2019; Hill et al., 2019; Berger et al., 2018; Verrelst et al., 2015).

Traditionally, the PROSPECT model is inverted upon directional-hemispherical reflectance and transmittance data across the VIS and infrared (IR) domains from 400 nm to 2500 nm. However, this approach has prompted poor retrieval success for some constituents, in particular LMA (Jiang et al., 2018). This may be caused by uncertainty in both the PROSPECT model and optical measurements as suggested by Féret et al. (2019), or uncertainty in the PROSPECT model's representation of the light absorption properties of molecules, such as those associated with LMA (Sun et al., 2018; Li et al., 2016), or leaf internal shadowing effects due to the dominant absorption of other constituents. To alleviate these problems, multiple studies suggest prior selection of optical subdomains for the estimation of specific constituents. Li and Wang (2011) defined a multistep iterative inversion procedure estimating PROSPECT parameters individually based on optimal spectral domains, and obtained improved estimation of Cab, EWT and LMA. However, Li and Wang (2011) only used reflectance data and did not test their approach on publicly available datasets. Moreover, the iterative procedure is computationally intensive. Wang et al. (2015) obtained improved retrieval of cellulose and lignin when performing PROSPECT inversion from 2,100 nm to 2,300 nm. However, Wang et al. (2015) focused on specific biochemicals of dry matter and did not investigate the parameters used in the publicly available version of PROSPECT. More recently, Féret et al. (2019) evidenced that PROSPECT inversion based on the spectral subdomain from 1,700 nm to 2,400 nm led to dramatic improvement in the retrieval of LMA and EWT. However, Féret et al. (2019) focused on the IR domain and did not investigate the generalization of optimal spectral subdomains in the VIS domain for the estimation of leaf pigments.

Different performances of PROSPECT inversion have also been reported when using both leaf reflectance and transmittance spectra together, leaf reflectance spectra only, or leaf transmittance spectra only. Sun et al. (2018) reported better retrieval accuracy for LMA when using only reflectance or only transmittance than when using reflectance and transmittance combined. Added to improved estimation of leaf constituents, the measurement of only reflectance or only transmittance may save significant time. However, Hill et al. (2019) reported a strong bias in the estimation of carotenoids and EWT from PROSPECT-D inversion when using reflectance only. Contrarily, Asner et al. (2011) found that transmittance spectral information is sufficient to accurately estimate Cab as well as Cxc, using PLSR models. In light of these contradictory results, an assessment of PROSPECT inversion performance when using only reflectance or only transmittance from publicly available datasets, along with traditional comprehensive inversion procedures, is needed to inform future research.

One source of uncertainty and potentially error in the estimation of leaf chemistry when using PROSPECT inversion with reflectance or transmittance only is the N parameter. The N parameter is usually inferred based on information from both reflectance and transmittance in the near infrared domain (NIR, 750 nm to 1400 nm) (Jacquemoud and Baret, 1990; Allen et al., 1970), and is the only model parameter not based upon a quantifiable leaf physiological trait. The performance of partially-informed PROSPECT inversion, with either reduced subdomains excluding NIR information, or only reflectance or transmittance, in estimating the N parameter has yet to be explored. Jacquemoud and Baret, (1990) showed a correlation between SLA and the N parameter, characterized by a hyperbolic relationship, with higher N values corresponding to lower SLA. Jacquemoud and Baret (1990) explained this by the fact that cell walls have a constant weight per unit area, meaning that an increasing number of cell-wall interfaces corresponds to an increasing anatomical complexity of the leaf and translates into an increase in N and a decrease in SLA. Qiu et al. (2018) reported a significant and moderate to strong correlation between N and LMA (r = 0.57), and between N and leaf thickness (r = 0.59, and a lower but still significant correlation between N and EWT (r = 0.34). The correlation between N and LMA ranged between 0.46 and 0.71 and the correlation between N and EWT ranged between -0.55 and 0.51 for six datasets analyzed by Féret et al. (2019) (unpublished results). Although the correlation between N and LMA appears as relatively consistent among datasets and among studies, it is usually moderate and using LMA as a proxy for the N parameter would lead to significant uncertainty for the simulation of leaf optical properties: the N parameter is the physical foundation of the PROSPECT model, as the major anatomical differentiation between leaves is the number of these homogenous plates (Jacquemoud and Baret, 1990). It is therefore the main factor influencing leaf optical properties in the spectral domains dominated by scattering effects, such as the NIR domain and part of the short wave infrared (SWIR, 1400 nm to 3000 nm) domain. As a result, uncertainty in N can directly lead to uncertainty in simulated leaf optical properties, and in the constituents estimated from PROSPECT inversion relying on these domains (Qiu et al., 2018).

Qiu et al. (2018) reported a strong correlation of 0.82 between the N parameter and the ratio between reflectance and transmittance measured in the NIR at 800 nm. Taking advantage of this correlation to estimate N requires measuring both leaf reflectance and transmittance, in line with the original method used to compute N from leaf optical properties, used during PROSPECT calibration and described by Jacquemoud et al. (1996). However, absorptance in the NIR domain is usually very low: Merzlyak et al. (2004) even suggest that absorptance in the domain ranging from 750 nm to 800 nm can be neglected. Qiu et al. (2019) reported the N parameter having a dominant influence on reflectance and transmittance from 750-800 nm over other PROSPECT parameters, as well as leaf surface reflectance. Thus, assuming light in the NIR is primarily either reflected or transmitted as a function of leaf structure, information about reflectance only or transmittance only might be sufficient to accurately estimate the N parameter with moderate uncertainty, following the hypothesis that absorptance is negligible. The estimation of N prior to PROSPECT inversion may therefore lead to improved estimation of leaf constituents when using optimal spectral subdomains with only reflectance or transmittance.

Our primary objective is to identify the optimal method for the estimation of leaf constituents based on PROSPECT inversion, including Cab, Cxc, EWT and LMA. Multiple recent studies proposed different alternatives to this problem, and our study compares these approaches when taken individually or combined. These approaches include i) use of reflectance, transmittance, or the combination of both, ii) definition of optimal spectral subdomains for specific leaf constituents, and iii) prior estimation of the N parameter from reflectance or transmittance only.

3.3 Methods

We utilized seven datasets for this study amounting to 1,432 leaf samples, comprising tropical, temperate and boreal species. Together these datasets include heterogeneous sets of information. ANGERS (Féret et al., 2008), and LOPEX (Hosgood et al., 1994) are publicly available datasets (see http://opticleaf.ipgp.fr/index.php?page=database) including directional-hemispherical reflectance in the full optical spectral domain from 400 nm to 2500 nm, and chemical measurements of biochemical constituents including Cab, Cxc, EWT and LMA. Discrepancies in the relation between pigment content and leaf optical properties provided for LOPEX were reported in previous studies (Féret et al., 2008). These discrepancies may be explained by the averaging of leaf optical properties and merging of different leaf samples for the destructive measurements of pigment content. Thus, we decided to discard the information corresponding to pigment content from LOPEX. DOGWOOD-1 (Gitelson et al., 2001; Merzlyak et al., 2008), HAZEL (Gitelson et al., 2009), and VIRGINIA datasets (Gitelson et al., 2009) correspond to three of the five datasets publicly available (see https://www.researchgate.net /publication/319213426_Foliar_reflectance_and_biochemistry_5_data_sets), including reflectance and transmittance in the VIS and NIR domains, as well as pigment content obtained from destructive measurements. ITATINGA and NOURAGUES datasets include directional-hemispherical reflectance and transmittance as well as destructive measurements of EWT and

LMA, and their comprehensive description can be found in Féret et al., 2019. Table 3-1 shows the collection and coverage information for each dataset.

The same measurement protocol was generally followed to obtain reflectance and transmittance measurements for each leaf sample. Directional-hemispherical reflectance and transmittance were measured with a spectroradiometer equipped with an integrating sphere. The spectral sampling resolution for these datasets ranges from 1-2 nm in the spectral region from 400 nm to 1000 nm, and from 2-5 nm in the spectral region from 1000 nm to 2500 nm, though all spectral data were resampled to 1 nm intervals. Together these datasets encompass a variety of leaf ages, including young, mature, and senescent, as well as monocot and dicot leaf morphologies, woody and herbaceous leaf types, and a diversity of solar exposures, including canopy and shaded leaves. The measurement protocol for wet chemistry estimation of pigments was also generally similar among datasets. Leaf discs were immediately collected with a cork borer following hyperspectral measurements. For the extraction of pigments, leaf discs were ground in a chilled mortar, and organic solvents such as 100% acetone, methanol, or 95% ethanol were used. The pigment content was then derived from the absorption of the solution with lab spectroscopy following the Lichtenthaler (1987) method and equations. The measurement protocol for EWT and LMA was also common for ANGERS, LOPEX, ITATINGA and NOURAGUES: one or several leaf discs were collected from fresh leaves using a cork borer, and the fresh weight of leaf discs was measured immediately before placing the discs in a drying oven at 85◦C for at least 48 hours, at which point the dry weight of leaf discs was measured to obtain EWT and LMA. For more information on the experimental protocols of published datasets, consult Hosgood et al. (1994), Féret et al. (2019; 2008), Gitelson et al. (2009; 2006; 2001), and Merzlyak et al. (2008).

Table 3-1. *Summary of datasets used in this study*

Dataset	**Reference**	**Nation**	**Spectral Range (nm)**	**Number of Leaves**	**Number of Species**	**Spectrometer**	**Empirical Constituents**
LOPEX	Hosgood et al. (1994)	Italy	400 -2500	330	46	Perkin Elmber Lambda 19	EWT, LMA
ANGERS	Féret et al. (2008, 2011); Le Maire et al. (2008)	France	400 -2500	308	43	ASD FieldSpec	Cab, Cxc, EWT, LMA
VIRGINIA	Gitelson et al. (2009); Merzlyak et al. (2008)	Russia	400 -800	81	1 (*Parthenocissus quinquefolia*)	150 -20 Hitachi	Cab, Cxc
HAZEL	Gitelson et al. (2009); Merzlyak et al. (2008)	Russia	400 -800	13	1 (*Corylus avellana*)	150 -20 Hitachi	Cxc
DOGWOOD-1	Gitelson et al. (2001, 2009); Merzlyak et al. (2008)	Russia	436 -796	23	1 (*Cornus alba*)	150 -20 Hitachi	Cab, Cxc
ITATINGA	Féret et al. (2019); Oliveira et al. (2017)	Brazil	400 -2500	415	4 (*Eucalyptus sp.*)	ASD FieldSpec Pro	EWT, LMA
NOURAGUES	Féret et al. (2019); Réjou-Méchain et al. (2015)	French Guiana	400 -2500	262	38	ASD FieldSpec 3	EWT, LMA

PROSPECT simulates leaf optical properties based upon the content of light absorbing biochemical constituents per unit of leaf surface and a leaf structural N parameter, the hypothetical number of internal leaf "plates" (Allen et al., 1970; Jacquemoud and Baret, 1990; Féret et al., 2017; Féret et al., 2019). Interactions between light and leaf tissues are modelled as a function of pigment content (including Cab, Cxc, anthocyanins and brown pigments), EWT, and LMA, and corresponding spectral specific absorption coefficients (SACs), as well as a spectral refractive index and the N parameter, which accounts for mesophyll structure. PROSPECT simulates directional-hemispherical reflectance and transmittance for wavelengths from 400 nm to 2500 nm, with 1 nm spectral resolution.

The inversion of PROSPECT allows for the estimation of leaf biochemistry based upon directional-hemispherical reflectance and/or transmittance spectra (Féret et al., 2008; Le Maire et al., 2008). The inversion of PROSPECT based on iterative optimization seeks to minimize the residuals between measured and modeled leaf optical properties using a merit function *M* over all available spectral wavelengths, by exploring the input parameter space of the model, each parameter being defined by an upper and a lower boundary physically meaningful:

$$M\left(N,\{C_i\}_{i=1:p}\right)=\sum_{\lambda=\lambda_1}^{\lambda_n}\left[W_{R,\lambda}\times\left(R_\lambda-\widehat{R_\lambda}\right)^2+W_{T,\lambda}\times\left(T_\lambda-\widehat{T_\lambda}\right)^2\right] \qquad 3\text{-}1$$

with *N* as the leaf structure parameter, *p* as the number of biochemical constituents to be retrieved, here four (Cab, Cxc, EWT, and LMA), C_i the biochemical constituent content per unit of leaf surface for constituent *i*, λ_1 and λ_n the first and final wavelengths included in the inversion, R_λ and $\widehat{R_\lambda}$, T_λ and $\widehat{T_\lambda}$, the measured and simulated reflectance and transmittance, respectively, and with $W_{R,\lambda}$ and $W_{T,\lambda}$ the weight applied to the squared residuals between measured and simulated reflectance and transmittance. We used PROSPECT-D (Féret et al., 2017) and implemented the inversion procedure with the Matlab constrained nonlinear optimization function *fmincon*, which finds a constrained minimum of a multivariate scalar function using an initial estimate. The weight applied to reflectance and transmittance in the merit function were either set to 1 when inverting PROSPECT from both reflectance and transmittance or set to 0 for all reflectance data or all transmittance data, when inverting PROSPECT either from transmittance alone or reflectance alone, respectively.

We used the NIR subdomain 1700-2400 nm for the retrieval of EWT and LMA, which was previously found to perform well through an iterative optimization procedure in Féret et al. (2019). We used a similar iterative optimization procedure to identify the optimal subdomain for the estimation of pigment content. We segmented the VIS and NIR domains into 17 evenly-sized segments of 20 nm from 460 nm to 799 nm. We then performed PROSPECT inversions to retrieve Cab and Cxc using reflectance and transmittance from each of the continuous spectral domains that can be generated from these 17 spectral segments, leading to 153 continuous subdomains. To evaluate the optimal spectral subdomain, we compiled all available data including either Cab or Cxc, and we computed the standardized RMSE (SRMSE) between estimated and measured Cab and Cxc for each subdomain, standardized by the Cab and Cxc estimated for each sample from reflectance and transmittance data from 460-799 nm. Based on this approach, we defined an optimal spectral domain for the estimation of Cab and an optimal spectral domain for the estimation of Cxc.

The computation of the N parameter is usually derived from information on both reflectance and transmittance measurements. During the calibration of PROSPECT specific absorption spectra for the N parameter, typically a simplified version of PROSPECT is inversed based on reflectance and transmittance measured at three wavelengths including the wavelength of minimum absorption, the wavelength of maximum reflectance, and the wavelength of maximum transmittance. This method was proposed by Jacquemoud et al. (1996) and also used by Féret et al. (2008, 2017) to calibrate the latest versions of PROSPECT, and is referred to as the 'standard N value' in this study. This N parameter is usually estimated simultaneously with other parameters during inversion based on iterative optimization, with few exceptions (Li and Wang, 2011).

The estimation of leaf chemical constituents from reflectance or transmittance has led to contrasting conclusions, and the inconsistency in these conclusions may be caused by uncertainty in the estimation of N, which is the most influential parameter on leaf optical properties in domains with low absorption, in particular the NIR domain. Therefore, the estimation of N directly from reflectance or transmittance measurements may be the key to more robust estimation of leaf constituents through PROSPECT inversion applied on only reflectance or only transmittance. Light absorption by leaves in the NIR domain is the source of some debate: most experimental datasets show low but existing absorption in this domain, but Merzlyak et al. (2004) proposed that absorption is negligible in the spectral domains of minimum absorption, and proposed a correcting factor for transmittance. The hypothesis of Merzlyak et al. (2004) is justified by the difficulty of accurately measuring leaf optical properties in the NIR domain due to incomplete collection of light leaving the highly scattering tissue. Even without the application of such a correcting factor, the following relationship holds when absorption is sufficiently low:

$$\frac{R_{Amin}}{T_{Amin}} \sim \frac{R_{Amin}}{1 - R_{Amin}} \sim \frac{1 - T_{Amin}}{T_{Amin}} \tag{3-2}$$

with R_{Amin} and T_{Amin} the reflectance and transmittance measured at the wavelength of minimum absorption. Therefore, combining Equation 3-2 with the result of Qiu et al. (2018), the N parameter should be strongly correlated with the different terms of Equation 3-2, allowing proper estimation of N from reflectance only or transmittance only.

Here, we first performed a correlation analysis between the N parameter and the three ratios defined in Equation 3-2, for each of our seven experimental datasets in order to verify the validity of the correlation reported by Qiu et al. (2018), and to test the hypothesis of negligible absorption of light at 800 nm formulated by Merzlyak et al. (2004).

Our second objective was to identify a robust relationship between N and the ratios defined in Equation 3-2 across datasets. To achieve this, we defined linear regression models linking N to these ratios adjusted based on leaf optical properties simulated with PROSPECT and validated on our experimental datasets. We simulated 1000 leaf optical property assemblages with PROSPECT, based on the random sampling of leaf constituents as defined in Table 3-2. The value for brown pigments and anthocyanins was set to 0. The resulting simulated dataset is referred to as SIMUL-N hereafter.

Table 3-2. *Definition of the ranges for the PROSPECT input parameters used for the simulated dataset.*

PROSPECT Parameter	**Range**
N	1 – 4
Cab (µg·cm^{-2})	0.5 – 100
Cxc (µg·cm^{-2})	0.5– 20
EWT (g·cm^{-2})	0.001– 0.02
LMA (g·cm^{-2})	0.001– 0.01

As the minimum absorption is not systematically located at 800 nm (Boren et al., 2019), we adjusted a simple linear regression model between N and $\frac{R}{1-R}$, and between N and $\frac{1-T}{T}$ for each wavelength between 400 nm and 2500 nm on this simulated dataset. Then we applied this regression model on each individual experimental dataset, and on the compilation of all these datasets, and identified the optimal spectral band leading to the minimum RMSE between the standard N value (obtained from a standard inversion of both R and T) and the N parameter estimated from the regression model. As the experimental datasets showed different spectral ranges, some of them covering the full spectral domain from 400 nm to 2500 nm while others were limited to the spectral domain from 400 nm to 800 nm, we defined an optimal spectral band for each spectral range (400 nm to 800 nm, and 400 nm to 2500 nm), and each ratio based either on reflectance or on transmittance.

We then estimated Cab, Cxc, EWT, and LMA from the experimental datasets using ten different inversion procedures of PROSPECT. We also estimated anthocyanin content, though due to most datasets lacking wet chemistry anthocyanin measurements, we did not include anthocyanins in our analysis. We evaluated the following inversion procedures:

1. Use of the full spectral domain available, with both reflectance and transmittance, and the simultaneous estimation of Cab, Cxc, EWT, and LMA.
2. Use of the full spectral domain available, with only reflectance or only transmittance, and the simultaneous estimation of Cab, Cxc, EWT, LMA, and N.
3. Use of the full spectral domain available, with only reflectance or only transmittance combined with corresponding prior estimation of N, and the simultaneous estimation of Cab, Cxc, EWT, and LMA.

4. Use of the optimal spectral subdomain for each of the variables Cab, Cxc, EWT, and LMA, with both reflectance and transmittance, and the simultaneous estimation of Cab, Cxc, EWT, LMA, and N.
5. Use of the optimal spectral subdomain for each of the variables Cab, Cxc, EWT, and LMA, with only reflectance, or only transmittance, and the simultaneous estimation of Cab, Cxc, EWT, LMA, and N.
6. Use of the optimal spectral subdomain for each of the variables Cab, Cxc, EWT, and LMA, with only reflectance or only transmittance combined with corresponding prior estimation of N, and the simultaneous estimation of Cab, Cxc, EWT, and LMA.

The performances of each of these inversion procedures were compared using the normalized root mean squared error (NRMSE, expressed in %), the RMSE of each leaf constituent estimation by each procedure normalized by the mean RMSE computed for all experimental data available for each leaf constituent.

3.4 Results

Figure 3-1 identifies the optimal spectral subdomains to be used for the estimation of Cab and Cxc. The optimal subdomain for the estimation of Cab corresponds extends from 700 nm to 720 nm, which coincides with the red edge. The optimal subdomain for the estimation of Cxc extends from 520 nm to 560 nm, which corresponds to the end of the domain of absorption of Cxc as defined in the SAC used in PROSPECT.

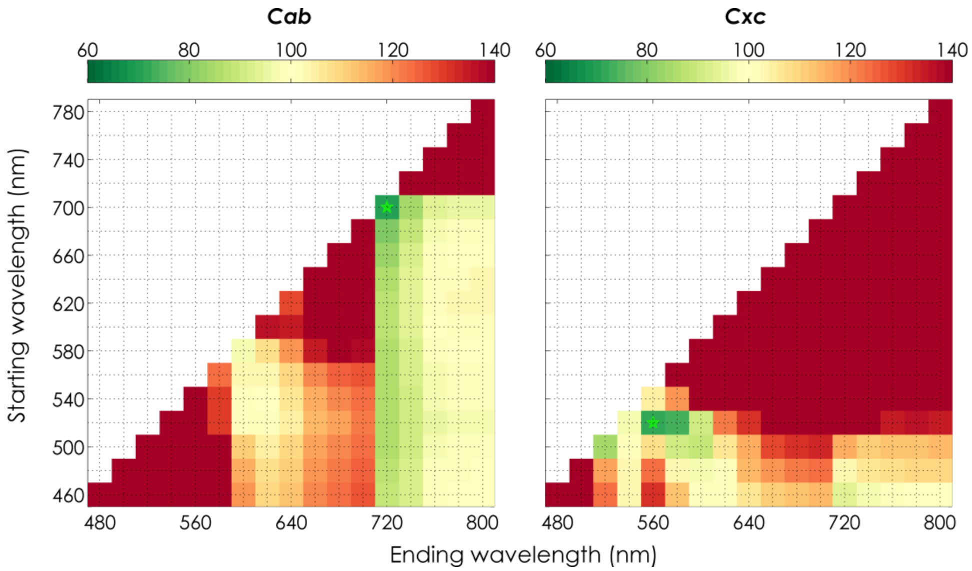

Figure 3-1. *SRMSE (%) obtained for the estimation of Cab (left) and Cxc (right) from PROSPECT inversion over all experimental datasets combined with each of the 153 spectral domain combinations. The green star indicates the spectral segment producing the best results.*

The correlation analysis between the standard N value and either $\frac{R_{800}}{T_{800}}$, $\frac{R_{800}}{1-R_{800}}$, or $\frac{1-T_{800}}{T_{800}}$ confirms the very strong correlation observed by Qiu et al. (2018), and even produces stronger correlations, with values > 0.97 for all datasets when comparing the standard N value to $\frac{R_{800}}{T_{800}}$. The correlation between the standard N value and ratios based on reflectance or transmittance only is also very strong, with values > 0.95 for all datasets except LOPEX and NOURAGUES, which still showed correlation > 0.75. Table 3-3 shows the correlation values between the standard N value and $\frac{R_{800}}{T_{800}}$, $\frac{R_{800}}{1-R_{800}}$, and $\frac{1-T_{800}}{T_{800}}$.

Table 3-3. *Correlation between standard N value and ratios computed from leaf optical properties at 800 nm.*

Dataset	$\frac{R_{800}}{T_{800}}$	$\frac{R_{800}}{1-R_{800}}$	$\frac{1-T_{800}}{T_{800}}$
SIMUL-N	1.00	0.98	0.99
LOPEX	0.97	0.76	0.75
ANGERS	1.00	0.96	0.98
VIRGINIA	1.00	1.00	1.00
HAZEL	1.00	1.00	1.00
DOGWOOD-1	1.00	1.00	1.00
ITATINGA	1.00	0.95	0.98
NOURAGUES	0.99	0.84	0.89

Figure 3-2 illustrates the RMSE between the standard N value and the N value estimated from the linear regression model established with the PROSPECT simulated dataset. For datasets limited to the VIS and red edge of the NIR domain (~400 nm to 800 nm), the optimal spectral band for the estimation of the N parameter varies slightly from 730 nm to 800 nm amongst datasets. For all datasets combined with spectra from the VIS to red edge, the optimal spectral band is 800 nm for reflectance, and 753 for transmittance.

For datasets including the full spectral range (400 nm to 2500 nm), the optimal spectral band varies amongst datasets, but remains in the NIR plateau. Finally, when combining all datasets, the optimal spectral band for reflectance and for transmittance are very close: the optimal estimation for N when using reflectance only is obtained with the wavelength 1131 nm ($\frac{R_{1131}}{1-R_{1131}}$), whereas the optimal estimation for N when using transmittance only is obtained with the wavelength 1121 nm ($\frac{1-T_{1121}}{T_{1121}}$). These wavelengths are situated in close proximity to the wavelength with a minimal absorption coefficient in PROSPECT-D, which is 1073 nm.

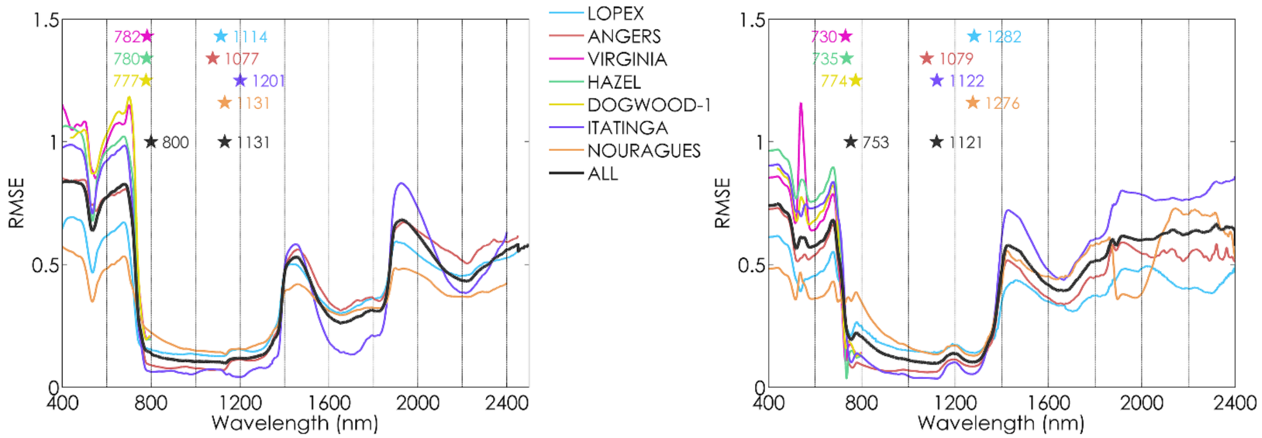

Figure 3-2. *RMSE between the standard N value and the N value estimated from a linear model based on PROSPECT simulation, using reflectance (left) or transmittance (right). The stars and numerical values indicate the location of the spectral band corresponding to the minimum RMSE for each spectral band. The values in black correspond to the optimal spectral bands obtained when combining all datasets, and considering either the spectral domain from 400 nm to 800 nm, or from 400 nm to 2500 nm.*

The linear models relating reflectance ratios to the N parameter, as well as transmittance ratios to the N parameter varied as a function of wavelength. Equations 3-3 to 3-6 correspond to the linear models linking N to the reflectance and transmittance ratios, either when only VIS and NIR (VNIR) spectral data are available from 400 nm to 800 nm, or when the leaf optical properties are measured over the full spectral range.

$$\boldsymbol{N_{VNIR,R} = 1.724 \times \frac{R_{800}}{1 - R_{800}} + 0.0795} \tag{3-3}$$

$$\boldsymbol{N_{VSWIR,R} = 1.830 \times \frac{R_{1131}}{1 - R_{1131}} + 0.0711} \tag{3-4}$$

$$\boldsymbol{N_{VNIR,T} = 1.162 \times \frac{1 - T_{753}}{T_{753}} + 0.187} \tag{3-5}$$

$$\boldsymbol{N_{VSWIR,T} = 1.340 \times \frac{1 - T_{1121}}{T_{1121}} + 0.121} \tag{3-6}$$

Optimal spectral subdomains with both reflectance and transmittance data performed the best in retrieving all leaf constituents combined, systematically outperforming traditional PROSPECT inversion of full domains for each constituent. The use of a reflectance or transmittance ratio to provide a prior estimation of the N parameter led to a modest to dramatic improvement over both full domain and optimal subdomain reflectance or transmittance in retrieving each constituent, with the sole exception of LMA. For LMA, full domain reflectance and optimal subdomain transmittance without prior estimation of the N parameter performed better by 14.2% and 0.8% NRMSE, respectively.

With the availability of only reflectance data, optimal spectral subdomains with prior estimation of the N parameter using a reflectance ratio performed best for the retrieval of Cab and LMA, though was second best for the retrieval of Cxc and EWT. Full domain reflectance with prior estimation of the N parameter using a reflectance ratio outperformed by optimal subdomains by 8.2% NRMSE and 1.8% NRMSE for Cxc and EWT, respectively. Conversely with the availability of only transmittance, optimal spectral subdomains with prior estimation of the N parameter using a transmittance ratio performed best in retrieving each parameter with the exception of LMA, for which optimal spectral subdomains with no prior estimation of the N parameter performed better by 0.8% NRMSE.

Relative to inverting PROSPECT on full domain reflectance data alone or transmittance data alone, prior estimation of the N parameter with a reflectance or transmittance ratio improved retrieval success by 20.2% (reflectance) to 23.3% (transmittance) NRMSE for Cab (Figure 3-3). The inversion of PROSPECT on optimal subdomains in junction with an estimation of the N parameter from a reflectance ratio further improved retrieval success over full domain reflectance alone by 22.0 % NRMSE, while for transmittance the use of optimal subdomains and a transmittance ratio to estimate the N parameter improved retrieval success by 25.3% NRMSE over full domain transmittance alone. The best method in estimating Cab with respect to either reflectance alone or transmittance alone was reflectance-based: optimal subdomain reflectance with a reflectance ratio to estimate the N parameter, followed by full domain reflectance with a reflectance ratio to estimate the N parameter, which in turn was followed by optimal subdomain transmittance with a transmittance ratio to estimate the N parameter.

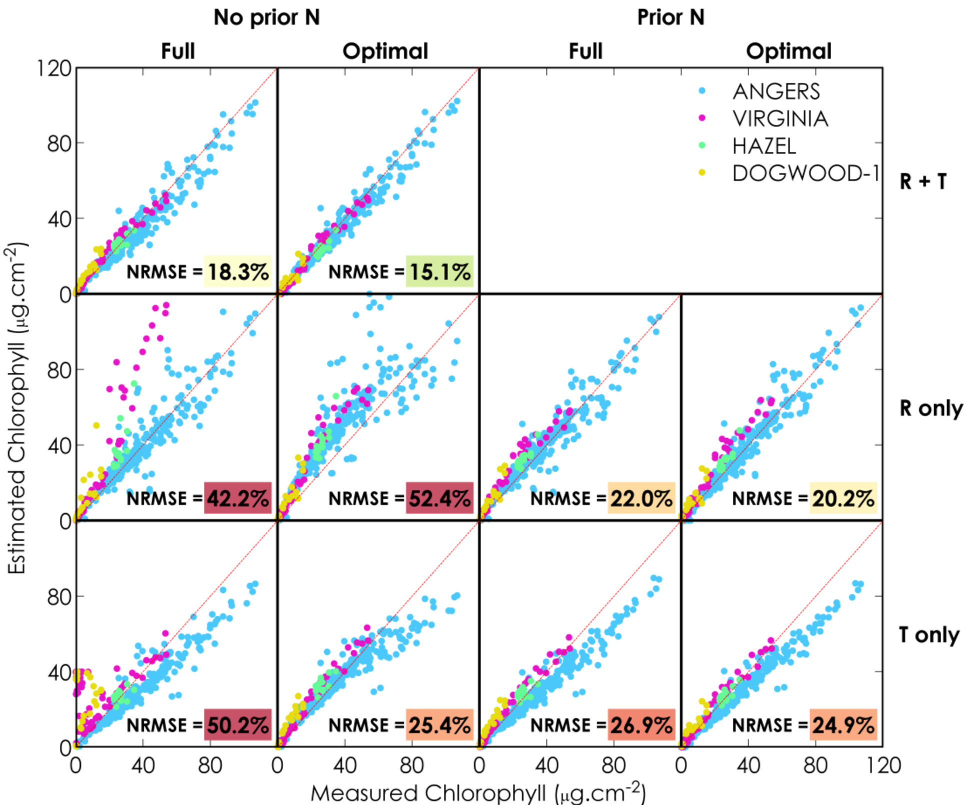

Figure 3-3. *Estimation of Cab using ten different strategies for PROSPECT inversion. NRMSE is provided for the compiled dataset, and the background color for NRMSE value indicates if the performances are improved (green) or worsened (red) compared to the inversion using both reflectance and transmittance over the full spectral domain without prior estimation of N.*

For Cxc, the benefit of estimating the N parameter with a reflectance or transmittance ratio for full domain reflectance data alone was more modest, with a reduction in NRMSE by 8%, while for transmittance NRMSE was reduced by 30.5% (Figure 3-4). The use of optimal subdomains in junction with a reflectance ratio to estimate the N parameter did not improve the retrieval success for Cxc over full domain reflectance, though the use of optimal subdomain transmittance and a transmittance ratio to estimate the N parameter improved retrieval success over full domain transmittance alone by 37.6% NRMSE. The most successful retrieval method for Cxc with the availability of only reflectance or transmittance was transmittance-based: optimal subdomain transmittance with a transmittance ratio to estimate the N parameter, followed by full domain reflectance with a reflectance ratio to estimate the N parameter, followed by full domain transmittance with a transmittance ratio to estimate the N parameter.

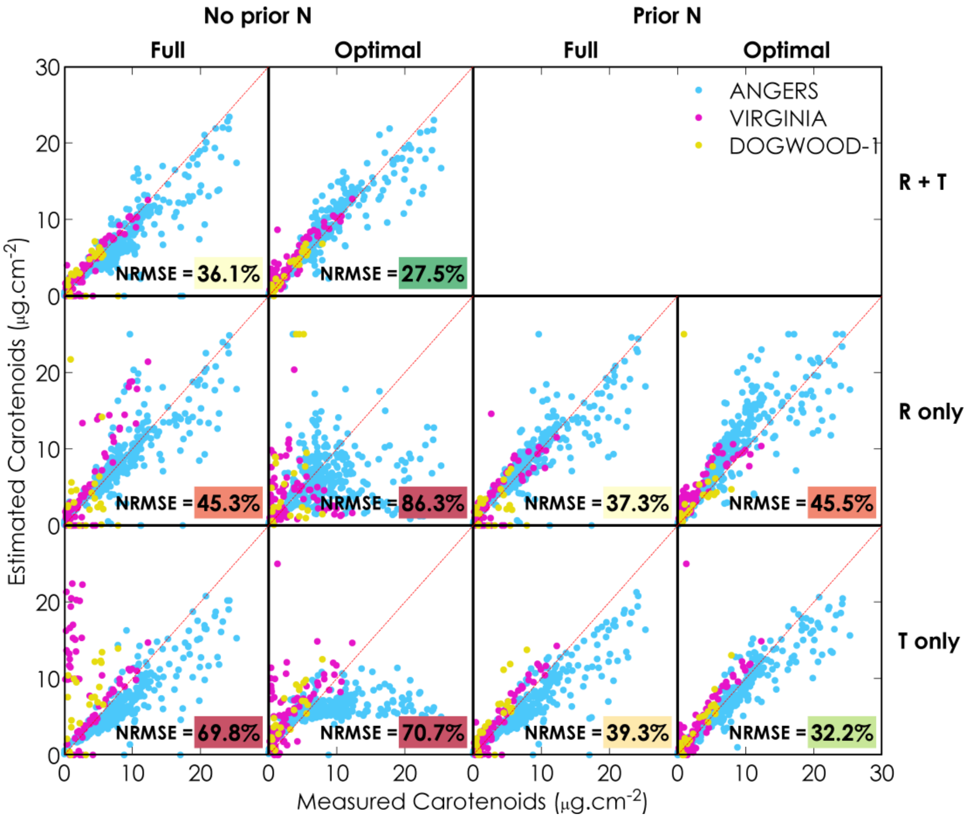

Figure 3-4. *Estimation of Cxc using ten different strategies for PROSPECT inversion. NRMSE is provided for the compiled dataset, and the background color for NRMSE value indicates if the performances are improved (green) or worsened (red) compared to the inversion using both reflectance and transmittance over the full spectral domain without prior estimation of N.*

In retrieving EWT with reflectance or transmittance data alone, estimating the N parameter with a reflectance or transmittance ratio improved retrieval success by 11.9% NRMSE in the case of reflectance, and 2.2% NRMSE in the case of transmittance (Figure 3-5). The use of optimal subdomain reflectance with prior estimation of the N parameter with a reflectance ratio improved retrieval success over full domain reflectance alone by 10.1% NRMSE, though reduced retrieval success by 1.8% NRMSE relative to full domain reflectance with a reflectance ratio to estimate the N parameter. The use of subdomain transmittance with prior estimation of the N parameter through a transmittance ratio improved retrieval success over full domain transmittance alone by 8.1% NRMSE, outperforming full domain transmittance with prior estimation of the N parameter through a transmittance ratio. The most successful method in estimating EWT from reflectance or transmittance alone was transmittance-based: optimal subdomain transmittance with estimation of the N parameter through a transmittance ratio, followed by optimal subdomain transmittance without prior estimation of the N parameter, followed by full domain transmittance with estimation of the N parameter through a transmittance ratio.

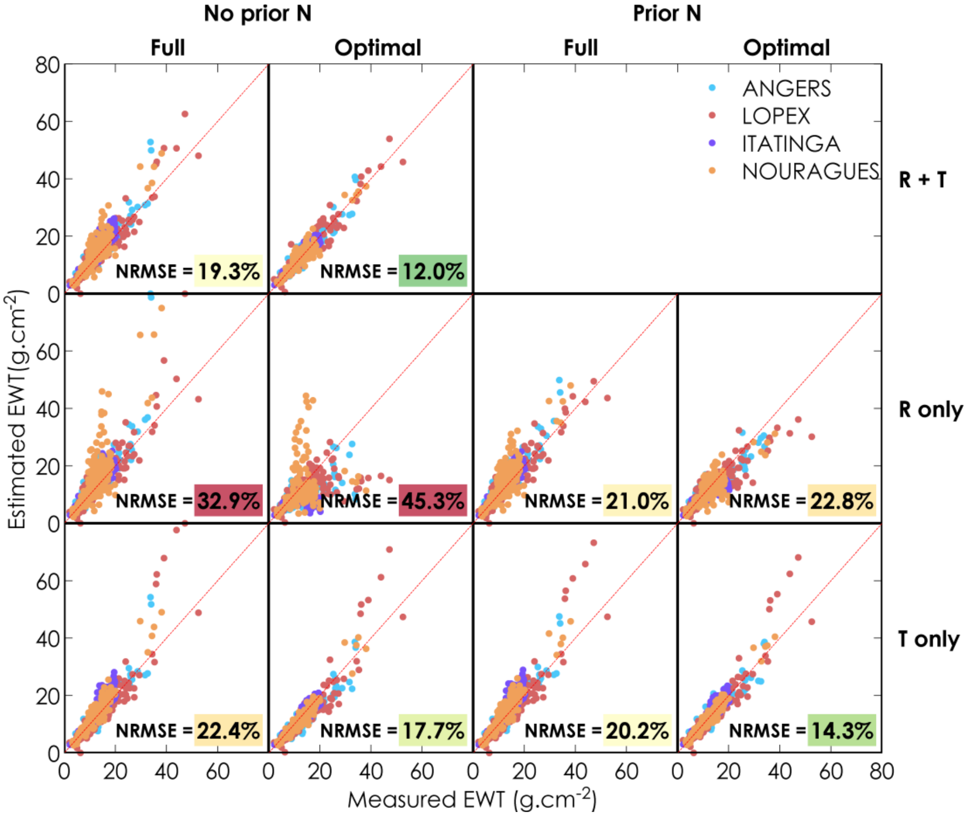

Figure 3-5. *Estimation of EWT using ten different strategies for PROSPECT inversion. NRMSE is provided for the compiled dataset, and the background color for NRMSE value indicates if the performances are improved (green) or worsened (red) compared to the inversion using both reflectance and transmittance over the full spectral domain without prior estimation of N.*

The retrieval success of LMA with full domain reflectance data alone or full domain transmittance data alone was reduced with the use of a reflectance ratio to estimate the N parameter, while it was unaffected (<1% NRMSE) with the use of a transmittance ratio to estimate the N parameter (Figure 3-6). The use of optimal subdomain reflectance with prior estimation of the N parameter through a reflectance ratio improved retrieval success by 8.8% NRMSE over full domain reflectance alone, and optimal subdomain transmittance with prior estimation of the N parameter through a transmittance ratio outperformed full domain transmittance by 13.9% NRMSE. The best method in retrieving LMA with respect to either reflectance alone or transmittance alone was transmittance-based: optimal subdomain transmittance without prior estimation of the N parameter through a transmittance ratio, followed closely (<1% more NRMSE) by optimal subdomain transmittance with prior estimation of the N through a transmittance ratio, which was in turn followed by optimal subdomain reflectance with prior estimation of the N parameter through a reflectance ratio. Optimal subdomain transmittance with and without prior estimation of the N parameter through a transmittance ratio both outperformed inversion of PROSPECT based on optimal subdomain reflectance and transmittance.

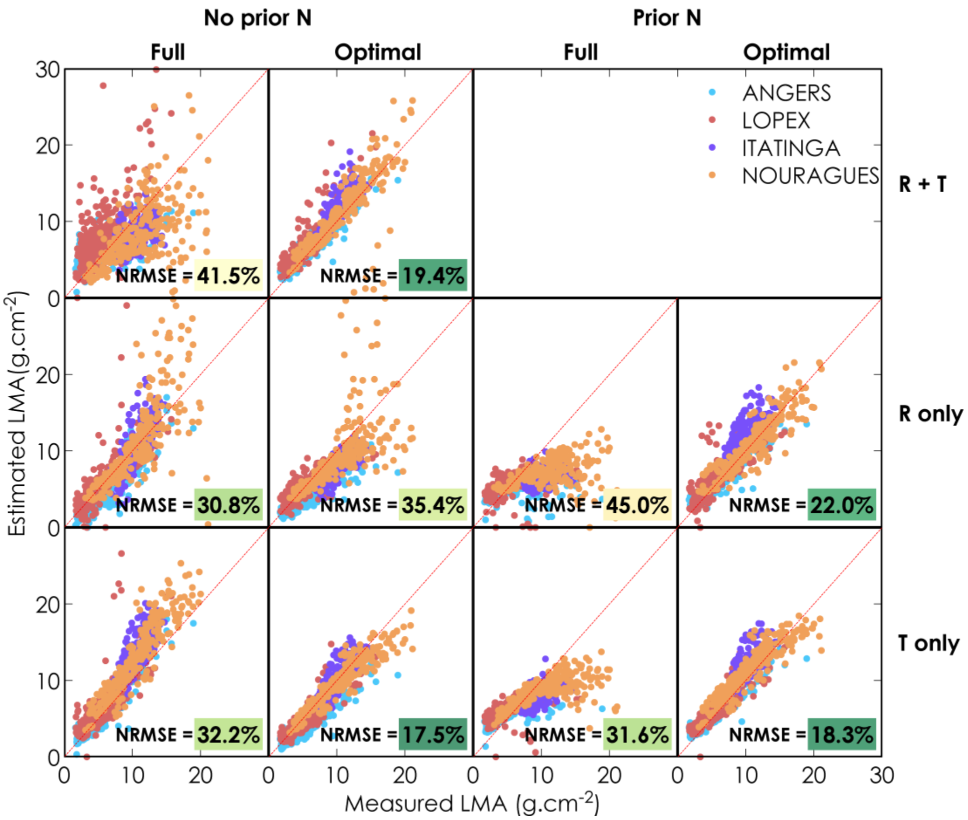

Figure 3-6. *Estimation of LMA using ten different strategies for PROSPECT inversion. NRMSE is provided for the compiled dataset, and the background color for NRMSE value indicates if the performances are improved (green) or worsened (red) compared to the inversion using both reflectance and transmittance over the full spectral domain without prior estimation of N.*

3.5 Discussion

The traditional means of estimating leaf constituents with full domain transmittance and reflectance can be modestly to dramatically improved when both reflectance and transmittance data are available through the use of optimal subdomains. This improvement is likely due to optimal subdomains maximizing the fit on the subdomain where the spectra are most sensitive to changes in particular constituent quantities and other constituent quantities are less influential. This finding is consistent with that of Féret et al. (2019) in regards to EWT and LMA, since the iterative inversion procedure is the same, as well as four of the six datasets. The success of optimal subdomains is new however with regards to Cab and Cxc. While Féret et al. (2019)

decided to select an optimal subdomain for the simultaneous estimation of EWT and LMA, here we chose to retrieve Cab and Cxc individually by using the subdomain from 700-720 nm for the retrieval of Cab, and the subdomain from 520-560 nm for the retrieval of Cxc. Sun et al. (2019) also reported improved retrieval success of Cab while inverting PROSPECT on restricted sets of wavelengths, which included 716 nm for PROSPECT-D, 726 nm for PROSPECT-4, and 732 nm for PROSPECT-5, mirroring the utility of the subdomain we found from 700-720 nm with PROSPECT-D for Cab. For Cxc, our retrieval success is comparable to Féret et al. (2017), who reported improved Cxc retrieval success over previous methods with the updating of carotenoid SACs in PROSPECT-D while inverting PROSPECT-D on full domain reflectance and transmittance, with three of the same datasets (ANGERS, VIRGINIA, and DOGWOOD-1).

Relative to Féret et al. (2017) we did find improved retrieval success of Cxc with the use of spectral subdomains and prior estimation of the N parameter, with both reflectance and transmittance (spectral subdomains) or just transmittance (spectral subdomains and prior estimation of the N parameter), as both of these techniques outperformed traditional full domain reflectance and transmittance inversion. Sonobe et al. (2017) employed hyperspectral indices as well as PROSPECT-D to estimate Cxc in leaves subjected to incremental shade treatments, and found the reflectance of wavelengths 510 nm and 521 nm to be especially informative. Sonobe et al. (2017) found both hyperspectral indices and a SAC-recalibrated version of PROSPECT-D to work well in estimating Cxc in shaded leaves, which suggests the use of optimal spectral subdomains as we have defined in the present study, would also work well for the estimation of Cxc in shaded leaves. While there was some variation among datasets, the fact that optimal subdomain reflectance and transmittance performed well globally over alternative approaches suggests that this approach is robust to variations between species and sites, as our combined datasets encompass extensive variation in leaf structural, biochemical, and optical characteristics. The application of optimal subdomains not only improves the efficacy of PROSPECT inversion in estimating Cab, Cxc, EWT, and LMA, though may also serve to improve the computational efficiency of physical approaches in retrieving these constituents, by removing extraneous wavelengths from the inversion process.

Similar to Sun et al. (2018) we observed the combination of reflectance and transmittance to perform secondarily to transmittance alone and transmittance with prior estimation of the N parameter in estimating LMA, when optimal subdomains were used. With respect to the retrieval of LMA, all except one method outperformed traditional full domain reflectance and transmittance PROSPECT inversion in retrieving LMA, the least successful method being full domain reflectance with prior estimation of the N parameter. With other leaf constituents, the traditional full domain reflectance and transmittance PROSPECT inversion method performed second (Cab), third (Cxc), or fourth (EWT) best relative to optimal spectral subdomains with reflectance and transmittance, demonstrating how dramatically traditional LMA retrieval stands to be improved with the use of alternative methods.

We found the N parameter to be strongly correlated to leaf optical spectra from the NIR, including the ratio of reflectance to transmittance, a reflectance ratio, or a transmittance ratio, demonstrating the utility of the NIR for estimating the N parameter. Resultantly, the use of a reflectance ratio at 1131 nm (or 800 nm for limited-extent spectral datasets), as well as a transmittance ratio at 1121 nm (or 753 nm for limited-extent spectral datasets), in junction with specific linear models allowed for successful estimations of the N parameter from reflectance spectra alone, as well as from transmittance spectra alone. This improved characterization of leaf structure through the N parameter in turn led to improved constituent retrievals over the inversion of PROSPECT with full domain and subdomain reflectance alone or transmittance alone, with the exception of LMA for which the inversion of PROSPECT based on full domain reflectance and optimal subdomain transmittance performed well without prior estimation of the N parameter. The N parameter represents internal leaf structure within the PROSPECT model (Jacquemoud and Baret, 1990) and influences spectral responses across both the VIS and NIR domains. The influence of the N parameter in the NIR is especially pronounced due to high light scattering inside the leaf, since no pigments absorb light in this spectral region. The precise characterization of the N parameter is therefore important to retrieve other constituent quantities, as demonstrated here by the robust performance of optimal spectral subdomain reflectance and transmittance and the meritorious performance of full domain reflectance and transmittance, as both of these inversion approaches include the most accurate N parameter characterization (the standard N value). Aside from conserving the performance of PROSPECT inversion, the N parameter also serves as a useful metric for quantifying structural diversity in leaves, which is unique from LMA and EWT, and rapidly measurable using hyperspectral techniques. The distribution of the N parameter among global leaves is also unexplored, with only a few studies to date considering the N parameter as an important characteristics of leaves (Nunes et al., 2017; Qiu et al., 2018). Given the success with which we estimated the N parameter using singular reflectance or transmittance, the N parameter may be a novel metric for characterizing leaf structural diversity, from the leaf to canopy level. This parameter could change in tandem with variation in the anatomical structure of leaves, such as the variation in the quantity of air to cell spaces observed with nutrient deficit (Battie-Laclau et al., 2014), serving as a signal of nutrient status.

Prior estimation of the N parameter is also relatively straightforward to apply to inversion procedures, with no considerable loss in computing efficiency. In addition, given the spectral regions of wavelengths we found to be optimal for N prediction, this technique could potentially be applicable to various scales of multispectral and hyperspectral remote sensing applications, as it avoids regions of high water absorption (Behmann et al., 2016; Arellano et al., 2015; Gevaert et al., 2015), but this remains to be tested in terms of canopy structure, background reflectance, acquisition geometries, etc. In addition, further work to improve how structural variation within and amongst leaves is represented by the N parameter could address the lack of cell-specific structural representation in PROSPECT. Currently surface epidermal cells, palisade columnar mesophyll cells, and spongy spherical mesophyll cells are all imperfectly assumed to be optically and structurally identical as components of N elementary homogenous layers (Li et al., 2018; Qiu et al., 2018; Gerber et al., 2011), despite their anatomical variation and relative abundance having an important influence on the path length of photons within leaves, and subsequently influencing reflectance on and transmittance through leaves. Qiu et al. (2018) developed a modification to PROSPECT, known as PROSPECT-g, to account for the effects of anisotropic scattering, introducing an additional parameter to account for internal light scattering beyond the N parameter. Qiu et al. (2018) reported improved retrieval success with 60%-70% of tested samples therein, including significant improvement in LMA retrieval, though the multi-step inversion procedure involved may be computationally demanding for some research applications. While estimating the N parameter through a reflectance or transmittance ratio in junction with a regression model as we have necessitates additional computational resources when inverting PROSPECT on reflectance or transmittance alone, this additional step is relatively inconsequential in comparison to the resources required for single or multiple PROSPECT inversion(s).

While reflectance and transmittance together carry the most information for PROSPECT inversion and robust retrieval of all leaf constituents, researchers may not have the capacity to measure both, and for logistical or financial reasons be obliged to choose one or another. This choice should be guided by the constituent(s) of interest to be estimated, as our results demonstrate that PROSPECT inversion on reflectance alone or transmittance alone produced variable results across constituents. Reflectance-based methods slightly outperformed transmittance-based methods for the retrieval of Cab, while for the retrieval of Cxc, EWT, and LMA, transmittance-based methods performed slightly better, though in each case the difference in NRMSE between top reflectance-based and top transmittance-based methods was small (less than 7% NRMSE). An alternative factor to retrieval success to consider when choosing between measuring reflectance or transmittance for the estimation of leaf constituents may be the scale of intended knowledge transformation. Reflectance has been measured from the leaf to canopy scale with spectroradiometers, unmanned aerial vehicles (Berni et al., 2009), near-remote sensors (Alberton et al., 2017; Steenweg et al., 2017), as well as satellite-based sensors (Tucker and Sellers, 1986), for decades, leading to a wealth of accumulated data for monitoring, analysis, and comparison. Transmittance can be measured at the leaf level with directional-hemispherical spectroradiometers but cannot be measured at greater spatial scales with current technologies (Sun et al., 2018) or even at the leaf-level with bidirectional spectroscopy (Arellano et al., 2017). A decision tree for choosing the best approach based upon logistical constraints and constituents of interests is presented in Figure 3-7, informed by our findings in the present study.

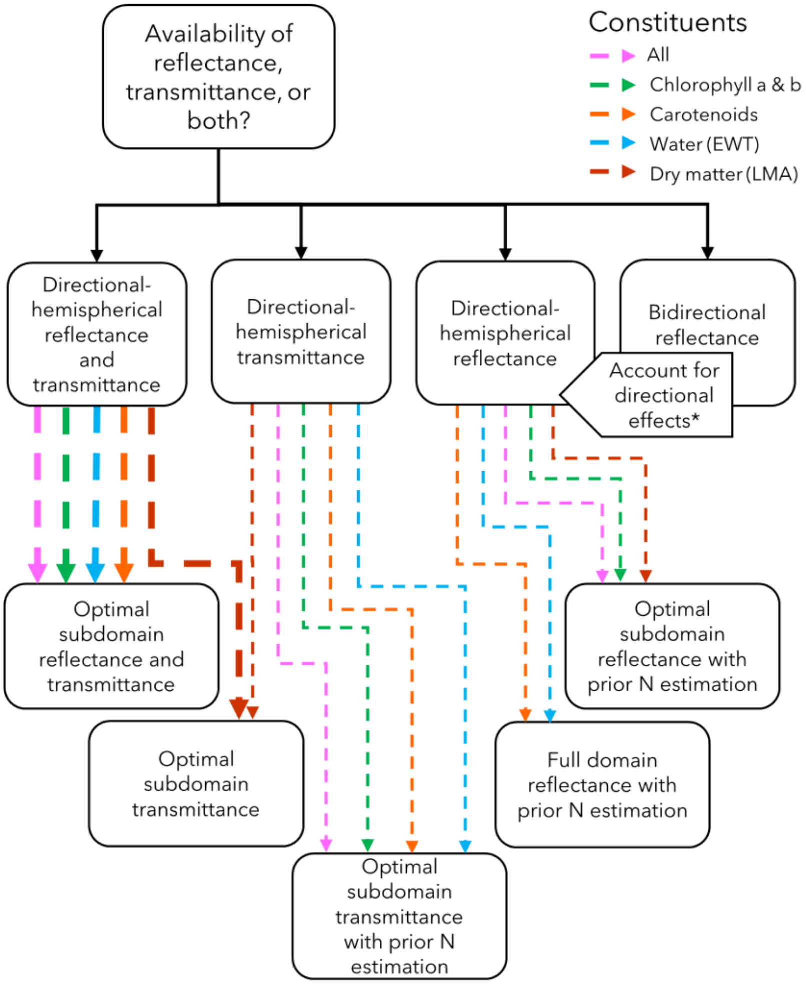

Figure 3-7. *A decision tree for choosing the best approach based upon logistical constraints (availability of reflectance, transmittance, or both) and leaf constituents of interest for estimation (the combination of chlorophyll a and b, carotenoids, EWT, LMA, or individually chlorophyll a and b, carotenoids, EWT, or LMA), based upon the approaches with the lowest corresponding NRMSE. The thickest lines correspond to the approach by which a constituent was best estimated globally. *For more information on accounting for directional effects consult Jay et al. (2016) and Li et al. (2019a; 2018).*

While reflectance measurements are ideally collected using an integrating sphere, producing directional-hemispherical measurements, leaf clips are becoming increasingly popular due to their relative affordability and ease of application. However, leaf clips generally provide bidirectional reflectance measurements and or transmittance estimations, rather than directional-hemispherical reflectance and transmittance as is required by traditional PROSPECT inversion methods. Directional-hemispherical reflectance is defined by Schaepman-Strub et al. (2006) as “the ratio of the radiant flux for light reflected by a unit surface area into the view hemisphere to the illumination radiant flux, when the surface is illuminated with a parallel beam of light from a single direction”, and bidirectional reflectance is therein defined as “the ratio of the reflected radiant flux from the surface area to the reflected radiant flux from an ideal and diffuse surface of the same area under identical view geometry and single direction illumination”. A number of studies have inverted PROSPECT directly on bidirectional reflectance measurements to estimate foliar constituents, not taking into the account the difference between directional-hemispherical and bidirectional information (Hill et al., 2019; Kattenborn et al., 2019; Lassalle et al., 2019; Lu et al., 2018; Sonobe et al., 2018; Arellano et al., 2017; Shiklomanov et al., 2016; Buddenbaum et al., 2012), reducing potential retrieval accuracy. Hill et al. (2019) reported poor performance of PROSPECT-D in retrieving pigments, especially Cxc, which therein was over-estimated by a factor of nearly 2. However, Hill et al. (2019) inversed PROSPECT-D supplied with bidirectional reflectance spectra from a spectroradiometer equipped with a leaf clip, using the minimization method of Jay et al. (2016), which was designed for directional-hemispherical spectra in junction with close-range bidirectional hyperspectral imagery rather than leaf level measurements. While Jay et al. (2016) propose an adaptation to directional-hemispherical RTMs such as PROSPECT for close-range applications, Jay et al. (2016) note that directional-hemispherical RTMs such as PROSPECT cannot be applied directly to leaf level bidirectional spectral measurements, which is well established (Boren et al., 2019; Bousquet et al., 2005).

Bidirectional spectral reflectance responses, such as those collected with a leaf clip or through imagery, differ from directional-hemispherical reflectance responses due to the contrasting geometries of incident light with respect to the leaf and sensor in each case, which results in distinct reflectance measurements from the specular properties of leaf surfaces as well as anisotropic scattering by leaf surfaces, despite the isotropic features of leaf internal structure. Several strategies have been developed to improve the utility of bidirectional spectral measurements, and overcome the directional limitations of PROSPECT. Jay et al. (2016) developed a complimentary model to PROSPECT known as COSINE (ClOse-range Spectral ImagiNg of lEaves), which accounts for the specular properties of leaf surfaces as well as leaf orientation with the light incident angle, and when coupled with PROSPECT allowed for accurate retrieval of pigments, EWT, and LMA from hyperspectral images. Li et al. (2018) present another approach to improve the directional flexibility of RTM applications, by combining a continuous wavelet transformation with PROSPECT (PROCWT), which resulted in the improved retrieval of pigments, EWT, and LMA from bidirectional reflectance due to suppressed surface reflectance effects and enhancement of absorption features. Li et al. (2019a) show that bidirectional reflectance spectra exhibit a higher amplitude in the VIS over directional-hemispherical reflectance spectra, and are associated with different wavelength-specific responses for estimating leaf chlorophyll content. The inversion method of Hill et al. (2019) and others who have attempted PROSPECT inversions supplied with bidirectional reflectance spectra with or without estimated transmittance could be improved by accounting for differences between bidirectional and directional-hemispherical leaf reflectance spectra. Future work is needed however to directly evaluate the success of PROSPECT inversion supplied with directionally corrected bidirectional reflectance data against the traditional approach with directional-hemispherical reflectance and transmittance data, as well as the success of inversions supplied with directionally corrected bidirectional reflectance data and the amendments we investigate here: optimal spectral subdomains and prior estimation of the N parameter.

As global leaf optical monitoring efforts are challenged by a lack of field-based validation data, and as global analyses suggest that half of all variation in leaf traits occurs at the community-level (Nunes et al., 2017; Wright et al., 2004), extensive leaf-level optical datasets are needed to facilitate global leaf functional diversity monitoring. For many hyperspectral researchers, the measurement of both directional-hemispherical reflectance and transmittance in the field is challenging due to experimental effort and/or cost. The measurement of reflectance only, or transmittance only, is much easier since there is no need to change the integrating sphere configuration for each measurement, and could additionally simplify the design of leaf field spectrometers. In effect, measuring reflectance alone or transmittance alone would allow for a higher number of leaf samples for a given experimental effort, though inverting PROSPECT directly on reflectance spectra only or transmittance spectra only may prompt substandard retrieval accuracy, owing to a poor representation of leaf structure. Our results demonstrate that retrieval accuracy in this case can be improved with prior estimation of the N parameter from a reflectance or transmittance ratio in junction with a linear model, as well as use of spectral subdomains (520-560 nm for Cxc, 700-720 nm for Cab, 1700-2400 nm for EWT and LMA). Additionally, for researchers with access to the means to measure both reflectance and transmittance, modification to traditional PROSPECT inversion by inverting PROSPECT instead on an optimal subdomain can lead to improved retrieval accuracies of Cab, Cxc, EWT, and LMA. Improved retrieval successes of the pigments Cab and Cxc will enable improved understandings of leaf function and age (Féret et al., 2017), and allow for comparison between different sites without the need to collect destructive training samples over space and time (Wu et al., 2016; Yang et al., 2016).

One rewarding application of leaf-level spectroscopy is the facilitation of global scale monitoring. RTMs such as PROSPECT have been proven to be useful not only at the leaf scale, but as a module of canopy RTMs as well, such as SAIL (Kattenborn et al., 2019; Jacquemoud et al., 2009; Verhoef and Bach, 2007) and DART (Oliveira et al., 2017; Gastell-Etchegorry et al., 2015). While previous spaceborne remote sensing platforms were limiting in spatial, spectral, and temporal resolution, new and upcoming satellite missions including the German Environmental Mapping and Analysis Program (EnMAP) (Berger et al., 2018; Guanter et al., 2018) and Sentinel-2 mission by the European Space Agency (Brown et al., 2019; Grabska et al., 2019; Vaduva et al., 2019) offer unprecedented opportunities due to improved resolutions, with spectral resolutions as fine as 5 nm, spatial resolution as fine as 10 m, and a revisit period as frequent as 5 days, as well as global open access data platforms. Thus the timely improvement of widely-applicable RTMs such as PROSPECT is needed to accelerate the efficacy of emerging remote sensing techniques in estimating leaf constituents. The combined use of the approaches we present here could readily enhance the information available from current and future reflectance databases, including those lacking complimentary transmittance measurements, facilitating improved understandings of trait-environment relationships from the leaf to global scale (Kattenborn et al., 2019; Moreno-Martínez et al., 2018), at a time when temporally extensive datasets are becoming increasingly valuable in monitoring the effects of global change.

3.6 Conclusions

While the inversion of the physically-based radiative transfer model PROSPECT has allowed for robust and rapid estimation of important leaf biochemical constituents from leaf samples worldwide for decades, limitations in PROSPECT performance and logistical feasibility have motivated the development of improved inversion approaches. We investigated adaptations of the traditional PROSPECT inversion approach, including optimal spectral subdomains, the use of reflectance spectra alone or transmittance spectra alone, prior estimations of the structural N parameter, and the combination of these approaches, on more than 1400 broadleaf samples. The use of spectral subdomains for reflectance and transmittance data from 700-720 nm and 520-560 nm was found to be the most successful method of PROSPECT inversion for the retrieval of chlorophyll a and b (Cab) and carotenoids (Cxc), respectively, while spectral subdomains from 1700-2400 nm were optimal for the retrieval of both water content (EWT) and dry matter content (LMA). Estimation of the N parameter from a reflectance ratio at 1131 nm, and separately from a transmittance ratio at 1121 nm in junction with a regression model prior to PROSPECT inversion improved constituent retrieval success when performing inversions with reflectance spectra alone or transmittance spectra alone, as well as in junction with optimal subdomains. To improve PROSPECT constituent retrievals, we recommend using optimal subdomains when either or both reflectance and transmittance spectra are available, and to optimize the utility of hyperspectral datasets with the availability of only reflectance or transmittance we additionally recommend the use of prior information on the N parameter.

Chapter 4. Climate-driven shifts in leaf senescence are greater for boreal species than temperate species in the Acadian Forest Region

This chapter is under review for publication in Ecology and Evolution (submitted on December 19th, 2022).

4.2 Introduction

Phenology, the timing of recurrent biological events, is influenced by climate and therefore an important indicator of the biological effects of climate change. To optimize growing season length and reproduction potential while avoiding exposure of vulnerable tissues to adverse conditions, plants undergo annual changes that are timed relative to environmental cues such as temperature and daylength (Vitasse et al., 2013). In the late growing season following budset, hormones from distal buds and leaves supress bud development in what is known as paradormancy (Cline and Deppong, 1999). Following this phase, plants enter a state known as endodormancy or dormancy from autumn to winter, in which internal mechanisms within the bud limit bud cell growth. After sufficient exposure to chilling temperatures, plants enter ecodormancy or quiescence in which suboptimal growing conditions limit cell growth. Following sufficient exposure to warm temperatures, known as 'forcing', and sufficient daylength, ecodormancy release is observed as bud burst in which new leaves become visible (Delpierre et al., 2016). Later in the growing season, plants undergo leaf senescence and dormancy induction as daylength is shortened and temperatures become cooler (Beil et al., 2021; Caffarra et al., 2011).

Climate change is altering the timing of plant phenological events through changes in seasonal temperature and moisture regimes (Piao et al., 2019; Cleland et al., 2007; Kunkel et al., 2004; Scheifinger et al., 2003). Recent warming has generally led to earlier leaf emergence and delayed leaf senescence for most mid to high latitude tree species, culminating in an extension of the growing season (Estiarte and Peñuelas 2015; Polgar and Primack, 2011; Peñuelas and Filella 2009). Changes in leaf phenology have important implications for a range of processes on various spatiotemporal scales, including carbon cycling, water cycling, ecological interactions, susceptibility to unfavourable growing conditions or events, and long-term biogeographical range shifts (Meier et al., 2021; Pureswaran et al., 2019; Kharouba et al., 2018; Renner and Zohner, 2018; Chuine and Régnière, 2017; Morin et al., 2009; Cleland et al., 2007). Consequently, characterizing and predicting future changes in leaf phenology is important for environmental and natural resource planning and climate change adaptation. Predicting future patterns in leaf phenology with increasing surface temperatures is challenging however due to limited understandings of drivers and evolved cues, especially for leaf senescence (Chen et al., 2019; Piao et al., 2019; Delpierre et al., 2016; Gallinat et al., 2015; Keenan and Richardson, 2015).

Process-based modelling of leaf phenology can provide insight into the species-specific responses of leaf phenology to climate change and aid in predicting future leaf phenology patterns. Previous efforts have provided insight into potential future responses to climate change. Examples include shortened leaf colouration periods in autumn due to warming, heat stress, or moisture stress (Zohner and Renner, 2019; Xie et al., 2018b), as well as non-linear leaf emergence responses to further warming due to the constraining influence of photoperiod and chilling controls (Moon et al., 2021a; Chen et al., 2019). Studies have also found evidence for additional nuanced controls of leaf phenology, such as bud albedo, interdependence between spring and autumn phenology, carbon uptake capacity limitation, response to biomass loss, variable sensitivity to drivers, and others (Vitasse et al., 2021; Lang et al., 2019; Piao et al., 2019; Keenan and Richardson, 2015). Local-scale experimental studies have developed valuable insights for process-based modelling, though Wolkovich et al. (2012) reported that experimental studies may considerably underestimate phenological responses to warming relative to long-term observations. Relatively few studies have yet explored species-specific process-based modelling employing observations over large regions to examine how broad controls in leaf phenology differ among species in natural contexts (Cook et al., 2012), as well as potential responses to future climate warming.

While databases of leaf phenology observations are now globally extensive, there has been sparse in-situ coverage of the Acadian Forest Region, especially for the Canadian province Nova Scotia. The Acadian Forest Region is a temperate-boreal transitional forest zone in eastern Canada and northeastern United States (Taylor et al., 2020; Rowe, 1972; Figure 4-1). While proposed geographic boundaries of the Acadian Forest Region differ among sources, it is generally considered to be situated in eastern North America covering the Canadian provinces of New Brunswick, Prince Edward Island, and Nova Scotia, as well as part of Quebec, and much of the neighbouring American region of New England (Noseworthy and Beckley, 2020). Therein, species which typically grow in a temperate climate zone can be found alongside species which typically grow in a boreal climate zone. The common Acadian species *Acer rubrum* (commonly known as red maple), *Betula papyrifera* (white/paper birch), *Abies balsamea* (balsam fir) have contrasting geographic distributions in North America. *Acer rubrum* is a more temperate-climate suited species which can be found growing as far south as Florida. *Betula papyrifera* and *Abies balsamea* are more boreal-climate suited species which are relatively uncommon south of the midwestern US. The central latitude for *Acer rubrum* based on probability of occurrence density is about 42° latitude, while for *Betula papyrifera* and *Abies balsamea* it is about 50° and 51° latitude, respectively (McKenney et al., 2014; 2011; 2007).

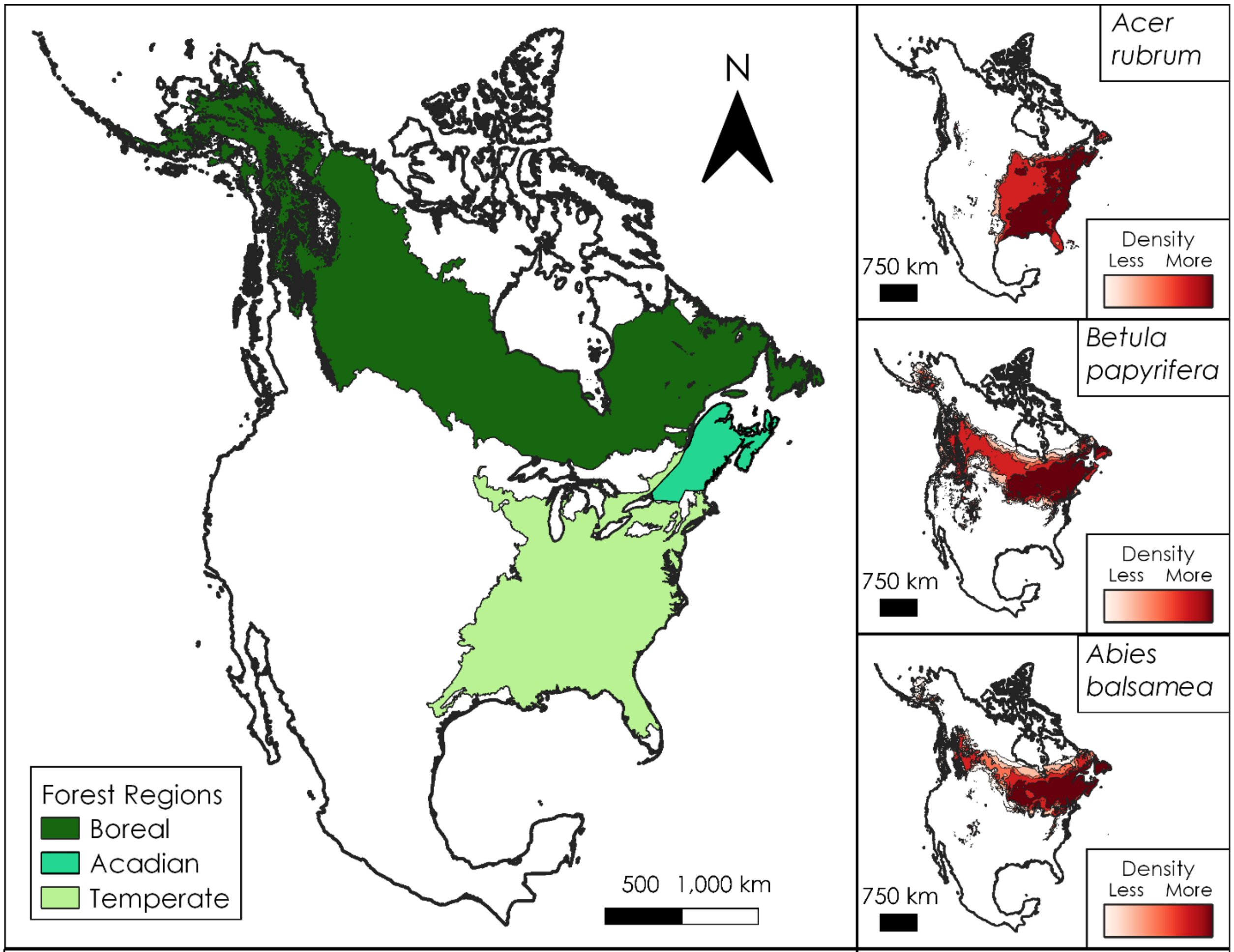

Boreal: Brandt, J.P. (2009). The extent of the North American boreal zone. Environmental Reviews 17:101–161.; Acadian: Two Countries, One Forest. (2014). Ecoregion Boundary. Northern Appalachian/Acadian Ecoregion Conservation Atlas.; Temperate: United States Environmental Protection Agency. (2022). Ecoregions of North America: Level I Ecoregions. CRS: NAD83 / STC Lambert

Based on relative probabilites from McKenney et al., 2014; 2011; 2007. CRS: NAD83/STC Lambert

Figure 4-1. *The distribution of the Boreal, Acadian, and Temperate Forest Regions within North America (left) and the distribution of Acer rubrum, Betula papyrifera, and Abies balsamea within North America (right). The "Acadian Forest Region" depiction is based on forest composition and stand characteristics and is distinct from more detailed ecozone and ecosite classifications which incorporate a greater variety of environmental variables (Neily et al., 2013). The precise extent of the Acadian Forest Region differs among sources (Two Countries One Forest, 2014; Rowe; 1972).*

The Acadian Forest Region presents an opportunity for monitoring the in-situ effects of climate change through leaf phenology for both temperate and boreal-typical species. Boreal species within the Acadian Forest Region such as *Betula papyrifera* and *Abies balsamea* are near the southern limits of their biogeographical range, while temperate species within the Acadian Forest Region such as *Acer rubrum* are near the northern limits of their range (Pearson and D'Orangeville, 2022; Fisichelli et al., 2014). Phenology is a trait that constrains where species can survive, as poorly timed phenology can lead to damage from changing environmental conditions, leading to often greater freeze injury risk for non-native species (Zanne et al., 2018; Vitasse et al., 2014). Trees which are located near their range limits may be more susceptible to environmental change (Wang et al., 2021; Körner et al., 2016). The Acadian Forest Region is therefore especially vulnerable to future changes in temperature and moisture regimes, and models have predicted a compositional decline of boreal species due to warming temperatures outside of the optimal biogeographical climate envelopes for these species (Taylor et al., 2017).

In addition, the Acadian Forest Region is subject to extreme weather in the form of hurricanes that lead to windthrow of shallow-rooted coniferous species such as *Abies balsamea* (Taylor et al., 2020). If the timing of fall leaf senescence is further delayed in the future, this could also make broadleaf species more susceptible to wind damage due to the added surface area (Gong et al., 2021). In the spring, increased climate variability leads to an increased risk of leaf-damaging frost events, which is compounded by the already highly dynamic nature of weather patterns in the maritime region of Canada due to the convergence of continental polar, maritime polar, and maritime tropical air masses (Garbary and Hill, 2021; Augspurger, 2013; Steenberg et al., 2013; Simmons et al., 1984). Trees within the Acadian Forest Region may also be at risk of deleterious drought effects as climate models predict an increased frequency and intensity of droughts, and phenology may play an important role in determining drought resilience (Pearson and D'Orangeville, 2022; Sánchez-Pinillos et al., 2022). The Acadian Forest Region therefore presents a unique and complex forest ecosystem, and better understandings of the leaf phenology of species therein and the potential effects of climate change are needed to predict future ecology and carbon uptake.

Understandings and predictions of future leaf phenology patterns in the eastern Acadian Forest Region are limited due to a lack of observational data, compounded by a highly variable climatic regime (MacLean et al., 2022; Pearson and D'Orangeville, 2022; Taylor et al., 2020; Garbary and Hill, 2021; Steenberg et al., 2013). A study comparing climate normals across Nova Scotia from 1961-1990 and 1991-2020 found that warming in the autumn has been more pronounced relative to spring, with a larger relative increase in the number of frost-free days in autumn (Garbary and Hill, 2021). Therefore, leaf senescence observations and modelling are crucial in addition to spring leaf emergence to understand the entire growing season phenology implications of climate change for the Acadian Forest Region. Inter-continental scale studies have found differing controls of phenology in North America versus Europe and Asia due to historical weather patterns (Zohner et al., 2020). Even within North America, phenological responses to environmental drivers and cues vary regionally (Melaas et al., 2016). This suggests that regional species-specific observations are needed to develop confident predictions of the response of vegetation to climate change throughout the 21st century for the Acadian Forest Region.

To better understand the environmental controls of leaf phenology for Acadian Forest Region tree species, we used phenocams to monitor the leaf phenology of three tree species across a natural climate gradient in the Canadian province of Nova Scotia throughout the 2019 to

2022 growing seasons. We also accessed records of leaf phenology across North America using the PhenoCam Network database (https://daac.ornl.gov/VEGETATION/guides/PhenoCam_V2.html; Seyednasrollah et al., 2019a). We selected the temperate-climate suited species *Acer rubrum* as well as the more boreal-climate suited species *Betula papyrifera* and *Abies balsamea*. These species are common to the Acadian Forest Region and currently monitored throughout the Acadian Phenocam Network and the PhenoCam Network. In this study we aim to parameterize a variety of species-specific process-based models of leaf phenology and simulate leaf phenology and growing season length for *Acer rubrum*, *Betula papyrifera*, and *Abies balsamea* under future climate change scenarios.

4.3 Methods

4.3.1 Acadian Phenocam Network

To monitor the leaf phenology of Acadian tree species we installed phenocams at twelve sites in the Canadian province of Nova Scotia before the onset of the 2019 growing season (Figure 4-2). These selected sites were upland, zonal forest sites with sufficient soil nutrients and moisture profiles to support long-lived, late-successional species and forests where successional pathways are dictated by climate and not constrained by site conditions (Baldwin et al., 2019). The ecosystem types selected – called ecosites in Nova Scotia’s Forest Ecosystem Classification system (Neily et al., 2013) – had both intermediate soil moisture regimes (i.e., fresh) and soil nutrient levels. Mixedwood stands are common on these sites and include broad leafed species like *Acer rubrum* (red maple), *Betula alleghaniensis* (yellow birch), and *B. papyrifera* (white/paper birch) and conifer species like *Abies balsamea* (balsam fir) and *Picea rubens* (red spruce). These phenocams were operational throughout the 2019-2020 growing seasons, with several observation gaps in the autumn of 2019 and spring of 2020 due to camera malfunctioning. In the 2020 growing season, we replaced these cameras with cellular trail cameras. Overall, we observed leaf emergence over the 2019-2022 growing seasons, and leaf senescence over the 2019-2021 growing seasons. The elevation for our sites ranges from 88 m to 322 m above sea level, with most sites located below 200 m.

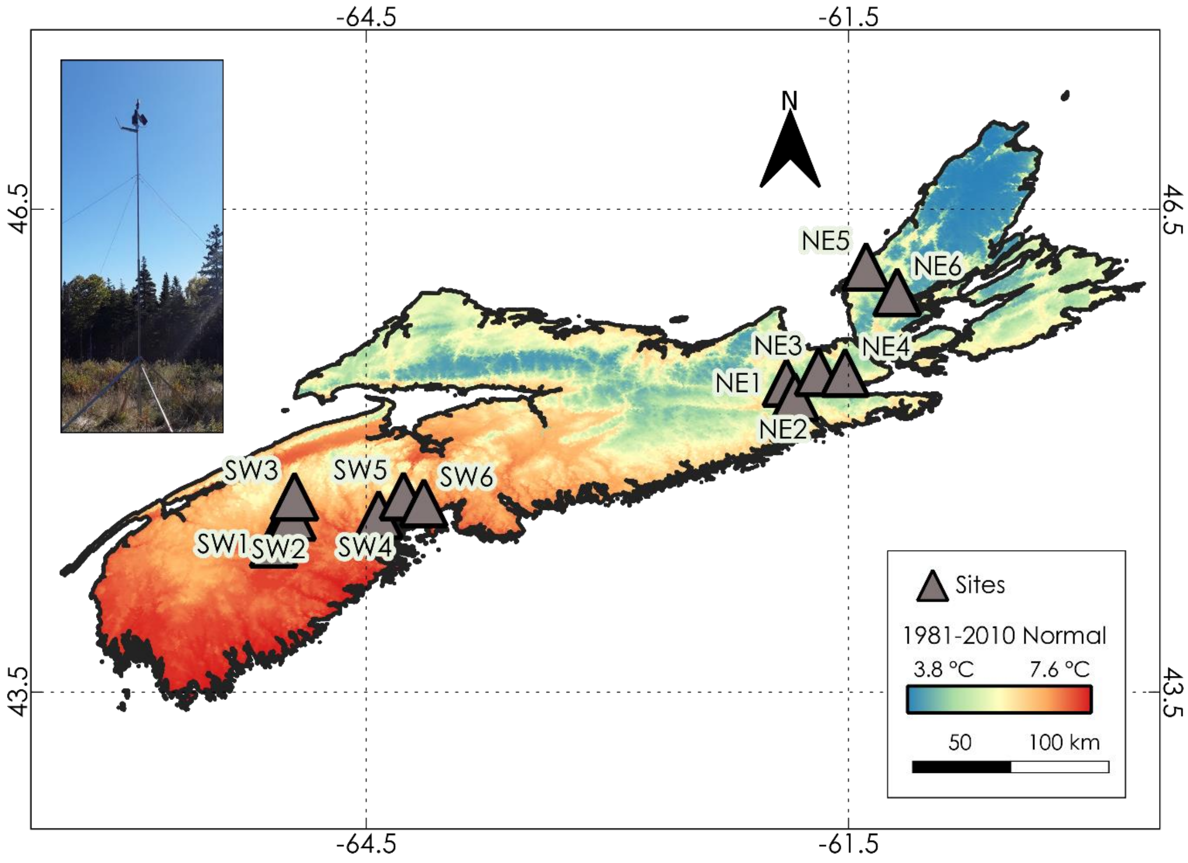

Figure 4-2. *Location of sites within the Acadian Phenocam Network with respect to the 1981-2010 temperature normal. An example station is shown on the top left. The spatial interpolation of mean annual air temperature normals calculated from 1981-2010 were obtained from Environment & Climate Change Canada (2022), McKenney et al. (2013), and Price et al. (2011).*

The technical specifications of each camera type in the Acadian Phenocam Network can be found in Table 4-1. The twelve cameras installed in 2019 were Moultrie M-50 trail cameras (https://www.moultriefeeders.com/m-50-game-camera). These cameras were then replaced with Spypoint Link-Evo (https://www.spypoint.com/en/support/cellular-trail-camera/product-link-evo.html) cameras. Each camera was solar-powered, north-facing and mounted at the top of a 6-m tower with a horizontal or else tilted ~5 ° downward landscape view, depending upon the local canopy situation. To ensure stability in the field of view, we used galvanized guy wire cables, aluminum angle tower leg braces, and a fixed aluminum angle base. All images were retrieved either remotely using the python selenium package (Python Software Foundation, 2022) (Spypoint cameras) or manually (Moultrie cameras) and catalogued by date and site. Regions of interest (ROIs) were delineated to encompass each distinct individual within the field of view of each camera, as well as the reference panel, using the phenopix package in R version 4.2.1 (R Core Team, 2022; Filippa et al., 2016). The timeseries of images for each site were reviewed to ensure ROIs were delineated without interference from background elements. The species identification of each ROI was confirmed manually in the field. We classified trees with heights below 5 m as immature and excluded these from analyses, as these tend to exhibit an earlier leaf emergence than mature or canopy-height conspecific trees, occluding climatic influences (Vitasse and Basler, 2014).

Table 4-1. *Imagery specifications for cameras utilized across the Acadian Phenocam Network. Image resolutions are shown with pixel and megapixel (MP) dimensions.*

Camera	Bits Per Channel	Resolution	Daily Image Frequency
Spypoint Link-Evo	8	1080X1920 (2 MP)	1-3
Moultrie M-50	24	3420X6080 (20 MP)	6
Brinno	24	1280X720 (0.9 MP)	6

Slight shifts in the field of view of each camera due to station maintenance over time were accommodated for by creating separate analysis ROI coordinates for images before and after each shift using the "locator()" function in the graphics package in R (R Core Team, 2022). Where a tilt in the field of view was detected, new ROIs were carefully delineated to match the targets of the ROIs from the previous field of view. The "extractVIs()" function in the phenopix package was used to extract average red, green, and blue colour channel intensity values within each ROI for each image. To extract the greenness timeseries we calculated the green chromatic coordinate (G_{CC}) or relative greenness as is shown in Equation 4-1.

$$G_{CC} = \frac{B_G}{B_G + B_R + B_B} \tag{4-1}$$

Therein, B_G corresponds to the intensity (brightness) of the green colour channel, B_R to the intensity of the red colour channel, and B_B to the intensity of the blue colour channel. The G_{CC} represents the intensity of the green colour channel versus the total intensity of all colour channels. We then filtered timeseries by three-day moving window 50th percentiles of G_{CC} values to remove both high and low outliers (Peltoniemi et al., 2018; Richardson et al., 2018a; 2018b). For further noise-reduction we applied an adapted version of the PhenoCam Network protocols. We exchanged outliers detected as 4 times greater than the standard deviations of residuals for the upper threshold and 2 times greater than the standard deviations of residuals for the lower threshold with locally estimated scatterplot smoothing (LOESS) curve-fitted values to further prioritize the removal of anomalous G_{CC} declines (Seyednasrollah et al. 2019b; Richardson et al., 2018a). For smoothing over the dormant period, we exchanged original dormant period G_{CC} values with that of the dormant season mode, calculated as the lowest local maxima in a density plot of G_{CC} values for a given year. We calculated the timing of leaf emergence and senescence as 50% of the amplitude of rising and falling G_{CC} curves (Figure 4-3). Growing season length was calculated as the time between leaf emergence and senescence. To obtain phenology estimates at the site-level, we selected sites with at least 3 individuals of a given species present and averaged each individual phenocam-derived phenology date to produce a site-level observation for each species and site-year, which are shown in Appendix III: Tables A3-5 and A3-6 for leaf emergence and senescence, respectively.

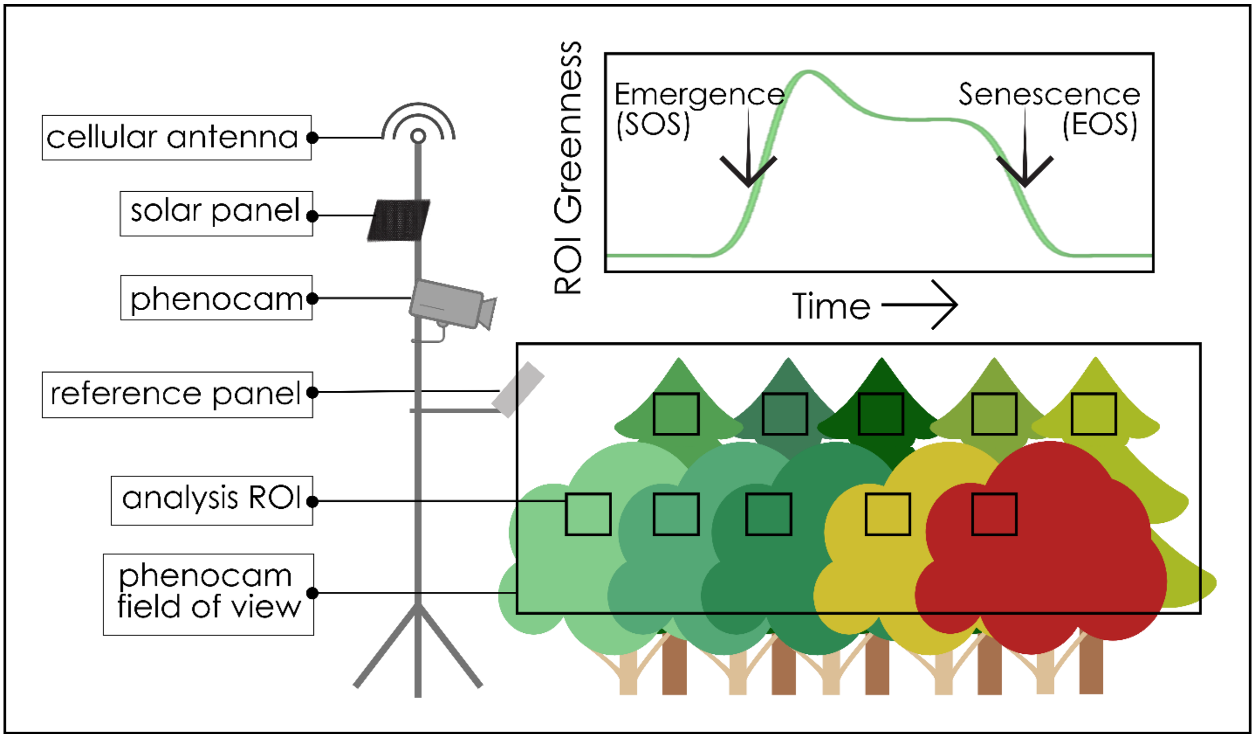

Figure 4-3. *Summary of the station infrastructure (left) and phenology extraction process (right) for Acadian Network phenocams. Here leaf emergence is synonymous with the start of season (SOS) and leaf senescence with the end of season (EOS).*

The Moultrie M-50 and Spypoint Link-Evo trail camera models deployed in this study do not have the option to fix the image white balance. Spurious vegetation transition signals may arise due to an automatic white balance (Seyednasrollah et al., 2019b; Richardson et al., 2018a). To ensure that the colour channel patterns observed through the cameras across our sites were due to changes in leaf canopy development rather than colour scaling artefacts, we utilized several means of validation and of quality control: 1) installation of grey non-reflective reference panels in the field of view of all cameras in 2020 onwards and normalization of vegetation G_{CC} timeseries following Delpierre et al. (2020) and Jacobs et al. (2009), 2) filtering threshold amplitude of G_{CC} timeseries twice that of the reference panel, 3) comparison of curve-estimated phenology to phenology obtained from daily (May) to weekly (June onwards) manual ground observations for three *Populus tremuloides* individuals at an external site in 2021, 4) comparison of curve-estimated phenology for 15 individuals to the estimation of leaf phenology via visual inspection of images for 2019, 2020, and 2021 site-years (Peltoniemi et al., 2018; Kosmala et al., 2016; Klosterman et al., 2014; Ahrends et al. 2009), and 5) comparison of leaf phenology derived from a Spypoint camera to that of a fixed white balance Brinno camera (https://brinno.com/pages/product-tlc200pro) at an external site. For both manual field and visual observations, we considered leaf emergence to occur when most leaves had emerged entirely from bud scales such that leaf midribs were visible and leaf senescence to occur when most leaves had begun to show autumn colouration. Curve-estimated leaf emergence dates for the three *Populus tremuloides* individuals at the external site for the Spypoint Link-Evo camera were equal to the reference manually observed date (May 22nd, 2021, for all individuals) and the Brinno camera estimate was four days early. Curve-estimated leaf emergence values had a correlation of 0.78 with the 15 visual estimates, while curve-estimated leaf senescence values had a correlation of 0.74. This performance was in line with previous studies which have shown correlation values of 0.52-0.99 for leaf emergence 0.61-0.99 for leaf senescence (Seyednasrollah et al., 2021; Zhang et al., 2020; Delpierre et al., 2020; Seyednasrollah et al., 2019b; Richardson et al., 2018a; Xie et al., 2018a; Peltoniemi et al., 2018; Klosterman and Richardson, 2017; Browning et al., 2017; Berra et al., 2016; Kosmala et al., 2016; Wingate et al., 2015; Keenan et al., 2014; Klosterman et al., 2014; Ahrends et al., 2009; Ahrends et al., 2008).

4.3.2 PhenoCam Network

To ensure our phenology model training dataset was representative of future climate space, we employed phenocam ROI site-year observations from the North American PhenoCam Network. For information on PhenoCam Network protocols refer to Seyednasrollah et al. (2019b) and Richardson et al. (2018a). Regions of interest from PhenoCam cameras are delineated to characterize the dominant vegetation in each field of view, and in some cases several ROIs are defined to distinguish between different plant functional types such as evergreen needleleaf versus deciduous needleleaf (Richardson et al., 2018c). The G_{CC} is then calculated as is shown in Equation 4-1 from red, green, and blue colour channel intensity values within each ROI for each image to produce greenness timeseries. For compatibility with Acadian Phenocam Network observations, we extracted the timing of 50% amplitude in the rising and falling portion of 3-day 50th percentile filtered G_{CC} records from the PhenoCam V2.0 dataset, which includes observations up until the end of the 2018 growing season (Seyednasrollah et al., 2019a). To populate our training dataset for each tree species, we selected phenocam records from the PhenoCamV2.0 dataset which had one of our species as the dominant species in the field of view (Table 4-2).

Table 4-2. *Summary of observations from the Acadian Network and PhenoCam Network. Each observation corresponds to one phenocam site-year.*

Species	Leaf Phenophase	Total Number of Site-years	Total Acadian Site-years	Total PhenoCam Site-years
Acer rubrum	Emergence	278	34	244
Betula papyrifera	Emergence	89	20	69
Abies balsamea	Emergence	43	28	15
Acer rubrum	Senescence	237	22	215
Betula papyrifera	Senescence	82	14	68
Abies balsamea	Senescence	29	15	14

4.3.3 Leaf Emergence models

We explored a variety of leaf emergence models with varying degrees of complexity in terms of environmental drivers, including thermal forcing, chilling exposure, and photoperiod from Hufkens et al. (2018) and Basler, (2016; Table 4-3). Each model generally simulates an accumulation until a critical threshold is reached and leaf emergence occurs, with a parameterized starting date for accumulation of drivers. Four of the models simulate a release from ecodormancy only, using either temperature forcing alone or in combination with photoperiod as drivers. The Thermal Time model accumulates forcing above a base temperature in a linear fashion until a critical threshold is reached and leaf emergence occurs (Hufkens et al., 2018; Basler, 2016; Wang 1960; Réaumur, 1735). The Thermal Time with Sigmoidal Temperature Response model also accumulates forcing above a base temperature until a critical threshold is reached and leaf emergence occurs, though with a sigmoidal accumulation function (Hufkens et al., 2018; Basler, 2016; Kramer, 1994; Hänninen, 1990). The Photo-Thermal Time model accumulates forcing above a base temperature in a linear fashion adjusted by daylength (Hufkens et al., 2018; Basler, 2016; Črepinšek et al., 2006; Masle, 1989). The Photo-Thermal Time with Sigmoidal Temperature Response model also accumulates forcing above a base temperature with a sigmoidal function adjusted by daylength until a critical threshold is reached and leaf emergence occurs (Hufkens et al., 2018; Basler, 2016; Črepinšek et al., 2006; Kramer, 1994; Hänninen, 1990; Masle, 1989). The M1 model is similar to the Photo-Thermal Time model, though with an additional exponential constant (Hufkens et al., 2018; Basler, 2016; Blümel and Chmielewski, 2012).

Two models simulate a release from endodormancy and ecodormancy with a combination of temperature forcing and chilling as drivers. The Alternating Model accumulates forcing and chilling exposure without the stipulation that chilling requirements are to be met prior to the onset of forcing accumulation. Within the Alternating Model each day can contribute to either requirement until accumulated forcing has surpassed a critical threshold which is altered by chilling exposure, and leaf emergence occurs (Hufkens et al., 2018; Basler, 2016; Murray et al., 1989; Cannel and Smith 1983). The Sequential Model assumes that chilling requirements are fulfilled prior to the onset of forcing accumulation with a bell-shaped chilling temperate response function. Once a critical threshold in chilling accumulation is reached, forcing accumulates until another critical threshold is reached and leaf emergence occurs (Hufkens et al., 2018; Basler, 2016; Kramer, 1994; Hänninen, 1990). Finally, the Dormphot model simulates dormancy induction, endodormancy release, and ecodormancy release with a combination of drivers including chilling, forcing, and daylength. Within the Dormphot model, dormancy induction occurs once accumulated cool temperatures and shortening daylengths in the fall reach a combined critical threshold. Once dormancy has been induced, chilling accumulates and adjusts a parameter which governs daylength and forcing accumulation until a critical threshold is reached and leaf emergence occurs (Hufkens et al., 2018; Basler, 2016; Caffarra et al., 2011).

All leaf emergence models were applied using the phenor package in R with species-specific training and validation for each available site-year (Hufkens et al., 2018). Model parameterization for each species was optimized using the initial parameter ranges from Hufkens et al. (2018) and general simulated annealing with the optimize_parameters function within the phenor package which is an extension of the GenSA optimization function within the GenSA package in R (Xiang et al., 2013). General simulated annealing is a technique of optimization which is analogous to the process of metal cooling. The GenSA function is based upon the Boltsmann machine and Cauchy machine simulated annealing approaches (Hufkens et al., 2018; Tsallis and Stariolo, 1996). General simulated annealing was constrained with a maximum of 50,000 iterations and a starting temperature of 10,000 for each annealing to achieve a global minimum in root mean squared error (RMSE). Equations and optimal parameters for each model from this process are shown in Appendix III: Table A3-1 and Table A3-2, respectively.

Table 4-3. *Leaf emergence models included in this study.*

Model	Process(es) Included	Reference
Thermal Time (TT)	Ecodormancy Release	Hufkens et al., 2018; Basler, 2016; Wang 1960; Réaumur, 1735
Thermal Time with Sigmoidal Temperature Response (TTs)	Ecodormancy Release	Hufkens et al., 2018; Basler, 2016; Kramer, 1994; Hänninen, 1990
Photo-Thermal Time (PTT)	Ecodormancy Release	Hufkens et al., 2018; Basler, 2016; Črepinšek et al., 2006; Masle, 1989
Photo-Thermal Time with Sigmoidal Temperature Response (PTTs)	Ecodormancy Release	Hufkens et al., 2018; Basler, 2016; Črepinšek et al., 2006; Kramer, 1994; Hänninen, 1990; Masle, 1989
M1	Ecodormancy Release	Hufkens et al., 2018; Basler, 2016; Blümel and Chmielewski, 2012
Alternating (AT)	Endodormancy & Ecodormancy Release	Hufkens et al., 2018; Basler, 2016; Murray et al., 1989; Cannel and Smith 1983
Sequential (SQ)	Endodormancy & Ecodormancy Release	Hufkens et al., 2018; Basler, 2016; Kramer, 1994; Hänninen, 1990
Dormphot (DP)	Dormancy Induction, Endodormancy & Ecodormancy Release	Hufkens et al., 2018; Basler, 2016; Caffarra et al., 2011

4.3.4 Leaf Senescence models

We explored a variety of leaf senescence models with various configurations of environmental drivers including temperatures, photoperiod, and the preceding estimated leaf emergence date from Liu et al. (2020; Table 4-4). As with the leaf emergence models, each leaf senescence model generally simulates an accumulation until a critical threshold is reached and leaf senescence occurs, though with a parameterized or fixed July 1st starting date. The White model is an exception which does not involve accumulation, and instead uses instant senescence triggers based on cooling temperatures and shortening daylength or else extreme cold temperatures (Liu et al., 2020; White et al., 1997). The Delpierre model accumulates cool temperatures and shortening daylength at a rate controlled by driver-specific weighting parameters until a critical threshold is reached and lead senescence occurs (Liu et al., 2020; Delpierre et al., 2009). The Jeong Model accumulates cool temperatures once daylength is sufficiently short until a critical threshold is reached and leaf senescence occurs (Liu et al., 2020; Jeong et al., 2014). The Dormphot Dormancy Induction Model is identical to the dormancy induction simulation within the full Dormphot leaf emergence model used above. Leaf senescence or dormancy therein occurs once cooling temperatures and shortening daylength accumulate to a critical value (Liu et al., 2020; Hufkens et al., 2018; Caffarra et al., 2011). Two models, the Delpierre model with Preceding Spring Leaf Emergence and the Dormphot Dormancy Induction Model with Preceding Spring Leaf Emergence, include the influence of the preceding leaf emergence timing which has been found to exert a constraint of leaf senescence timing. For these models, the Photo-Thermal Time with Sigmoidal Temperature Response model is used to provide an estimated leaf emergence timing which incorporates both forcing and daylength (Liu et al., 2020; Keenan and Richardson, 2015). The timing of the preceding leaf emergence relative to the long-term average estimated from a 30-year daily average temperature window influences the critical threshold for leaf senescence for these two models.

The parameter ranges for each leaf senescence model were determined by reviewing local climate data, the available literature for each model, and the range of optimal values from Liu et al. (2020). All leaf senescence models were applied in R with species-specific training and validation for each available site-year. As with the leaf emergence models, senescence model parameterizations were optimized for each species using general simulated annealing with a maximum of 50,000 iterations and a starting temperature of 10,000 for each annealing to find model parameters which corresponded to a global minimum RMSE. Equations and optimal parameters for each model from this process are shown in Appendix III: Table A3-3 and Table A3-4, respectively.

Table 4-4. Leaf senescence models included in this study.

Model	Process(es) Included	Reference
White (WM)	Dormancy Induction	Liu et al., 2020; White et al., 1997
Delpierre (DM)	Dormancy Induction	Liu et al., 2020; Delpierre et al., 2009
Jeong (JM)	Dormancy Induction	Liu et al., 2020; Jeong et al., 2014
Dormphot with just Dormancy Induction (DPDI)	Dormancy Induction	Liu et al., 2020; Hufkens et al., 2018; Caffarra et al., 2011
Delpierre with Preceding Spring Leaf Emergence (DMs)	Preceding Ecodormancy Release & Dormancy Induction	Liu et al., 2020; Delpierre et al., 2009
Dormphot Dormancy Induction with Preceding Spring Leaf Emergence (DPDIs)	Preceding Ecodormancy Release & Dormancy Induction	Liu et al., 2020; Caffarra et al., 2011

4.3.5 Model Performance Evaluation

To evaluate the performance of each model for each species, we calculated RMSE between model predicted and that of phenocam-derived leaf emergence and senescence timings for each site-year observation with a pooled-sample or global validation. This metric is commonly used to describe model performance in phenology modelling studies (Hufkens et al., 2018; Basler, 2016). We calculated the Null model RMSE as the RMSE between observed values and the average observed training dataset value to compare model performances to the assumption of a fixed mean value. We considered the model with the lowest RMSE to be the best performing model for each validation exercise.

To examine the regional transferability of each model, we performed a smaller scale calibration and validation with observations just from the Acadian Phenocam Network. To examine the regional specificity of the models, we also trained the models with all observations and then validated the models with just observations from the Acadian Phenocam Network. We also calculated the bias between model-estimated and observed phenophases for each validation exercise to examine potential systematic over-and under-estimations. To examine globally parameterized model performances for warm site-years and for cold-site years, we selected validation site-years with annual average temperatures within the top 25th percentile of annual average temperatures for warm site-years and within the lower 25th percentile for cold site-years. We then computed the RMSE and bias for these site-years for globally parameterized models. To examine how well these models performed with independent validation, we also performed a leave-one-out cross-validation and a k-fold cross-validation. For efficiency with these two validations each model was parameterized with a maximum of 4,000 iterations. The value of 'k' was allowed to vary such that each sample group had five or more samples, which is an effective model quality assessment approach with a range in dataset sizes (Jiang and Wang, 2017; Yadav and Shukla, 2016).

4.3.6 Obtaining Driver Data

To train each phenology model, we obtained daily estimated weather data for each site-year in both the Acadian and PhenoCam Network datasets up until 2021 from the Daymet: Daily Surface Weather Data on a 1-km Grid for North America, Version 4 R1 dataproduct using the daymetr package in R (Thornton et al., 2022; Hufkens et al., 2018). Long-term mean temperatures from 1980-2021 were also obtained for each site from this dataset using the daymetr package. For January-July of 2022 for the Acadian Network, we obtained daily weather data from the Daymet Version 4 dataset (Thornton et al., 2021; https://daac.ornl.gov/cgi-bin/dsviewer.pl?ds_id=1904). We used 1 km X 1 km grids with the nearest central coordinates to each site locations for each site-year.

To project leaf phenology for each of our three species for the Acadian Forest Region sites, we simulated leaf phenology from 2001-2100 with each leaf species-calibrated phenology model under the effects of climate warming with three representative concentration pathways (RCPs): RCP 2.6 (low emissions), RCP 4.5 (intermediate emissions), and RCP 8.5 (high emissions). We obtained simulated daily temperature data with the Coupled Model Intercomparison Project 5 (CMIP5) model ensemble of 24 climate models from Climatedata.ca, (2022; https://climatedata.ca/download/). Each climate model output was downscaled and bias-adjusted using the Bias Correction/ Constructed Analogues with Quantile delta mapping reordering (BCCAQv2) method (Cannon et al., 2015). We extracted data from the 300 arc second spatial resolution (1/12°, ~10 km) grid cells with central coordinates closest to our site locations.

4.4 Results

4.4.1 Leaf Phenology Training Data

Leaf phenology patterns in relation to temperature were similar for the Acadian and PhenoCam Networks (Figure 4-4). Within the Acadian Phenocam Network, each species generally showed a spatial pattern in leaf emergence dates reflecting the climate gradient used in their establishment, with later emergence at the colder northeastern sites and earlier at the warmer southwestern sites. In contrast, leaf senescence dates for each species did not exhibit a distinct climate pattern. Surprisingly, several sites in the warmer region of the Acadian Network had earlier leaf senescence dates than that of the colder region, suggesting the timing of preceding leaf emergence may have had an important influence on the timing of leaf senescence. Leaf emergence was earlier for warmer springs for all species, with a significant linear relationship (adjusted R^2:0.81, $p < 0.001$ for *Acer rubrum*, adjusted R^2:0.56, $p < 0.001$ for *Betula papyrifera*, adjusted R^2:0.25, $p < 0.001$ for *Abies balsamea*). The more boreal-typical species *Betula papyrifera* and *Abies balsamea* had reduced coverage of the growing season temperature ranges relative to *Acer rubrum*, though under similar temperatures tended to have similar or earlier timings of leaf emergence and senescence. Under similar temperatures, *Abies balsamea* in the Acadian Network tended to have a later leaf emergence in comparison to the PhenoCam Network. In contrast, leaf senescence had no clear linear relationship with late summer-early autumn temperatures. While there is some overlap in leaf senescence timings for *Abies balsamea* in both networks, within the Acadian Network under similar conditions it tended to be earlier, prompting a reduced season length. Season lengths tended to increase with increasing mean annual temperatures across site-years, though with values ranging on the order of weeks at a given annual average temperature within and among species. Overall, the Acadian Phenocam Network is situated with cold-intermediate seasonal temperatures relative to the PhenoCam Network, though for these species tend towards later leaf emergence and earlier leaf senescence, leading to a reduced season length.

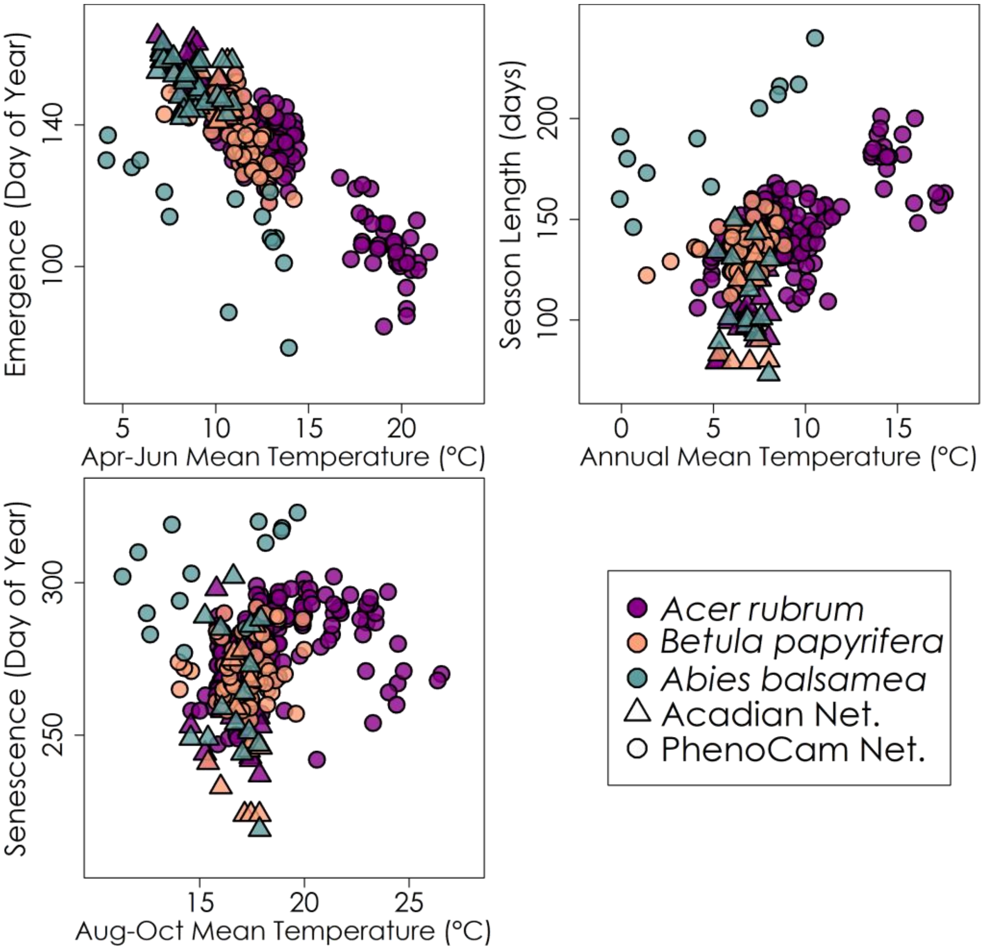

Figure 4-4. *Leaf phenology patterns according to seasonal or annual temperature averages for both the Acadian and PhenoCam Networks.*

4.4.2 Leaf Emergence models

No one leaf emergence model had exceptional performance relative to the other models across species and validation exercises, though all generally managed to outperform the Null model (Figures 4-5, 4-6, and 4-7). For the global validation, the Dormphot and M1 models were amongst the top two models with the lowest RMSE relative to other models for each species. All eight models outperformed the Null model for each species and validation, each process model having typically a week or less in RMSE for *Acer rubrum* (Figure 4-5) and *Betula papyrifera* (Figure 4-6) and less than two weeks for *Abies balsamea* (Figure 4-7). Training and validating with just the Acadian Phenocam Network generally prompted a similar pattern in model performance to the global evaluation, though the Dormphot model outperformed the M1 model for *Betula papyrifera*. In contrast, global training and validation with just the Acadian Phenocam Network prompted a different pattern in model performance, favoring the Photo-Thermal Time with Sigmoidal Temperature Response model for *Betula papyrifera* and *Acer rubrum*, though the Dormphot model for *Abies balsamea*. When predicting leaf emergence for warm site-years the M1 model was optimal for *Betula papyrifera* while the Dormphot model was optimal for the other species. During cold site-years, the M1 model was optimal for *Abies balsamea* while the Photo-Thermal Time with Sigmoidal Temperature Response model was optimal for the other species. For k-fold and leave-one-out cross-validation, the M1 model was generally optimal, though the Alternating Time model was optimal for k-fold cross-validation with *Abies balsamea*. For both *Acer rubrum* and *Betula papyrifera*, the Dormphot model failed to outperform the Null model with one or both of the k-fold and leave-one-out cross-validations, suggesting the performance of this complex model is sensitive to validation sample size. Overall, optimal models across validation exercises and species were the Dormphot, M1, and Photo-Thermal Time with Sigmoidal Temperature Response models, suggesting these models are well suited to application across different species when conducting species-specific parameterizations. For *Acer rubrum* and *Abies balsamea* performance across models ranged by about two days, while for *Betula payrifera* RMSE values ranged by less than half a day. Bias varied in direction and magnitude across validations. For *Abies balsamea* (Figure 4-7), global training and Acadian validation prompted an early bias while for *Acer rubrum* (Figure 4-5) and *Betula papyrifera* (Figure 4-6) the same validation prompted a mixed bias. All models had an early bias of prediction for warm site-years and a late bias for cold site-years. The simple thermal time model was amongst the top three models with the greatest absolute bias for a variety of validation exercises across species, including global training and validation, validation with just the Acadian Network, with warm years and with cold years.

Figure 4-5. *Root mean squared error and mean bias for each of eight leaf emergence models and a Null model for seven different validation exercises for Acer rubrum. The total number of Acer rubrum leaf emergence observations for is shown on the top right. The model with the lowest root mean squared error for each validation exercise is denoted with an asterisk.*

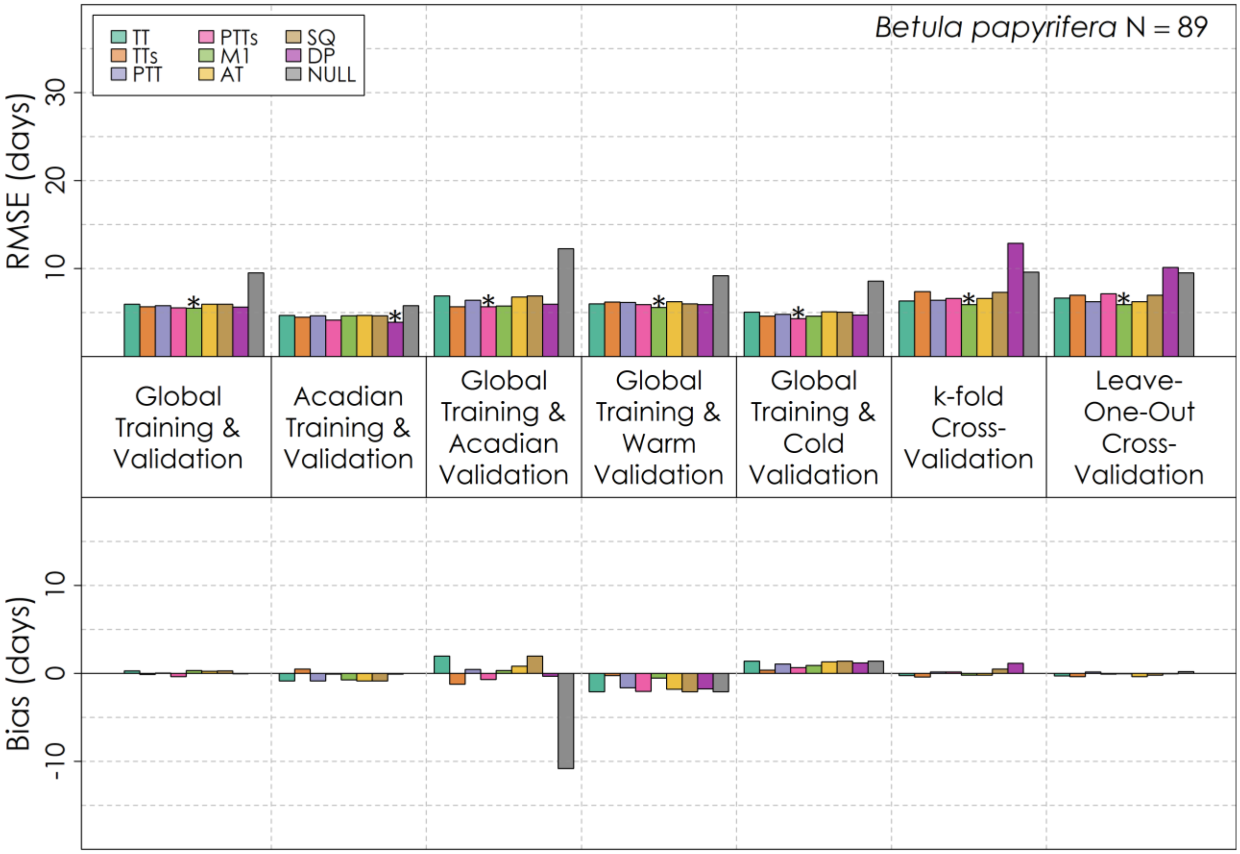

Figure 4-6. *Root mean squared error and mean bias for each of eight leaf emergence models and a Null model for seven different validation exercises for* *__Betula papyrifera__*. *The total number of* *__Betula papyrifera__* *leaf emergence observations for is shown on the top right. The model with the lowest root mean squared error for each validation exercise is denoted with an asterisk.*

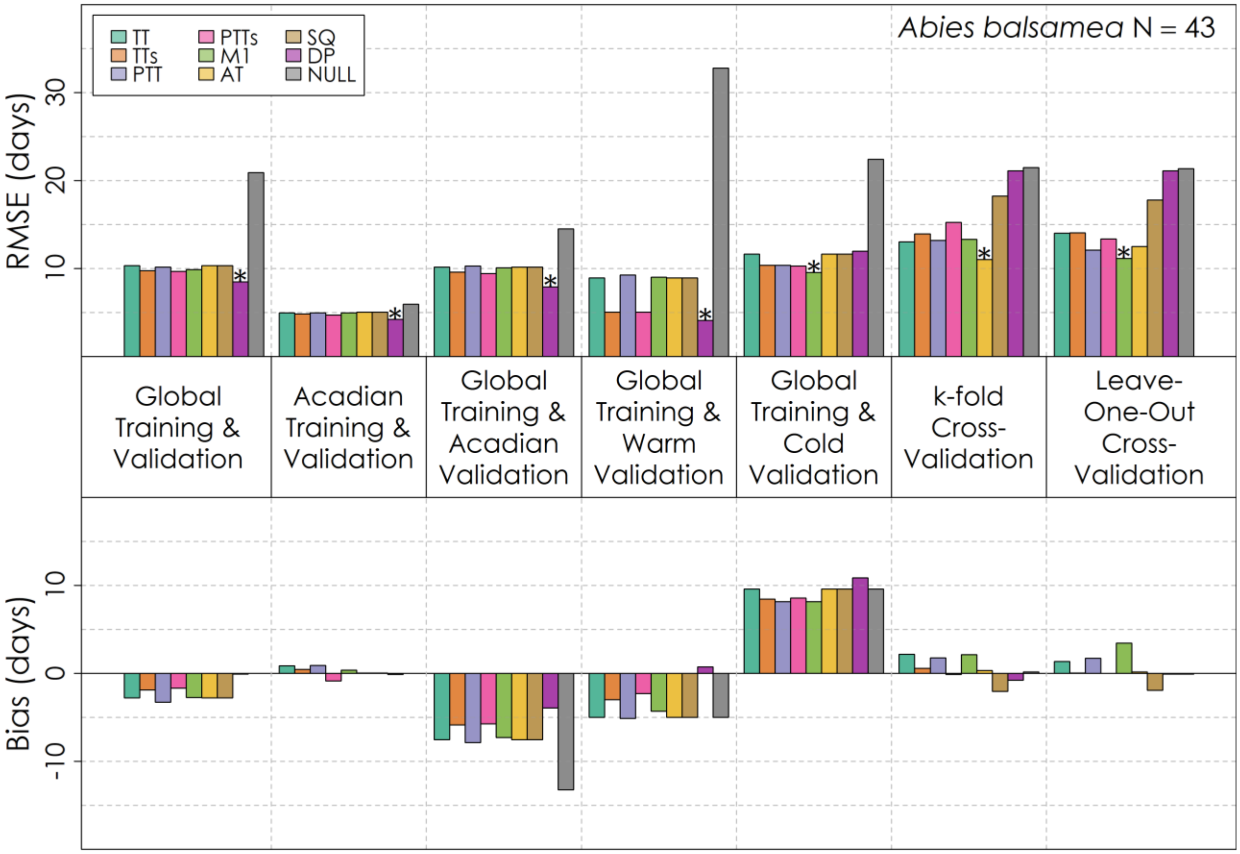

Figure 4-7. *Root mean squared error and mean bias for each of eight leaf emergence models and a Null model for seven different validation exercises for Abies balsamea. The total number of Abies balsamea leaf emergence observations for is shown on the top right. The model with the lowest root mean squared error for each validation exercise is denoted with an asterisk.*

4.4.3 Leaf Senescence models

Similarly, no one leaf senescence model had exceptional global performance relative to the others, with some failing to outperform the Null model for several validations (Figures 4-8, 4-9, and 4-10). For the global validation, the Delpierre model was optimal for *Abies balsamea* (Figure 4-10) and *Betula papyrifera* (Figure 4-9), while the Dormphot model with just Dormancy Induction was optimal for *Acer rubrum* (Figure 4-8). Across models, species, and validations, RMSE ranged from less than two weeks to about four weeks. Model RMSE values were high for each species relative to leaf emergence models, and among species highest for *Abies balsamea*.

For *Acer rubrum* performance across process models was very similar, ranging by less than half a day, while for *Betula papyrifera* RMSE values ranged by about one day, and for *Abies balsamea* ranged by about five days. Training and validating with just the Acadian Network favoured the Delpierre with Preceding Spring Leaf Emergence for *Acer rubrum*, and the White model for the other species. When globally trained and validated with just the Acadian Network, the Delpierre model was optimal for all species. For warm site-years, the White model was optimal for *Acer rubrum* while the Delpierre model was optimal for other species. Alternatively, during cold site-years, the Delpierre model was optimal for *Acer rubrum* and *Abies balsamea*, while the Dormphot model with just Dormancy Induction was optimal for *Betula papyrifera*. For the k-fold cross-validation, the White model was best for *Acer rubrum* and *Abies balsamea*, while the Jeong model was optimal for *Betula papyrifera*. Overall, the Delpierre, White, and Dormphot with just Dormancy Induction models were amongst the top performing models for each validation exercise across species. Bias varied in magnitude and direction across validation exercises, and even across species for the same validation exercises in some cases. With global training and validation with just the Acadian Network, each model predicted a late timing of leaf senescence by about one to more than two weeks across species, though the Delpierre model had the lowest absolute bias. Models predicted early and late leaf senescence for warm and cold site-years, respectively, for *Acer rubrum* (Figure 4-8), though mixed and early leaf senescence for *Abies balsamea* (Figure 4-10) and *Betula papyrifera* (Figure 4-9). Despite its occasionally preferable RMSE scores, the simple trigger-based White model was often amongst the top three models with the greatest absolute bias across validation exercises for each species.

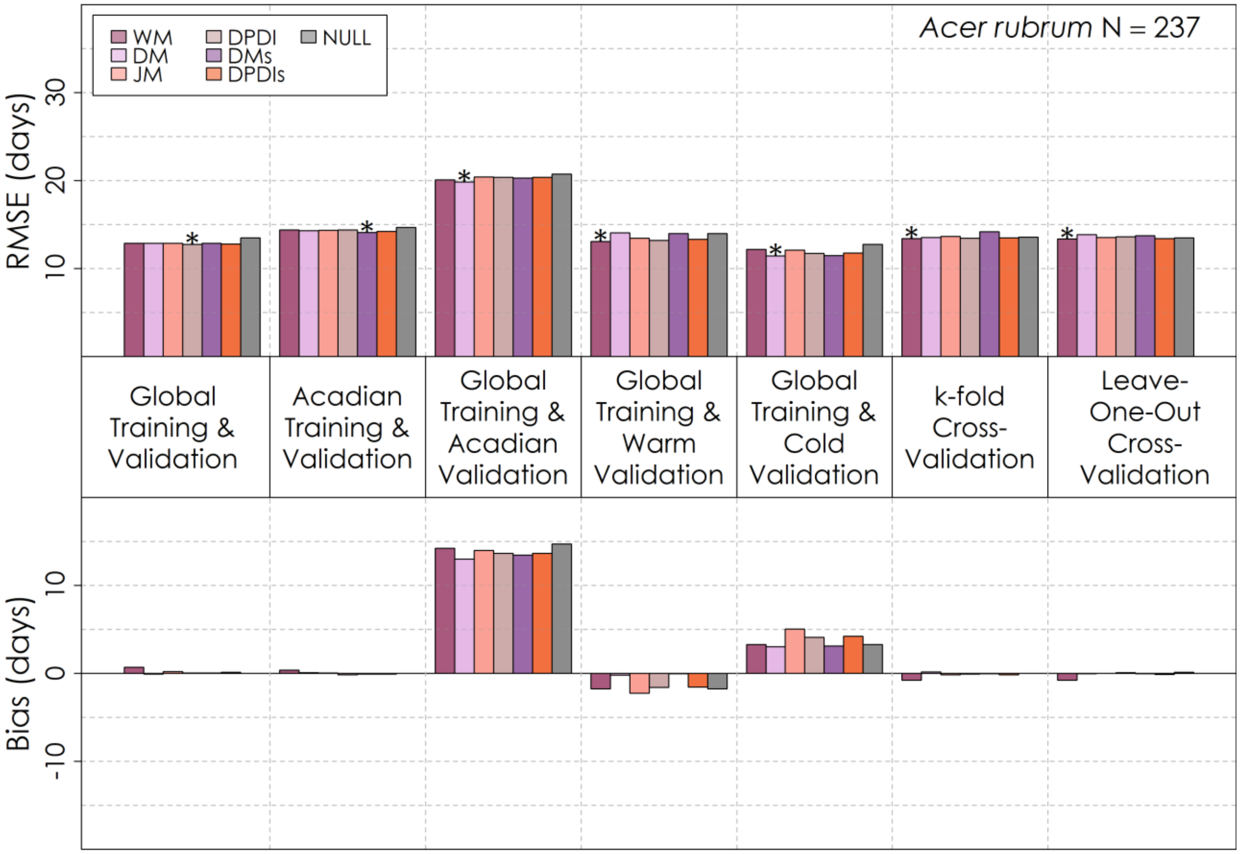

Figure 4-8. *Root mean squared error and mean bias for each of six leaf senescence models and a Null model for seven different validation exercises for Acer rubrum. The total number of Acer rubrum leaf senescence observations for is shown on the top right. The model with the lowest root mean squared error for each validation exercise is denoted with an asterisk.*

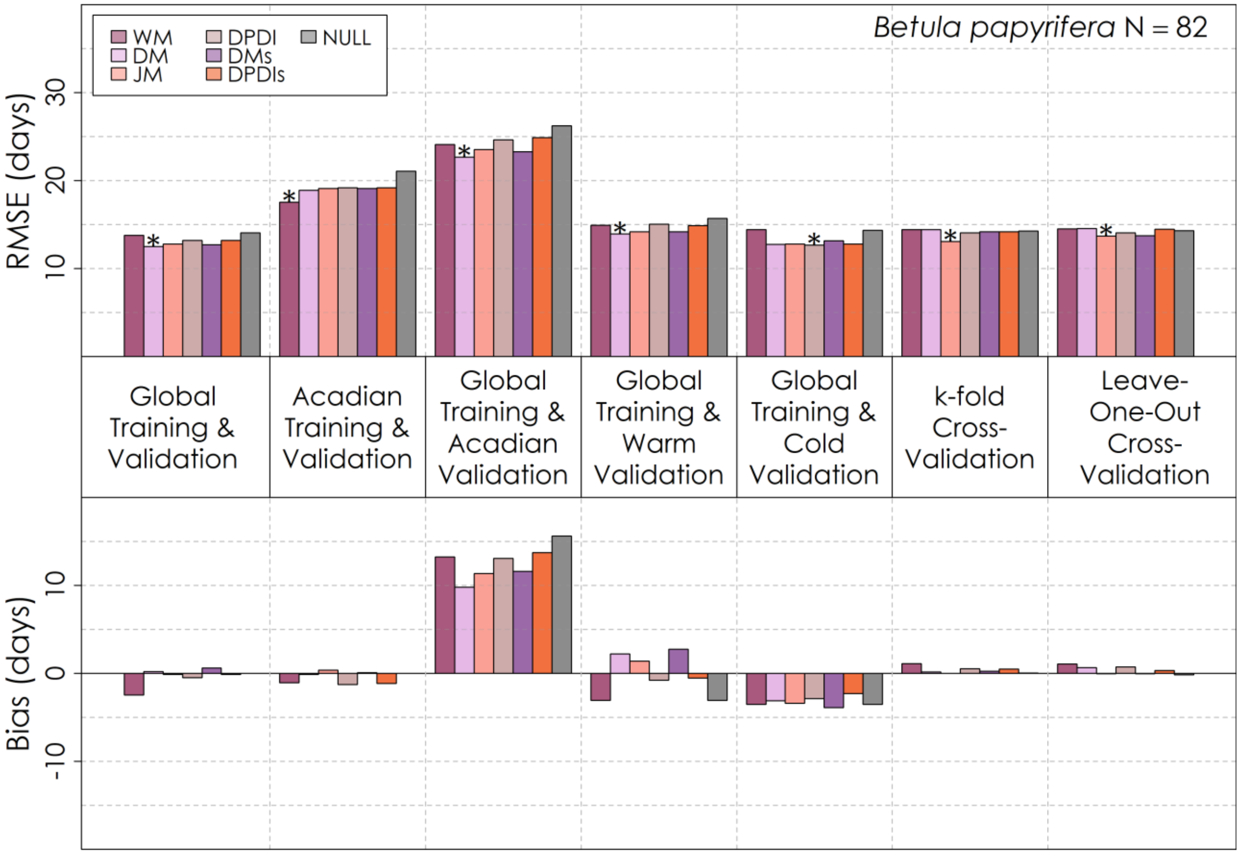

Figure 4-9. *Root mean squared error and mean bias for each of six leaf senescence models and a Null model for seven different validation exercises for* *__Betula papyrifera__*. *The total number of* *__Betula papyrifera__* *leaf senescence observations for is shown on the top right. The model with the lowest root mean squared error for each validation exercise is denoted with an asterisk.*

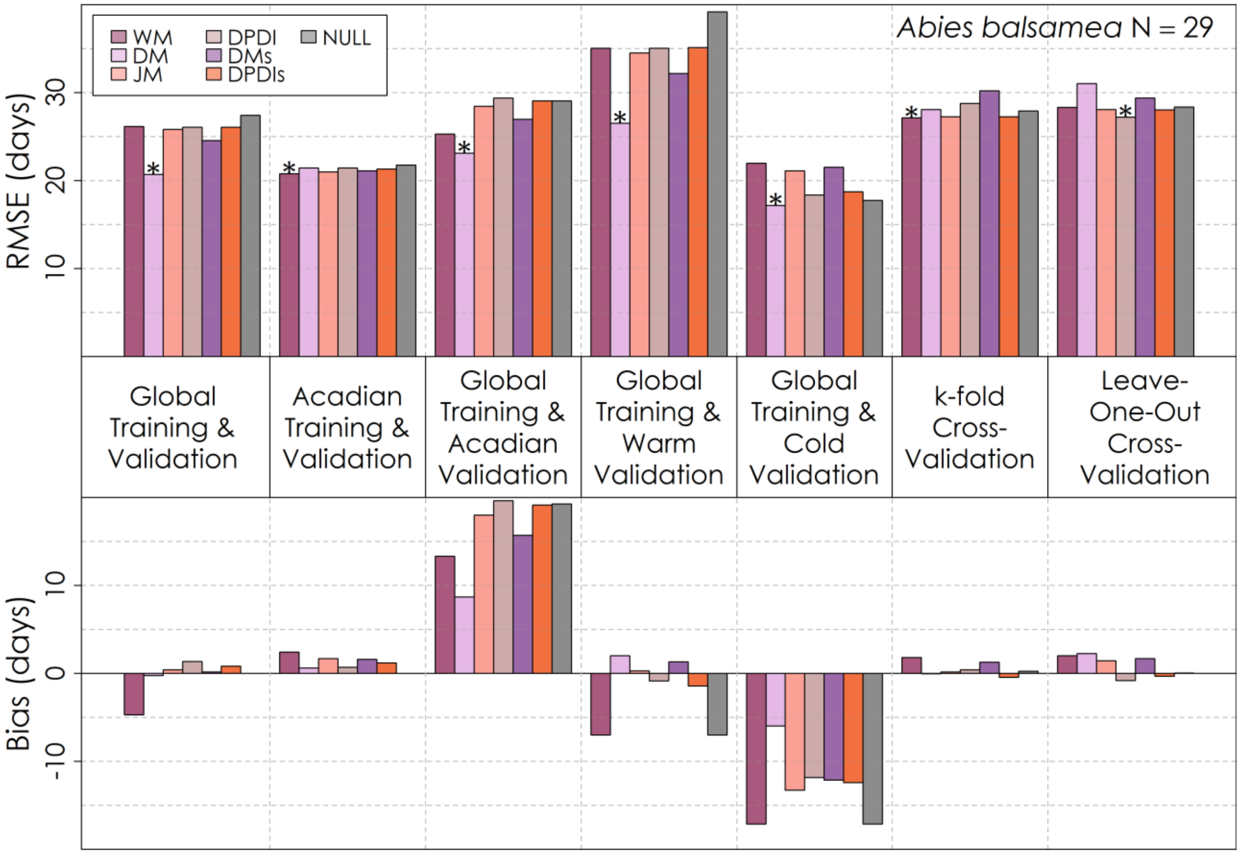

Figure 4-10. *Root mean squared error and mean bias for each of six leaf senescence models and a Null model for seven different validation exercises for* Abies balsamea. *The total number of* Abies balsamea *leaf senescence observations for is shown on the top right. The model with the lowest root mean squared error for each validation exercise is denoted with an asterisk.*

4.4.4 Projected Climate

Under the RCP 8.5 scenario, annual average temperatures in the year 2100 were projected to increase by about 4°C from 7°C to 11°C relative to 1990-2020 across our twelve sites (Figure 4-11). For the RCP 2.6 scenario a more moderate temperature increase of about 1°C was projected. The projected temperature change for northeastern sites was equivalent to warming them to the temperature of the southwestern sites for each emissions scenario. The projected annual average temperatures for our sites in 2100 under the RCP 8.5 scenario are within the range of training dataset annual average temperatures for *Acer rubrum* (annual average ~4-18°C) and *Abies balsamea* (annual average ~0-11°C), though slightly beyond the range for *Betula papyrifera* (annual average ~1-9°C) (Figure 4-4).

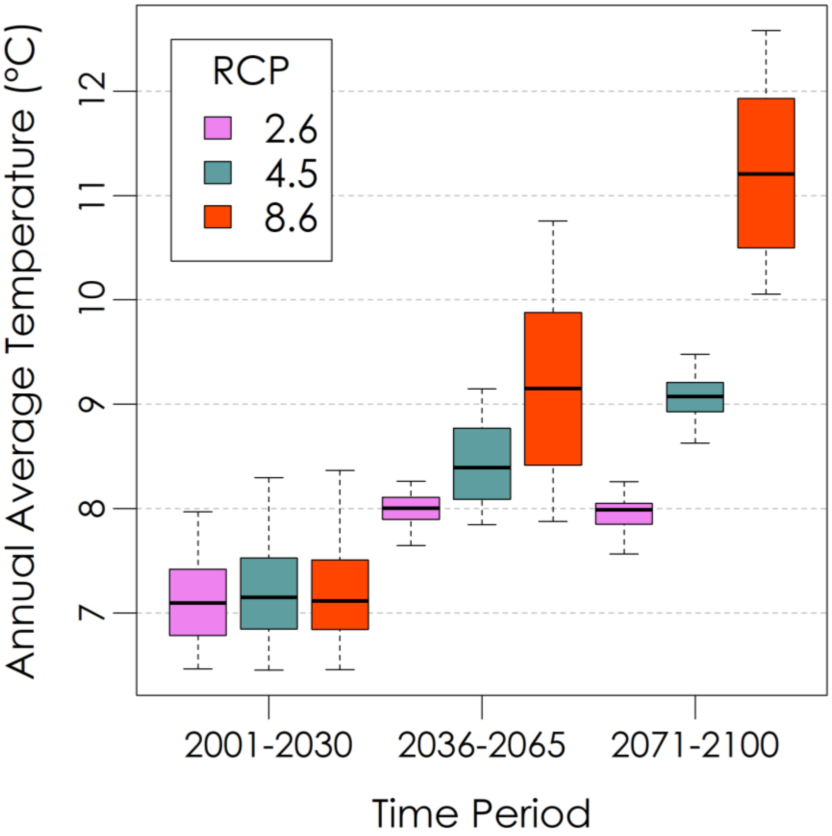

Figure 4-11. *Projected annual average temperatures across sites in the Acadian Phenocam Network.*

4.4.5 Projected Leaf Phenology

For each site, phenology model, and species, the projected phenology and season length varied each year throughout the 21st century among climate models (Figure 4-12). For each phenology model, variation in predicted leaf emergence dates among climate models was generally greater each year than variation in predicted leaf senescence dates. The predicted leaf emergence for some years was anomalous with respect to adjacent years and the longer record for several climate models.

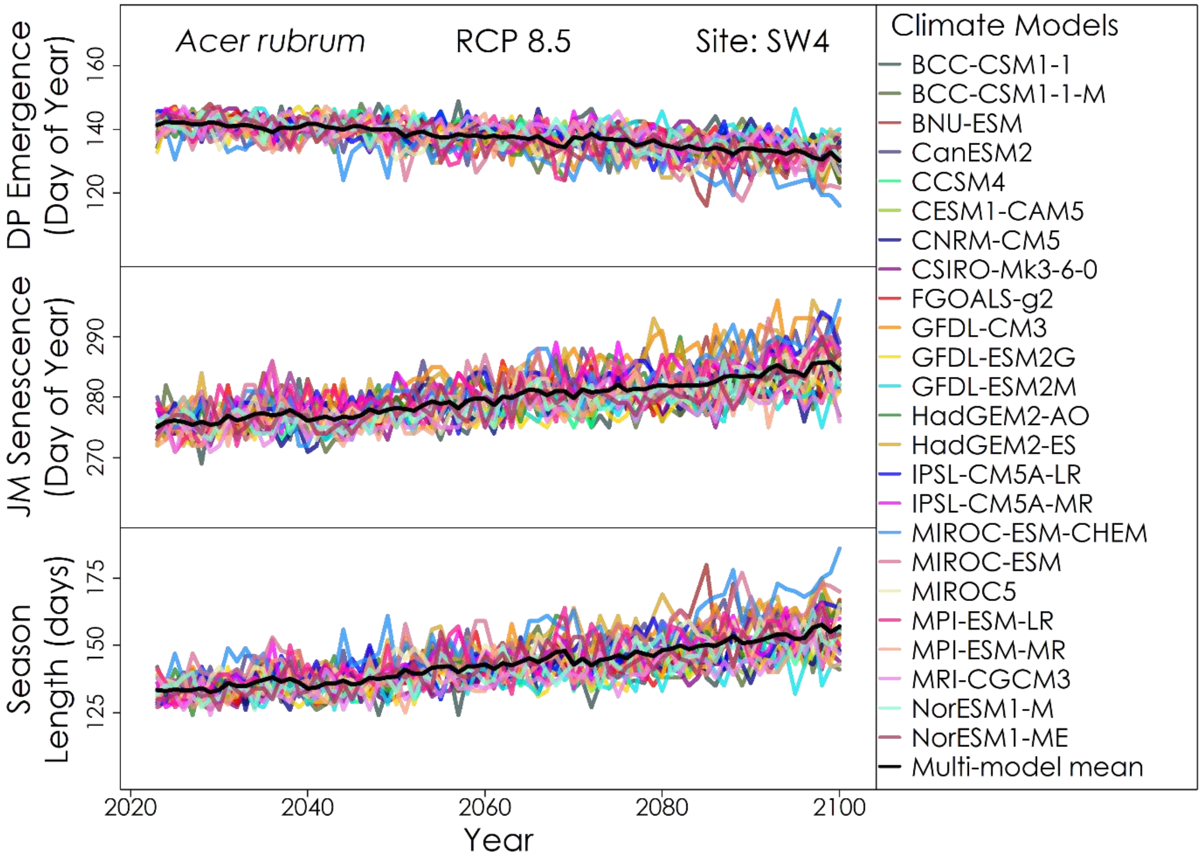

Figure 4-12. *Example timeseries of predicted Acer rubrum leaf emergence and senescence timings and the corresponding length of season with the Dormphot leaf emergence model and the Jeong leaf senescence model for each CMIP5 climate model under RCP 8.5 at site SW4.*

The projected change in the timing of leaf emergence, leaf senescence, and the corresponding season length for the mid-and late-21st century for each phenology model and emissions scenario is shown in Figure 4-13 for *Acer rubrum*, Figure 4-14 for *Betula papyrifera*, and Figure 4-15 for *Abies balsamea*. For each species and phenology model, leaf emergence is projected to advance and leaf senescence is projected to be delayed, though by varying degrees among species and models. Interestingly, the counteracting effects of warming on leaf emergence represented in the Dormphot model show a lesser advance relative to other models for *Acer rubrum* under all emissions scenarios. In contrast, the projected delay in leaf senescence increased continuously with both time and emissions in a similar fashion across leaf senescence models, though with the exception of the trigger-based White model. On average under a high emissions scenario by the end of the 21st century, the length of the growing season is to be extended by about three weeks for *Acer rubrum* and five or more weeks for *Betula papyrifera* and *Abies balsamea*, respectively. For each species, the relative extension in season length due to either the earlier leaf emergence or later leaf senescence varies. For *Acer rubrum* 69% of the extension in season length is due to an earlier leaf emergence (16 days of 22-day average). In contrast, for *Betula papyrifera* and *Abies balsamea*, about half of the extension in season length is due to an earlier leaf emergence (18 days of 37-day average and 20 days of 40-day average, respectively). On average, advances in leaf emergence under high emissions by the end of the 21st century were similar across species ranging from 16-22 days, while delays in leaf senescence vary from just 7 days for *Acer rubrum* to 19 and 20 days for *Betula papyrifera* and *Abies balsamea*, respectively.

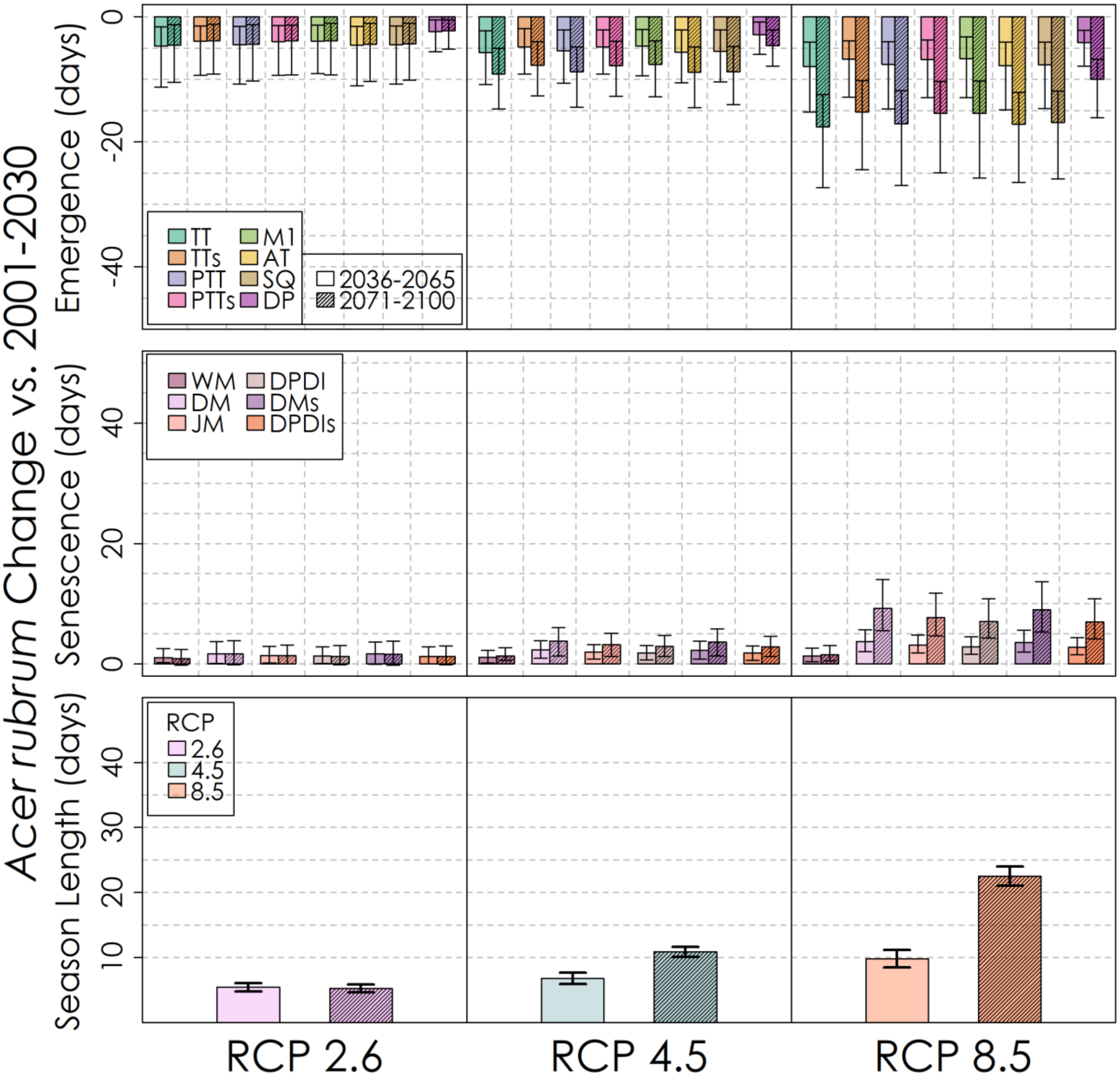

Figure 4-13. *Predicted change in* <u>*Acer rubrum*</u> *leaf phenology and growing season length for each leaf phenology model and RCP scenario. Uncertainty bars denote the* 5^{th}*-*95^{th} *percentile change values.*

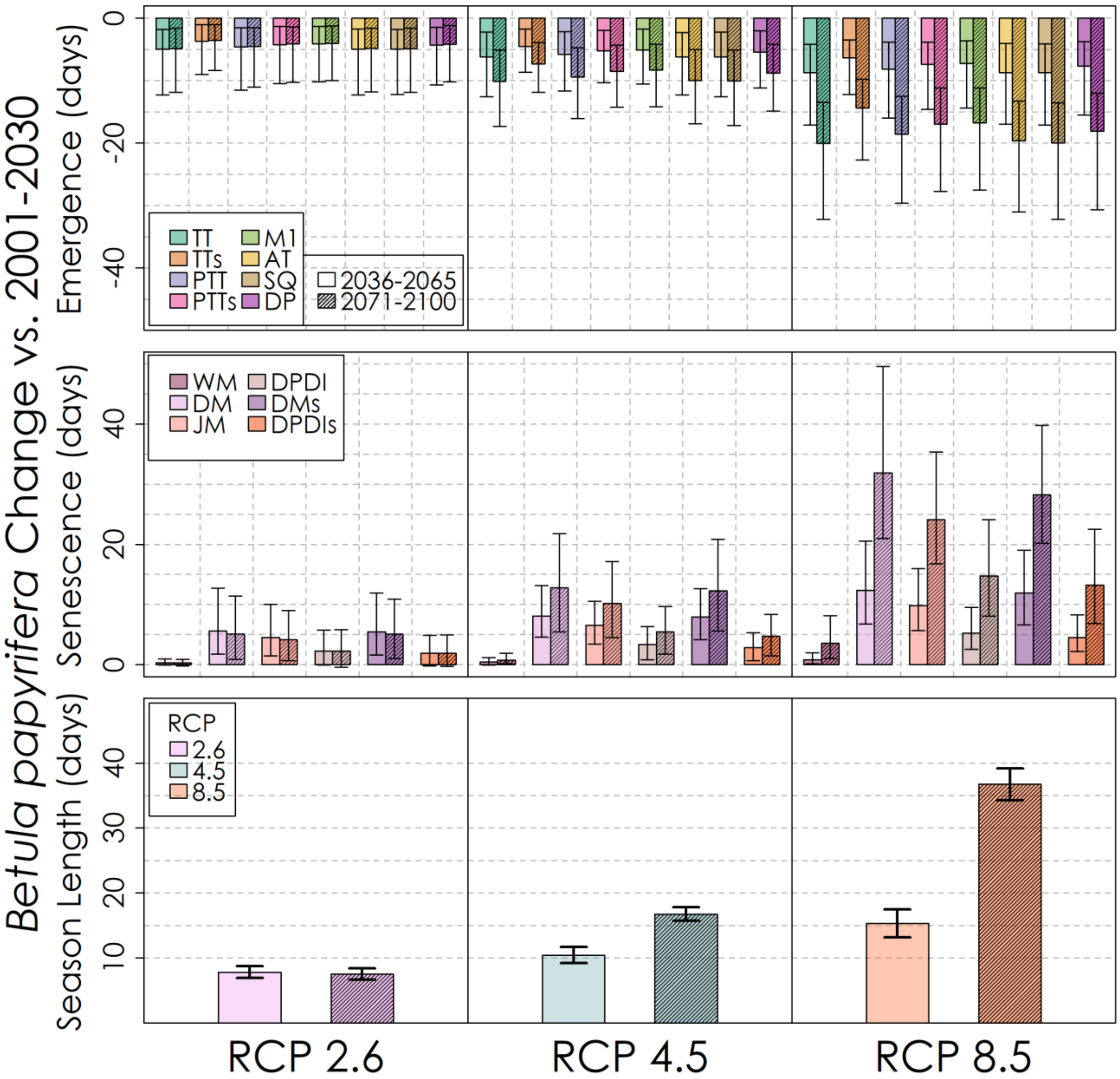

Figure 4-14. *Predicted change in* <u>*Betula papyrifera*</u> *leaf phenology and growing season length for each leaf phenology model and RCP scenario. Uncertainty bars denote the 5th-95th percentile change values.*

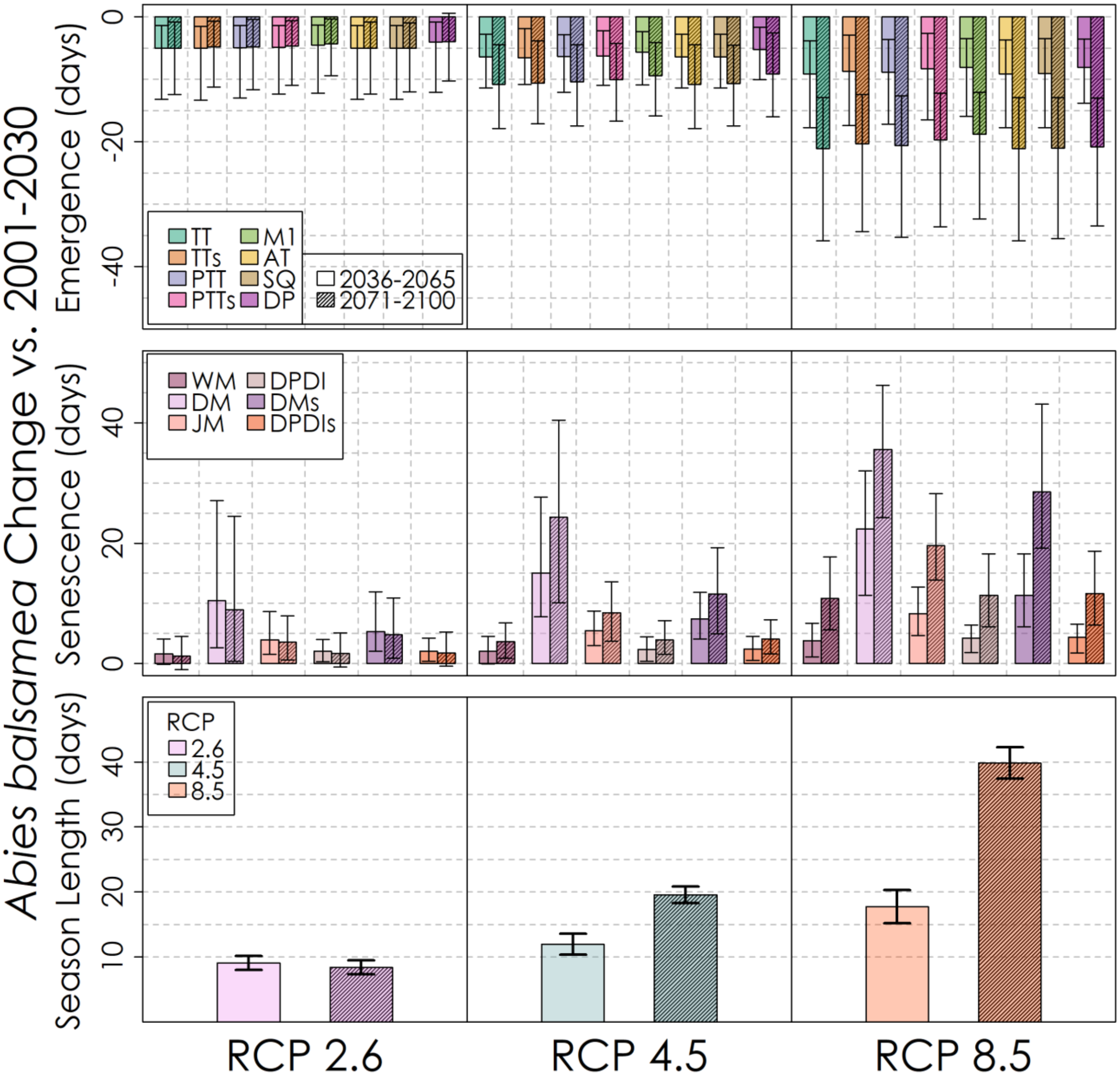

Figure 4-15. *Predicted change in* *<u>Abies balsamea</u>* *leaf phenology and growing season length for each leaf phenology model and RCP scenario. Uncertainty bars denote the 5th-95th percentile change values.*

4.5 Discussion

Here we present novel phenocam observations and predictions of leaf phenology for three tree species of the Acadian Forest Region using species-specific calibrated process models. An extension of the growing season in the context of warming is likely for all species by the late 21st century under both moderate and high emissions scenarios with a variety of leaf phenology models. The magnitude of this extension varies depending upon species, with a greater extension predicted for more boreal-climate suited species *Betula papyrifera* and *Abies balsamea* versus more temperate-climate suited *Acer rubrum* due to a more pronounced leaf senescence delay. The species-specific projections from our models agree with the findings of a five-year experimental study by Montgomery et al. (2020) in which species with a higher latitude of origin had a greater response to experimental warming. Given the expected northward expansion of the more temperate-climate suited species like *Acer rubrum*, the species-specific differences in projected phenology and season length have important implications for carbon uptake and ecological interactions within the Acadian Forest Region (Kharouba et al., 2018; Lafleur et al., 2010).

4.5.1 Model Performances

Our study provided a novel demonstration of the parameterization of species-specific leaf phenology models using phenocam observations for species with broadly distinct biogeographical ranges. Most models showcased similar performance with no singular outstanding model despite the diversity of biogeographical ranges across species, suggesting each model is well suited for the purposes of phenology modelling. This is in agreement with previous studies (Liu et al., 2020; Hufkens et al., 2018; Basler, 2016). Nevertheless, the optimal model varied across validation exercises for each species, suggesting different underlying cue mechanisms for these species despite their cohabitation.

The Dormphot leaf emergence model was originally calibrated with experimentation on *Betula pubescens* and found to be superior to simpler models with datasets from across Europe (Caffarra et al., 2011). The high performance of this model for a variety of training and validation sample configurations we found suggests this model is flexible and transferable to other regions such as the Acadian Forest Region. The suitability of the Dormphot model along with other models which included photoperiod shows that photoperiod likely exerts an important control on the process of leaf emergence for species in the Acadian Forest Region as well as across the PhenoCam Network.

For leaf senescence modelling, incorporating the influence of the preceding spring leaf emergence did not lead to overall improved model performance, though it improved regional applicability for the Acadian Phenocam Network in the case of *Acer rubrum*. Model performance among leaf senescence models was consistent between models relative to leaf emergence. Prediction error among leaf senescence models was approximately twice that of leaf emergence models. The parameterization of several of the leaf senescence models used in this study are mathematically similar to leaf emergence models, despite the distinction in the relationship for each phenophase to growing season temperatures (Figure 4-4). This indicates there is ample potential for improving leaf senescence models. Future leaf senescence model development would benefit with the exploration of novel cues and parameterizations that are more distinct from leaf emergence models.

The environmental context for both training and validation datasets was highly influential on ultimate model performance. We found variable model performance when models were validated with warm site-years versus cold site-years, with different optimal models depending upon each context for both leaf emergence and senescence. Another study using satellite-based observations and modelling also found model performances varied based on validation temperatures (Fu et al., 2014). Together this performance bias suggests that despite the satisfactory performance of these phenology models, novel parameterizations and potentially additional drivers are needed to improve the models' general applicability to a range of seasonal conditions.

The magnitude of error for each model was generally within the range from previous studies for both leaf emergence (~one week) and senescence models (~one to three weeks; Fang et al., 2022; Liu et al., 2020; Basler, 2016). Leaf senescence model error found with *Abies balsamea* was relatively high. In a study which also used the PhenoCam Version 2.0 dataset with a simplified version of the Delpierre model (Delpierre et al., 2009) for leaf senescence, Fang et al. (2022) reported RMSE values of ~17 days for evergreen needleleaf forest sites though just ~7 days for deciduous broadleaf forest sites. The higher leaf senescence error observed for evergreen needleleaf species such as *Abies balsamea* in our study and other studies may be due to the greater challenge of obtaining precise leaf phenology observations for evergreen needleleaf species. Evergreen needleleaf species exhibit more subtle and gradual changes in colour than deciduous species, resulting in seasonal greenness curves with reduced amplitudes and subsequently less precise phenology extraction. In addition, the rising portion of the greenness curve for evergreen needleleaf species is the result of both the emergence of new leaves as well as the greening of existing leaves, compounding uncertainty for process model development with phenocam observations (Seyednasrollah et al., 2021). Despite this, the error for leaf emergence estimation with *Abies balsamea* in our study was only slightly higher than the other species while for Fang et al. (2022) RMSE was similarly high for both phenophases for evergreen needleleaf forest sites relative to deciduous broadleaf sites. More work is needed to improve the precision of leaf phenology extraction from phenocam-derived observations of evergreen needleleaf vegetation. That being said, constraining amplitude thresholds in photosynthetic leaf phenology based on colour changes through phenocams rather than manually observable leaf phenophase changes may allow for broad comparisons between observations of leaf phenology for evergreen species (Seyednasrollah et al., 2021).

Another source of uncertainty influencing both leaf emergence and senescence models may be regionally differing phenological constraints which are not always captured by model equations and parameters, such as with a fixed daylength threshold. For example, Moon et al. (2021a) reported a transition in the relative importance of temperature and photoperiod affecting leaf emergence around the 10°C isotherm. The high and sometimes consistent model error for leaf senescence models herein over that of leaf emergence models may be due to each leaf senescence model including only temperature and photoperiod as drivers. Additional phenomena are known to influence the timing of leaf senescence, such as moisture availability, the seasonal timing of warming anomalies, minimum temperatures, frost frequency, consecutive dry days, heat stress, drought, consecutive rainy days, and consecutive heavy rain days (Bigler and Vitasse, 2021; Liu et al., 2020; Lang et al., 2019; Zohner and Renner, 2019; Xie et al., 2018a; Xie et al., 2018b). In addition, there is growing evidence that the probability of frost has an important influence on leaf phenology (Marquis et al., 2020). Incorporating these variables and potentially new variables yet to be discovered may help to improve the performance of both leaf emergence and senescence models. In addition, more observations and modelling studies focused on autumn phenology are needed as there is a deficit of research on leaf senescence relative to leaf emergence (Fang et al., 2022; Gallinat et al., 2015).

For the global combination of samples in our study, complex leaf emergence models representing the combination of dormancy induction, endodormancy, and ecodormancy release slightly outperformed more simple models for several validation exercises. In contrast, when we conducted leave-one-out and k-fold cross-validations, we found that complex models performed less well than simple models such as the M1 model. For the pooled combination of samples within our study, complex leaf senescence models incorporating the influence of the preceding ecodormancy release generally performed less well than simpler models. This may be due to the distinction in season length across regions, such that the parameterization for the constraint of growing season length in one region is less applicable to another region. When we conducted leave-one-out and k-fold cross-validations for leaf senescence, we again found that complex models performed less well than simple models such as the trigger-based White model. Together these findings are consistent with Basler (2016) for both global and regional transferability error evaluations in relation to model complexity. This is likely due to the trade-off between global performance and local specificity with complex models, which achieve greater performance with higher validation sample sizes. Globally trained models tended to predict an earlier date of leaf emergence and later date of senescence than is observed for the Acadian Forest Region. This suggests that both model complexity and training dataset spatial coverage should be considered when parameterizing, validating, and developing models. Additionally, this indicates that relationships between leaf phenology and environmental influences may vary in a non-linear fashion between regions, calling for more local and regional scale studies to inform broad leaf phenology mechanism understandings.

Despite the broad range of observational and training contexts in our study, all species and validations agree in that the simple Thermal Time model is not optimal relative to other models which include additional drivers. The Thermal Time model is often used to simulate leaf phenology within Dynamic Global Vegetation Models that form the terrestrial vegetational component of Land Surface Models within Earth System Models (Arora and Boer, 2005; Cox, 2001). The Thermal Time model is also commonly used to communicate expected changes in the duration of the vegetational growing season (Government of Canada, 2022; https://www.nrcan.gc.ca/climate-change/climate-change-impacts-forests/forest-change-indicators/growing-season/18470). Model performances in our study indicate that the inclusion of additional drivers for leaf emergence and senescence could improve the realism of dynamic global vegetation models and predictions of vegetation growing season length.

4.5.2 Future Leaf Phenology for Acadian Forest Region

In the Acadian Forest Region, future leaf emergence in the context of both moderate and high emissions will be earlier while leaf senescence will be later, though more work is needed to better predict the magnitude of these changes. The ensemble of models in our study predicts about 2, 2-3, and 3 weeks advance in leaf emergence and 1, 2-3, and 2-3 week(s) delay in leaf senescence by the end of this century with high emissions for *Acer rubrum*, *Betula papyrifera*, and *Abies balsamea*, respectively. In projecting future leaf phenology patterns, we found divergent patterns between simple and complex models. Under high emissions in the later century, leaf emergence shows lesser advancement within the models including endodormancy release chilling constraints, such as the Dormphot model, relative to other models. For leaf senescence, complex models including the influence of the preceding spring leaf emergence show similar or lesser delays in leaf senescence over time and emissions intensity in comparison to their counterpart models. The complex Dormphot model performed well in warmer years, suggesting it is a valuable tool for projecting leaf emergence in the context of future climate, and that the constrained advancement in leaf emergence it predicts is therefore likely (Caffarra et al., 2011). The reduced advancement in leaf emergence over time predicted with the Dormphot model agrees with the non-linearity for leaf emergence temperature sensitivity found by Chen et al. (2019) with observations from 1950-2013 and for Flynn and Wolkovich, (2018) with an experimental study. This suggests that as winter temperatures increase, the advancement in leaf emergence may be constrained by reduced chilling exposure accumulation for each of our species.

Caution is warranted in the interpretation of this apparent diminishing response of leaf emergence phenology to temperature change as more work is needed to thoroughly examine this finding. The aggregated weather patterns from the CMIP5 models may underestimate local interannual variability, omit the important role of anomalous seasonal conditions, and underestimate phenological temperature sensitivity due to uncertainty in projected temperatures (Keenan et al., 2020). For leaf senescence during warm site-years, the trigger-based White model and the Delpierre model without the preceding spring leaf emergence influence outperformed other models. These models also produced widely divergent predictions of leaf senescence delay with time, the White model predicted a week or less delay across species while the Delpierre model predicted as much as four weeks delay. Despite the constrained advance in leaf emergence, it was still greater or similar to the projected delay in leaf senescence across species. This somewhat contrasts the findings of Fu et al. (2018). With both a cooling and warming treatment for the European species *Fagus sylvatica*, Fu et al. (2018) found a greater temperature sensitivity for leaf senescence than emergence. Together this suggests that different species in different climate regions may exhibit diverse phenological responses to changing temperature regimes. The greater leaf emergence advancement relative to leaf senescence delay was most pronounced for the temperate species *Acer rubrum*, which had only a minor projected leaf senescence delay. Improved leaf senescence models are therefore needed to foster more confident projections of growing season length.

The continuous leaf senescence delay we found with time and emissions intensity agrees with the sustained leaf senescence temperature sensitivity found by Chen et al. (2019) with observations from 1950-2013. A study projecting changes in leaf senescence timing by the late 21st century including *Acer rubrum* and *Betula papyrifera* reported a similar delay in the onset of fall colouration for these species, though while using different predictive models which included moisture availability effects (Xie et al., 2018b). The projected delay in leaf colouration onset therein was about one week for *Acer rubrum* and just over two weeks for *Betula papyrifera* (Xie et al., 2018b). While a limited advancement in leaf emergence overtime translates to a potentially limited lengthening in the growing season, the expected continuous delay in leaf senescence may still promote increased seasonal carbon uptake as Wu et al. (2013) found that the timing of leaf senescence was more influential on seasonal carbon uptake than leaf emergence. If alternatively, the timing of leaf senescence depends upon the timing of leaf emergence as some studies have found and our Acadian Network observations suggest (Liu et al., 2020; Keenan and Richardson, 2015), this may constrain the length of growing season and subsequently carbon uptake. Another important consideration is the occurrence of anomalously early leaf emergence timings with respect to adjacent years or the long-term record, as this makes leaves susceptible to frost damage and may lead to carbon losses (Montgomery et al., 2020; Chamberlain et al., 2019; Richardson et al., 2018c; Vitasse et al., 2018; Augspurger, 2013; Augspurger, 2009; Gu et al., 2008). In addition, while not represented in our models, climate change has the potential influence leaf phenology through alternative effects including changes in moisture availability and disturbance legacy effects (Wu et al., 2022; Meier et al., 2021; Angulo-Sandoval et al., 2004). For example, variable water availability over seasonal and interannual periods can have cascading future effects on both leaf emergence and senescence, such as observed through a phenocam in the Kings Canyon National Park from 2012-2015, with shortened leafing periods due to limited water availability (Richardson et al., 2018b; Stephenson et al., 2018). Figure 4-4 herein shows the phenology response to a range of growing condition contexts for our study species, with a near-linear relationship between phenology in the form of leaf emergence timing and temperature for all species. In contrast, our model projections indicate that there is potential for acclimation in phenology responses to warming. A reduced leaf emergence advancement for *Acer rubrum* was projected by the Dormphot model, while a reduced leaf senescence delay was projected by all senescence models relative to other species. Together this indicates more regional-scale species-specific observation and modelling efforts are needed to understand regionally variable controls of leaf senescence as well as leaf emergence.

4.5.3 Future Implications

A substantial annual temperature increase of ~4°C is predicted for the Acadian Forest Region under a high emissions scenario. This change in conditions will surpass the optimal growing temperature for boreal-climate suited species like *Abies balsamea* and *Betula papyrifera* (Dhar et al., 2014; Wang et al., 1998; Frank, 1990). Previous studies have predicted a decline in the proportion of boreal species in the Acadian Forest by the late 21st century due to suboptimal growing conditions (Taylor et al., 2017), which is supported by the dramatic shifts predicted with our phenology models for the 21st century. An experimental study by Vaughn et al. (2021) found reduced mortality and sustained height growth in the context of drought for temperate-climate suited *Acer rubrum* in comparison to colder-climate adapted species such as *Abies balsamea*. In a synthesis of the effects of climate change on *Abies balsamea* regeneration Collier et al. (2022) alternatively found that the adverse impacts to *Abies balsamea* may occur with a complex combination of processes including reduced competitive fitness and mortality of overstory trees.

The potentially extensive delay in the timing of leaf senescence found in our study for boreal species in the Acadian Forest Region suggests that future nutrient resorption success may be diminished for these species in comparison to temperate species. Leaf senescence functions primarily as a means of conserving nutrients for deciduous tree species which are used in the development of new leaves in the following spring (Estiarte and Peñuelas, 2015). A delayed senescence leads to greater risk of nutrient losses due to fall hurricanes prematurely removing or damaging leaf tissues, disrupting the normal course of nutrient recycling achieved through senescence. Together this indicates that more boreal-typical species like *Abies balsamea* in the Acadian Forest may suffer declined growth, greater mortality, reduced fitness, a shift in optimal biogeographical envelopes beyond their current range, and perhaps a substantially reduced longevity in the context of climate change in the 21st century. This has important implications for forest structure and ecological interactions across the Acadian Forest Region, which is already vulnerable due to most species therein being near the limit of their ranges (Pearson and D'Orangeville, 2022; Wang et al., 2021; Körner et al., 2016; Fisichelli et al., 2014).

The predicted lengthening of the carbon uptake period prompted by an earlier leaf emergence and later leaf senescence for each species found in our study may be expected to lead to increased carbon uptake (Wu et al., 2013). On the contrary, increased mortality, disturbance, and suboptimal growing conditions in the context of climate change may lead to reduced carbon uptake across the Acadian Forest Region (Taylor et al., 2020), losses which may more than compensate for potential carbon uptake gains from warming (D'Orangeville et al., 2018). Further, the potential for the increased establishment of more temperate-climate suited species like *Acer rubrum* may be limited throughout the 21st century due to the physical occupation of space by boreal species (Taylor et al., 2017). As species ranges shift northward and weather patterns exhibit more frequent and intense anomalies in the context of climate change, there is also a greater potential for carbon losses due to late spring frost events which may be more damaging for species outside their native ranges (Zanne et al., 2018; Vitasse et al., 2014). Therefore, the composition of the Acadian Forest Region is likely to change under a high emissions scenario by the late 21st century, as well as the capacity for carbon uptake within the Acadian Forest Region. Understanding which phenological strategy is optimal in response to such changes is necessary for promoting the migration of suitable species and provenances therein (Ding and Brouard, 2022).

Beyond biogeochemistry, the constrained delay in leaf senescence for temperate species such as *Acer rubrum* found in our study has important implications for the autumn colour ecotourism industry in the Acadian Forest Region (Spencer and Holecek, 2007; Ivakhiv, 2005). *Acer rubrum* are responsible for the vibrant red colours which contrast with the predominant yellow autumn colouration of other species in much of the Acadian Forest Region. Divergence in the relative timing of leaf senescence for deciduous species of the Acadian Forest may have important implications for the future appearance and appeal of the fall colours, as well as for ecological interactions between species (Kharouba et al., 2018; Renner and Zohner, 2018; Cleland et al., 2007). Cleland et al. (2012) found that species which do not respond as acutely to temperature changes may in fact be at a disadvantage in terms of ecological performance relative to other species, despite the better potential avoidance of suboptimal growing conditions with such strategies.

4.6 Conclusions

The Acadian Forest Region is a unique transitional zone composed of both boreal and temperate forest species in eastern North America. Leaf phenology, the timing of season leaf life cycle events, responds directly to climate change, and thus serves as an important biological indicator. Stationary timelapse cameras, known as phenocams, are cost-effective monitoring tools which can provide spatially and temporally replicated species-specific observations of leaf phenology in a range of climatic contexts. We collected four growing seasons of observations for the species *Acer rubrum* (red maple), *Betula papyrifera* (paper/white birch), and *Abies balsamea* (balsam fir) across the Acadian Phenocam Network and accessed multiple growing season observations of these species from the North American PhenoCam Network. With these observations, we conducted species-specific parameterizations of eight leaf emergence and six leaf senescence models which encompass a range in process and driver representation, resulting in 42 unique leaf phenology models. With these models, we simulated future patterns in leaf emergence, senescence, and season length (senescence minus emergence) for these species at sites within the Acadian Phenocam Network based on projected weather from Climate Models within the Fifth Phase of the Coupled Model Intercomparison Project (CMIP5). All models performed similarly well, with model errors in the range observed by previous studies for both leaf emergence and senescence. Leaf emergence was better predicted by more complex models while leaf senescence was better predicted by relatively simple models. By the end of the 21st century with moderate or high emissions, leaf emergence will likely be two weeks earlier while the magnitude of leaf senescence change varies across species and models. Temperate species like *Acer rubrum* may have as little as a one-week delay in leaf senescence while leaf senescence for boreal species like *Betula papyrifera* and *Abies balsamea* may be two to four weeks later. Consequently, the length of growing season extension varies from about three weeks for *Acer rubrum* to more than five weeks for *Betula papyrifera* and *Abies balsamea*. This differential response pattern between boreal and temperate species in the Acadian Forest Region has important implications for forest ecology as well as biogeochemistry and forest-based sectors of the economy (e.g., forestry, ecotourism). A promising avenue to enhance the confidence of leaf phenology predictions in the context of climate change is the improved monitoring and modelling of leaf senescence. Our work demonstrates phenocams have the potential to rapidly advance process-based model development and therefore foster more confident predictions of leaf phenology.

Chapter 5. Leaf phenology as an indicator of ecological integrity

This chapter was accepted for publication in Ecosphere on January 17th, 2023, Manuscript ID: ECS22-0592.

5.2 Introduction

Phenology is the study of recurring biological events and their causes with respect to abiotic forces (Lieth 1974). ‘Plant phenology’ typically refers to the timing of seasonal changes in leaves and flowers, including spring leaf emergence and fall leaf senescence. Observations show that global warming has advanced leaf emergence for deciduous species over the past five decades (Piao et al., 2019; Peñuelas and Filella 2009; Menzel et al., 2006) and to a lesser extent delayed leaf senescence (Xie et al., 2018b; Estiarte and Peñuelas 2015; Peñuelas et al., 2002; Menzel and Fabian, 1999). Climate-driven increases in extreme weather and changes in leaf phenology together may lead to an increased risk of damage from disturbance such as frost, ice storms, herbivory, and hurricanes (Marquis et al., 2022; Taylor et al., 2020; Casson et al., 2019; Pureswaran et al., 2019; Bascietto et al., 2018; Delpierre et al., 2017; Allstadt et al., 2015; Augspurger, 2013; Lechowicz, 1984). Climate change has also led to a change in the frequency of stress from drought or excessive precipitation, due to both an extension of the growing season and an alteration of global hydrology (Charlet de Sauvage et al., 2022; Etzold et al., 2022; Meier et al., 2021; Sangüesa-Barreda et al., 2021; Lukasová et al., 2020; Čehulić et al., 2019). The detrimental effects of climate change may lead to reduced carbon uptake, counteracting the potential enhanced uptake afforded by earlier leaf emergence and later senescence (Curtis and Gough, 2018). The unprecedented rate of ongoing climate change challenges the suitability of vegetation strategies for responding to warming and enhanced variability in temperatures, as these were evolved for relatively stable historical climates (Vitasse et al., 2022; Zohner et al., 2020; Casson et al., 2019; Richardson et al., 2018c; Martin et al., 2010; Norby et al., 2003). The combination of increased disturbance and stress in the context of climate change may culminate in impaired ecosystem processes and deteriorated resilience for ecosystems that are susceptible to such effects (Price et al., 2013; Niinemets, 2010). For example, Stephens et al. (2018) reported the transition from a carbon sink to source for a stand of *Populus tremuloides* during a growing season with insect defoliation, with lower primary production than the previous 20 years of previous records. Hufkens et al. (2012b) also reported annual gross productivity was reduced by as much as 14% following a late spring frost in 2010 in more than 8000 km^2 of forest in the northeastern United States. Along with climate-driven changes in leaf phenology the effects of increased disturbance and stress have considerable implications ranging from species to ecosystem levels, with potential for alterations to community structure and impaired ecosystem function (Kharouba et al., 2018).

A near-remote sensing technique of leaf phenology monitoring via phenocam employs time-lapse digital cameras installed at the ground level (Browning et al., 2019; Richardson, 2019; Brown et al., 2016; Sonnentag et al., 2012; Richardson et al., 2007). Globally, there are now extensive networks of phenocams including the North American PhenoCam Network (https://phenocam.nau.edu/webcam/ ; Seyednasrollah et al., 2021) and European Phenology Camera Network (http://european-webcam-network.net/; Wingate et al., 2015). Phenocams produce near-continuous sub-daily resolution observations of leafing status at the individual tree-level in the form of seasonal greenness curves (Liu et al., 2021; Delpierre et al., 2020). Leaf phenology can also be observed at the individual tree level using manual techniques in the field, though this approach can be limiting for conservation managers due to time and financial resource constraints. Phenocams present an automated, affordable, and robust approach to monitoring the timing of seasonal leaf development as well as the effects of disturbance or stress (Parmentier et al., 2021; Toomey et al., 2015).

Ecological integrity is a measure of the viability of an ecosystem based on the cohesion of processes resulting from interactions between its abiotic and biotic components (Jenssen et al., 2021). Disturbance and stress can threaten ecological integrity through interruptions to ecosystem processes and alterations to ecosystem structure (Ordóñez & Duinker, 2012; LaPaix et al., 2009). Key forest ecosystem processes affected by disturbance or stress include primary production, water cycling, nutrient cycling, and energy flow, among others (Bonan and Shugart, 1989). The composition and structure of forest ecosystems are also impacted by disturbance and stress, as susceptible species may exhibit reduced fitness and reproduction. Alternatively, disturbance and stress may have limited impacts on ecological integrity for resilient forest ecosystems. In order to determine whether or not disturbance or stress has undermined ecological integrity in forest ecosystems, it is necessary to monitor ecosystem processes before, during, and following disturbance and stress. Leaf damage or defoliation during the optimal growing season period can indicate disruptions to ecosystem processes (Stephens et al., 2018). Some approaches to monitoring ecological integrity include the designation of indicator thresholds to differentiate between different levels of integrity in comparison to a reference state (Dubé et al., 2013; Parks Canada Agency, 2011). Phenocams can capture quantitative data of moderate to extensive leaf damage due to disturbance or stress, as well as recovery (Richardson et al., 2018c; Stephens et al., 2018; Matiu et al., 2017; Nagler et al., 2014). Phenocams can also aid in documenting baseline leaf function prior to disturbance or stress. Together these processes impart important implications for ecological integrity (Smith et al., 2022; Taylor et al., 2020; Chamberlain et al., 2019; Halman et al., 2011; Scheffer et al., 2009). Despite this potential, little work has been done to explore the implementation of phenocam-derived leaf phenology observations as an indicator of ecological integrity for conservation efforts. This may be due in part to the considerable challenge of designating indicator thresholds to convey critical adverse effects on the ecology of an ecosystem (Hansen et al., 2021).

Many factors complicate the development of ecological integrity indicator thresholds in relation to leaf phenology. In the context of disturbance or stress, leaf phenology alone may not provide a pronounced signal of leaf functional decline. For example, the work of Zohner et al. (2020) shows that leaf phenology does not always deviate notably in response to damaging late spring frost events relative to alternative drivers of interannual variability. Given this inherent background variability with multiple drivers of variation in leaf phenology beyond disturbance or stress, an alternative signal of leaf functional declines may be necessary. A promising alternative signal of leaf function is the duration of leaf developmental periods approximated from the canopy greenness timeseries or greenness curve. Depending upon how leaf developmental periods are defined along the greenness curve, these periods can be stable within a few days for an individual region of interest over time in the absence of disturbance or stress. Examples of these periods include the greenness rising portion of the greenness curve from 10-90% amplitude, the greenness plateau following the seasonal peak in greenness, and the entire leaf-on period from 50% amplitude in the rising portion of the curve to 50% amplitude in the falling portion of the curve. If the duration of leaf developmental periods signals disturbance or stress-related leaf damage more often for a given species than adaptation can overcome, this species may be susceptible to adverse global change impacts, with potential consequences for ecosystem processes, structure, and composition (Cavers and Cottrell, 2015).

Both field studies and phenocam studies indicate that spring disturbances, such as false springs, in which warm spring conditions are followed by a late frost event, can result in an extended greenness rising period due to the time necessary for recovery following disturbance (Hufkens et al., 2012a; Menzel et al., 2015; Augspurger, 2009; Kaitaniemi et al., 1997). These springtime disturbances may in turn delay the senescence process (Zohner et al., 2019). A reduced period is also possible if anomalously warm springs conducive of frost damage give rise to rapid early leaf development before frost (Hufkens et al., 2012b). Additionally, frost may lead to reduced seasonal peak greenness values, prompting a reduced greenness rising period. A notable deviation in this period between budburst and leaf maturity in the form of either an extension or reduction can therefore be a signal of disturbance effects having an impact on ecosystem processes. Later in the growing season, the severity of stress or disturbance can translate into commensurately advanced senescence (Bigler and Vitasse, 2021; Xie et al., 2015), which would reduce the leaf maturity period or the entire period between leaf emergence and senescence. Studies have shown with a variety of cameras that following disturbance which led to leaf damage there may be a pronounced decline in canopy seasonal maximum greenness, which would impact various leaf stages extracted from the greenness curve (Richardson et al., 2018c; Menzel et al., 2015; Keenan et al., 2014, Mizunuma et al., 2013; Hufkens et al., 2012b; Ide et al., 2011). These studies also show such a decline is distinct from the greenness patterns at nearby sites or growing seasons with no recorded disturbance at the same site, suggesting this feature is a promising signal of disruption to ecosystem processes due to disturbance or stress.

Leaf phenology is currently monitored at more than 500 phenocam sites throughout the North American PhenoCam Network, with some site-records spanning over a decade (Seyednasrollah et al., 2021). We hypothesized that disturbance or stress associated with an impact to leaf function will be evidenced through one or more of the following: A) the time between the onset of leaf growth and the seasonal peak in greenness; B) the duration of the greenness plateau or slow decline following the seasonal peak in greenness; or C) the duration of the entire leaf-on period for that site (Figure 5-1). Additionally, we hypothesized that such deviations would differ substantially from alternative reference growing seasons, allowing the designation of indicator thresholds based on the magnitude of deviation. We will examine these periods from known site-years with disturbance or stress that affected the leafing status of vegetation within the PhenoCam Network. We will then examine how distinct these periods are under circumstances of disturbance or stress in comparison to other years across the PhenoCam Network. Finally, we will develop an approach to detect such anomalous periods. This would allow for the detection of leaf functional declines and associated impacts to ecological integrity within networks such as the PhenoCam Network.

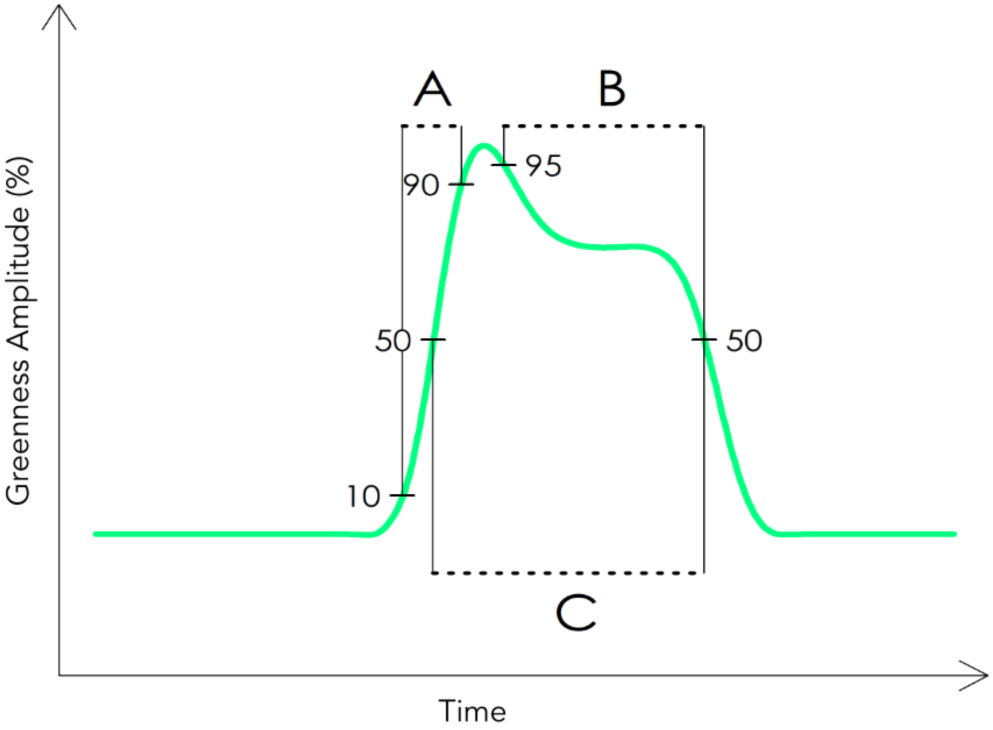

Figure 5-1. *The delineation of three periods which may be affected by disturbance or stress: A) the greenness rising portion of the curve between the onset of leaf growth and the seasonal peak in greenness calculated as the time between the 10% and 90% amplitude, B) the greenness plateau following the seasonal peak in greenness calculated as the time between 95% and 50% amplitude in the falling portion of the greenness curve, C) the entire leaf-on period calculated as the time between 50% amplitude in the rising portion and 50% amplitude in the falling portion of the greenness curve.*

5.3 Methods

5.3.1 PhenoCam Network

For information on PhenoCam Network protocols refer to Seyednasrollah et al. (2019b) and Richardson et al. (2018a). Regions of interest (ROIs) from PhenoCam cameras are delineated to characterize the dominant vegetation in each field of view, and in some cases several ROIs are defined to distinguish between different plant functional types such as evergreen needleleaf versus deciduous needleleaf (Richardson et al., 2018c). The green chromatic coordinate (GCC) is then calculated as is shown in Equation 5-1 from red, green, and blue color channel intensity values within each ROI for each image to produce greenness timeseries:

$$G_{CC} = \frac{B_G}{B_G + B_R + B_B} \tag{5-1}$$

where B_G corresponds to the intensity (brightness) of the green color channel, B_R to the intensity of the red color channel, and B_B to the intensity of the blue color channel. The GCC represents the intensity of the green color channel versus the total intensity of all color channels. For examination of the greenness timeseries from PhenoCam Network cameras, we extracted original and 3-day 50th percentile filtered GCC records from the PhenoCam V2.0 data set, which includes observations up until the end of the 2018 growing season (Seyednasrollah et al., 2019a). We also downloaded select records for currently active phenocam sites with cases of disturbance or stress which had limited reference growing season observations prior to 2018 from a pre-release of the PhenoCam V3.0 data set (https://phenocam.nau.edu/phenocam_explorer _prerelease/;Hufkens et al., 2018; Richardson et al., 2018a). Images which were too dark or too bright were removed from these datasets prior to their release using digital number threshold quality control filters. Regions of interest for PhenoCam Network sites can be accessed online through the PhenoCam Network portal at https://phenocam.nau.edu/webcam/, as well as through the PhenoCam V2.0 data set in Seyednasrollah et al. (2019a).

5.3.2 Exploration of Ecological Integrity Indicators from Greenness Timeseries

We selected fourteen cases of disturbance or stress captured by phenocams from the PhenoCam Network (Table 5-1). These cases were selected through visual inspection of images and in some cases ancillary data (Richardson et al., 2018c; Stephens et al., 2018; Stephenson et al., 2018; Keenan et al., 2014; Hufkens et al., 2012b) which indicated these cases of disturbance or stress were associated with impaired leaf function and thus a decline in ecological integrity. The disturbances we investigated included hurricanes, windstorms, spring frost, insect herbivory, and a winter ice storm. The case of stress we investigated was drought mortality. We used imagery data from the PhenoCam Network to include a spatial and temporally replicated data set of seasonal greenness curve records, in the context of disturbance and stress as well as under normal conditions. This allowed us to examine the stability of our indicator in the absence of disturbance or stress, as well as the detectability of leaf damage from known cases of disturbance or stress.

Table 5-1. *PhenoCam Network sites with recorded instances of disturbance or stress included in our study.*

Camera name	**Location & Full site name**	**Disturbance or Stress**	**Reference Years**
elverde	Lat: 18.3207 Lon: -65.8199 El Verde Field Station, El Yunque National Forest, Northeastern Puerto Rico, United States	Hurricane Maria (September 2017)	2015, 2016, 2019
NEON.D07.GRSM.DP1.00033	Lat: 35.6890 Lon: -83.5020 NEON Site -D07 (Appalachians and Cumberland Plateau) Great Smoky Mountains National Park, Tennessee, United States	Spring windstorm (May 2017), Hurricane Irma (September 2017), Derecho (May 2020)	2018, 2019, 2021
woodshole	Lat: 41.5495 Lon: -70.6432 Woods Hole Research Center, Falmouth, Massachusetts, United States	Hurricane Irene (August 2011)	2013-2018
spruceT9P17	Lat: 47.5060 Lon: -93.4527 Marcell Experimental Forest, north of Grand Rapids, Minnesota, United States	Frost (April 2016)	2017 & 2018
arbutuslake	Lat: 43.9821 Lon: -74.2332 Arbutus Lake, Huntington Wildlife Forest, Newcomb, New York, United States	Frost (May 2010)	2011-2014
proctor	Lat: 44.5250 Lon: -72.8660 University of Vermont, Proctor Maple Research Center, Underhill, Vermont, United States	Frost (May 2010)	2009, 2011-2018
mammothcave	Lat: 37.1858 Lon: -86.1019	Frost (April 2007)	2004, 2005, 2008, 2009,

	Environmental Learning Center, Mammoth Cave National Park, Kentucky, United States		2011-2014, 2016-2018
canadaOA	Lat: 53.6289 Lon: -106.1978 BERMS Old Aspen Site, Prince Albert National Park, Saskatchewan, Canada	Herbivory (May 2016)	2012-2015
millhaft	Lat: 52.8008 Lon: -2.2988 Norbury, Staffordshire, United Kingdom	Herbivory (April 2018 & 2019)	2016, 2017, 2020, 2021
worcester	Lat: 42.2697 Lon: -71.8428 Worcester State University, Worcester, Massachusetts, United States	Herbivory (June 2018)	2014-2017, 2019-2021
harvard	Lat: 42.5378 Lon: -72.1715 EMS Tower, Harvard Forest, Petersham, Massachusetts, United States	Ice Storm (December 2008)	(2008, 2010-2019)
sequoia	Lat: 36.5658 Lon: -118.7772 Lower Kaweah, Sequoia / Kings Canyon National Park, California, United States	Drought Mortality (2015)	2012-2014

We calculated the duration of three leaf developmental periods based on the transition time between different amplitude values in the rising and falling portions of the greenness curve as is shown in Figure 5-1. To ensure our approach utilized optimal amplitude values, we explored different amplitude thresholds to denote the start and end of each period. Amplitude thresholds which corresponded to the best compromise between signal in response to disturbance or stress and noise in the absence of disturbance or stress were selected. We calculated the duration of the greenness rising period as the time between the first instances of 10% and 90% amplitude in the rising portion of the greenness curve following Klosterman et al. (2018). We also examined the time between the first instances of 25% and 90% amplitude in the rising portion of the greenness curve as the duration of the greenness rising period and found this to fluctuate slightly more across site-years in the absence of disturbance or stress without commensurate increases in signal response to disturbance or stress. We calculated the duration of the apparent greenness plateau as the time between the first instance (if there was more than one instance in a single year) of 95% and the final instance (if there was more than one instance in a single year) of 50% amplitude in the falling portion of the greenness curve to capture greenness declines potentially due to disturbance or stress (Klosterman et al., 2014). We also tested the time between the first instance of 95% and the final instance of 75% amplitude in the falling portion of the greenness curve as the greenness plateau period, though found variability in this duration in the absence of disturbance or stress to occlude signal responses to disturbance or stress. We calculated the duration of the total non-dormancy period or leaf-on period as the time between the first instance of 50% amplitude in the rising portion and the final instance of 50% amplitude in the falling portion of the greenness curve following common approaches (Misra et al., 2018). The duration between these amplitude values were optimal over that of between 25% amplitude in the rising and falling portions of the greenness curve, for which variability in the absence of disturbance or stress was reduced though signal responses to disturbance or stress were also much reduced.

To explore how these leaf developmental periods differed in comparison to a reference state, we then computed the percentage change and ratios of the duration of these periods in years with disturbance or stress to the average duration of these periods in years without evident disturbance or stress. To more broadly establish how this ratio varies in the absence of disturbance or stress for other sites, we computed the probability density function of these ratios for all other sites in the PhenoCam Network, comparing each year to the average of all other years as a reference state proxy. We filtered available data to remove annual data sets which were less than 300 days in length, multi-year data sets which were less than four years in length, as well as data sets with observed periods which were less than the 25% quantile – 1.5 times the interquartile range or else more than the 75% quantile + 1.5 times the interquartile range to address the influence of potential artefacts associated with field of view shifts or data gaps (Tian et al., 2021; Seyesnasrollah et al., 2019b; Richardson et al., 2018b). It is possible that some of these values may have been associated with disturbance or stress, though we wished to refine our focus to data sets with representative stability from across the PhenoCam Network for this exercise. To examine the likelihood of positively identifying disturbance or stress based upon the duration of these periods in a given year relative to other years, we designated threshold average ratios to serve as indicators of probable disturbance or stress warranting concern regarding ecological integrity. We designated these ratios to achieve an optimal compromise between detection of true cases of disturbance or stress and the avoidance of false detections. We then computed the probability of correct detections using these threshold average ratios.

5.4 Results

5.4.1 Cases of Disturbance or Stress from the PhenoCam Network

Cases of disturbance or stress from the PhenoCam Network confirmed that disturbance or stress can lead to detectable deviations in one or more of the following in comparison to reference years: A) the duration of the greenness rising portion of the curve between the onset of leaf growth and the seasonal peak in greenness; B) the duration of the leaf maturity period greenness plateau following the seasonal peak in greenness prior to the fall decline; and C) the duration of the entire leaf-on period. Frost and herbivory led to both reductions and extensions in the rising period. Hurricanes and windstorms typically coincided with a reduced plateau or overall leaf-on period. However, in some cases, disturbance effects on these greenness curve developmental periods were mild or not evident. Stress in the form of drought led to reductions in all periods for a site with evergreen vegetation.

5.4.2 Disturbance: Hurricanes and Windstorms

Hurricane Maria was a category 4 hurricane which made landfall on September 20th, 2017, on the island of Puerto Rico, resulting in widespread forest damage (Zhu et al., 2021). Greenness signals captured by the '*elverde*' PhenoCam from March to February show a seasonally early decline in greenness immediately following Hurricane Maria relative to previous years (Figure 5-2). The plateau period was reduced by 58 days (40%) in 2017 relative to the 143-day average from the reference growing seasons 2015, 2016, and 2019. The entire leaf-on period was reduced by 52 days (29%) in 2017 relative to the 177-day average from reference growing seasons. Interpolation with available data and inspection of images from the 2018 growing season suggests there was an extended recovery into the growing season following Hurricane Maria, and that these periods were also affected in 2018. Alternatively, the greenness curve from the 2019 growing season is similar to that of the 2015 and 2016 growing seasons. The rising period in 2018 was lengthened by 39 days (124%) relative to the 32-day average of reference growing seasons. As in 2017, the plateau period was also approximately reduced by 58 days (40%) in 2018 relative to reference years. The leaf-on period in 2018 was 159 days, an 18-day reduction (10%) from the 177-day average of reference growing seasons. This suggests that Hurricane Maria led to sufficiently severe damage to impact seasonal leaf developmental periods in the 2017 and 2018 growing seasons. Visual inspection of available images for 2019 onwards suggests a return to pre-storm foliage levels, although a recovery transition in seasonal greenness may have still been underway in 2019. As more complete growing season records become available the recovery can be further assessed.

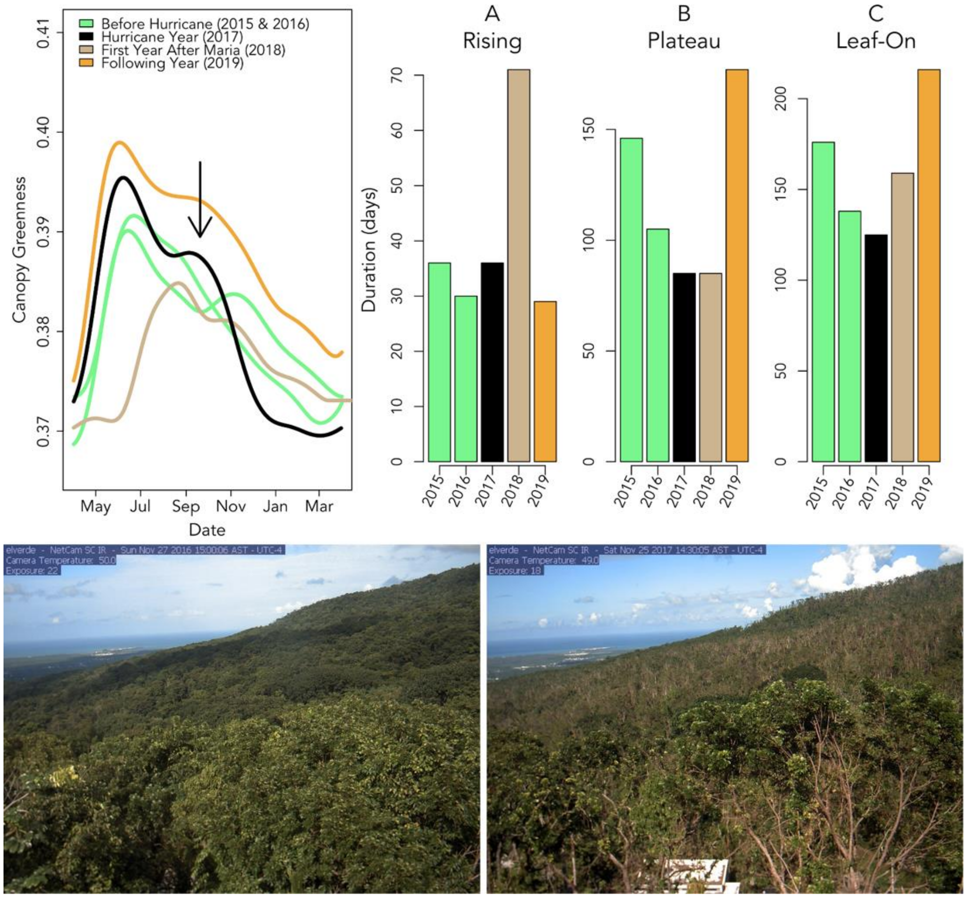

Figure 5-2. *Greenness signals from before and after a severe drought during the 2015 growing season as well as following Hurricane Maria (Sept. 20th, 2017) captured by the 'elverde' phenocam located at the El Verde Field Station, El Yunque National Forest, Northeastern Puerto Rico. The time of year during which Hurricane Maria occurred in 2017 is denoted with an arrow. Greenness timeseries are shown for spline-smoothed 3-day 50th percentile GCC values on the top left. The duration of the A (rising), B (plateau), and C (leaf-on) periods are shown on the top right. Phenocam images from before and after Hurricane Maria are shown on the bottom.*

A windstorm with wind speeds approaching 100 miles per hour (160 km per hour) led to widespread damage in the Great Smoky Mountains National Park on May 4th, 2017 (Ahillen, 2017). The storm led to a reversal in the rising greenness signal usually observed in May, with a sudden decline in greenness which was captured by the ‘*NEON.D07.GRSM.DP1.00033*’ phenocam at the Great Smoky Mountains National Park, Tennessee (Figure 5-3). Another disturbance event impacted local vegetation later in the 2017 growing season as Hurricane Irma travelled through eastern Tennessee as a tropical depression on September 12th before dissipating on the 13th. The 2020 growing season also saw canopy damage due to wind disturbance. A complex of severe long-lasting thunderstorms designated as a derecho moved across Tennessee on May 3rd, 2020, with windspeeds approaching 80 miles per hour (~129 km per hour) (US Department of Commerce, 2020). In the 2017 growing season, the seasonal greenness peak was both reduced and late relative to reference years without disturbance (2018, 2019, and 2021). In the fall of 2017, the late-growing season decline in greenness also began notably earlier in 2017 than reference years. The rising period in 2017 was 17 days longer (53%) than the 32-day average period from reference years. The plateau period was 33 days shorter (22%) than the 146-day average period observed in reference growing seasons, while the leaf-on period was just 7 days longer (4%) in 2017 versus the 183-day average from reference years. Three years later in 2020, the seasonal greenness peak was also late relative to reference growing seasons. In 2020, the rising period was 16 days longer (50%) than the 32-day average from reference years, similar to that of 2017. Additionally, in 2020 the plateau period was 22 days shorter (15%) than the 146-day average period observed in reference years. The leaf-on period in 2020 was only 5 days shorter (3%) than the 183-day average from reference growing seasons. This suggests that these disturbance events led to sufficient damage to impact leaf developmental periods in both the 2017 and 2020 growing seasons.

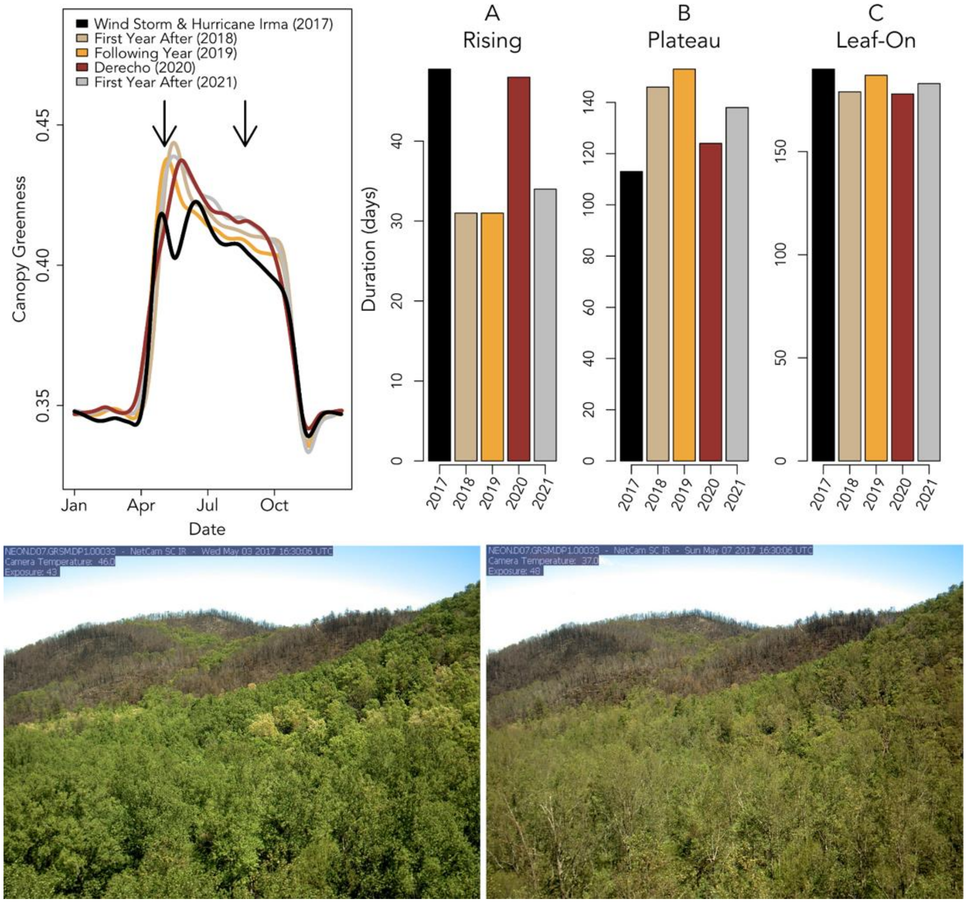

Figure 5-3. *Greenness signals from before and after a spring windstorm and Hurricane Irma captured by the 'NEON.D07.GRSM.DP1.00033' phenocam. The timings of disturbance events in 2017 and 2020 are denoted with an arrow. Greenness timeseries are shown for spline-smoothed 3-day 50th percentile GCC values on the top left. The duration of the A (rising), B (plateau), and C (leaf-on) periods are shown on the top right. Phenocam images from immediately before and after the spring windstorm are shown on the bottom.*

Hurricane Irene caused extensive damage due to flooding following excessive rainfall as well as a combination of high winds, tornadoes, and storm surges across the North American Acadian region in 2011 (Matyas, 2017). Hurricane Irene led to a seasonally early and rapid decline in greenness in August of 2011 captured by the '*woodshole*' phenocam at the Woods Hole Research Center in Massachusetts (Richardson et al., 2018b; Figure 5-4). The length of the plateau and leaf-on periods in 2011 were 35 (30%) and 40 days (26%) shorter than the 117-day and 156-day averages from subsequent seasons, respectively. The length of the rising period following Hurricane Irene did not vary beyond the range of subsequent years. This suggests that Irene led to sufficient damage to truncate the plateau and leaf-on periods in the 2011 growing season.

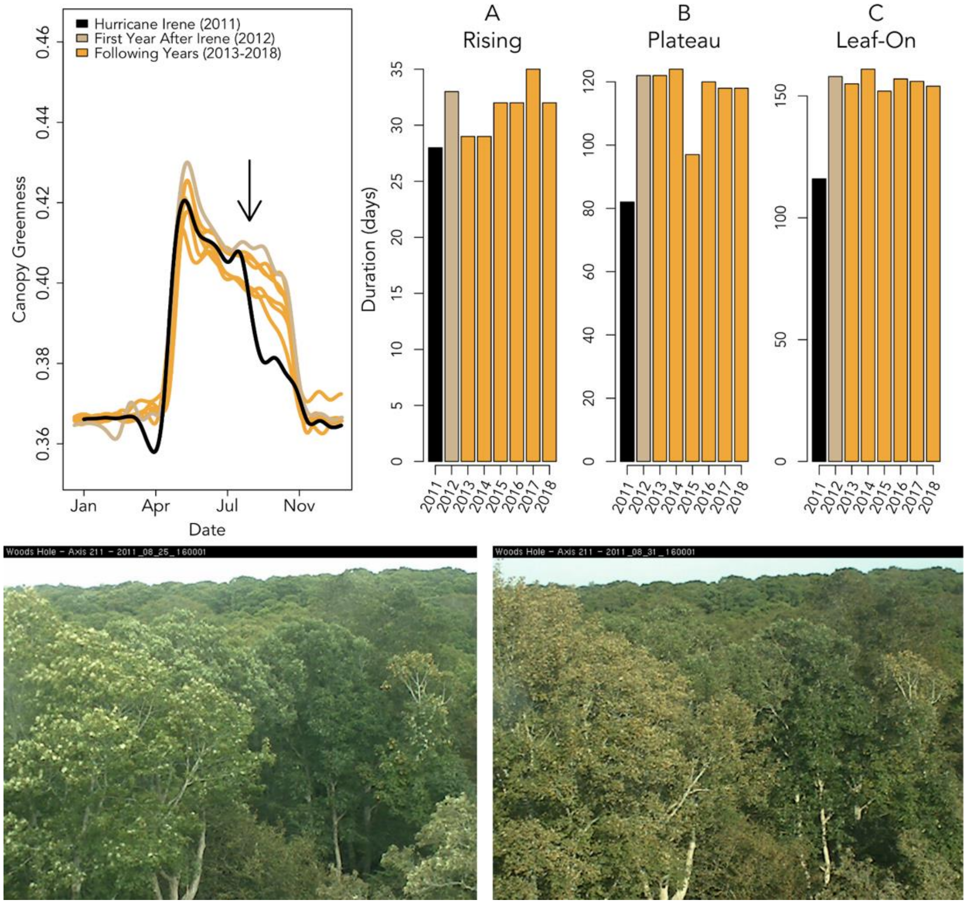

Figure 5-4. *Greenness signals from before and after Hurricane Irene captured by the 'woodshole' phenocam. The timing of the Hurricane in 2011 is denoted with an arrow. Greenness timeseries are shown for spline-smoothed 3-day 50th percentile GCC values on the top left. The duration of the A (rising), B (plateau), and C (leaf-on) periods are shown on the top right. Phenocam images from days before and after Hurricane Irene are shown on the bottom.*

5.4.3 Disturbance: Frost

Warmer than average March temperatures in 2016 were followed by a frost event on April 9th which led to leaf damage in an experimental warming chamber of the SPRUCE (Spruce and Peatland Responses Under Changing Environments) experiment located in the USDA Forest Service Marcell Experimental Forest (MEF) north of Grand Rapids, Minnesota, captured by the ‘*spruceT9P17*’ phenocam (Richardson et al., 2018c). The +9°C warming above ambient temperatures in this chamber led to a premature loss of frost hardiness, resulting in damage following this frost event in which ambient temperatures dropped below -15°C. The rising greenness signal usually observed in April was temporarily reversed after reaching a relatively reduced seasonal peak and declined until a local minimum was reached in late April (Figure 5-5). Following this, the greenness signal once again rose to a local peak in mid-June over approximately a 45-day period. The warming treatment led to both an advanced green-up as well as advanced peak in greenness prior to the frost event (Richardson et al., 2018c). Following the frost event greenness signals remained below the initial peak value. This interruption in the green-up process had the effect of substantially reducing the apparent rising period in comparison to subsequent years. The length of the rising portion of the greenness curve in 2016 was 25 days shorter (47%) than the 53-day average from subsequent seasons. Due to the early green-up, the duration of the apparent plateau period was substantially extended by 112 days (102%) relative to the 110-day average from subsequent years. The leaf-on period was also extended by 86 days (53%) relative to the 163-day average from other years. This suggests that the combined influence of warming and severe frost event in 2016 led to sufficient damage to impact seasonal leaf developmental periods.

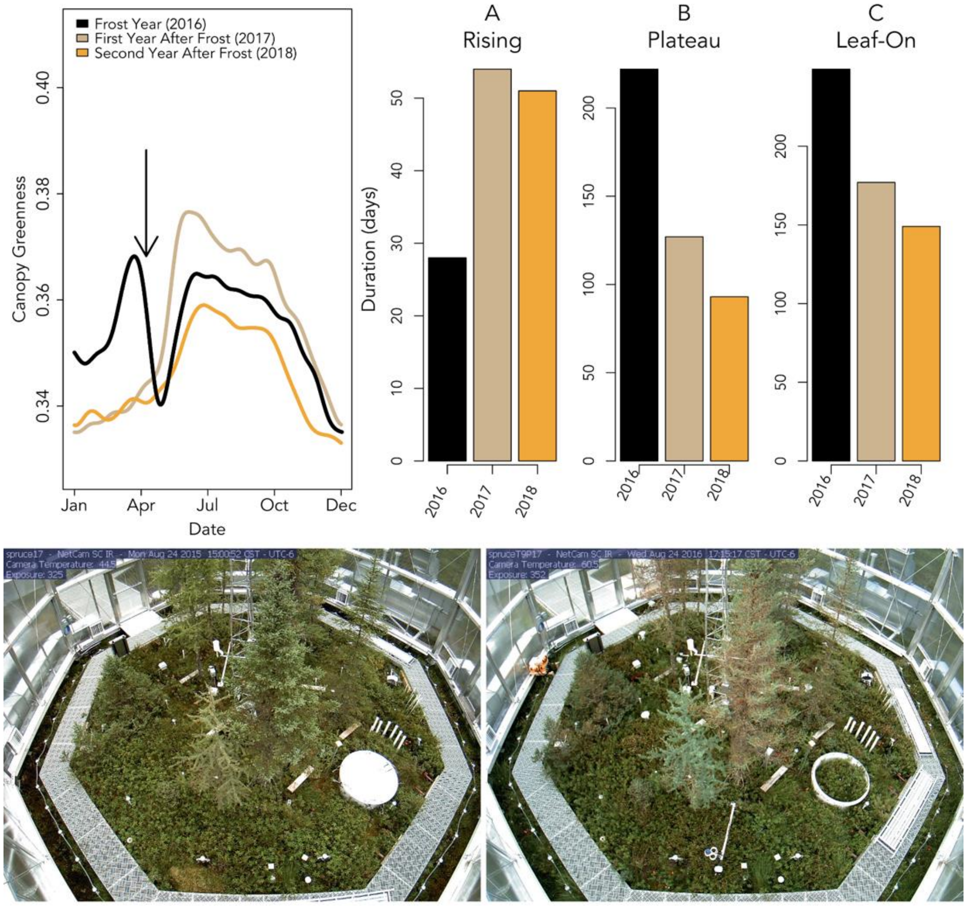

Figure 5-5. *Greenness signals from before and after a frost event on April 9th, 2016, which led to leaf damage in an experimental warming chamber of the SPRUCE experiment captured by the 'spruceT9P17' phenocam (Richardson et al., 2018c). The time of year during which the frost damage occurred in 2016 is denoted with an arrow. Greenness timeseries are shown for spline-smoothed 3-day 50th percentile GCC values on the top left. The duration of the A (rising), B (plateau), and C (leaf-on) periods are shown on the top right. Phenocam images from before and after this frost event are shown on the bottom.*

An unusually warm spring was followed by a severe frost event in May of 2010 across the northeastern United States. This led to widespread frost damage of newly emerging leaves, part of which was captured by both the '*arbutuslake*' and '*proctor*' phenocams, which are located near Arbutus Lake and on the University of Vermont campus, respectively (Hufkens et al., 2012b). For the *arbutuslake* phenocam, the combination of this warm spring and late frost event led to a sufficiently early leaf development such that leaves were vulnerable at the time of frost (Figure 5-6). The rising greenness signal usually observed in May was temporarily reversed on approximately May 8th before increasing once more following May 12th. The 2010 growing season greenness curve had an early and reduced seasonal peak greenness value relative to other years. The duration of the rising period in 2010 intermediate to that of subsequent years. The plateau period was 9 days longer (9%) than the 94-day average of other years, and the leaf-on period was 14 days longer (11%) than the 126-day average of other years. This suggests that the combination of this warm spring and late frost event was of sufficient severity to influence seasonal leaf developmental periods in 2010.

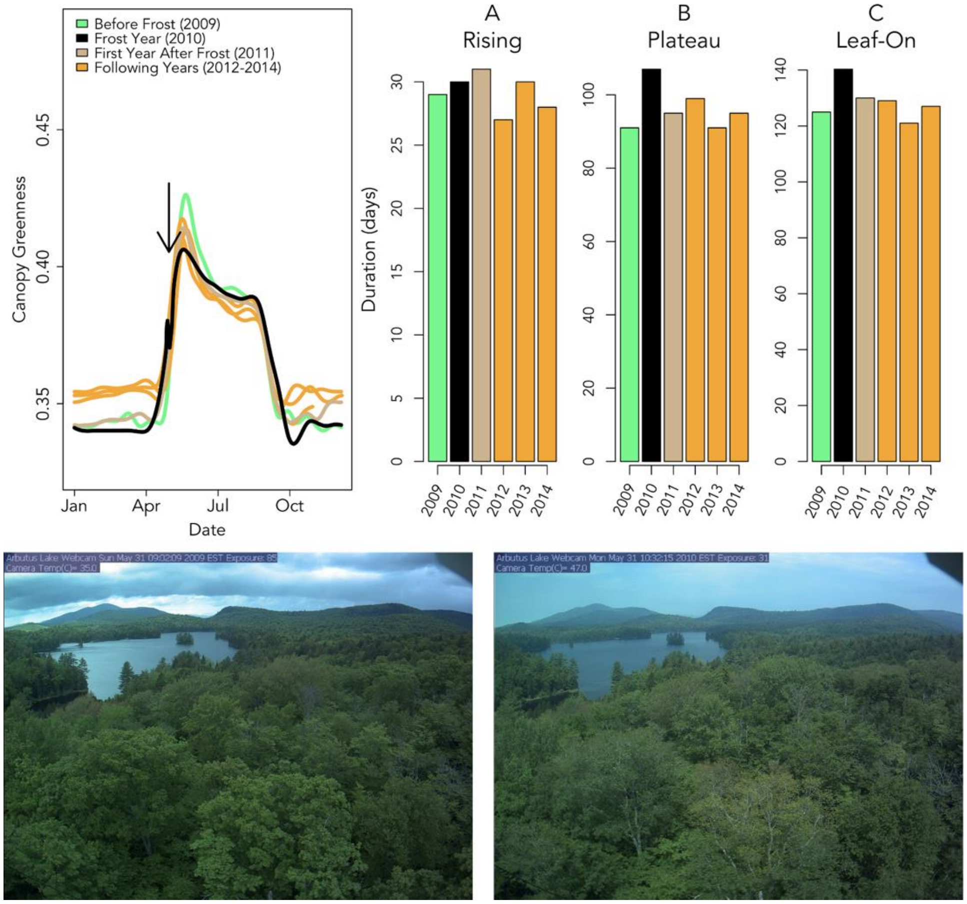

Figure 5-6. *Greenness signals from before and after a widespread warm spring and late frost event in 2010 captured by the 'arbutuslake' phenocam. The timing of the frost in 2010 is denoted with an arrow. Greenness timeseries are shown for spline-smoothed 3-day 50th percentile GCC values on the top left. The duration of the A (rising), B (plateau), and C (leaf-on) periods are shown on the top right. Phenocam images from one year before and immediately after the frost event are shown on the bottom.*

This warm spring and late frost event also affected vegetation captured by the *proctor* phenocam in 2010 (Hufkens et al., 2012b). For the *proctor* phenocam, the combination of this warm spring and late frost event also led to a sufficiently early leaf development such that leaves were vulnerable at the time of frost, and a reduced seasonal maximum greenness value was observed in 2010 as well as a quicker decline from the seasonal maximum (Figure 5-7). The calculated length of the rising, plateau, and leaf-on periods were not anomalous in 2010, however, compared to other years. This suggests that despite this warm spring and late frost event leading to visible damage and a reduced seasonal greenness peak value, we were unable to detect anomalous leaf developmental periods with the amplitude thresholds we utilized. If the plateau period is calculated as the time between 95% and 75% amplitude in the falling portion of the greenness curve instead of between 95% and 50% amplitude, there is a notable reduction by 56 days (93%) relative to the 60-day average from other years in 2010. However, this calculation approach leads to pronounced variability in growing seasons without known cases of disturbance or stress, and it produces a similar magnitude of deviation with an apparent 39-day (65%) reduction in the plateau period for the year 2014. In addition, this alternative approach to calculating the plateau period resulted in pronounced variability for other sites across the PhenoCam Network in the absence of disturbance or stress.

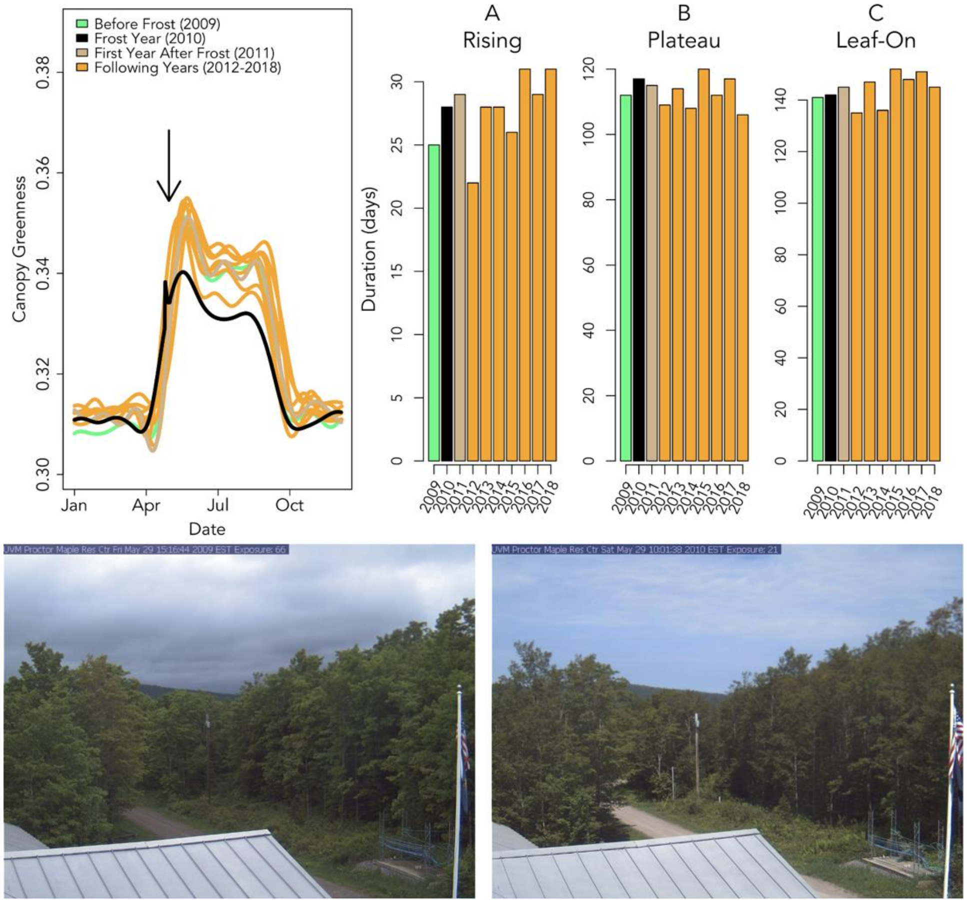

Figure 5-7. *Greenness signals from before and after a widespread warm spring and late frost event in 2010 captured by the 'proctor' phenocam. The timing of the frost in 2010 is denoted with an arrow. Greenness timeseries are shown for spline-smoothed 3-day 50*th *percentile GCC values on the top left. The duration of the A (rising), B (plateau), and C (leaf-on) periods are shown on the top right. Phenocam images from before and after the frost event are shown on the bottom.*

In early April of 2007, a widespread frost event following an unusually warm March affected vegetation across much of the eastern United States (Richardson et al., 2018b; Hufkens et al., 2012a; Gu et al., 2008). This frost event was captured by the '*mammothcave*' phenocam at the Environmental Learning Center in Mammoth Cave National Park, Kentucky. This frost event resulted in a reversal in the rising greenness signal observed in early April until a local minimum was reached shortly after in mid-April (Figure 5-8). Following this, the greenness signal rose to late seasonal greenness peak in early June. The length of the rising period was 28 days longer (75%) in 2007 than the 37-day average from other years, while the lengths of the plateau and leaf-on periods were not distinct from other years. This suggests that the frost event led to sufficient damage to impact leaf developmental periods in the 2007 growing season.

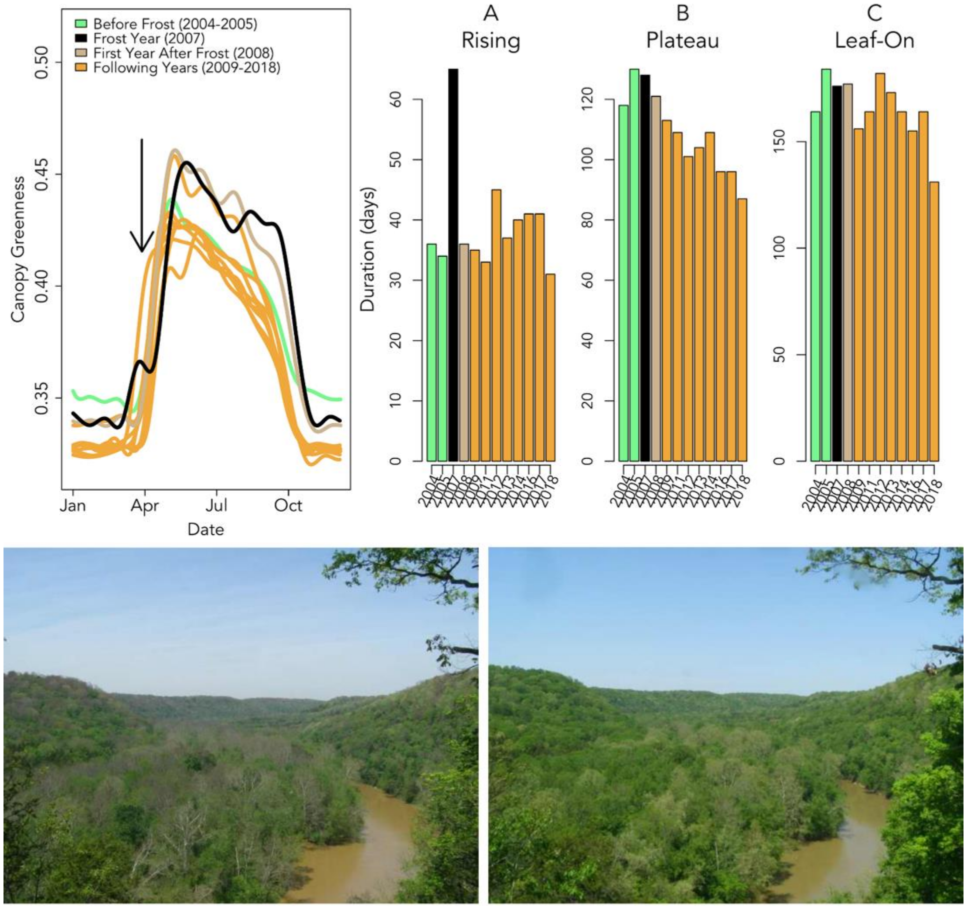

Figure 5-8. *Greenness signals from before and after a frost event on April 8th, 2007, which led to leaf damage captured by the 'mammothcave' phenocam. Several years were excluded from analysis for this phenocam due to field of view shifts or data gaps occurring during the growing season. The time of year during which the frost damage occurred in 2007 is denoted with an arrow. Greenness timeseries are shown for spline-smoothed 3-day 50th percentile GCC values on the top left. The duration of the A (rising), B (plateau), and C (leaf-on) periods are shown on the top right. Phenocam images from immediately after and one year after the frost event are shown on the bottom.*

5.4.4 Disturbance: Insect Defoliation

A forest tent caterpillar (*Malacosoma disstria*) outbreak in the Canadian province of Saskatchewan led to widespread defoliation in 2016, with a defoliation onset date of May 13th captured by the '*canadaOA*' phenocam in Prince Albert, Saskatchewan (Stephens et al., 2018).

The rising greenness signal usually observed in May was temporarily reversed immediately following the outbreak and exhibited a decline until a local minimum was reached in mid-June (Figure 5-9). Following this, the greenness signal rose to a peak in early July over an approximately 24-day period. This seasonal peak in greenness was both reduced and late relative to previous seasons. Insect herbivory by the forest tent caterpillar led to a rising period that was lengthened by 44 days (149%) in 2016 relative to the previous four-year average of 30 days. The duration of the plateau period was reduced by 34 days (34%) relative to the previous four-year average of 98 days. Additionally, the length of the leaf-on period was reduced by 30 days (23%) relative to the 131-day average of previous years. This suggests that the outbreak of forest tent caterpillar led to sufficient damage to impact seasonal leaf developmental periods in the 2016 growing season.

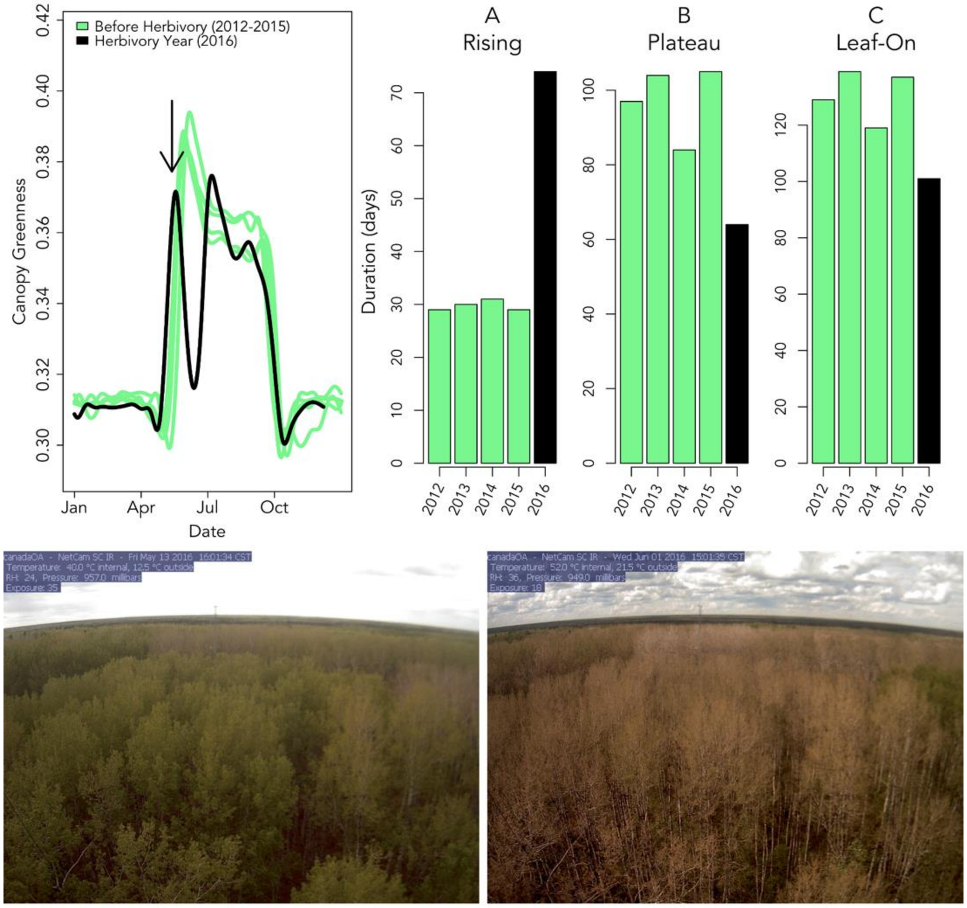

Figure 5-9. *Greenness signals from before and after insect defoliation by the forest tent caterpillar captured by the 'canadaOA' phenocam (Stephens et al., 2018), with an onset date of May 13th, 2016. The timing of the onset of defoliation in 2016 is denoted with an arrow. Greenness timeseries are shown for spline-smoothed 3-day 50th percentile GCC values on the top left. The duration of the A (rising), B (plateau), and C (leaf-on) periods are shown on the top right. Phenocam images from before and after the defoliation are shown on the bottom.*

Herbivory primarily by the European winter moth (*Operophtera brumata*) led to visibly evident defoliation in 2018, with an estimated onset date of April 20th, captured by the '*millhaft*' phenocam in Norbury, Staffordshire, UK according to site metadata notes. Herbivory also occurred in 2019, with an estimated onset date of April 25th, though to a lesser extent. The rising greenness signal usually observed in April and May was delayed immediately following the outbreak in 2018 (Figure 5-10). Following this, the greenness signal increased to a peak that was reduced relative to the disturbance-free reference years of 2016, 2017, 2020, and 2021. Insect herbivory by the winter moth led to a plateau period that was shortened by 46 days (33%) in 2018 relative to the average of 141 days from reference years. The duration of the leaf-on period was reduced by 52 days (29%) relative to the 179-day average from reference years. Conversely, the extent of the rising period was not distinct in 2018 relative to reference years. In 2019, the rising greenness signal was temporarily reversed in early and mid-May until it rose over a 33-day period to a seasonal greenness peak which was late and reduced relative to reference growing seasons. The greenness rising period in 2019 was 39 days longer (118%) than the 33-day average of reference years. The plateau period was 59 days shorter (42%) in 2019 than that of the 141-day average from reference years. The leaf-on period was also shortened in 2019 though to a lesser extent of 23 days (13%) relative to the 179-day average from reference years. This suggests that the herbivory of the winter moth prompted sufficient damage to impact seasonal leaf development in both the 2018 and 2019 growing seasons.

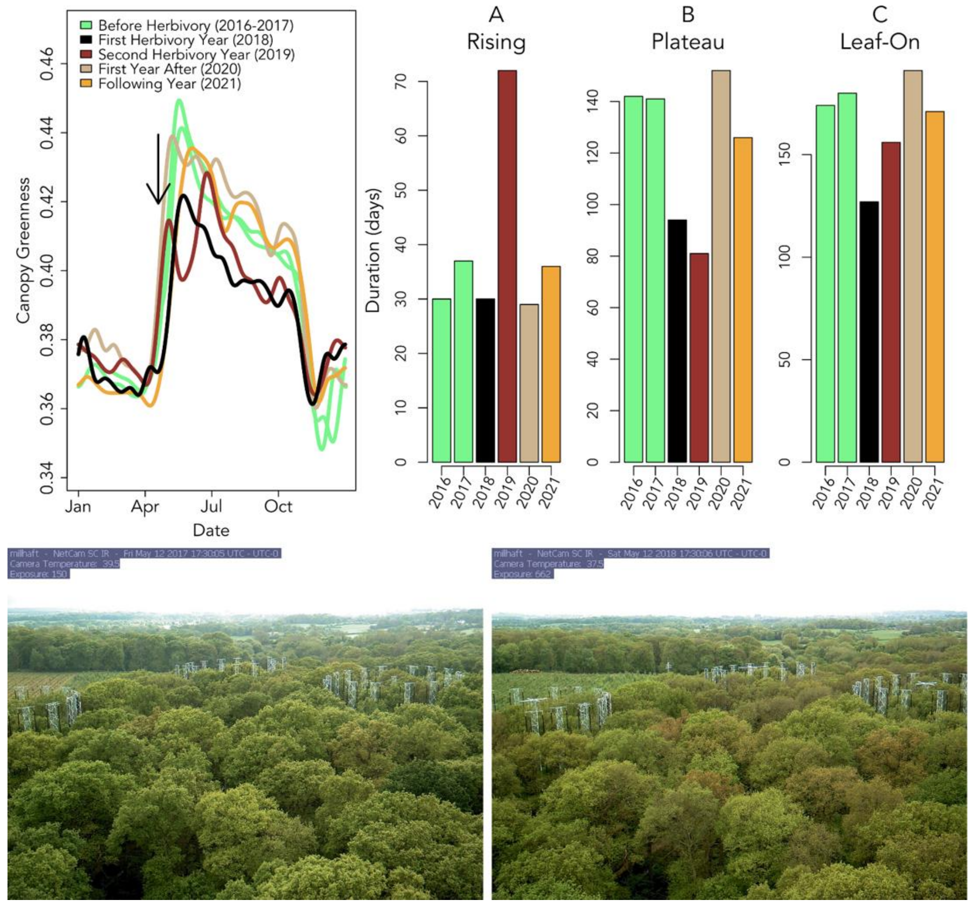

Figure 5-10. *Greenness signals from before and after insect defoliation by the European winter moth captured by the 'millhaft' phenocam, with estimated onset dates in April 2018 and 2019. The timing of the estimated onset of defoliation in 2018 is denoted with an arrow. Greenness timeseries are shown for spline-smoothed 3-day 50th percentile GCC values on the top left. The duration of the A (rising), B (plateau), and C (leaf-on) periods are shown on the top right. Phenocam images from one year before and immediately following the defoliation are shown on the bottom.*

Drought conditions led to an enhanced gypsy moth (*Lymantria dispar*) outbreak in 2015 in Massachusetts and widespread defoliation over subsequent growing seasons across more than 1,544 mi^2 (4,000 km^2) of the eastern United States (Pasquarella et al., 2018). Defoliation by the gypsy moth was captured by the '*worcester*' phenocam on the Worcester State University campus in Worcester, Massachusetts, with an estimated onset date of June 10th, 2018. The gradual post-peak decline in the greenness signal usually observed in June exhibited a steep decline before stabilizing and rising to a local maximum over a 26-day period in late July (Figure 5-11). The reduced greenness peak prompted by this herbivory led to an apparent rising period that was shortened by 7 days (21%) in 2018 relative to the 34-day average from reference years without disturbance from 2014-2017 and 2019-2021. This detected reduction prior to the onset of defoliation was likely due to the herbivory reducing the peak greenness value and thus the time between 10% and 90% amplitude in the rising portion of the greenness curve, even though the herbivory occurred following the greenness peak. Surprisingly, the plateau period was not distinct in comparison to reference growing seasons, as the early timing of 95% amplitude in the falling portion of the curve was followed by an early timing of 50% amplitude in the falling portion of the curve, which was two weeks earlier than the average of reference years. The leaf-on period was reduced by 13 days (8%) in comparison to the 159-day average from reference growing seasons. This suggests that herbivory by the gypsy moth led to sufficient damage to impact seasonal leaf developmental periods in the 2018 growing season.

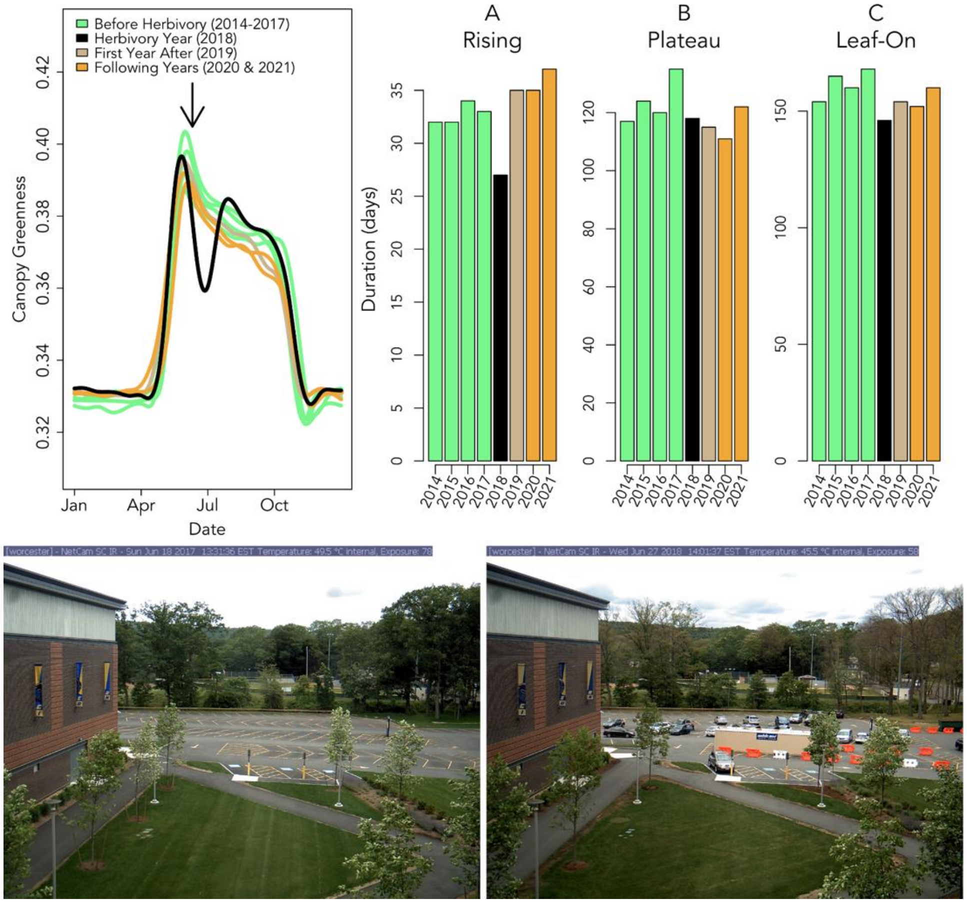

Figure 5-11. *Greenness signals from before and after insect defoliation by the gypsy moth captured by the 'worcester' phenocam, with an estimated onset date of June 10th, 2018. The timing of the estimated onset of defoliation in 2018 is denoted with an arrow. Greenness timeseries are shown for spline-smoothed 3-day 50th percentile GCC values on the top left. The duration of the A (rising), B (plateau), and C (leaf-on) periods are shown on the top right. Phenocam images from one year before and immediately following the defoliation are shown on the bottom (note the vegetation in the top center to top right portion of the image following defoliation).*

5.4.5 Disturbance: Winter Ice Storm

An ice storm on December 11th and 12th of 2008 damaged canopy vegetation in the Harvard Forest, including vegetation captured the by '*harvard*' phenocam. Minimal influence in the greenness timeseries was evident but there was a substantial reduction in LAI from ground data by 22% following this storm in the 2009 growing season relative to 2008 (Keenan et al., 2014). Mid-summer leaf area index values showed a gradual recovery to near-pre-ice storm levels by 2012, and seasonal maximum greenness values continually increased following 2009, while our length metrics did not follow any such trend (Figure 5-12). The length of the rising period in 2009 was six days longer than that observed in either 2008 or 2010, though only four days longer (12%) than the 31-day average from all other years. The length of the plateau and leaf-on periods in 2009 were intermediate relative to other years. Despite this ice storm impacting local leaf area index values, our approach did not yield detection of anomalous leaf developmental periods.

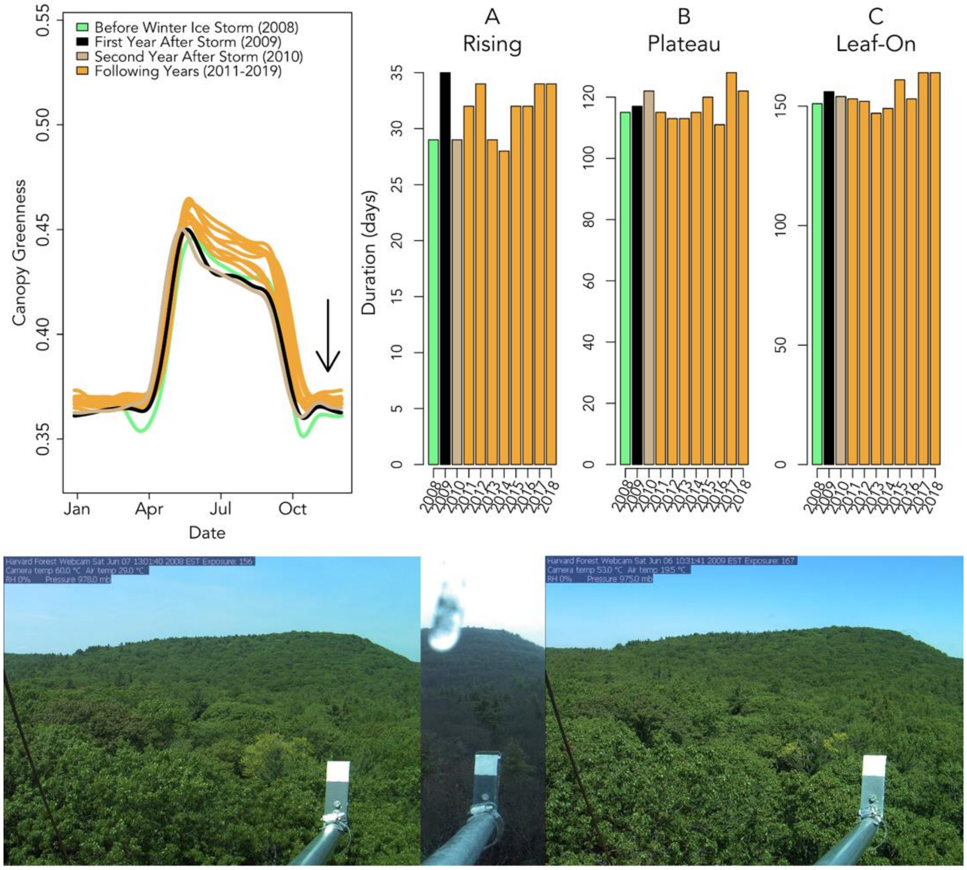

Figure 5-12. *Greenness signals from before and after an ice storm in December of 2008 captured by the 'harvard' phenocam. The timing of the ice storm in 2008 is denoted with an arrow. Greenness timeseries are shown for spline-smoothed 3-day 50*th *percentile GCC values on the top left. The duration of the A (rising), B (plateau), and C (leaf-on) periods are shown on the top right. Phenocam images from before, during, and after the ice storm are shown on the bottom (note the gaps in the canopy following the storm).*

5.4.6 Stress: Drought Mortality

Four successive years of drought in the Kings Canyon National Park, California, led to unprecedented forest dieback with mortality becoming evident in the summer of 2015 captured by the '*sequoia*' phenocam (Richardson et al., 2018b; Stephenson et al., 2018). This led to a continuous decline in the maximum greenness signal observed during the growing season, with a considerable 60% reduction in the 2015 spline-smoothed greenness curve amplitude relative to 2012 (Figure 5-13). Each of the rising, plateau, and leaf-on periods were reduced in 2015 by 25 (43%), 35 (58%), and 55 (42%) days, respectively relative to 58, 61, and 132-day averages from the previous three years. This suggests that this drought led to sufficient damage to impact seasonal leaf developmental periods in the 2015 growing season.

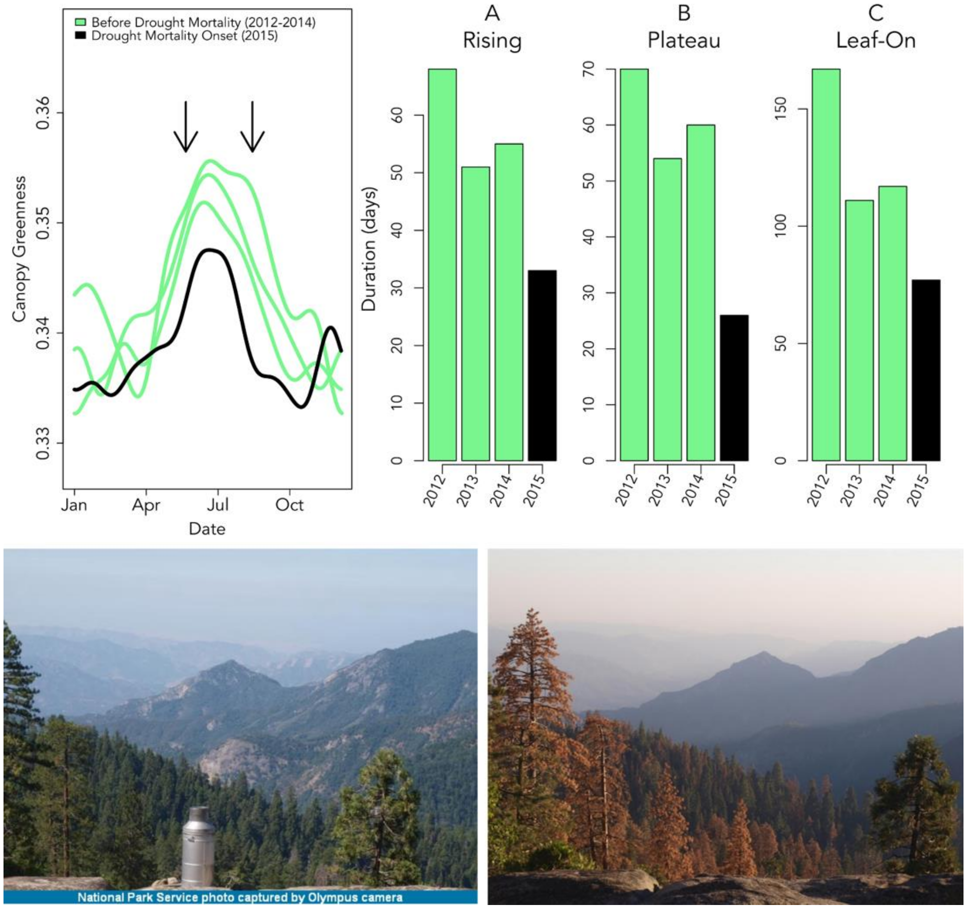

Figure 5-13. *Greenness signals during successive years of drought captured by the 'sequoia' phenocam (Stephenson et al., 2018), with drought-induced foliage dieback becoming evident in 2015. Arrows provide a reference for comparing successive years of greenness signals over the June-August growing season period. Greenness timeseries are shown for spline-smoothed 3-day 50th percentile GCC values on the top left. The duration of the A (rising), B (plateau), and C (leaf-on) periods are shown on the top right. Phenocam images from before (August 2011) and after (July 2016) the onset of drought mortality are shown on the bottom.*

5.4.7 Indicator Potential for Disturbance or Stress Detection

To better assess the aptitude of leaf developmental periods extracted from the greenness curve as indicators, we examined how these deviations compare to interannual fluctuations observed in the absence of disturbance or stress across the PhenoCam Network. Probability density functions of the ratio of each period in a given year to the reference average for other years is shown in Figure 5-14 for all broadleaf and needleleaf sites from the PhenoCam Network without known cases of disturbance or stress. Together these probability density functions demonstrate that these periods are generally stable under normal conditions and fluctuate in response to disturbance or stress. As the rising period was shorter than other periods, cases of disturbance or stress which influenced the rising period led to greater relative deviations from the average, though the probability density function was also more extensive (Figure 5-14A). Typical interannual variability for the ratio of the rising period in a given year to the average of alternate years in the absence of disturbance or stress corresponds to an interquartile range of 1±0.06 times the average (25th to 75th percentile). Several of the rising period ratios observed in the context of stress or disturbance were more extreme than all non-disturbance rising period average ratios from the PhenoCam Network. These extreme cases included the 2007 rising period ratio of 1.76 observed by the *mammothcave* phenocam, the 2016 rising period rising period ratio of 2.47 observed by the *canadaOA* phenocam, the 2016 rising period ratio of 0.52 observed by the *spruceT9P17* phenocam, the 2017 and 2020 rising period ratios of 1.53 and 1.5 observed by the *NEON.D07.GRSM.DP1.00033* phenocam, the 2018 rising period ratio of 2.14 observed by the *elverde phenocam*, and the 2019 rising period ratio of 2.18 observed by the *millhaft* phenocam. A spring rising period of 0.57 times that of the average for other years, such as observed with the *sequoia* phenocam in 2015, is equivalent to a probability of less than 1% more extreme values. In contrast, the rising period observed by the *worcester* phenocam in 2018, which corresponded to a ratio of 0.79 times the average of reference years was associated with a probability of approximately 4% more extreme values in non-disturbance rising period average ratios from the PhenoCam Network.

The duration of the plateau period was generally reduced in the context of disturbance or stress, with the exception of the warming treatment and frost event observed by the *spruceT9P17* phenocam (Figure 5-14B). The degree of deviation relative to the reference average for the plateau period was less pronounced in terms of probability than that of the spring rising period, though greater than that of the leaf-on period. Similar to that observed for the rising period average ratio, typical interannual variability for the ratio of the plateau period in a given year to the average of reference years without disturbance or stress corresponds to an interquartile range of 1±0.06 times the average (25th to 75th percentile). Two of the plateau period ratios observed in the context of stress or disturbance were more extreme than all non-disturbance plateau period average ratios from the PhenoCam Network. These included the extended plateau period observed by the *spruceT9P17* phenocam in 2016 which was 1.75 times the average, as well as the reduced plateau period observed by the *sequoia* phenocam in 2015 which was just 0.43 times the average from previous years. Several of the plateau period ratios observed in the context of disturbance or stress were associated a probability of less than 1% in detecting more extreme values in the absence of disturbance or stress. These included the plateau period ratio of 0.71 times the average observed by the *woodshole* phenocam in 2011, the plateau period ratios of 0.67 and 0.58 observed by the *millhaft* phenocam in 2018 and 2019, the plateau period ratios both equal to 0.6 observed by the *elverde* phenocam in 2017 and 2018, as well as the plateau period ratio of 0.65 observed by the *canadaOA* phenocam in 2016. In contrast, the plateau period ratio of 0.78 observed by the *NEON.D07.GRSM.DP1.00033* phenocam in 2017 corresponded to a greater probability of 3% more extreme cases.

The length of the leaf-on period was found to respond less acutely to disturbance or stress relative to the other periods (Figure 5-14C). This may be due to reductions in the rising and plateau periods due to disturbance or stress being compensated to some degree by a delayed or extended senescence process (Zohner et al., 2019). The leaf-on period also had reduced interannual variability in the absence of stress or disturbance compared to the rising and plateau periods. The ratio of the leaf-on period in a given year to the average of reference years without disturbance or stress corresponds to an interquartile range of 1±0.04 times the average (25th to 75th percentile). Four of the leaf-on period ratios observed in the context of stress or disturbance were more extreme than all non-disturbance leaf-on period average ratios from the PhenoCam Network. The most distinct deviation in the leaf-on period was observed by the *spruceT9P17* phenocam in 2016, with a ratio of 1.53 times the average of reference years. Other leaf-on period average ratios which were unprecedented in the absence of stress or disturbance across the PhenoCam Network included the leaf-on period ratio of 0.58 observed by the *sequoia* phenocam in 2015, the leaf-on period ratio of 0.71 observed by the *elverde* phenocam in 2017, and the leaf-on period ratio of 0.72 observed in 2018 by the *millhaft* phenocam. Similarly, the leaf-on periods observed in 2011 by the *woodshole* phenocam and in 2016 by the *canadaOA* phenocam were 0.74 and 0.77 times the average of other years, each corresponding to a probability of less than 1% more extreme cases. The leaf-on period observed in 2019 by the *millhaft* phenocam was 0.87 times the average of reference years, corresponding to a probability of about 3% more extreme values. A less distinct leaf-on period of 0.9 times the average was observed by the *elverde* phenocam in 2018, which corresponded to a probability of about 7 % more extreme values. The only two extended leaf-on periods were observed in 2010 by the *arbutuslake* phenocam and 2016 by the *spruceT9P17* phenocam. The *arbutuslake* phenocam leaf-on period in 2010 was 1.11 times that of the average from other years, corresponding to a probability of approximately 6% more extreme cases, while the leaf-on period was observed by the *spruceT9P17* phenocam in 2016 as mentioned above was 1.53 times the average of reference years.

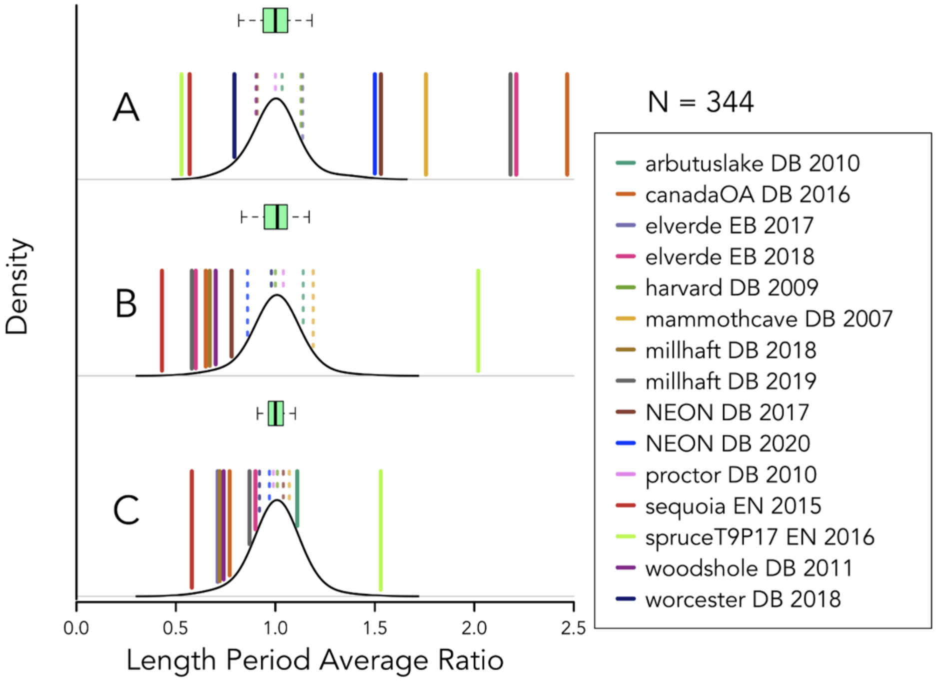

Figure 5-14. *Probability density functions of the ratio of the length of a period during a given year compared to the average for all other years from PhenoCam sites hosting broadleaf and needleleaf plant functional type vegetation without known cases of disturbance or stress for a total of 344 site-years. Boxplots denote the median and ± 1.5 times the interquartile range for the average ratio of each period. Solid vertical lines denote examples of known cases of disturbance or stress affecting one or more of these periods. Dashed vertical lines denote examples of disturbance or stress which had mild effects on one or more of these periods. The A (rising) period is shown on the top, the B (plateau) period is shown in the middle, and the C (leaf-on) period is shown on the bottom. The phenocam names for each case of disturbance or stress along with the dominant plant functional type (DB = deciduous broadleaf, EN = evergreen needleleaf) is shown in the legend. "NEON" stands for the NEON.D07.GRSM.DP1.00033 phenocam.*

A confusion matrix conveying the prevalence of true damage detection due to disturbance or stress shifting one or more of the rising, plateau, and leaf-on periods beyond an indicator threshold is shown in Figure 5-15. We designated threshold indicator ratios based upon the probability density functions presented in Figure 5-14 to optimize the signal to noise ratio in detecting anomalous periods while avoiding the false classification of periods as anomalous. These threshold ratios therefore differ from the interquartile ranges presented above to limit the misclassification of slightly unusual periods as the result of disturbance or stress. If disturbance or stress which led to leaf functional decline shifted one or more of these periods beyond our indicator thresholds, it was counted as a true detection. If, on the other hand, leaf functional decline was known to have occurred though none of the periods were shifted beyond the threshold, this was considered a false non-detection of damage. Likewise, if no disturbance or stress was known to have occurred, we assumed there was no leaf functional decline or damage. If under these circumstances one or more of these periods was beyond our indicator thresholds, we considered this a false detection. Under the same circumstances, if instead these periods were not beyond our indicator thresholds, we considered these cases to be examples of true non-detection. This matrix also includes the incidences of false detections, true non-detections, and false non-detections, based upon the probability density functions above. A designated indicator ratio of the spring rising period being beyond 1 ± 0.2 times the average correctly detected nine cases of disturbance or stress as anomalous rising periods. This indicator ratio corresponds to a combined probability of approximately 9% being false positives. Several of the 29 non-disturbance site-years which were associated with rising periods beyond 1 ± 0.2 times the average were observed at SPRUCE experimental sites which may have shown these fluctuations in response to experimental treatments as well as the spring frost event in 2016. For the plateau period, an indicator ratio of the period being 1 ± 0.2 times the average from other years would correctly detect the nine cases of disturbance and or stress influencing the plateau period observed from the PhenoCam Network, with a probability of approximately 9% being false positives. Several of the 26 non-disturbance site-years which were associated with plateau periods beyond 1 ± 0.2 times the average were also observed at SPRUCE experimental sites. Lastly, an indicator ratio of the leaf-on period being beyond 1 ± 0.1 times the average from other years would capture the nine cases of disturbance and or stress influencing the leaf-on period observed from the PhenoCam Network, with a probability of approximately 15% being false positives. A minor adjustment of this indicator ratio by just 0.01 would omit the case of disturbance observed through the *arbutuslake* phenocam, necessitating the relatively high false detection error rate. As with the other indicator periods, several of the 32 non-disturbance site-years which were associated with leaf-on periods beyond 1 ± 0.1 times the average were observed at SPRUCE experimental sites. Disturbance cases observed by the *harvard* and *proctor* phenocams were not detected as anomalous rising, plateau, or leaf-on periods through our approach, amounting to the 14% false negative error rate across indicator periods. Twelve of fourteen cases were correctly detected amounting to an 86% true detection rate. Together the combined application of anomalous rising, plateau, or leaf-on periods as an indicator of probable disturbance or stress effects amounts to an 11% average probability of false positives, and an 89% probability of true classifications of non-damage.

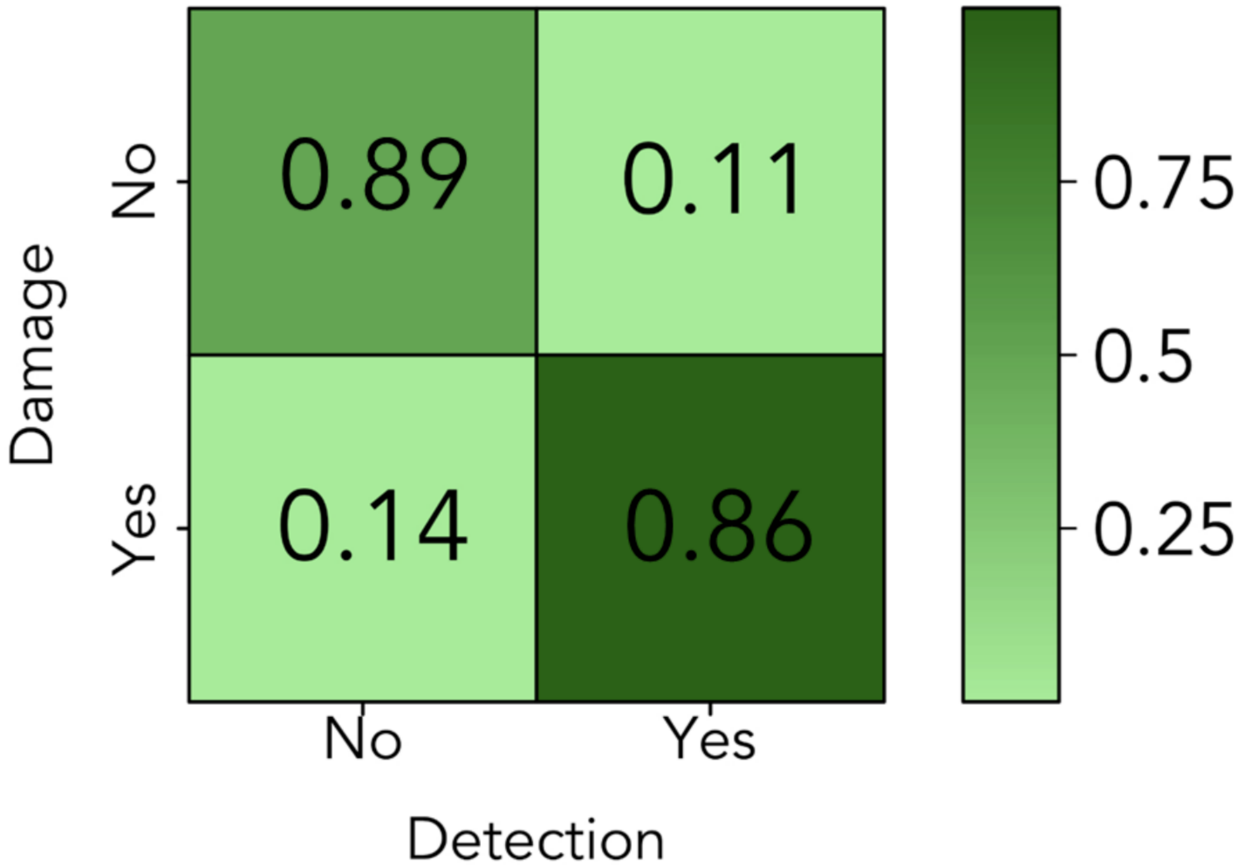

Figure 5-15. *Confusion matrix for the combined detection of anomalous rising, plateau, or leaf-on periods associated with leaf damage due to either disturbance or stress versus normal conditions. The x-axis labels correspond to the predicted classification or detection while the y-axis labels correspond to the true classification. True predictions are along the diagonal. The proportion of each classification is shown as a number and color in each matrix cell, with higher proportions corresponding to a darker green hue.*

5.5 Discussion

Here we provide a novel and comprehensive exploration of the potential of phenocams to capture declines in leaf function associated with various forms of disturbance and stress. With analysis of phenocam records, we detected disturbance and stress-driven declines which occurred in the early, middle, and late growing season for both deciduous and evergreen vegetation. The disturbance and stress agents we examined included hurricanes, windstorms, frost, herbivory, and drought. This highlights the applicability of phenocams for monitoring ecologically relevant phenomena beyond leaf phenology.

The approach of classifying disturbance-related impaired leaf function based upon vegetation indices timeseries has been previously applied with satellite-based observations and found to perform well following ground validation (Löw and Koukal, 2020; Bascietto et al., 2018). The application of phenocams we present here allows for the sensitive detection of leaf functional decline at a fine spatial scale, with the potential for developing species-specific insights (Berra et al., 2021; Hufkens et al., 2012a). Previous studies have shown leaf damage or defoliation resulting from disturbance or stress during the optimal growing season period can disrupt forest ecosystem processes (Stephens et al., 2018; Bonan and Shugart, 1989). As ecological integrity is determined by the cohesion of ecosystem processes, monitoring leaf function through phenocams provides valuable insights for the purposes of ecological integrity monitoring. The scale of observation afforded by phenocams is equivalent to that of manual ground-based observations, though with the potential for quantitative monitoring with enhanced perception beyond the capabilities of human eyesight. The imagery records produced by phenocams provide a means to precisely detect and review the evolution of disturbance or stress effects both through computational processing and from visual inspection of images. This allows for precise characterization of the timeline of such effects and an enhanced insight into probable cause. Additionally, phenocams enable the exploration of how fine scale ecological and microclimate contexts influence susceptibility to disturbance or stress (Field et al., 2020; Lukasová et al., 2020). A previous study employing more than 40 years of observations classified premature fall discoloration as when the date occurred within the lower 5% percentile of a normal distribution, which was 2-3 months earlier than typical (Bigler and Vitasse, 2021).

The methods we proposed here are capable of autonomously identifying such acute deviations, as well as some more moderate deviations which may be associated with stress or disturbance. Given the streamlined PhenoCam Network processing chain of image collection, storage, and processing, the detection of anomalous leaf developmental periods associated with potential disturbance or stress presented here could be delivered in real-time for conservation managers. The methods we propose here would similarly be promising for the recently established Acadian Phenocam Network in eastern Canada, which spans three provinces and five National Parks. Figure 5-16 provides a conceptual framework for the designation of our indicator periods.

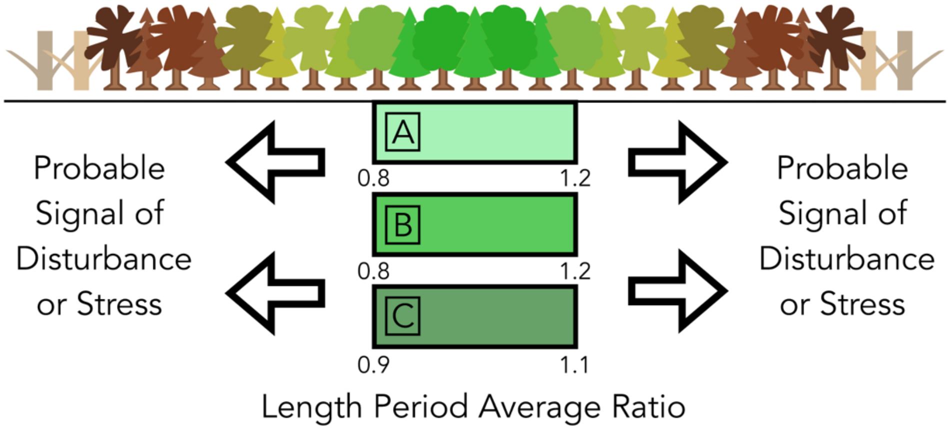

Figure 5-16. *Conceptual representation of the probabilistic relationship between leaf function and deviation in the length of the A, B, or C periods each year relative to the average of other years. Period A is the greenness rising portion of the curve between the onset of leaf growth and the seasonal peak in greenness calculated as the time between the 10% and 90% amplitude, period B is the greenness plateau following the seasonal peak in greenness calculated as the time between 95% and 50% amplitude in the falling portion of the greenness curve, and period C is the entire leaf-on period calculated as the time between 50% amplitude in the rising portion and 50% amplitude in the falling portion of the greenness curve. The numbers at the bottom edge of each row denote the threshold indicative of probable disturbance or stress effects rather than interannual variability. An A rising period of beyond 1 ± 0.2 time the average, a B plateau period of beyond 1 ± 0.2 times the average, and a C leaf-on period of beyond 1 ± 0.1 times the average corresponds to probable disturbance or stress.*

These metrics allow for the quantification of impacts in terms of the deviation in the duration of leaf developmental periods, though further investigation is needed to distinguish between fluctuations consistent with immediate defoliation versus prolonged declines in leaf function. While our duration metrics fluctuated more in response to disturbance or stress than due to inherent variation for some sites, caution is warranted in assigning indicator scores from these periods due to the relatively few phenocam timeseries available to monitor such effects. Additionally, recovery transitions may continue to occur more than a growing season following disturbance or stress, altering the utility of apparent reference growing seasons for our duration metrics. A strategic approach for classifying future observations would be to use our duration metrics as a means of assigning priority for further investigation. With each growing season, the reference average and interannual variability for these periods can be automatically refined as periods are iteratively re-calculated, or manually refined by conservation managers familiar with site characteristics. Additionally, some disturbances did not result in a deviation of leaf developmental periods outside that of the range from years without disturbance, such as for the phenocams *proctor* and *harvard*. These latter cases may be due to disturbance events having a mild influence on phenocam-derived greenness curves due to saturation in the greenness metric (Keenan et al., 2014; Yang et al., 2014), or else due to our length metrics not encompassing the portions of the curve that were most affected by these events. In some cases, such as for the *arbutuslake* phenocam, the detected deviation in indicator periods was mild, which may have been due in part to the monitored region of interest including a variety of species which were affected to different degrees by the frost event. Additionally, we also explored the use of original unsmoothed spring greenness timeseries for the *proctor* and *arbutuslake* phenocams and found this still did not result in pronounced anomalous periods for the 2010 frost year. This indicates that the additional research is needed to develop a more sensitive indicator for detection of frost damage. Further investigation is warranted to optimize the indicator potential of periods calculated from a greater variety of amplitude thresholds, especially for between the beginning of senescence and the onset of dormancy to better understand the impact of disturbance or stress to the senescence process. A promising avenue for future research is to examine change over time in leaf maturation and senescence rates, as this would allow for the detection of gradual changes in leaf phenological states over time. A stable representation of the integrated area under the growing season greenness curve may provide an alternative approach to detecting deleterious disturbance or stress effects. We conducted a preliminary analysis which yielded an anomalous integrated area for the 2010 spring frost growing season for the *proctor* phenocam, though variable areas for some of the other sites in the absence of disturbance or stress. Another promising avenue for future research is the development of a resiliency indicator through the quantification of leaf damage severity in terms of the rate of change in greenness following disturbance or stress, as well as the rate of subsequent recovery, which may contribute to ongoing works within the ecological community (Smith et al., 2022; Scheffer et al., 2009). In addition, the interaction between disturbance or stress effects and the status of vegetation prior to disturbance or stress could be investigated with the use of phenocam data. For example, disturbance in the form of severe insect defoliation is often a consequence of drought or other pre-existing stress factors, and there may be pre-emptive signals preceding such disturbance events which may provide actionable insights to conservation managers (Anderegg et al., 2015; McLennan and Zorn, 2005).

Using the length of time between different amplitude percentages of the greenness curve as ecological indicator metrics rather than the timing of a given phenophase extracted from the greenness curve is potentially advantageous in reducing the influence of uncertainty due to extraction approaches (Toomey et al., 2015). A previous phenocam study found that greenness amplitude thresholds were suitable proxies for various stages of leaf development (Zhang et al., 2020). Additionally, this approach provided a clear signal for the drought mortality onset observed through the *sequoia* phenocam which is focused on evergreen needleleaf vegetation, which typically has a lower seasonal amplitude and potentially greater uncertainty in curve derived phenology relative to deciduous broadleaf vegetation across both phenocam and satellite-based observation platforms (Ling et al., 2022; Seyednasrollah et al., 2021). However, this approach is also susceptible to reduction in the greenness curve amplitude due to disturbance influencing the time between amplitude percentages in unexpected ways, and potentially eclipsing disturbance or stress signals. Rigorous quality control in the form of omitting records with instability in target regions of interest and extensive observational gaps during the leaf-on period is necessary to avoid false attribution of anomalous periods to disturbance or stress effects. Another promising avenue for future research would be to examine the influence of site ecological memory on the stability of these indicator periods. One benefit of the approach of automated leaf phenology monitoring with phenocams is the option to re-process archived imagery data using new and improved techniques. In addition, the establishment of long-term monitoring programs with phenocams in a variety of environmental contexts for species can provide enhanced insight into typical ranges of periods between leaf phenology stages for a given species.

Toomey et al. (2015) and Matiu et al. (2017) both found correspondence between phenocam-derived greenness and gross primary production over time, indicating that greenness can be used as a dynamic ecosystem function indicator beyond the timing of leaf phenology. We also explored the timing of leaf phenology itself as an ecological integrity indicator, though found that variation due to other factors was of a similar magnitude or in some cases greater than variation due to disturbance or stress, and that this approach neglects the role of developed frost hardiness which may not vary consistently with phenology between species (see Zohner et al., 2020). Extreme weather like Hurricane Dorian (>10,000 ha of forest damage) which led to widespread forest damage on the order of >500 ha may affect Nova Scotia, the province in which 22 of the 33 Acadian Phenocam Network cameras are managed, as frequently as once every seven years (MacLean et al., 2022; Taylor et al., 2020). Insect outbreaks such as that of *Choristoneura fumiferana,* the spruce budworm, which lead to widespread damage of predominant native tree species, may also occur in Nova Scotia once every 30-40 years (Smith et al., 2010). Additionally, two of the Acadian Phenocam Network phenocams are focused on eastern hemlock (*Tsuga canadensis*) within the Kejimkujik National Park, amidst an ongoing invasion of the hemlock wooly adelgid (*Adelges tsugae*) which began in 2017 and has already led to hemlock mortality. The hemlock wooly adelgid is an invasive pest known to rapidly defoliate entire stands with wide-reaching ecological impacts, as the eastern hemlock is a foundational species providing specialized habitat for both terrestrial and aquatic species (Emilson and Statsny, 2019; Brantley et al., 2015). Therefore, monitoring protocols such as those we explored here are promising in allowing for the sensitive individual-scale detection of both gradual and abrupt decline in leaf function and ecological integrity due to global change throughout both the Acadian Phenocam Network and PhenoCam Network, and beyond. The insights gathered from monitoring of leaf developmental periods can also help to understand the changing frequencies of cases of leaf damage due to disturbance or stress in the context of global change, and the implications of these cumulative effects for ecosystem functioning and the carbon cycle (Curtis and Gough, 2018; Dubé, et al., 2013). While our investigation was focused on disturbance and stress, another important consideration is community level phenological synchrony in the context of global change. Further work is required to understand what level of change may jeopardize the continued synchrony of ecological interactions, and how to correctly attribute variation in phenology over time (Renner and Zohner, 2018).

This study provides a novel means to systematically quantify the severity of disturbance or stress effects on leaf function with ground-based imagery provided by phenocams, which is increasingly valuable in the context of ongoing global change. The duration of leaf developmental periods explored here can provide a framework for assessment of the vegetation functional component of ecological integrity, and insight towards characterization of ecological tipping points consistent with critical adverse effects on ecosystem ecology. The application of the duration of periods from phenocam-derived greenness patterns as an ecological integrity indicator may be more complex than other traditional indicators in that it requires a nuanced consideration of a variety of factors, such as signal quality, species, and environment. Despite this complexity, the use of phenocams for ecological integrity monitoring provides several distinct advantages including automation, cost-efficiency, fine-scale sensitivity, and quantitative monitoring, with the potential for reduced complexity as new monitoring insights are developed. Other traditional methods for the monitoring of disturbance or stress effects such as aerial or field surveys require considerable time and financial resources for conservation managers. Phenocams also provide potential for ancillary research objectives with image timeseries including the dynamics of ice, snow, flowering, and other ecologically important phenomena in the scene (Jacobs et al., 2009). Understanding which species are robust, resilient, or susceptible to global change through the monitoring protocol we proposed here will provide insight for effective conservation and management activities (Chamberlain et al., 2019). This would allow for informed decisions regarding ecological forestry practices in the context of global change, which species to plant for remediation following disturbance events, and which species may require additional focus for protection from disturbance agents (MacLean et al., 2022; Taylor et al., 2020; Price et al., 2013).

5.6 Conclusions

Leaf phenology serves as a direct and integrative indicator of the biological effects of climate change. Near-continuous observations from phenocams allow for the quantitative monitoring of seasonal leaf development. Ecological integrity, or the intactness of ecosystem processes, such as water and carbon cycling, is a crucial assessment tool for conservation efforts. Phenocams are a promising ecological integrity monitoring tool, as they can be efficiently applied and produce high resolution quantitative data of leaf function and potential disruptions due to disturbance or stress. Here we examined phenocam observations of vegetative responses to disturbance and stress with fourteen site-year examples from the PhenoCam Network, including disturbances in the form of hurricanes, windstorms, spring frost, insect defoliation, and a winter ice storm, as well as stress due to drought. Reductions or extensions of at least ±20% in the rising section in the seasonal greenness curve, ±20% in the plateau section following the greenness peak, and ±10% for the entire leaf-on period were indicative of a response to a major disturbance or stress. The duration of these periods each year in comparison to the average for other years with these thresholds resulted in average true detection rates of 86% and false positive detection rates of 11% when sampling from probability density functions of 344 broadleaf and needleleaf PhenoCam site-years. True negative detection rates were 89% on average, while average false negative detection rates were 14%. Together these rates indicate that the duration of the rising, plateau, and leaf-on periods serve as sensitive indicators of disturbance and stress, and that these periods may provide novel insights into species-specific recovery processes. Despite the complexity of phenocam-derived leaf developmental periods as ecological integrity indicators, their application is strategic in providing a wealth of information with cost-effective operation. Phenocams present a promising means to assess which forest ecosystems are robust, resilient, or susceptible to global change, which will facilitate informed conservation practices.

Chapter 6: Conclusions and Future Directions

Observations of vegetation function at the leaf to canopy scale will play a pivotal role in elucidating the feedback of terrestrial vegetation to climate change. The chapters of this thesis provide promising insights and technical developments to reduce uncertainty surrounding terrestrial vegetation feedbacks to climate change. The summarized findings from each chapter are as follows, and more detailed insights are presented below:

- Chapter 2 of this thesis indicates that climate sensitivity as well as the portion of anthropogenic carbon in the atmosphere taken up by the terrestrial biosphere predominate uncertainty in the relationship between cumulative anthropogenic CO_2 emissions and global temperature change.
- Chapter 3 of this thesis shows that leaf structure exerts an important influence on the optical properties of leaves, and with an adapted physical model inversion approach, the success of hyperspectral models for estimating the quantity of leaf biochemical constituents can be readily improved.
- Chapter 4 of this thesis reveals divergent leaf phenology responses between co-located species to future climate warming under a variety of emissions scenarios, and the importance of photoperiod and winter chilling in influencing the timing of leaf emergence.
- Chapter 5 provides a novel approach to detecting declines in leaf function and subsequently carbon uptake associated with extreme weather, which is expected to occur more frequently and with a greater intensity in the context of climate change.

Several promising avenues for future research stem from these chapters. In chapter 2, *Quantifying the probability distribution function of the transient climate response to cumulative CO_2 emissions (TCRE)*, I show that climate sensitivity along with the land-borne fraction of CO_2 emissions exert an important influence on the TCRE, and that the probability distribution function of the TCRE is best characterized as log-normal. While characterizing the probability distribution function of the TCRE and the key drivers of variation in the TCRE contributes to understandings of the TCRE, important questions remain regarding the TCRE. Non-CO_2 emissions may make up between one seventh to one third of carbon budgets, though are generally not included in the TCRE. Towards this end, recently Jenkins et al. (2021) has provided an adapted carbon budget arising form the TCRE including non-CO_2 radiative forcing. In addition, the validity of the TCRE in the context of declining or negative emissions is uncertain (Zickfeld et al., 2016). Future studies on the TCRE should strive to address these sources of uncertainty.

In Chapter 3, *Spectral subdomains and prior estimation of leaf structure improves PROSPECT inversion on reflectance or transmittance alone*, I demonstrate the importance of leaf structure in influencing the optical properties of leaves. Future work to better accommodate the physical differences between directional-hemispherical measurements required for current PROSPECT model inversion approaches and the commonly used bidirectional leaf reflectance measurements and transmittance estimations would be impactful. This would allow researchers to directly estimate leaf foliar constituents with just bidirectional leaf reflectance measurements and transmittance estimations. While this chapter provides modifications to traditional PROSPECT inversion approaches towards this end, and some advancements have been made in this area (Li et al., 2019a; 2018; Jay et al., 2016), more work is needed to precisely and physically link bidirectional and directional-hemispherical observations for convenient estimations of leaf biochemistry.

For Chapter 4, *Climate-driven shifts in leaf senescence are greater for boreal species than temperate species in the Acadian Forest Region*, I demonstrate the likelihood for divergent leaf phenology responses to climate change between co-located species in the Acadian Forest. This chapter also shows the utility of networked phenocams for calibrating and validating process models. Future work is needed to apply phenocam-trained species-specific leaf phenology models over greater spatial scales and with a greater variety of species. In addition, the improvement or development of novel leaf senescence process models would be advantageous in reducing uncertainty involving future leaf phenology patterns and the length of the leafing period in the context of climate change. An understudied driver of variation in leaf phenology timings is that of soil moisture (Delpierre et al., 2017), and future studies on this topic should strive to include a representation of the constraint of water availability on leaf phenology to develop more comprehensive understandings of future patterns in leaf phenology. Another promising avenue for future work from this chapter would be how to integrate predictions of changes in leaf phenology patterns into strategies of both climate change and mitigation, such as the strategic selection of tree species to plant in the coming decades.

For Chapter 5, *Leaf phenology as an indicator of ecological integrity*, I provide a novel indicator approach based upon regions of seasonal greenness curves extracted from phenocam observations to detect incidents of interruptions in ecosystem processes. While this chapter includes 14 cases of disturbance or stress which affected leaf function, more work is needed to examine how well this indicator performs for a more replicated sampling of disturbance and stress cases in a greater variety of forest canopies. Additionally, future work on this topic should include a means to quantify the speed of recovery following such disturbances or stressful events, and the role of ecological site memory (Gong et al., 2021). To assess the far-reaching ecological implications of changes in leaf phenology in response to both gradual and abrupt environmental changes, another promising avenue for future work is the examination of phenological synchrony between interacting species (Pureswaran et al., 2019; Renner et al., 2018). Towards this end, phenocams can help to rapidly scale-up ongoing monitoring projects to better attribute and quantify leaf phenology changes associated with climate change.

Overall I have shown that terrestrial vegetation has the potential to alter the trajectory of climate change, and in turn be dynamically influenced by climate change over seasonal to centennial timescales. To understand the course of these changes, more observations of leaf function in terms of both biochemistry and leaf phenology are needed. If the portion of excess CO_2 emissions taken up by terrestrial vegetation were to be substantially reduced, climate change could be much more severe than previously thought. My thesis incorporates two dimensions of complexity related to future vegetational carbon uptake: climate change will likely lengthen the seasonal carbon uptake period for temperate and boreal tree species, though will also lead to more disruptions in vegetational carbon uptake due to disturbances such as hurricanes and frost events. With the use of hyperspectral measurements, high temporal frequency observations such as through phenocams, and powerful physical models such as PROSPECT and the leaf phenology models I presented herein, we can monitor and developed informed predictions of vegetation function in the context of climate change.

Another direction for future investigation linking all of the chapters in this thesis is that of the carbon implications of leaf phenology changes with respect to leaf emergence, leaf senescence, and the overall seasonal lifespan of leaves. Modelling and observational studies in mid-to high-latitude forests, as well as chapters 4 and 5 of this thesis, have postulated that earlier leaf emergence and later leaf senescence in the context of warmer growing conditions will increase long term carbon uptake in forests, substantially reducing the severity of climate change (Gu et al., 2022; Wang et al., 2020; Sakalli et al., 2017; Keenan et al., 2014; Wu et al., 2012). Few studies have directly validated the assumption of a linkage between leaf phenology and stable carbon sequestration via wood formation despite its importance for climate change mitigation. Contrary to common assumptions, wood growth may be limited despite lengthening leafing periods due to environmental and physiological constraints (Zani et al., 2020; D'Orangeville et al., 2018; Way and Montgomery, 2015). Several studies have reported a decoupling or variable relationship between leaf phenology and wood formation across a variety of species and regions (Camarero et al., 2022; Dow et al., 2022; Etzold et al., 2022; Marchand et al., 2021; Delpierre et al., 2017; Čufar et al., 2015), though few studies include direct monitoring of leaf emergence and senescence along with wood formation. More in-situ studies of both leaf and wood formation phenology at a variety of sites are needed to evaluate the potential independence between the leaf-on period and woody growth. An investigation on this topic will likely be the subject of my upcoming postdoctoral work.

One of the most useful tools for projecting climate change, the future capacity for vegetation to uptake carbon, and how climate change might affect vegetation, is that of Earth System Models (ESMs). Earth System Models simulate the exchange of energy and matter through coupled land, ocean, and atmospheric components. The land components of ESMs are known as land surface models, and vegetation is therein simulated through the use of Dynamic Vegetation Models (DGVMs). Many important global climate change feedback phenomena have been realized because of ESMs, as well as impactful metrics such as the TCRE. The utility of

DGVMs and subsequently ESMs could be further enhanced with more realistic process representations therein of terrestrial biogeochemistry, especially with respect to terrestrial carbon, nitrogen, and phosphorus cycles, as well as how plants function over time (Arora et al., 2020; Lovenduski and Bonan, 2017). Within DGVMs, leaf phenology is often prescribed or prognostically simulated based on just temperature (Ziehn et al., 2020; Lawrence et al., 2019; Green et al., 2019; Anav et al., 2015). Chapter 4 demonstrates that the inclusion of additional drivers for leaf emergence and senescence, such as photoperiod, could improve the realism of dynamic global vegetation models and predictions of vegetation growing season length. In addition, model structures within DGVMs often assume all plants belong to a limited number of plant functional types, underrepresenting the functional diversity of plants observed in nature, though more functional diversity is being added over time to DGVMs (Harper et al., 2018; 2016; Funk et al., 2017). Future work to include more detailed and dynamic representations of leaf phenology, along with plant functional diversity, could improve the aptitude of ESMs and provide more impactful insights for climate change policy.

Bibliography

Aasen, H., Kirchgessner, N., Walter, A., & Liebisch, F. (2020). PhenoCams for field phenotyping: using very high temporal resolution digital repeated photography to investigate interactions of growth, phenology, and harvest traits. *Frontiers in Plant Science*, 11, 593.

Achard, F., Beuchle, R., Mayaux, P., Stibig, H. J., Bodart, C., Brink, A., & Simonetti, D. (2014). Determination of tropical deforestation rates and related carbon losses from 1990 to 2010. *Global Change Biology*, 20(8), 2540-2554.

Ahillen, S. (2017, May 9). Mountain wave sparked Gatlinburg wildfires, May 4 destruction. *Knox News*. Retrieved June 6, 2022, from https://www.knoxnews.com/story/news/local/tennessee/gatlinburg/2017/05/09/mountain-wave-sparked-gatlinburg-fires-may-4-destruction/312821001/.

Ahrends, H. E., Brügger, R., Stöckli, R., Schenk, J., Michna, P., Jeanneret, F., Wanner, H., & Eugster, W. (2008). Quantitative phenological observations of a mixed beech forest in northern Switzerland with digital photography. *Journal of Geophysical Research: Biogeosciences*, 113(G4).

Ahrends, H. E., Etzold, S., Kutsch, W. L., Stöckli, R., Brügger, R., Jeanneret, F., Wanner, H., Buchmann, N., & Eugster, W. (2009). Tree phenology and carbon dioxide fluxes: use of digital photography for process-based interpretation at the ecosystem scale. *Climate Research*, 39(3), 261-274.

Ainsworth, E. A., & Long, S. P. (2005). What have we learned from 15 years of free-air CO_2 enrichment (FACE)? A meta-analytic review of the responses of photosynthesis, canopy properties and plant production to rising CO_2. *New phytologist*, 165(2), 351-372.

Alberton, B., Torres, R. D. S., Cancian, L. F., Borges, B. D., Almeida, J., Mariano, G. C., dos Santos, J., & Morellato, L. P. C. (2017). Introducing digital cameras to monitor plant phenology in the tropics: applications for conservation. *Perspectives in Ecology and Conservation*, 15(2), 82-90.

Ali, A.M., Darvishzadeh, R., Skidmore, A.K., van Duren, I., Heiden, U., Heurich, M. (2016). Estimating leaf functional traits by inversion of PROSPECT: assessing leaf dry matter content and specific leaf area in mixed mountainous forest. *International Journal of*

Applied Earth Observation and Geoinformation, 45, 66–76. https://doi.org/10.1016/j.jag.2015.11.004.

Allen, C. D., Macalady, A. K., Chenchouni, H., Bachelet, D., McDowell, N., Vennetier, M., Kitzberger, T., Rigling, A., Breshears, D. D., Hogg, E. T., Gonzalez, P. (2010). A global overview of drought and heat-induced tree mortality reveals emerging climate change risks for forests. *Forest Ecology and Management*, 259(4), 660–684.

Allen, M. R., Frame, D. J., Huntingford, C., Jones, C. D., Lowe, J. A., Meinshausen, M., & Meinshausen, N. (2009). Warming caused by cumulative carbon emissions towards the trillionth tonne. *Nature*, 458(7242), 1163-1166.

Allen, W.A., Gausman, H.W., Richardson, A.J. (1970). Mean effective optical constants of cotton leaves. *Journal of the Optical Society of America*, 60, 542–547. https://doi.org/10.1364/JOSA.60.000542.

Allen, W.A., Gausman, H.W., Richardson, A.J., Thomas, J.R. (1969). Interaction of isotropic light with a compact plant leaf. *Journal of the Optical Society of America*, 59, 1376–1379. https://doi.org/10.1364/JOSA.59.001376.

Allstadt, A. J., Vavrus, S. J., Heglund, P. J., Pidgeon, A. M., Thogmartin, W. E., & Radeloff, V. C. (2015). Spring plant phenology and false springs in the conterminous US during the 21st century. *Environmental Research Letters*, 10(10), 104008.

Ameztegui, A., Paquette, A., Shipley, B., Heym, M., Messier, C., & Gravel, D. (2017). Shade tolerance and the functional trait: demography relationship in temperate and boreal forests. *Functional Ecology*, 31(4), 821-830.

Amthor, J. S. (2000). The McCree–de Wit–Penning de Vries–Thornley respiration paradigms: 30 years later. *Annals of Botany*, 86(1), 1-20.

Anav, A., Friedlingstein, P., Beer, C., Ciais, P., Harper, A., Jones, C., & Zhao, M. (2015). Spatiotemporal patterns of terrestrial gross primary production: A review. *Reviews of Geophysics*, 53(3), 785-818.

Anav, A., Friedlingstein, P., Kidston, M., Bopp, L., Ciais, P., Cox, P., Jones, C., Jung, M., Myneni, R., & Zhu, Z. (2013). Evaluating the land and ocean components of the global carbon cycle in the CMIP5 earth system models. *Journal of Climate*, 26(18), 6801-6843.

Anderegg, W. R., Hicke, J. A., Fisher, R. A., Allen, C. D., Aukema, J., Bentz, B., Hood, S., Lichstein, J.W., Macalady, A.K., McDowell, N., Pan, Y., & Zeppel, M. (2015). Tree mortality from drought, insects, and their interactions in a changing climate. *New Phytologist*, 208(3), 674-683.

Anderson, T. R., Hawkins, E., & Jones, P. D. (2016). CO_2, the greenhouse effect and global warming: from the pioneering work of Arrhenius and Callendar to today's Earth System Models. *Endeavour*, 40(3), 178-187.

Andrews, T., Gregory, J. M., Webb, M. J., & Taylor, K. E. (2012). Forcing, feedbacks and climate sensitivity in CMIP5 coupled atmosphere-ocean climate models. *Geophysical Research Letters*, 39(9).

Angulo-Sandoval, P., Fernández-Marín, H., Zimmerman, J. K., & Alde, T. M. (2004). Changes in patterns of understory leaf phenology and herbivory following hurricane damage. *Biotropica*, 36(1), 60-67.

Aono, Y., & Kazui, K. (2008). Phenological data series of cherry tree flowering in Kyoto, Japan, and its application to reconstruction of springtime temperatures since the 9th century. *International Journal of Climatology: A Journal of the Royal Meteorological Society*, 28(7), 905-914.

Arellano, P., Tansey, K., Balzter, H., Boyd, D. S. (2015). Detecting the effects of hydrocarbon pollution in the Amazon forest using hyperspectral satellite images. *Environmental Pollution*, 205, 225–239.

Arellano, P., Tansey, K., Balzter, H., Boyd, D. S. (2017). Field spectroscopy and radiative transfer modelling to assess impacts of petroleum pollution on biophysical and biochemical parameters of the Amazon rainforest. *Environmental Earth Sciences*, 76, 217.

Arora, V. K. (2003). Simulating energy and carbon fluxes over winter wheat using coupled land surface and terrestrial ecosystem models. *Agricultural and Forest Meteorology*, 118(1-2), 21-47.

Arora, V. K., & Boer, G. J. (2005). A parameterization of leaf phenology for the terrestrial ecosystem component of climate models. *Global Change Biology*, 11(1), 39-59.

Arora, V. K., & Boer, G. J. (2005). A parameterization of leaf phenology for the terrestrial ecosystem component of climate models. *Global Change Biology*, 11(1), 39-59.

Arora, V. K., & Boer, G. J. (2010). Uncertainties in the 20th century carbon budget associated with land use change. *Global Change Biology*, 16(12), 3327-3348.

Arora, V. K., & Boer, G. J. (2014). Terrestrial ecosystems response to future changes in climate and atmospheric CO_2 concentration. *Biogeosciences*, 11(15), 4157-4171.

Arora, V. K., Boer, G. J., Friedlingstein, P., Eby, M., Jones, C. D., Christian, J. R., ... & Wu, T. (2013). Carbon–concentration and carbon–climate feedbacks in CMIP5 Earth system models. *Journal of Climate*, 26(15), 5289-5314.

Arora, V. K., Katavouta, A., Williams, R. G., Jones, C. D., Brovkin, V., Friedlingstein, P., ... & Ziehn, T. (2020). Carbon–concentration and carbon–climate feedbacks in CMIP6 models and their comparison to CMIP5 models. *Biogeosciences*, 17(16), 4173-4222.

Arora, V. K., Katavouta, A., Williams, R. G., Jones, C. D., Brovkin, V., Friedlingstein, P., & Ziehn, T. (2020). Carbon–concentration and carbon–climate feedbacks in CMIP6 models and their comparison to CMIP5 models. *Biogeosciences*, 17(16), 4173-4222.

Arora, V.K., Boer, G.J., Friedlingstein, P., Eby, M., Jones, C.D., Christian, J.R., Bonan, G., Bopp, L., Brovkin, V., Cadule, P., & Hajima, T. (2013). Carbon–concentration and carbon–climate feedbacks in CMIP5 Earth system models. *Journal of Climate*, 26(15), 5289-5314.

Asner, G. P., Martin, R. E., Anderson, C. B., Knapp, D. E. (2015). Quantifying forest canopy traits: Imaging spectroscopy versus field survey. *Remote Sensing of Environment*, 158, 15–27.

Asner, G. P., Martin, R. E., Carranza-Jiménez, L., Sinca, F., Tupayachi, R., &erson, C. B., Martinez, P. (2014). Functional and biological diversity of foliar spectra in tree canopies throughout the Andes to Amazon region. *New Phytologist*, 204, 127–139. https://doi.org/10.1111/nph.12895.

Asner, G. P., Martin, R. E., Knapp, D. E., Tupayachi, R., &erson, C., Carranza, L., Martinez, P., Houcheime, M., Sinca, F., Weiss, P. (2011). Spectroscopy of canopy chemicals in humid tropical forests. *Remote Sensing of Environment*, 115, 3587–3598.

Augspurger, C. K. (2009). Spring 2007 warmth and frost: phenology, damage and refoliation in a temperate deciduous forest. *Functional Ecology*, 23(6), 1031-1039.

Augspurger, C. K. (2013). Reconstructing patterns of temperature, phenology, and frost damage over 124 years: spring damage risk is increasing. *Ecology*, 94(1), 41-50.

Avitabile, V., Herold, M., Heuvelink, G. B., Lewis, S. L., Phillips, O. L., Asner, G. P., & Willcock, S. (2016). An integrated pan-tropical biomass map using multiple reference datasets. *Global Change Biology*, 22(4), 1406-1420.

Baccini, A. G. S. J., Goetz, S. J., Walker, W. S., Laporte, N. T., Sun, M., Sulla-Menashe, D., ... & Houghton, R. (2012). Estimated carbon dioxide emissions from tropical deforestation improved by carbon-density maps. *Nature Climate Change*, 2(3), 182-185.

Baldwin, K. A., Chapman, K., Meidinger, D., Uhlig, P., Allen, L., Basquill, S., Faber-Langendoen, D., Flynn, N., Kennedy, C., Mackenzie, W., & Saucier, J. P. (2019). *The Canadian national vegetation classification: principles, methods and status*. Information Report GLC-X-23. Natural Resources Canada, Canadian Forest Service, Great Lakes Forestry Centre.

Bardgett, R. D., Manning, P., Morriën, E., De Vries, F. T. (2013). Hierarchical responses of plant–soil interactions to climate change: consequences for the global carbon cycle, *Journal of Ecology*, 101, 334–343.

Baret, F., Hagolle, O., Geiger, B., Bicheron, P., Miras, B., Huc, M., ... & Leroy, M. (2007). LAI, fAPAR and fCover CYCLOPES global products derived from VEGETATION: Part 1: Principles of the algorithm. *Remote Sensing of Environment*, 110(3), 275-286.

Bascietto, M., Bajocco, S., Mazzenga, F., & Matteucci, G. (2018). Assessing spring frost effects on beech forests in Central Apennines from remotely-sensed data. *Agricultural and Forest Meteorology*, 248, 240-250.

Basler, D. (2016). Evaluating phenological models for the prediction of leaf-out dates in six temperate tree species across central Europe. *Agricultural and Forest Meteorology*, 217, 10-21.

Batjes, N. H. (2016). Harmonized soil property values for broad-scale modelling (WISE30sec) with estimates of global soil carbon stocks. *Geoderma*, 269, 61-68.

Battie-Laclau, P., Laclau, J. P., Beri, C., Mietton, L., Muniz, M. R. A., Arenque, B. C., de Cassia Piccolo, M., Jordan-Meille, L., Bouillet, J.P., Nouvellon, Y. (2014). Photosynthetic and anatomical responses of Eucalyptus grandis leaves to potassium and sodium supply in a field experiment. *Plant, Cell and Environment*, 37, 70-81.

Baumgarten, F., Zohner, C. M., Gessler, A., & Vitasse, Y. (2021). Chilled to be forced: the best dose to wake up buds from winter dormancy. *New Phytologist*, 230(4), 1366-1377.

Bäurle, I., Laplaze, L., & Martin, A. (2023). Preparing for an uncertain future: molecular responses of plants facing climate change. *Journal of Experimental Botany*. In press, ff10.1093/jxb/erac493/6902002ff. ffhal-03934837.

Beaubien, E. G., & Hall-Beyer, M. (2003). Plant phenology in western Canada: trends and links to the view from space. *Environmental Monitoring and Assessment*, 88(1), 419-429.

Beer, C., Reichstein, M., Tomelleri, E., Ciais, P., Jung, M., Carvalhais, N., & Papale, D. (2010). Terrestrial gross carbon dioxide uptake: global distribution and covariation with climate. *Science*, 329(5993), 834-838.

Behmann, J., Mahlein, A.-K., Paulus, S., Dupuis, J., Kuhlmann, H., Oerke, E.-C., Plümer, L. (2016). Generation and application of hyperspectral 3D plant models: methods and challenges. *Machine Vision and Applications*, 27, 611–624.

Beil, I., Kreyling, J., Meyer, C., Lemcke, N., & Malyshev, A. V. (2021). Late to bed, late to rise—warmer autumn temperatures delay spring phenology by delaying dormancy. *Global Change Biology*, 27(22), 5806-5817.

Berger, K., Wang, Z., Danner, M., Wocher, M., Mauser, W., Hank, T. (2018). Simulation of Spaceborne Hyperspectral Remote Sensing to Assist Crop Nitrogen Content Monitoring in Agricultural Crops. *In IGARSS 2018-2018 IEEE International Geoscience and Remote Sensing Symposium*, 3801-3804.

Berni, J. A., Zarco-Tejada, P. J., Suárez, L., Fereres, E. (2009). Thermal and narrowband multispectral remote sensing for vegetation monitoring from an unmanned aerial vehicle. *IEEE Transactions on Geoscience and Remote Sensing*, 47(3), 722-738.

Berra, E. F., & Gaulton, R. (2021). Remote sensing of temperate and boreal forest phenology: A review of progress, challenges and opportunities in the intercomparison of in-situ and satellite phenological metrics. *Forest Ecology and Management*, 480, 118663.

Berra, E. F., Gaulton, R., & Barr, S. (2016). Use of a digital camera onboard a UAV to monitor spring phenology at individual tree level. In *2016 IEEE International Geoscience and Remote Sensing Symposium,* (pp. 3496-3499). IEEE.

Bigler, C., & Vitasse, Y. (2021). Premature leaf discoloration of European deciduous trees is caused by drought and heat in late spring and cold spells in early fall. *Agricultural and Forest Meteorology*, 307, 108492.

Blackard, J. A., Finco, M. V., Helmer, E. H., Holden, G. R., Hoppus, M. L., Jacobs, D. M., & Tymcio, R. P. (2008). Mapping US forest biomass using nationwide forest inventory data and moderate resolution information. *Remote Sensing of Environment*, 112(4), 1658-1677.

Blümel, K., & Chmielewski, F. M. (2012). Shortcomings of classical phenological forcing models and a way to overcome them. *Agricultural and Forest Meteorology*, 164, 10-19.

Bokhorst, S. F., Bjerke, J. W., Tømmervik, H., Callaghan, T. V., & Phoenix, G. K. (2009). Winter warming events damage sub-Arctic vegetation: consistent evidence from an experimental manipulation and a natural event. *Journal of Ecology*, 97(6), 1408-1415.

Bonan, G. B., & Shugart, H. H. (1989). Environmental factors and ecological processes in boreal forests. *Annual Review of Ecology and Systematics*, 1-28.

Bonan, G. B., Levis, S., Sitch, S., Vertenstein, M., & Oleson, K. W. (2003). A dynamic global vegetation model for use with climate models: concepts and description of simulated vegetation dynamics. *Global Change Biology*, 9(11), 1543-1566.

Bonan, G. B., Lombardozzi, D. L., Wieder, W. R., Oleson, K. W., Lawrence, D. M., Hoffman, F. M., & Collier, N. (2019). Model structure and climate data uncertainty in historical simulations of the terrestrial carbon cycle (1850–2014). *Global Biogeochemical Cycles*, 33(10), 1310-1326.

Bond-Lamberty, B., Bailey, V. L., Chen, M., Gough, C. M., & Vargas, R. (2018). Globally rising soil heterotrophic respiration over recent decades. *Nature*, 560(7716), 80-83.

Boren, E. J., Boschetti, L., & Johnson, D. M. (2019). Characterizing the Variability of the Structure Parameter in the PROSPECT Leaf Optical Properties Model. *Remote Sensing*, 11(10), 1236.

Boucher, O., Servonnat, J., Albright, A. L., Aumont, O., Balkanski, Y., Bastrikov, V., ... & Vuichard, N. (2020). Presentation and evaluation of the IPSL-CM6A-LR climate model. *Journal of Advances in Modeling Earth Systems*, 12(7), e2019MS002010.

Bousquet, L., Lachérade, S., Jacquemoud, S., Moya, I. (2005). Leaf BRDF measurements and model for specular and diffuse components differentiation. *Remote Sensing of Environment*, 98, 201–211.

Bowyer, P. and Danson, F. (2004). Sensitivity of spectral reflectance to variation in live fuel moisture content at leaf and canopy level. *Remote Sensing of Environment*, 92, 297–308, https://doi.org/10.1016/j.rse.2004.05.020.

Brantley, S. T., Miniat, C. F., Elliott, K. J., Laseter, S. H., & Vose, J. M. (2015). Changes to southern Appalachian water yield and stormflow after loss of a foundation species. *Ecohydrology*, 8(3), 518-528.

Breece H.T. Holmes R.A. (1971. Bidirectional scattering characteristics of healthy green soybeans and corn leaves in vivo. *Applied Optics*, 10(1), 119-127.

Breshears, D. D., Adams, H. D., Eamus, D., McDowell, N., Law, D. J., Will, R. E., Williams, A. P., Zou, C. B. (2013). The critical amplifying role of increasing atmospheric moisture demand on tree mortality and associated regional die-off. *Frontiers in Plant Science*, 4, 266.

Bronson, D. R., & Gower, S. T. (2010). Ecosystem warming does not affect photosynthesis or aboveground autotrophic respiration for boreal black spruce. *Tree Physiology*, 30(4), 441-449.

Brown, L. A., Ogutu, B. O., Dash, J. (2019). Estimating Forest Leaf Area Index and Canopy Chlorophyll Content with Sentinel-2: An Evaluation of Two Hybrid Retrieval Algorithms. *Remote Sensing*, 11(15), 1752.

Brown, T. B., Hultine, K. R., Steltzer, H., Denny, E. G., Denslow, M. W., Granados, J., Henderson, S., Moore, S., Nagai, S., SanCelments, M., Sánchez-Azofeifa, A., Sonnentag, O., Tazik, D., & Richardson, A. D. (2016). Using phenocams to monitor our changing Earth: toward a global phenocam network. *Frontiers in Ecology and the Environment*, 14(2), 84-93.

Browning, D. M., Karl, J. W., Morin, D., Richardson, A. D., & Tweedie, C. E. (2017). Phenocams bridge the gap between field and satellite observations in an arid grassland ecosystem. *Remote Sensing*, 9(10), 1071.

Browning, D. M., Snyder, K. A., & Herrick, J. E. (2019). Plant phenology: taking the pulse of rangelands. *Rangelands*, 41(3), 129-134.

Buddenbaum, H., Stern, O., Stellmes, M., Stoffels, J., Pueschel, P., Hill, J., Werner, W. (2012). Field imaging spectroscopy of beech seedlings under dryness stress. *Remote Sensing*, 4, 3721–3740.

Buitenwerf, R., Rose, L., & Higgins, S. I. (2015). Three decades of multi-dimensional change in global leaf phenology. *Nature Climate Change*, 5(4), 364.

Buraczyk, W., Tulik, M., Konecka, A., Szeligowski, H., Czacharowski, M., & Będkowski, M. (2022). Does leaf mass per area (LMA) discriminate natural pine populations of different origins?. *European Journal of Forest Research*, 141(6), 1177-1187.

Caffarra, A., Donnelly, A., & Chuine, I. (2011). Modelling the timing of Betula pubescens budburst. II. Integrating complex effects of photoperiod into process-based models. *Climate Research*, 46(2), 159-170.

Camarero, J. J., Campelo, F., Colangelo, M., Valeriano, C., Knorre, A., Solé, G., & Rubio-Cuadrado, Á. (2022). Decoupled leaf-wood phenology in two pine species from contrasting climates: Longer growing seasons do not mean more radial growth. *Agricultural and Forest Meteorology*, 327, 109223.

Cannell, M. G. R., & Smith, R. I. (1983). Thermal time, chill days and prediction of budburst in Picea sitchensis. *Journal of Applied Ecology*, 951-963.

Cannon, A.J., Sobie, S.R., & Murdock, T. (2015). Bias Correction of GCM Precipitation by Quantile Mapping: How Well Do Methods Preserve Changes in Quantiles and Extremes? *Journal of Climate*, 28, 6938-6959.

Cao, Z., Wang, Q., & Zheng, C. (2015). Best hyperspectral indices for tracing leaf water status as determined from leaf dehydration experiments. *Ecological Indicators*, 54, 96-107.

Caparros-Santiago, J. A., Rodriguez-Galiano, V., & Dash, J. (2021). Land surface phenology as indicator of global terrestrial ecosystem dynamics: A systematic review. *ISPRS Journal of Photogrammetry and Remote Sensing*, 171, 330-347.

Carvalhais, N., Forkel, M., Khomik, M., Bellarby, J., Jung, M., Migliavacca, M., Mu, M., Saatchi, S., Santoro, M., Thurner, M., Weber, U., Ahrens, B., Beer, C., Cescatti, A., Randerson, J. T., and Reichstein, M. (2014). Global covariation of carbon turnover times with climate in terrestrial ecosystems. *Nature*, *514*(7521), 213-217.

Casson, N. J., Contosta, A. R., Burakowski, E. A., Campbell, J. L., Crandall, M. S., Creed, I. F., Eimers, M.C., Garlick, S., Lutz, D.A., Morison, M.Q., Morzillo, A.T., & Nelson, S. J. (2019). Winter weather whiplash: impacts of meteorological events misaligned with natural and human systems in seasonally snow-covered regions. *Earth's Future*, 7(12), 1434-1450.

Cavers, S., & Cottrell, J. E. (2015). The basis of resilience in forest tree species and its use in adaptive forest management in Britain. *Forestry: An International Journal of Forest Research*, 88(1), 13-26.

Čehulić, I., Sever, K., Katičić Bogdan, I., Jazbec, A., Škvorc, Ž., & Bogdan, S. (2019). Drought impact on leaf phenology and spring frost susceptibility in a Quercus robur L. provenance trial. *Forests*, 10(1), 50.

Chamberlain, C. J., Cook, B. I., García de Cortázar-Atauri, I., & Wolkovich, E. M. (2019). Rethinking false spring risk. *Global Change Biology*, 25(7), 2209-2220.

Charlet de Sauvage, J., Vitasse, Y., Meier, M., Delzon, S., & Bigler, C. (2022). Temperature rather than individual growing period length determines radial growth of sessile oak in the Pyrenees. *Agricultural and Forest Meteorology*, 317, 108885.

Chavana-Bryant, C., Malhi, Y., Wu, J., Asner, G. P., Anastasiou, A., Enquist, B. J., Caravasi, E. G. C., Doughty, C. E., Saleska, S. R., Martin, R. E., Gerard, F. F. (2017). Leaf aging of Amazonian canopy trees as revealed by spectral and physiochemical measurements. *New Phytologist*, 214, 1049–1063. https://doi.org/10.1111/nph.13853.

Chen, L., Huang, J. G., Ma, Q., Hänninen, H., Tremblay, F., & Bergeron, Y. (2019). Long-term changes in the impacts of global warming on leaf phenology of four temperate tree species. *Global change biology*, 25(3), 997-1004.

Chen, X. (2013). East Asia. *In: Phenology: an integrative environmental science*. pp 9-22. Springer, Dordrecht.

Cheng, T., Rivard, B., Sánchez-Azofeifa, A. G., Féret, J.-B., Jacquemoud, S., Ustin, S. L. (2014). Deriving leaf mass per area (LMA) from foliar reflectance across a variety of plant species using continuous wavelet analysis. *ISPRS Journal of Photogrammetry and Remote Sensing*, 87, 28–38.

Cherubini, F., Gasser, T., Bright, R. M., Ciais, P., & Strømman, A. H. (2014). Linearity between temperature peak and bioenergy CO_2 emission rates. *Nature Climate Change*, 4(11), 983-987.

Chmielewski, F. M., & Rötzer, T. (2002). Annual and spatial variability of the beginning of growing season in Europe in relation to air temperature changes. *Climate Research*, 19(3), 257-264.

Chu, C. (1921). New monthly calendar. *Bulletin of the Chinese Meteorological Society*, 6, 1-14.

Chu, H., Baldocchi, D. D., John, R., Wolf, S., and Reichstein, M. (2017). Fluxes all of the time? A primer on the temporal representativeness of Fluxnet. *Journal of Geophysical Research: Biogeosciences*, *122*(2), 289-307.

Chuine, I., & Régnière, J. (2017). Process-based models of phenology for plants and animals. *Annual Review of Ecology, Evolution, and Systematics*, 48, 159-182.

Chuine, I., Cambon, G., & Comtois, P. (2000). Scaling phenology from the local to the regional level: advances from species-specific phenological models. *Global Change Biology*, *6*(8), 943-952.

Chuine, I., Yiou, P., Viovy, N., Seguin, B., Daux, V., & Ladurie, E. L. R. (2004). Grape ripening as a past climate indicator. *Nature*, 432(7015), 289-290.

Ciais, P., Reichstein, M., Viovy, N., Granier, A., Ogée, J., Allard, V., Aubinet, M., Buchmann, N., Bernhofer, C., Carrara, A., Chevallier, F. (2005). Europe-wide reduction in primary productivity caused by the heat and drought in 2003. *Nature*, 437, 529.

Ciais, P., Sabine, C., Bala, G., Bopp, L., Brovkin, V., Canadell, J., Chhabra, A., DeFries, R., Galloway, J., Heimann, M., Jones, C., Le Quéré, C., Myneni, R. B., Piao, S., and Thornton, P. (2013). Carbon and Other Biogeochemical Cycles. In T. F Stocker, D Qin, G.-K. Plattner, M Tignor, S. K Allen, J Boschung, et al. (Eds.), *Climate Change 2013: The Physical Science Basis. Contribution of Working Group I to the Fifth Assessment Report of the Intergovernmental Panel on Climate Change*. Cambridge, UK and New York: Cambridge University Press.

Ciais, P., Tan, J., Wang, X., Roedenbeck, C., Chevallier, F., Piao, S.-L., Moriarty, R., Broquet, G., Le Quéré, C., Canadell, J. G., Peng, S., Poulter, B., Liu, Z., and Tans, P. (2019). Five decades of northern land carbon uptake revealed by the interhemispheric CO_2 gradient. *Nature*, 568(7751), 221– 225.

Clark, D. B., Mercado, L. M., Sitch, S., Jones, C. D., Gedney, N., Best, M. J., Pryor, M., Rooney, G. G., Essery, R. L. H., Blyth, E., Boucher, O., Harding, R. J., Huntingford, C., and Cox, P. M. (2011). The Joint UK Land Environment Simulator (JULES), model description– Part 2: carbon fluxes and vegetation dynamics. *Geoscientific Model Development*, *4*(3), 701-722.

Cleland, E. E., Allen, J. M., Crimmins, T. M., Dunne, J. A., Pau, S., Travers, S. E., Zavaleta, E.S., & Wolkovich, E. M. (2012). Phenological tracking enables positive species responses to climate change. *Ecology*, 93(8), 1765-1771.

Cleland, E. E., Chuine, I., Menzel, A., Mooney, H. A., & Schwartz, M. D. (2007). Shifting plant phenology in response to global change. *Trends in Ecology & Evolution*, 22(7), 357-365.

ClimateData.ca. (2022, April 22). Climate data for a Resilient Canada. *Climate Data Canada*. Retrieved October 7, 2022, from https://climatedata.ca/.

Cline, M. G., & Deppong, D. O. (1999). The role of apical dominance in paradormancy of temperate woody plants: a reappraisal. *Journal of plant physiology*, 155(3), 350-356.

Collier, J., MacLean, D. A., D'Orangeville, L., & Taylor, A. R. (2022). A review of climate change effects on the regeneration dynamics of balsam fir. *The Forestry Chronicle*, 98(1), 1-12.

Collier, N., Hoffman, F. M., Lawrence, D. M., Keppel-Aleks, G., Koven, C. D., Riley, W. J., Mu, M., and Randerson, J. T. (2018). The International Land Model Benchmarking (ILAMB) system: design, theory, and implementation. *Journal of Advances in Modeling Earth Systems*, *10*(11), 2731-2754.

Collins, M., Knutti, R., Arblaster, J., Dufresne, J. L., Fichefet, T., Friedlingstein, P., Gao, X., Gutowski, W.J., Johns, T., Krinner, G. and Shongwe, M., & Booth, B. B. (2013). Long-term climate change: projections, commitments and irreversibility. *In Climate change 2013-The physical science basis: Contribution of working group I to the Fifth Assessment Report of the Intergovernmental Panel on Climate Change* (pp. 1029-1136). Cambridge University Press.

Cook, B. I., Wolkovich, E. M., Davies, T. J., Ault, T. R., Betancourt, J. L., Allen, J. M., Bolmgren, K., Cleland, E.E., Crimmins, T.M., Kraft, N.J., Lancaster, L.T., & Travers, S. E. (2012). Sensitivity of spring phenology to warming across temporal and spatial climate gradients in two independent databases. *Ecosystems*, 15(8), 1283-1294.

Coussement, J., Henke, M., Lootens, P., Roldán-Ruiz, I., Steppe, K., De Swaef, T. (2018). Modelling leaf spectral properties in a soybean functional–structural plant model by integrating the prospect radiative transfer model. *Annals of Botany*, 122, 669–676. https://doi.org/10.1093/aob/mcy105.

Cox, P. M. (2001). Description of the TRIFFID dynamic global vegetation model: Hadley Centre Technical Note 24. *Met. Office, Bracknell, UK) available on-line http://www. metoffice. gov. uk/research/hadleycentre/pubs/HCTN/HCTN_24. pdf.*

Cox, P. M., Pearson, D., Booth, B. B., Friedlingstein, P., Huntingford, C., Jones, C. D., & Luke, C. M. (2013). Sensitivity of tropical carbon to climate change constrained by carbon dioxide variability. *Nature*, 494(7437), 341-344.

Croft, H., Chen, J. M., Luo, X., Bartlett, P., Chen, B., & Staebler, R. M. (2017). Leaf chlorophyll content as a proxy for leaf photosynthetic capacity. *Global Change Biology*, 23(9), 3513-3524.

Čufar, K., De Luis, M., Prislan, P., Gričar, J., Črepinšek, Z., Merela, M., & Kajfež-Bogataj, L. (2015). Do variations in leaf phenology affect radial growth variations in Fagus sylvatica?. *International Journal of Biometeorology*, 59(8), 1127-1132.

Curtis, P. S., & Gough, C. M. (2018). Forest aging, disturbance and the carbon cycle. *New Phytologist*, *219*(4), 1188-1193.

D'Orangeville, L., Houle, D., Duchesne, L., Phillips, R. P., Bergeron, Y., & Kneeshaw, D. (2018). Beneficial effects of climate warming on boreal tree growth may be transitory. *Nature communications*, 9(1), 1-10.

Dai, M., Yin, Z., Meng, F., Liu, Q., and Cai, W. J. (2012). Spatial distribution of riverine DOC inputs to the ocean: an updated global synthesis. *Current Opinion in Environmental Sustainability*, *4*(2), 170-178.

Danabasoglu, G., Lamarque, J. F., Bacmeister, J., Bailey, D. A., DuVivier, A. K., Edwards, J., Emmons, L.K., Fasullo, J., Garcia, R., Gettelman, A., and Strand, W. G. (2020). The community earth system model version 2 (CESM2). *Journal of Advances in Modeling Earth Systems*, *12*(2).

Davies-Barnard, T., Meyerholt, J., Zaehle, S., Friedlingstein, P., Brovkin, V., Fan, Y., Wiltshire, A. J., et al., (2020). Nitrogen cycling in CMIP6 land surface models: progress and limitations. *Biogeosciences*, *17*(20), 5129-5148.

de Kauwe, M. G., Disney, M. I., Quaife, T., Lewis, P., and Williams, M. (2011). An assessment of the MODIS Collection 5 leaf area index product for a region of mixed coniferous forest. *Remote Sensing of Environment*, 115(2), 767– 780.

de Mora, L. D., Butenschön, M., and Allen, J. I. (2013). How should sparse marine in situ measurements be compared to a continuous model: An example. *Geoscientific Model Development*, *6*(2), 533-548.

Defourny, P., Boettcher, M., Bontemps, S., Kirches, G., Lamarche, C., Peters, M., Santoro, M., and Schlerf, M. (2016). Land cover CCI Product user guide version 2. Technical report, *European Space Agency*.

Delire, C., Séférian, R., Decharme, B., Alkama, R., Calvet, J. C., Carrer, D., Gibelin, A., Joetzjer, E., Morel, X., Rochner, M., and Tzanos, D. (2020). The global land carbon cycle simulated with ISBA-CTRIP: Improvements over the last decade. *Journal of Advances in Modeling Earth Systems*, *12*(9), e2019MS001886.

Delpierre, N., Dufrêne, E., Soudani, K., Ulrich, E., Cecchini, S., Boé, J., & François, C. (2009). Modelling interannual and spatial variability of leaf senescence for three deciduous tree species in France. *Agricultural and Forest Meteorology*, 149(6-7), 938-948.

Delpierre, N., Guillemot, J., Dufrêne, E., Cecchini, S., & Nicolas, M. (2017). Tree phenological ranks repeat from year to year and correlate with growth in temperate deciduous forests. *Agricultural and Forest Meteorology*, 234, 1-10.

Delpierre, N., Soudani, K., Berveiller, D., Dufrêne, E., Hmimina, G., & Vincent, G. (2020). "Green pointillism": detecting the within-population variability of budburst in temperate deciduous trees with phenological cameras. *International Journal of Biometeorology*, 64(4), 663-670.

Delpierre, N., Vitasse, Y., Chuine, I., Guillemot, J., Bazot, S., & Rathgeber, C. B. (2016). Temperate and boreal forest tree phenology: from organ-scale processes to terrestrial ecosystem models. *Annals of Forest Science*, *73*(1), 5-25.

Denéchère, R., Delpierre, N., Apostol, E. N., Berveiller, D., Bonne, F., Cole, E., Delzon, S., Dufrêne, E., Gressler, E., Jean, F., & Vincent, G. (2021). The within-population variability of leaf spring and autumn phenology is influenced by temperature in temperate deciduous trees. *International Journal of Biometeorology*, 65(3), 369-379.

Desai, A. R., Richardson, A. D., Moffat, A. M., Kattge, J., Hollinger, D. Y., Barr, A., and Stauch, V. J. (2008). Cross-site evaluation of eddy covariance GPP and RE decomposition techniques. *agricultural and forest meteorology*, *148*(6-7), 821-838.

Deser, C., Lehner, F., Rodgers, K. B., Ault, T., Delworth, T. L., DiNezio, P. N., Ting, M. (2020). Insights from Earth system model initial-condition large ensembles and future prospects. *Nature Climate Change*, *10*(4), 277-286.

Dhami, N., & Cazzonelli, C. I. (2020). Environmental impacts on carotenoid metabolism in leaves. *Plant Growth Regulation*, 92(3), 455-477.

Dhar, A., Balliet, N., & Hawkins, C. D. (2014). Variability in height growth, survival and nursery carryover effect of Betula papyrifera provenances. *Scandinavian Journal of Forest Research*, 29(2), 132-143.

Ding, C., & Brouard, J. S. (2022). Assisted migration is plausible for a boreal tree species under climate change: A quantitative and population genetics study of trembling aspen (Populus tremuloides Michx.) in western Canada. *Ecology and Evolution*, 12(10), e9384.

Dow, C., Kim, A. Y., D'Orangeville, L., Gonzalez-Akre, E. B., Helcoski, R., Herrmann, V., Harley, G.L., Maxwell, J.T., McGregor, I.R., McShea, W.J., McMahon, S.M., & Anderson-Teixeira, K. J. (2022). Warm springs alter timing but not total growth of temperate deciduous trees. *Nature*, 608(7923), 552-557.

Dubé, M. G., Duinker, P., Greig, L., Carver, M., Servos, M., McMaster, M., & Munkittrick, K. R. (2013). A framework for assessing cumulative effects in watersheds: an introduction to Canadian case studies. *Integrated Environmental Assessment and Management*, 9(3), 363-369.

Dunne, J. P., Horowitz, L. W., Adcroft, A. J., Ginoux, P., Held, I. M., John, J. G., Krasting, J. P., Malyshev, S., Naik1, V., Paulot, F., Shevliakova, E., Stock, C. A., Zadeh, N., Balaji, V., Blanton, C., Dunne, K. A., Dupuis, C., Durachta, J., Dussin, R., Gauthier, P. P. G., Griffies, S. M., Guo, H., Hallberg, R. W., Harrison, M., He, J., Hurlin, W., McHugh, C., Menzel, R., Milly, P. C. D., Nikonov, S., Paynter, D. J., Ploshay, J., Radhakrishnan, A., Rand, K., Reichl, B. G., Robinson, T., Schwarzkopf, D. M., Sentman, L. T., Underwood, S., Vahlenkamp, H., Winton, M., Wittenberg, A. T., Wyman, B., Zeng, Y., and Zhao, M. (2020). The GFDL Earth System Model version 4.1 (GFDL-ESM 4.1): Overall coupled model description and simulation characteristics. *Journal of Advances in Modeling Earth Systems*, *12*(11), e2019MS002015.

Dusenge, M. E., Duarte, A. G., & Way, D. A. (2019). Plant carbon metabolism and climate change: elevated CO_2 and temperature impacts on photosynthesis, photorespiration and respiration. *New Phytologist*, 221(1), 32-49.

Eby, M., Weaver, A. J., Alexander, K., Zickfeld, K., Abe-Ouchi, A., Cimatoribus, A. A., Crespin, E., Drijfhout, S.S., Edwards, N.R., Eliseev, A.V. Feulner, G., & Zhao, F. (2013). Historical and idealized climate model experiments: an intercomparison of Earth system models of intermediate complexity. *Climate of the Past*, 9(3), 1111-1140.

Eby, M., Zickfeld, K., Montenegro, A., Archer, D., Meissner, K. J., & Weaver, A. J. (2009). Lifetime of anthropogenic climate change: Millennial time scales of potential CO_2 and surface temperature perturbations. *Journal of Climate*, 22(10), 2501-2511.

Ehlers, I., Augusti, A., Betson, T. R., Nilsson, M. B., Marshall, J. D., and Schleucher, J. (2015). Detecting long-term metabolic shifts using isotopomers: CO2-driven suppression of photorespiration in C3 plants over the 20th century. *Proceedings of the National Academy of Sciences*, *112*(51), 15585-15590.

Ehlert, D., Zickfeld, K., Eby, M., & Gillett, N. (2017). The sensitivity of the proportionality between temperature change and cumulative CO_2 emissions to ocean mixing. *Journal of Climate*, 30(8), 2921-2935.

Ellwood, E. R., Gallinat, A., Primack, R. B., & Lloyd-Evans, T. L. (2015). Autumn migration of North American landbirds. *Phenological synchrony and bird migration: changing climate and seasonal resources in North America. Studies in Avian Biology*, (47), 193-205.

Emilson, C. E., & Stastny, M. (2019). A decision framework for hemlock woolly adelgid management: Review of the most suitable strategies and tactics for eastern Canada. *Forest Ecology and Management*, *444*, 327-343.

Environment & Climate Change Canada (2022). Canadian Climate Normals 1981-2010 Station Data: Nova Scotia. https://climate.weather.gc.ca/climate_normals/index_e.html.

Erkkilä, K. M., Ojala, A., Bastviken, D., Biermann, T., Heiskanen, J. J., Lindroth, A., and Mammarella, I. (2018). Methane and carbon dioxide fluxes over a lake: comparison between eddy covariance, floating chambers and boundary layer method. *Biogeosciences*, *15*(2), 429-445.

Estiarte, M., & Peñuelas, J. (2015). Alteration of the phenology of leaf senescence and fall in winter deciduous species by climate change: effects on nutrient proficiency. *Global Change Biology*, 21(3), 1005-1017.

Etzold, S., Sterck, F., Bose, A. K., Braun, S., Buchmann, N., Eugster, W., Gessler, A., Kahmen, A., Peters, R.L., Vitasse, Y., Walthert, L., & Zweifel, R. (2022). Number of growth days and not length of the growth period determines radial stem growth of temperate trees. *Ecology Letters*, 25(2), 427-439.

Euskirchen, E. S., McGuire, A. D., Chapin III, F. S., Yi, S., & Thompson, C. C. (2009). Changes in vegetation in northern Alaska under scenarios of climate change, 2003–2100: implications for climate feedbacks. *Ecological Applications*, 19, 1022–1043.

Eyring, V., Bock, L., Lauer, A., Righi, M., Schlund, M., Andela, B., Zimmermann, K., et al., (2020). ESMValToolv2.0 v2. 0 Extended set of large-scale diagnostics for quasi-operational and comprehensive validation of Earth system models in CMIP. *Geoscientific Model Development*, *13*.

Eyring, V., Bony, S., Meehl, G. A., Senior, C. A., Stevens, B., Stouffer, R. J., and Taylor, K. E. (2016a). Overview of the Coupled Model Intercomparison Project Phase 6 (CMIP6) experimental design and organization. *Geoscientific Model Development*, *9*(5), 1937-1958.

Eyring, V., Cox, P. M., Flato, G. M., Gleckler, P. J., Abramowitz, G., Caldwell, P., Collins, W. D., Gier, B. K., Hall, A. D., Hoffman, F. M., Hurtt, G. C., Jahn, A., Jones, C. D., Klein, S. A., Krasting, J. P., Kwiatkowski, L., Lorenz, R., Maloney, E., Meehl, G. A., Pendergrass, A. G., Pincus, R., Ruane, A. C., Russell, J. L., Sanderson, B. M., Santer, B. D., Sherwood, S. C., Simpson, I. R., Stouffer, R. J., and Williamson, M. S. (2019). Taking climate model validation to the next level. *Nature Climate Change*, *9*(2), 102-110.

Eyring, V., Righi, M., Lauer, A., Evaldsson, M., Wenzel, S., Jones, C., Anav, A., Andrews, O., Cionni, I., Davin, E.L., Williams, K. D., et al., (2016b). ESMValToolv2.0 (v1. 0)–a community diagnostic and performance metrics tool for routine validation of Earth system models in CMIP. *Geoscientific Model Development*, *9*(5), 1747-1802.

Falkner, R. (2016). The Paris Agreement and the new logic of international climate politics. *International Affairs*, 92(5), 1107-1125.

Fan, J., Chen, B., Wu, L., Zhang, F., Lu, X., and Xiang, Y. (2018). Evaluation and development of temperature-based empirical models for estimating daily global solar radiation in humid regions. *Energy*, *144*, 903-914.

Fan, N., Koirala, S., Reichstein, M., Thurner, M., Avitabile, V., Santoro, M., and Carvalhais, N.

(2020). Apparent ecosystem carbon turnover time: uncertainties and robust features. *Earth System Science Data*, *12*(4), 2517-2536.

Fang, J., Lutz, J. A., Shugart, H. H., Wang, L., Liu, F., & Yan, X. (2022). Continental-scale parameterization and prediction of leaf phenology for the North American forests. *Global Ecology and Biogeography*, *31*(8), 1603-1615.

FAO. (2012). Harmonized World Soil Database v 1.2. Retrieved January 29, 2021, from http://www.fao.org/soils-portal/data-hub/soil-maps-and-databases/harmonized-world-soil-database-v12/en/.

Fatichi, S., Pappas, C., Zscheischler, J., & Leuzinger, S. (2019). Modelling carbon sources and sinks in terrestrial vegetation. *New Phytologist*, 221(2), 652-668.

Faucon, M.-P., Houben, D., & Lambers, H. (2017). Plant functional traits: soil and ecosystem services. *Trends in Plant Science*, 22, 385–394.

Féret, J. B., Berger, K., De Boissieu, F., & Malenovský, Z. (2021). PROSPECT-PRO for estimating content of nitrogen-containing leaf proteins and other carbon-based constituents. *Remote Sensing of Environment*, 252, 112173.

Féret, J. B., Le Maire, G., Jay, S., Berveiller, D., Bendoula, R., Hmimina, G., Cheraiet, A., Oliveira, J., Ponzoni, F., Solanki, T., de Boissieu, F., Chave, J., Nouvellon, Y., Porcar-Castell, A., Proisy, C., Soudani, K., Gastellu-Etchegorry, J.-P., & Lefèvre-Fonollosa, M.J. (2019). Estimating leaf mass per area and equivalent water thickness based on leaf optical properties: Potential and limitations of physical modeling and machine learning. *Remote Sensing of Environment*, 231, 110959.

Féret, J.-B., François, C., Asner, G. P., Gitelson, A. A., Martin, R. E., Bidel, L. P., Ustin, S. L., Le Maire, G., & Jacquemoud, S. (2008). PROSPECT-4 and 5: Advances in the leaf optical properties model separating photosynthetic pigments. *Remote Sensing of Environment*, 112, 3030– 3043.

Féret, J.-B., François, C., Gitelson, A., Asner, G. P., Barry, K. M., Panigada, C., Richardson, A. D., & Jacquemoud, S. (2011). Optimizing spectral indices and chemometric analysis of leaf chemical properties using radiative transfer modeling. *Remote Sensing of Environment*, 115, 2742–2750.

Féret, J.-B., Gitelson, A., Noble, S., Jacquemoud, S. (2017). PROSPECT-D: Towards modeling leaf optical properties through a complete life-cycle. *Remote Sensing of Environment*, 193, 204–215. https://doi.org/10.1016/j.rse.2017.03.004.

Field, E., Castagneyrol, B., Gibbs, M., Jactel, H., Barsoum, N., Schönrogge, K., & Hector, A. (2020). Associational resistance to both insect and pathogen damage in mixed forests is modulated by tree neighbour identity and drought. *Journal of Ecology*, 108(4), 1511-1522.

Filippa, G., Cremonese, E., Migliavacca, M., Galvagno, M., Forkel, M., Wingate, L., Tomelleri, E., Di Cella, U.M., & Richardson, A. D. (2016). Phenopix: AR package for image-based vegetation phenology. *Agricultural and Forest Meteorology*, 220, 141-150.

Fisher, R. A., Wieder, W. R., Sanderson, B. M., Koven, C. D., Oleson, K. W., Xu, C., and Lawrence, D. M. (2019). Parametric controls on vegetation responses to biogeochemical forcing in the CLM5. *Journal of Advances in Modeling Earth Systems*, *11*(9), 2879-2895.

Fisher, R.A., Koven, C.D., Anderegg, W.R., Christoffersen, B.O., Dietze, M.C., Farrior, C.E., Holm, J.A., Hurtt, G.C., Knox, R.G., Lawrence, P.J., & Lichstein, J.W. (2018). Vegetation demographics in Earth System Models: A review of progress and priorities. *Global Change Biology*, 24(1), 35-54.

Fisichelli, N. A., Abella, S. R., Peters, M., & Krist Jr, F. J. (2014). Climate, trees, pests, and weeds: Change, uncertainty, and biotic stressors in eastern US national park forests. *Forest Ecology and Management*, 327, 31-39.

Flato, G., Marotzke, J., Abiodun, B., Braconnot, P., Chou, S. C., Collins, W., Cox, P., Driouech, F., Emori, S., Eyring, V., Forest, C., Gleckler, P., Guilyardi, E., Jakob, C., Kattsov, V., Reason, C., and Rummukainen, M. (2013). Evaluation of climate models. In *Climate change 2013: the physical science basis. Contribution of Working Group I to the Fifth Assessment Report of the Intergovernmental Panel on Climate Change* (pp. 741-866). Cambridge University Press.

Fleischer, K., Rammig, A., De Kauwe, M. G., Walker, A. P., Domingues, T. F., Fuchslueger, L., Lapola, D. M. (2019). Amazon forest response to CO_2 fertilization dependent on plant phosphorus acquisition. *Nature Geoscience*, *12*(9), 736-741.

Flynn, D. F. B., & Wolkovich, E. M. (2018). Temperature and photoperiod drive spring phenology across all species in a temperate forest community. *New Phytologist*, 219(4), 1353-1362.

Fowler, D., Coyle, M., Skiba, U., Sutton, M. A., Cape, J. N., Reis, S., Sheppard, L. J., Jenkins, A., Grizzetti, B., Galloway, J. N., Vitousek, P., Leach, A., Bouwman, A. F., Butterbach-Bahl, K., Dentener, F., Stevenson, D., Amann, M., and Voss, M. (2013). The global nitrogen cycle in the twenty-first century. *Philosophical Transactions of the Royal Society, B: Biological Sciences*, 368(1621), 20130164–20130164.

Frank, R. M. (1990). Abies balsamea (L.) Mill. balsam fir. *Silvics of North America*, 1, 26-35.

Fridley, J. D. (2012). Extended leaf phenology and the autumn niche in deciduous forest invasions. *Nature*, 485(7398), 359.

Friedlingstein, P. (2015). Carbon cycle feedbacks and future climate change. *Philosophical Transactions of the Royal Society A: Mathematical, Physical and Engineering Sciences*, 373(2054), 20140421.

Friedlingstein, P., Meinshausen, M., Arora, V. K., Jones, C. D., Anav, A., Liddicoat, S. K., & Knutti, R. (2014). Uncertainties in CMIP5 climate projections due to carbon cycle feedbacks. *Journal of Climate*, 27(2), 511-526.

Friedlingstein, P., O'Sullivan, M., Jones, M. W., Andrew, R. M., Hauck, J., Olsen, A., Peters, G. P., Peters, W., Pongratz, J., Sitch, S., Le Quéré, C., Canadell, J. G., Ciais, P., Jackson, R. B., Alin, S., Aragao, L. E. O. C., Arneth, A., Arora, V., Bates, N. R., Becker, M., Benoit-Cattin, A., Bittig, H. C., Bopp, L., Bultan, S., Chandra, N., Chevallier, F., Chini, L. P., Evans, W., Florentie, L., Forster, P. M., Gasser, T., Gehlen, M., Gilfillan, D., Gkritzalis, T., Gregor, L., Gruber, N., Harris, I., Hartung, K., Haverd, V., Houghton, R. A., Ilyina, T., Jain, A. K., Joetzjer, E., Kadono, K., Kato, E., Kitidis, V., Korsbakken, J. I., Landsch\"utzer, P., Lef\`evre, N., Lenton, A., Lienert, S., Liu, Z., Lombardozzi, D., Marland, G., Metzl, N., Munro, D. R., Nabel, J. E. M. S., Nakaoka, S.-I., Niwa, Y., O'Brien, K., Ono, T., Palmer, P. I., Pierrot, D., Poulter, B., Resplandy, L., Robertson, E., R\"odenbeck, C., Schwinger, J., S\'ef\'erian, R., Skjelvan, I., Smith, A. J. P., Sutton, A. J., Tanhua, T., Tans, P. P., Tian, H., Tilbrook, B., van der Werf, G., Vuichard, N., Walker, A. P., Wanninkhof, R., Watson, A. J., Willis, D., Wiltshire, A. J., Yuan, W., Yue, X., and Zaehle, S. (2020). Global carbon budget 2020. *Earth System Science Data*, *12*(4), 3269-

3340.

Friedlingstein, P., O'Sullivan, M., Jones, M. W., Andrew, R. M., Gregor, L., Hauck, J., & Zheng, B. (2022). Global carbon budget 2022. *Earth System Science Data*, 14(11), 4811-4900.

Friedlingstein, P., Jones, M. W., O'Sullivan, M., Andrew, R. M., Hauck, J., Peters, G. P., Peters, W., Pongratz, J., Sitch, S., Le Quéré, C., Bakker, D. C. E., Canadell, J. G., Ciais, P., Jackson, R. B., Anthoni, P., Barbero, L., Bastos, A., Bastrikov, V., Becker, M., Bopp, L., Buitenhuis, E., Chandra, N., Chevallier, F., Chini, L. P., Currie, K. I., Feely, R. A., Gehlen, M., Gilfillan, D., Gkritzalis, T., Goll, D. S., Gruber, N., Gutekunst, S., Harris, I., Haverd, V., Houghton, R. A., Hurtt, G., Ilyina, T., Jain, A. K., Joetzjer, E., Kaplan, J. O., Kato, E., Klein Goldewijk, K., Korsbakken, J. I., Landschützer, P., Lauvset, S. K., Lefèvre, N., Lenton, A., Lienert, S., Lombardozzi, D., Marland, G., McGuire, P. C., Melton, J. R., Metzl, N., Munro, D. R., Nabel, J. E. M. S., Nakaoka, S.-I., Neill, C., Omar, A. M., Ono, T., Peregon, A., Pierrot, D., Poulter, B., Rehder, G., Resplandy, L., Robertson, E., Rödenbeck, C., Séférian, R., Schwinger, J., Smith, N., Tans, P. P., Tian, H., Tilbrook, B., Tubiello, F. N., van der Werf, G. R., Wiltshire, A. J., and Zaehle, S. (2019). Global carbon budget 2019. *Earth System Science Data*, *11*(4), 1783-1838.

Frölicher, T. L., & Paynter, D. J. (2015). Extending the relationship between global warming and cumulative carbon emissions to multi-millennial timescales. *Environmental Research Letters*, 10(7), 075002.

Fu, P., Meacham-Hensold, K., Guan, K., & Bernacchi, C. J. (2019). Hyperspectral leaf reflectance as proxy for photosynthetic capacities: an ensemble approach based on multiple machine learning algorithms. *Frontiers in Plant Science*, 10, 730.

Fu, Y. H., Piao, S., Delpierre, N., Hao, F., Hänninen, H., Liu, Y., Sun, W., Janssens, I.A., & Campioli, M. (2018). Larger temperature response of autumn leaf senescence than spring leaf-out phenology. *Global Change Biology,* 24(5), 2159-2168.

Fu, Y., Zhang, H., Dong, W., & Yuan, W. (2014). Comparison of phenology models for predicting the onset of growing season over the Northern Hemisphere. *PloS one*, 9(10), e109544.

Funk, J. L., Larson, J. E., Ames, G. M., Butterfield, B. J., Cavender-Bares, J., Firn, J., Laughlin, D.C., Sutton-Grier, A.E., Williams, L., & Wright, J. (2017). Revisiting the Holy G rail:

using plant functional traits to understand ecological processes. *Biological Reviews*, 92(2), 1156-1173.

Furbank, R. T., Silva-Perez, V., Evans, J. R., Condon, A. G., Estavillo, G. M., He, W., & He, Z. (2021). Wheat physiology predictor: predicting physiological traits in wheat from hyperspectral reflectance measurements using deep learning. *Plant Methods*, 17(1), 1-15.

Gallinat, A. S., Primack, R. B., & Wagner, D. L. (2015). Autumn, the neglected season in climate change research. *Trends in ecology and evolution*, 30(3), 169-176.

Galloway, J. N., Dentener, F. J., Capone, D. G., Boyer, E. W., Howarth, R. W., Seitzinger, S. P., Asner, G. P., Cleveland, C. C., Green, P. A., Holland, E. A., Karl, D. M., Michaels, A. F., Porter, J. H., Townsend, A. R., and Vo, C. J. (2004). Nitrogen cycles: past, present, and future. *Biogeochemistry*, *70*(2), 153-226.

Galloway, J. N., Leach, A. M., Bleeker, A., and Erisman, J. W. (2013). A chronology of human understanding of the nitrogen cycle. *Philosophical Transactions of the Royal Society B: Biological Sciences*, *368*(1621), 20130120.

Galloway, J. N., Townsend, A. R., Erisman, J. W., Bekunda, M., Cai, Z., Freney, J. R., Martinelli, L. A., Seitzinger, S. P., and Sutton, M. A. (2008). Transformation of the nitrogen cycle: recent trends, questions, and potential solutions. *Science*, *320*(5878), 889-892.

Gara, T. W., Darvishzadeh, R., Skidmore, A. K., Wang, T., & Heurich, M. (2019). Accurate modelling of canopy traits from seasonal Sentinel-2 imagery based on the vertical distribution of leaf traits. *ISPRS Journal of Photogrammetry and Remote Sensing*, 157, 108-123.

Garbary, D. J., & Hill, N. M. (2021). Climate change in Nova Scotia: temperature increases from 1961 to 2020. *Proceedings of the Nova Scotian Institute of Science (NSIS)*, *51*(2), 32.

Ge, Q., Zheng, J., Fang, X., Man, Z., Zhang, X., Zhang, P., & Wang, W. C. (2003). Winter half-year temperature reconstruction for the middle and lower reaches of the Yellow River and Yangtze River, China, during the past 2000 years. *The Holocene*, *13*(6), 933-940.

Gerber, F., Marion, R., Olioso, A., Jacquemoud, S., Da Luz, B. R., & Fabre, S. (2011). Modeling directional–hemispherical reflectance and transmittance of fresh and dry leaves from 0.4 μm to 5.7 μm with the PROSPECT-VISIR model. *Remote Sensing of Environment*, 115(2), 404-414.

Gevaert, C. M., Suomalainen, J., Tang, J., & Kooistra, L. (2015). Generation of spectral–temporal response surfaces by combining multispectral satellite and hyperspectral UAV imagery for precision agriculture applications. *IEEE Journal of Selected Topics in Applied Earth Observations and Remote Sensing*, 8, 3140–3146.

Gibbs, H. K. (2006). Olson's Major World Ecosystem Complexes Ranked by Carbon in Live Vegetation: An Updated Database Using the GLC2000 Land Cover Product NDP-017b. *Oak Ridge National Laboratory, Oak Ridge, TN.*

Giglio, L., Randerson, J. T., van der Werf, G. R., Kasibhatla, P. S., Collatz, G. J., Morton, D. C., and DeFries, R. S. (2010). Assessing variability and long-term trends in burned area by merging multiple satellite fire products. *Biogeosciences*, 7(3), 1171– 1186.

Gillett, N. P., Arora, V. K., Matthews, D., & Allen, M. R. (2013). Constraining the ratio of global warming to cumulative CO 2 emissions using CMIP5 simulations. *Journal of Climate*, 26(18), 6844-6858.

Gitelson, A. A., Chivkunova, O. B., & Merzlyak, M. N. (2009). Nondestructive estimation of anthocyanins and chlorophylls in anthocyanic leaves. *American Journal of Botany*, 96, 1861–1868.

Gitelson, A. A., Gamon, J. A., & Solovchenko, A. (2017). Multiple drivers of seasonal change in PRI: Implications for photosynthesis 1. Leaf level. *Remote Sensing of Environment*, 191, 110–116.

Gitelson, A. A., Keydan, G. P., & Merzlyak, M. N. (2006). Three-band model for noninvasive estimation of chlorophyll, carotenoids, and anthocyanin contents in higher plant leaves. *Geophysical Research Letters*, 33(11), L11402.

Gitelson, A. A., Merzlyak, M. N., & Chivkunova, O. B. (2001). Optical properties and nondestructive estimation of anthocyanin content in plant leaves. *Photochemistry and Photobiology*, 74, 38–45.

Gleckler, P. J., Doutriaux, C., Durack, P. J., Taylor, K. E., Zhang, Y., Williams, D. N., and Servonnat, J. (2016). A more powerful reality test for climate models. *Eos*, *97*(12), 20-24.

Global Monitoring Laboratory. (2005). Global monitoring Laboratory -carbon cycle greenhouse gases. Retrieved February 04, 2021, from https://www.esrl.noaa.gov/gmd/ccgg/trends/.

Global Soil Data Task Group (2002). Global Gridded Surfaces of Selected Soil Characteristics (IGBP-DIS), Tech. rep., https://doi.org/10.3334/ORNLDAAC/569.

GLOBAL VIEW-CO_2: Cooperative Global Atmospheric Data Integration Project. (2013), updated annually. Multi-laboratory compilation of synchronized and gap-filled atmospheric carbon dioxide records for the period 1979-2012. NOAA, Boulder, CO. doi: 10.3334/OBSPACK/1002.

Goetz, A., Gao, B., Wessman, C., & Bowman, W. (1990). Estimation of biochemical constituents from fresh, green leaves by spectrum matching techniques. *Proceedings of the 10th International Geoscience & Remote Sensing Symposium (IGARSS'90)*, 2, 971-974.

Goll, D. S., Brovkin, V., Liski, J., Raddatz, T., Thum, T., and Todd-Brown, K. E. (2015). Strong dependence of CO_2 emissions from anthropogenic land cover change on initial land cover and soil carbon parametrization. *Global Biogeochemical Cycles*, *29*(9), 1511-1523.

Goll, D. S., Winkler, A. J., Raddatz, T., Dong, N., Prentice, I. C., Ciais, P., and Brovkin, V. (2017). Carbon–nitrogen interactions in idealized simulations with JSBACH (version 3.10). *Geoscientific Model Development*, *10*(5), 2009-2030.

Gong, T., Feldstein, S., & Lee, S. (2017). The role of downward infrared radiation in the recent Arctic winter warming trend. *Journal of Climate*, 30(13), 4937-4949.

Gong, Y., Staudhammer, C. L., Kenney, G., Wiesner, S., Zhang, Y., & Starr, G. (2021). Vegetation structure drives forest phenological recovery after hurricane. *Science of the Total Environment*, 774, 145651.

Goodwin, P., Katavouta, A., Roussenov, V. M., Foster, G. L., Rohling, E. J., & Williams, R. G. (2018). Pathways to 1.5°C and 2°C warming based on observational and geological constraints. *Nature Geoscience*, 11(2), 102-107.

Goodwin, P., Williams, R. G., & Ridgwell, A. (2015). Sensitivity of climate to cumulative carbon emissions due to compensation of ocean heat and carbon uptake. *Nature Geoscience*, 8(1), 29-34.

Government of Canada, (2022, April 26). Growing season. *Government of Canada*. Retrieved November 25, 2022 from https://www.nrcan.gc.ca/climate-change/climate-change-impacts-forests/forest-change-indicators/growing-season/18470.

Grabska, E., Hostert, P., Pflugmacher, D., & Ostapowicz, K. (2019). Forest stand species mapping using the Sentinel-2 time series. *Remote Sensing*, 11(10), 1197.

Graham, R. M., Cohen, L., Petty, A. A., Boisvert, L. N., Rinke, A., Hudson, S. R., & Granskog, M. A. (2017). Increasing frequency and duration of Arctic winter warming events. *Geophysical Research Letters*, 44(13), 6974-6983.

Gray, S. B. and Brady, S. M. (2016). Plant developmental responses to climate change. *Developmental Biology*, 419, 64–77.

Green, J. K., Seneviratne, S. I., Berg, A. M., Findell, K. L., Hagemann, S., Lawrence, D. M., & Gentine, P. (2019). Large influence of soil moisture on long-term terrestrial carbon uptake. *Nature*, 565(7740), 476-479.

Gregory, J. M., & Andrews, T. (2016). Variation in climate sensitivity and feedback parameters during the historical period. *Geophysical Research Letters*, 43(8), 3911-3920.

Gregory, J. M., Jones, C. D., Cadule, P., & Friedlingstein, P. (2009). Quantifying carbon cycle feedbacks. *Journal of Climate*, 22(19), 5232-5250.

Gross, N., Suding, K. N., & Lavorel, S. (2007). Leaf dry matter content and lateral spread predict response to land use change for six subalpine grassland species. *Journal of Vegetation Science*, 18, 289–300.

Gruber, N., and Galloway, J. N. (2008). An Earth-system perspective of the global nitrogen cycle. *Nature*, *451*(7176), 293-296.

Gu, L., Hanson, P. J., Post, W. M., Kaiser, D. P., Yang, B., Nemani, R., Pallardy, S.G., & Meyers, T. (2008). The 2007 eastern US spring freeze: increased cold damage in a warming world?. *BioScience*, 58(3), 253-262.

Guanter, L., Segl, K., Foerster, S., Chabrillat, S., Fischer, S., Gentz, B., Rossner, G., Schrader, S. & Storch, T. (2018). The EnMAP German Imaging Spectroscopy Mission: Status and Summary of Preparatory Activities. *In IGARSS 2018-2018 IEEE International Geoscience and Remote Sensing Symposium*, 168-170.

Gulden, L. E., Rosero, E., Yang, Z. L., Wagener, T., and Niu, G. Y. (2008). Model performance, model robustness, and model fitness scores: A new method for identifying good land-surface models. *Geophysical research letters*, *35*(11).

Hajima, T., Watanabe, M., Yamamoto, A., Tatebe, H., Noguchi, M. A., Abe, M., Ohgaito, R., Ito, A., Yamazaki, D., Okajima, H., Ito, A., Takata, K., Ogochi, K., Watanabe, S., and Kawamiya, M. (2020). Development of the MIROC-ES2L Earth system model and the evaluation of biogeochemical processes and feedbacks. *Geoscientific Model*

Development, *13*(5), 2197-2244.

Halman, J. M., Schaberg, P. G., Hawley, G. J., & Hansen, C. F. (2011). Potential role of soil calcium in recovery of paper birch following ice storm injury in Vermont, USA. *Forest Ecology and Management*, 261(9), 1539-1545.

Hänninen, H. (1990). Modelling bud dormancy release in trees from cool and temperate regions. *Acta Forestalia Fennica*. 213, 1–47.

Hansen, A. J., Noble, B. P., Veneros, J., East, A., Goetz, S. J., Supples, C., Watson, J.E., Jantz, P.A., Pillay, R., Jetz, W., Ferrier, S., & Virnig, A. L. (2021). Towards monitoring ecosystem integrity within the Post-2020 Global Biodiversity Framework. *Ecoevorxiv*, https://doi.org/10.32942/osf.io/eyqw5.

Hansen, J., Sato, M., Kharecha, P., von Schuckmann, K., Beerling, D. J., Cao, J., & Ruedy, R. (2016). Emissions, Young People's Burden: Requirement of Negative CO_2. *Earth System Dynamics: Discussions*, 8, 577-616.

Harper, A. B., Wiltshire, A. J., Cox, P. M., Friedlingstein, P., Jones, C. D., Mercado, L. M., ... & Duran-Rojas, C. (2018). Vegetation distribution and terrestrial carbon cycle in a carbon cycle configuration of JULES4. 6 with new plant functional types. *Geoscientific Model Development*, 11(7), 2857-2873.

Harper, A.B., Cox, P.M., Friedlingstein, P., Wiltshire, A.J., Jones, C.D., Sitch, S., Mercado, L.M., Groenendijk, M., Robertson, E., Kattge, J., & Bönisch, G. (2016). Improved representation of plant functional types and physiology in the Joint UK Land Environment Simulator (JULES v4. 2) using plant trait information. *Geoscientific Model Development*, 9(7), 2415-2440.

Harper, A.B., Wiltshire, A.J., Cox, P.M., Friedlingstein, P., Jones, C.D., Mercado, L.M., Sitch, S., Williams, K., & Duran-Rojas, C. (2018). Vegetation distribution and terrestrial carbon cycle in a carbon cycle configuration of JULES4. 6 with new plant functional types. *Geoscientific Model Development*, 11, 2857-2873.

Hashimoto, S., Carvalhais, N., Ito, A., Migliavacca, M., Nishina, K., and Reichstein, M. (2015). Global spatiotemporal distribution of soil respiration modeled using a global database. *Biogeosciences*, 12, 4121– 4132.

He, Y., Piao, S. L., Li, X. Y., Chen, A. P., and Qin, D. H. (2018). Global patterns of vegetation carbon use efficiency and their climate drivers deduced from MODIS satellite data and process-based models. *Agricultural and Forest Meteorology*, 256–257, 150– 158.

Heimann, M., and Reichstein, M. (2008). Terrestrial ecosystem carbon dynamics and climate feedbacks. *Nature*, *451*(7176), 289-292.

Helman, D. (2017). Land surface phenology: What do we really ‘see’ from space?. *Science of The Total Environment*, 618, 665-673.

Hernández-Clemente, R., Navarro-Cerrillo, R. M., & Zarco-Tejada, P. J. (2012). Carotenoid content estimation in a heterogeneous conifer forest using narrow-band indices and PROSPECT+DART simulations. *Remote Sensing of Environment*, 127, 298 – 315, https://doi.org/https://doi.org/10.1016/j.rse.2012.09.014.

Herridge, D. F., Peoples, M. B., and Boddey, R. M. (2008). Global inputs of biological nitrogen fixation in agricultural systems. *Plant and soil*, *311*(1), 1-18.

Herrington, T., & Zickfeld, K. (2014). Path independence of climate and carbon cycle response over a broad range of cumulative carbon emissions. *Earth System Dynamics*, 5(2), 409-422.

Hill, J., Buddenbaum, H., & Townsend, P. A. (2019). Imaging Spectroscopy of Forest Ecosystems: Perspectives for the Use of Space-borne Hyperspectral Earth Observation Systems. *Surveys in Geophysics*, 40, 553–588.

Hoffman, F. M., Randerson, J. T., Arora, V. K., Bao, Q., Cadule, P., Ji, D., Jones, C.D., Kawamiya, M., Khatiwala, S., Lindsay, K., and Wu, T. (2014). Causes and implications of persistent atmospheric carbon dioxide biases in Earth System Models. *Journal of Geophysical Research: Biogeosciences*, *119*(2), 141-162.

Hofmann, D. J., Butler, J. H., Dlugokencky, E. J., Elkins, J. W., Masarie, K., Montzka, S. A., & Tans, P. (2006). The role of carbon dioxide in climate forcing from 1979 to 2004: introduction of the Annual Greenhouse Gas Index. *Tellus B: Chemical and Physical Meteorology*, 58(5), 614-619.

Holland, E. A., Post, W. M., Matthews, E., Sulzman, J. M., Staufer, R., and Krankina, O. N. (2015). A global database of litterfall mass and litter pool carbon and nutrients. *ORNL DAAC*.

Hosgood, B., Jacquemoud, S., Andreoli, G., Verdebout, J., Pedrini, G., & Schmuck, G. (1994). Leaf optical properties experiment 93 (LOPEX93). *Joint Research Centre, Institute for Remote Sensing Applications*, Report EUR, 16095.

Houlton, B. Z., Marklein, A. R., and Bai, E. (2015). Representation of nitrogen in climate change forecasts. *Nature Climate Change*, *5*(5), 398-401.

Hourdin, F., Rio, C., Grandpeix, J.-Y., Madeleine, J.-B., Cheruy, F., Rochetin, N., Musat, I., Idelkadi, A., Fairhead, L., Foujols, M.-A., Ghattas, J., Mellul, L., Traore, A.-K., Gastineau, G., Dufresne, J.-L., Lefebvre, M.-P., Millour, E., Vignon, E., Jouaud, J., Bonazzola, M. and Lott, F. (2020). LMDZ6: Improved atmospheric component of the IPSL coupled model. *J. Adv. Model. Earth Sy*, *12*, e2019MS001892.

Hovenden, M., & Newton, P. (2018). Plant responses to CO2 are a question of time. *Science*, 360(6386), 263-264.

Hufkens, K., Basler, D., Milliman, T., Melaas, E. K., & Richardson, A. D. (2018). An integrated phenology modelling framework in R. *Methods in Ecology and Evolution*, 9(5), 1276-1285.

Hufkens, K., Friedl, M. A., Keenan, T. F., Sonnentag, O., Bailey, A., O'Keefe, J., & Richardson, A. D. (2012b). Ecological impacts of a widespread frost event following early spring leaf-out. *Global Change Biology*, 18(7), 2365-2377.

Hufkens, K., Friedl, M., Sonnentag, O., Braswell, B. H., Milliman, T., & Richardson, A. D. (2012a). Linking near-surface and satellite remote sensing measurements of deciduous broadleaf forest phenology. *Remote Sensing of Environment*, 117, 307-321.

Hugelius, G., Bockheim, J. G., Camill, P., Elberling, B., Grosse, G., Harden, J. W., Johnson, K., Jorgenson, T., Koven, C. D., Kuhry, P., Michaelson, G., Mishra, U., Palmtag, J., Ping, C.-L., O'Donnell, J., Schirrmeister, L., Schuur, E. A. G., Sheng, Y., Smith, L. C., Strauss, J., and Yu, Z. (2013). A new data set for estimating organic carbon storage to 3 m depth in soils of the northern circumpolar permafrost region. *Earth System Science Data*, *5*(2), 393-402.

Huntzinger, D. N., Michalak, A. M., Schwalm, C., Ciais, P., King, A. W., Fang, Y., Schaefer, K., Wei, Y., Cook, R.B., Fisher, J.B., Hayes, D., & Zhao, F. (2017). Uncertainty in the response of terrestrial carbon sink to environmental drivers undermines carbon-climate feedback predictions. *Scientific Reports*, 7(1), 1-8.

Huntzinger, D. N., Schwalm, C., Michalak, A. M., Schaefer, K., King, A. W., Wei, Y., Jacobson, A., Liu, S., Cook, R. B., Post, W. M., Berthier, G., Hayes, D., Huang, M., Ito, A., Lei, H., Lu, C., Mao, J., Peng, C. H., Peng, S., Poulter, B., Riccuito, D., Shi, X., Tian, H., Wang, W., Zeng, N., Zhao, F., and Zhu, Q. (2013). The north american carbon program multi-scale synthesis and terrestrial model intercomparison project–part 1: Overview and experimental design. *Geoscientific Model Development*, *6*(6), 2121-2133.

Ide, R., Nakaji, T., Motohka, T., & Oguma, H. (2011). Advantages of visible-band spectral remote sensing at both satellite and near-surface scales for monitoring the seasonal dynamics of GPP in a Japanese larch forest. *Journal of Agricultural Meteorology*, 1104050093-1104050093.

IPCC, (2013). *Climate Change 2013: The Physical Science Basis: Working Group I Contribution to the Fifth Assessment Report of the Intergovernmental Panel on Climate Change*. [Stocker, T.F., D. Qin, G.-K. Plattner, M. Tignor, S.K. Allen, J. Boschung, A. Nauels, Y. Xia, V. Bex and P.M. Midgley (eds.)]. Cambridge University Press, Cambridge, United Kingdom and New York, NY, USA, 1535 pp.

IPCC, (2021). *Climate Change 2021: The Physical Science Basis. Contribution of Working Group I to the Sixth Assessment Report of the Intergovernmental Panel on Climate Change*. [Masson-Delmotte, V., P. Zhai, A. Pirani, S.L. Connors, C. Péan, S. Berger, N. Caud, Y. Chen, L. Goldfarb, M.I. Gomis, M. Huang, K. Leitzell, E. Lonnoy, J.B.R. Matthews, T.K. Maycock, T. Waterfield, O. Yelekçi, R. Yu, and B. Zhou (eds.)]. Cambridge University Press, Cambridge, United Kingdom and New York, NY, USA, 2391 pp. doi:10.1017/9781009157896.

Ito, A. (2011). A historical meta-analysis of global terrestrial net primary productivity: are estimates converging?. *Global Change Biology*, *17*(10), 3161-3175.

Ito, A., and Inatomi, M. (2012). Use of a process-based model for assessing the methane budgets of global terrestrial ecosystems and validation of uncertainty. *Biogeosciences*, *9*(2), 759-773.

Ito, A., Hajima, T., Lawrence, D. M., Brovkin, V., Delire, C., Guenet, B., Jones, C., Malyshev, S., Materia, S., McDermid, S., Peano, D., Pongratz, J., Robertson, E., Shevliakova, E., Vuichard, N., Warlind, D., Wiltshire, A., and Ziehn, T. (2020). Soil carbon sequestration simulated in CMIP6-LUMIP models: implications for climatic mitigation. *Environmental Research Letters*, *15*(12), 124061.

Ivakhiv, A. (2005). Colouring cape Breton "Celtic": Topographies of culture and identity in cape Breton Island. *Ethnologies*, 27(2), 107-136.

Jacobs, N., Burgin, W., Fridrich, N., Abrams, A., Miskell, K., Braswell, B. H., Richardson, A.D., & Pless, R. (2009). The global network of outdoor webcams: properties and applications. In *Proceedings of the 17th ACM SIGSPATIAL International Conference on Advances in Geographic Information Systems* (pp. 111-120).

Jacquemoud, S., & Baret, F. (1990). PROSPECT: a model of leaf optical properties spectra. *Remote Sensing of Environment*, 34, 75–91. https://doi.org/10.1016/0034-4257(90)90100-Z.

Jacquemoud, S., Ustin, S.L., Verdebout, J., Schmuck, G., Andreoli, G., & Hosgood, B. (1996). Estimating leaf biochemistry using the PROSPECT leaf optical properties model. *Remote Sensing of Environment*, 56, 194–202. https://doi.org/10.1016/0034-4257(95)00238-3.

Jacquemoud, S., Verhoef, W., Baret, F., Bacour, C., Zarco-Tejada, P.J., Asner, G.P., François, C., & Ustin, S.L. (2009). PROSPECT+ SAIL models: a review of use for vegetation characterization. *Remote Sensing of Environment*, 113, S56–S66. https://doi.org/10.1016/j.rse.2008.01.026.

Jay, S., Bendoula, R., Hadoux, X., Féret, J.-B., Gorretta, N. (2016). A physically-based model for retrieving foliar biochemistry and leaf orientation using close-range imaging spectroscopy. *Remote Sensing of Environment*, 177, 220–236.

Jenkins, S., Cain, M., Friedlingstein, P., Gillett, N., Walsh, T., & Allen, M. R. (2021). Quantifying non-CO_2 contributions to remaining carbon budgets. *NPJ Climate and Atmospheric Science,* 4(1), 1-10.

Jenssen, M., Nickel, S., Schütze, G., & Schröder, W. (2021). Reference states of forest ecosystem types and feasibility of biocenotic indication of ecological soil condition as part of ecosystem integrity and services assessment. *Environmental Sciences Europe*, 33(1), 1-18.

Jeong, S. J., & Medvigy, D. (2014). Macroscale prediction of autumn leaf colouration throughout the continental United States. *Global Ecology and Biogeography*, 23(11), 1245-1254.

Jeong, S. J., Medvigy, D., Shevliakova, E., & Malyshev, S. (2012). Uncertainties in terrestrial carbon budgets related to spring phenology. *Journal of Geophysical Research*: Biogeosciences, 117(G1).

Jiang, G., & Wang, W. (2017). Error estimation based on variance analysis of k-fold cross-validation. *Pattern Recognition*, *69*, 94-106.

Jiang, J., Comar, A., Burger, P., Bancal, P., Weiss, M., & Baret, F. (2018). Estimation of leaf traits from reflectance measurements: comparison between methods based on vegetation indices and several versions of the PROSPECT model. *Plant Methods*, 14, 23, https://doi.org/10.1186/s13007-018-0291-x.

Jiang, N., Shen, M., Ciais, P., Campioli, M., Peñuelas, J., Körner, C., & Zhao, W. (2022). Warming does not delay the start of autumnal leaf coloration but slows its progress rate. *Global Ecology and Biogeography*, 31(11), 2297-2313.

Joetzjer, E., Delire, C., Douville, H., Ciais, P., Decharme, B., Carrer, D., Verbeeck, H., de Weirdt, M., and Bonal, D. (2015). Improving the ISBA CC land surface model simulation of water and carbon fluxes and stocks over the Amazon forest. *Geoscientific Model Development*, *8*(6), 1709-1727.

Johns, T. C., Royer, J. F., Höschel, I., Huebener, H., Roeckner, E., Manzini, E., May, W., Dufresne, J.L., Otterå, O.H., Van Vuuren, D.P., Salas y Melia, D., & Hewitt, C. D. (2011). Climate change under aggressive mitigation: the ENSEMBLES multi-model experiment. *Climate Dynamics*, 37(9), 1975-2003.

Johnson, G. C., Lyman, J. M., & Loeb, N. G. (2016). Improving estimates of Earth's energy imbalance. *Nature Climate Change*, 6(7), 639-640.

Jones, C. D., Arora, V., Friedlingstein, P., Bopp, L., Brovkin, V., Dunne, J., Graven, H., Hoffman, F., Ilyina, T., John, J.G., and Zaehle, S. (2016). C4MIP–The coupled climate–carbon cycle model intercomparison project: Experimental protocol for CMIP6. *Geoscientific Model Development*, *9*(8), 2853-2880.

Jones, C., Robertson, E., Arora, V., Friedlingstein, P., Shevliakova, E., Bopp, L., Brovkin, V., Hajima, T., Kato, E., Kawamiya, M., Liddicoat, S., & Tjiputra, J. (2013). Twenty-first-century compatible CO_2 emissions and airborne fraction simulated by CMIP5 earth system models under four representative concentration pathways. *Journal of Climate*, 26(13), 4398-4413.

Jonsson, A., Åberg, J., Lindroth, A., and Jansson, M. (2008). Gas transfer rate and CO_2 flux between an unproductive lake and the atmosphere in northern Sweden. *Journal of Geophysical Research: Biogeosciences*, *113*(G4).

Jung, M., Reichstein, M., and Bondeau, A. (2009). Towards global empirical upscaling of Fluxnet eddy covariance observations: validation of a model tree ensemble approach using a biosphere model. *Biogeosciences*, *6*(10), 2001-2013.

Jung, M., Reichstein, M., Ciais, P., Seneviratne, S. I., Sheffield, J., Goulden, M. L., Bonan, G., Cescatti, A., Chen, J., De Jeu, R., and Zhang, K. (2010). Recent decline in the global land evapotranspiration trend due to limited moisture supply. *Nature*, *467*(7318), 951-954.

Jung, M., Reichstein, M., Margolis, H. A., Cescatti, A., Richardson, A. D., Arain, M. A., Arneth, A., Bernhofer, C., Bonal, D., Chen, J., Gianelle, D., Gobron, N., Kiely, G., Kutsch, W., Lasslop, G., Law, B. E., Lindroth, A., Merbold, L., Montagnani, L., Moors, E. J., Papale, D., Sottocornola, M., Vaccari, F., and Williams, C. (2011). Global patterns of land-atmosphere fluxes of carbon dioxide, latent heat, and sensible heat derived from eddy covariance, satellite, and meteorological observations. *Journal of Geophysical Research: Biogeosciences*, *116*(G3).

Jung, M., Reichstein, M., Schwalm, C. R., Huntingford, C., Sitch, S., Ahlström, A., Arneth, A., Camps-Valls, G., Ciais, P., Friedlingstein, P., Gans, F., Ichii, K., Jain, A. K., Kato, E., Papale, D., Poulter, B., Raduly, B., Rödenbeck, C., Tramontana, G., Viovy, N., Wang, Y.-P., Weber, U., Zaehle, S., and Zeng, N. (2016) FLUXCOM (RS+METEO) Global Land Carbon Fluxes using CRUNCEP climate data. FLUXCOM Data Portal https://doi.org/10.17871/FLUXCOM_RS_METEO_CRUNCEPv6_1980_2013_v1

Jung, M., Schwalm, C., Migliavacca, M., Walther, S., Camps-Valls, G., Koirala, S., Anthoni, P., Besnard, S., Bodesheim, P., Carvalhais, N., Chevallier, F., Gans, F., Goll, D. S., Haverd, V., Köhler, P., Ichii, K., Jain, A. K., Liu, J., Lombardozzi, D., Nabel, J. E. M. S., Nelson, J. A., O'Sullivan, M., Pallandt, M., Papale, D., Peters, W., Pongratz, J., Rödenbeck, C., Sitch, S., Tramontana, G., Walker, A., Weber, U., and Reichstein, M. (2020). Scaling carbon fluxes from eddy covariance sites to globe: synthesis and evaluation of the FLUXCOM approach. *Biogeosciences*, *17*(5), 1343-1365.

Jung, M., Reichstein, M., Schwalm, C. R., Huntingford, C., Sitch, S., Ahlström, A., Arneth, A., Camps-Valls, G., Ciais, P., Friedlingstein, P., Gans, F., Ichii, K., Jain, A. K., Kato, E., Papale, D., Poulter, B., Raduly, B., Rödenbeck, C., Tramontana, G., Viovy, N., Wang, Y., Weber, U., Zaehle, S., and Zeng, N. (2017). Compensatory water effects link yearly global land CO_2 sink changes to temperature. *Nature*, 541(7638), 516– 520.

Kaitaniemi, P., Ruohomäki, K., & Haukioja, E. (1997). Consequences of defoliation on phenological interaction between Epirrita autumnata and its host plant, mountain birch. *Functional Ecology*, 11(2), 199-208.

Katavouta, A., Williams, R. G., & Goodwin, P. (2019). The effect of ocean ventilation on the transient climate response to emissions. *Journal of Climate*, 32(16), 5085-5105.

Katavouta, A., Williams, R. G., Goodwin, P., & Roussenov, V. (2018). Reconciling atmospheric and oceanic views of the transient climate response to emissions. *Geophysical Research Letters*, 45(12), 6205-6214.

Kattenborn, T., Fassnacht, F. E., & Schmidtlein, S. (2019). Differentiating plant functional types using reflectance: which traits make the difference?. *Remote Sensing in Ecology and Conservation*, 5, 5–19.

Kattenborn, T., Fassnacht, F. E., Pierce, S., Lopatin, J., Grime, J. P., & Schmidtlein, S. (2017). Linking plant strategies and plant traits derived by radiative transfer modelling. *Journal of Vegetation Science*, 28, 717–727, https://doi.org/10.1111/jvs.12525.

Kattge, J., Knorr, W., Raddatz, T., and Wirth, C. (2009). Quantifying photosynthetic capacity and its relationship to leaf nitrogen content for global-scale terrestrial biosphere models. *Global Change Biology*, *15*(4), 976-991.

Keenan, T. F., & Richardson, A. D. (2015). The timing of autumn senescence is affected by the timing of spring phenology: implications for predictive models. *Global Change Biology*, 21(7), 2634-2641.

Keenan, T. F., Darby, B., Felts, E., Sonnentag, O., Friedl, M. A., Hufkens, K., O'Keefe, J., Klosterman, S., Munger, J.W., Toomey, M., & Richardson, A. D. (2014). Tracking forest phenology and seasonal physiology using digital repeat photography: a critical assessment. *Ecological Applications*, 24(6), 1478-1489.

Keenan, T. F., Richardson, A. D., & Hufkens, K. (2020). On quantifying the apparent temperature sensitivity of plant phenology. *New Phytologist*, 225(2), 1033-1040.

Kellndorfer, J., Walker, W., Kirsch, K., Fiske, G., Bishop, J., Lapoint, L., Hoppus, M., Westfall, J. (2013). NACP aboveground biomass and carbon baseline data, V.2 (NBCD 2000), U.S.A., 2000.

Kharouba, H. M., Ehrlén, J., Gelman, A., Bolmgren, K., Allen, J. M., Travers, S. E., & Wolkovich, E. M. (2018). Global shifts in the phenological synchrony of species interactions over recent decades. *Proceedings of the National Academy of Sciences*, 115(20), 5211-5216.

Kindermann, G., McCallum, I., Fritz, S., and Obersteiner, M. (2008). A global forest growing stock, biomass and carbon map based on FAO statistics. *Silva Fennica*, *42*(3), 387-396.

Klosterman, S. T., & Richardson, A. D. (2017). Observing spring and fall phenology in a deciduous forest with aerial drone imagery. *Sensors*, 17(12), 2852.

Klosterman, S. T., Hufkens, K., Gray, J. M., Melaas, E., Sonnentag, O., Lavine, I., Mitchell, L., Norman, R., Friedl, M.A., & Richardson, A. D. (2014). Evaluating remote sensing of deciduous forest phenology at multiple spatial scales using PhenoCam imagery. *Biogeosciences*, 11(16), 4305-4320.

Klosterman, S., Hufkens, K., & Richardson, A. D. (2018). Later springs green-up faster: the relation between onset and completion of green-up in deciduous forests of North America. *International Journal of Biometeorology*, 62(9), 1645-1655.

Knutti, R., & Rogelj, J. (2015). The legacy of our CO_2 emissions: a clash of scientific facts, politics and ethics. *Climatic Change*, 133(3), 361-373.

Knutti, R., Rugenstein, M. A., & Hegerl, G. C. (2017). Beyond equilibrium climate sensitivity. *Nature Geoscience*, 10(10), 727-736.

Kobayashi, K., and Salam, M. U. (2000). Comparing simulated and measured values using mean squared deviation and its components. *Agronomy Journal*, *92*(2), 345-352.

Koch, J., Siemann, A., Stisen, S., and Sheffield, J. (2016). Spatial validation of large-scale land surface models against monthly land surface temperature patterns using innovative performance metrics. *Journal of Geophysical Research: Atmospheres*, *121*(10), 5430-5452.

Kokoska, S., & Zwillinger, D. (2000). CRC standard probability and statistics tables and formulae. *CRC Press*.

Körner, C., Basler, D., Hoch, G., Kollas, C., Lenz, A., Randin, C. F., Vitasse, Y., & Zimmermann, N. E. (2016). Where, why and how? Explaining the low-temperature range limits of temperate tree species. *Journal of Ecology*, 104(4), 1076-1088.

Kosmala, M., Crall, A., Cheng, R., Hufkens, K., Henderson, S., & Richardson, A. D. (2016). Season Spotter: Using citizen science to validate and scale plant phenology from near-surface remote sensing. *Remote Sensing*, 8(9), 726.

Koven, C. D., Hugelius, G., Lawrence, D. M., and Wieder, W. R. (2017). Higher climatological temperature sensitivity of soil carbon in cold than warm climates. *Nature Climate Change*, *7*(11), 817-822.

Kowalczyk, E. A., Stevens, L., Law, R. M., Dix, M., Wang, Y. P., Harman, I. N., Haynes, K., Srbinovsky, J., Pak, B., and Ziehn, T. (2013). The land surface model component of ACCESS: description and impact on the simulated surface climatology. *Aust. Meteorol. Oceanogr. J*, *63*(1), 65-82.

Kowalczyk, E. A., Wang, Y. P., Law, R. M., Davies, H. L., McGregor, J. L., and Abramowitz, G. (2006). The CSIRO Atmosphere Biosphere Land Exchange (CABLE) model for use in climate models and as an offline model. *CSIRO Marine and Atmospheric Research Paper*, *13*, 42.

Kramer, K. (1994). Selecting a model to predict the onset of growth of Fagus sylvatica. *Journal of Applied Ecology*, 172-181.

Krasting, J. P., Dunne, J. P., Shevliakova, E., & Stouffer, R. J. (2014). Trajectory sensitivity of the transient climate response to cumulative carbon emissions. *Geophysical Research Letters*, 41(7), 2520-2527.

Krause, A., Pugh, T. A., Bayer, A. D., Li, W., Leung, F., Bondeau, A., ... & Arneth, A. (2018). Large uncertainty in carbon uptake potential of land-based climate-change mitigation efforts. *Global Change Biology*, 24(7), 3025-3038.

Kumar, S. V., Peters-Lidard, C. D., Santanello, J., Harrison, K., Liu, Y., and Shaw, M. (2012). Land surface Verification Toolkit (LVT)–a generalized framework for land surface model evaluation. *Geoscientific Model Development*, *5*(3), 869-886.

Kunkel, K. E., Easterling, D. R., Hubbard, K., & Redmond, K. (2004). Temporal variations in frost-free season in the United States: 1895–2000. *Geophysical Research Letters*, 31(3).

Lafleur, B., Pare, D., Munson, A. D., & Bergeron, Y. (2010). Response of northeastern North American forests to climate change: Will soil conditions constrain tree species migration?. *Environmental Reviews*, 18(NA), 279-289.

Lamarque, J.-F., Bond, T. C., Eyring, V., Granier, C., Heil, A., Klimont, Z., Lee, D., Liousse, C., Mieville, A., Owen, B., Schultz, M. G., Shindell, D., Smith, S. J., Stehfest, E., Van Aardenne, J., Cooper, O. R., Kainuma, M., Mahowald, N., McConnell, J. R., Naik, V., Riahi, K., and Van Vuuren, D. P. (2010). Historical (1850–2000) gridded anthropogenic and biomass burning emissions of reactive gases and aerosols: Methodology and application. *Atmospheric Chemistry and Physics Discussions*, 10(2), 4963– 5019.

Lang, W., Chen, X., Qian, S., Liu, G., & Piao, S. (2019). A new process-based model for predicting autumn phenology: How is leaf senescence controlled by photoperiod and temperature coupling?. *Agricultural and Forest Meteorology*, *268*, 124-135.

Lantz, T. C., & Turner, N. J. (2003). Traditional phenological knowledge of Aboriginal peoples in British Columbia. *Journal of Ethnobiology*, 23(2), 263-286.

LaPaix, R., Freedman, B., & Patriquin, D. (2009). Ground vegetation as an indicator of ecological integrity. *Environmental Reviews*, 17(NA), 249-265.

Lassalle, G., Fabre, S., Credoz, A., Hédacq, R., Bertoni, G., Dubucq, D., & Elger, A. (2019). Application of PROSPECT for estimating Total Petroleum Hydrocarbons in contaminated soils from leaf optical properties. *Journal of Hazardous Materials*, 377, 409 – 417.

Lasslop, G., Reichstein, M., Kattge, J., and Papale, D. (2008). Influences of observation errors in eddy flux data on inverse model parameter estimation. *Biogeosciences*, *5*(5), 1311-1324.

Lasslop, G., Reichstein, M., Papale, D., Richardson, A. D., Arneth, A., Barr, A., Stoy, P., Wohlfahrt, G. (2010). Separation of net ecosystem exchange into assimilation and respiration using a light response curve approach: Critical issues and global evaluation. *Global Change Biology*, 16(1), 187– 208.

Lauscher, F. (1978). Neue Analysen altester und neuerer phänologischer Reihen. *Archiv für Meteorologie Geophysik und Bioklimatologie Serie B,* 28, 373–385.

Law, K., Stuart, A., and Zygalakis, K. (2015). Data assimilation: A Mathematical Introduction, Texts in Applied Mathematics. *Cham, Switzerland: Springer*, 141(1), 242.

Lawrence, D. M., Fisher, R. A., Koven, C. D., Oleson, K. W., Swenson, S. C., Bonan, G., Collier, N., Ghimire, B., van Kampenhout, L., Kennedy, D., and Zeng, X. (2019). The Community Land Model version 5: Description of new features, benchmarking, and impact of forcing uncertainty. *Journal of Advances in Modeling Earth Systems*, *11*(12), 4245-4287.

Lawrence, P. J., Feddema, J. J., Bonan, G. B., Meehl, G. A., O'Neill, B. C., Oleson, K. W., Levis, S., Lawrence, D.M., Kluzek, E., Lindsay, K., and Thornton, P. E. (2012).

Simulating the biogeochemical and biogeophysical impacts of transient land cover change and wood harvest in the Community Climate System Model (CCSM4) from 1850 to 2100. *Journal of Climate*, *25*(9), 3071-3095.

Le Maire, G., Francois, C., & Dufrene, E. (2004). Towards universal broad leaf chlorophyll indices using PROSPECT simulated database and hyperspectral reflectance measurements. *Remote Sensing of Environment*, 89, 1–28.

Le Maire, G., François, C., Soudani, K., Berveiller, D., Pontailler, J.-Y., Bréda, N., Genet, H., Davi, H., & Dufrêne, E. (2008). Calibration and validation of hyperspectral indices for the estimation of broadleaved forest leaf chlorophyll content, leaf mass per area, leaf area index and leaf canopy biomass. *Remote Sensing of Environment*, 112, 3846–3864.

Le Maire, G., Marsden, C., Verhoef, W., Ponzoni, F. J., Seen, D. L., Bégué, A., Stape, J.-L., & Nouvellon, Y. (2011). Leaf area index estimation with MODIS reflectance time series and model inversion during full rotations of Eucalyptus plantations. *Remote Sensing of Environment*, 115, 586–599.

Le Maire, G., Nouvellon, Y., Christina, M., Ponzoni, F. J., Gonçalves, J. L. M., Bouillet, J.-P., & Laclau, J.-P. (2013). Tree and stand light use efficiencies over a full rotation of single- and mixed-species Eucalyptus grandis and Acacia mangium plantations. *Forest Ecology and Management*. 288, 31–42.

Le Quéré, C., Andrew, R. M., Canadell, J. G., Sitch, S., Korsbakken, J. I., Peters, G. P., Manning, A. C., Boden, T. A., Tans, P. P., Houghton, R. A., Keeling, R. F., Alin, S., Andrews, O. D., Anthoni, P., Barbero, L., Bopp, L., Chevallier, F., Chini, L. P., Ciais, P., Currie, K., Delire, C., Doney, S. C., Friedlingstein, P., Gkritzalis, T., Harris, I., Hauck, J., Haverd, V., Hoppema, M., Klein Goldewijk, K., Jain, A. K., Kato, E., Körtzinger, A., Landschützer, P., Lefèvre, N., Lenton, A., Lienert, S., Lombardozzi, D., Melton, J. R., Metzl, N., Millero, F., Monteiro, P. M. S., Munro, D. R., Nabel, J. E. M. S., Nakaoka, S., O'Brien, K., Olsen, A., Omar, A. M., Ono, T., Pierrot, D., Poulter, B., Rödenbeck, C., Salisbury, J., Schuster, U., Schwinger, J., Séférian, R., Skjelvan, I., Stocker, B. D., Sutton, A. J., Takahashi, T., Tian, H., Tilbrook, B., van der Laan-Luijkx, I. T., van der Werf, G. R., Viovy, N., Walker, A. P., Wiltshire, A. J., and Zaehle, S., (2016). Global carbon budget 2016. *Earth System Science Data*, *8*(2), 605-649.

Le Quéré, C., Andrew, R. M., Friedlingstein, P., Sitch, S., Hauck, J., Pongratz, J., Pickers, P. A., Korsbakken, J. I., Peters, G. P., Canadell, J. G., Arneth, A., Arora, V. K., Barbero, L., Bastos, A., Bopp, L., Chevallier, F., Chini, L. P., Ciais, P., Doney, S. C., Gkritzalis, T., Goll, D. S., Harris, I., Haverd, V., Hoffman, F. M., Hoppema, M., Houghton, R. A., Hurtt, G., Ilyina, T., Jain, A. K., Johannessen, T., Jones, C. D., Kato, E., Keeling, R. F., Goldewijk, K. K., Landschützer, P., Lefèvre, N., Lienert, S., Liu, Z., Lombardozzi, D., Metzl, N., Munro, D. R., Nabel, J. E. M. S., Nakaoka, S., Neill, C., Olsen, A., Ono, T., Patra, P., Peregon, A., Peters, W., Peylin, P., Pfeil, B., Pierrot, D., Poulter, B., Rehder, G., Resplandy, L., Robertson, E., Rocher, M., Rödenbeck, C., Schuster, U., Schwinger, J., Séférian, R., Skjelvan, I., Steinhoff, T., Sutton, A., Tans, P. P., Tian, H., Tilbrook, B., Tubiello, F. N., van der Laan-Luijkx, I. T., van der Werf, G. R., Viovy, N., Walker, A. P., Wiltshire, A. J., Wright, R., Zaehle, S., and Zheng, B., (2018). Global carbon budget 2018. *Earth System Science Data*, *10*(4), 2141-2194.

Le Quéré, C., Andrew, R. M., Friedlingstein, P., Sitch, S., Hauck, J., Pongratz, J., Pickers, P.A., Korsbakken, J.I., Peters, G.P., Canadell, J.G., & Arneth, A. (2018). Global carbon budget 2018. *Earth System Science Data (Online)*, 10(4).

Le Quéré, C., Peters, GP., Andres, RJ., Andrew, RM., Boden, TA., Ciais, P., Friedlingstein, P., Houghton, RA., Marland, G., Moriarty, R., Sitch, S., Tans, P., Arneth, A., Arvanitis, A., Bakker, DCE., Bopp, L., Canadell, JG., Chini, LP., Doney, SC., Harper, A., Harris, I., House, JI., Jain, AK., Jones, SD., Kato, E., Keeling, RF., Klein, Goldewijk, K., Körtzinger, A., Koven, C., Lefèvre, N., Maignan, F., Omar, A., Ono, T., Park, G-H., Pfeil, B., Poulter, B., Raupach, MR., Regnier, P., Rödenbeck, C., Saito, S., Schwinger, J., Segschneider, J., Stocker, BD., Takahashi, T., Tilbrook, B., van, Heuven, S., Viovy, N., Wanninkhof, R., Wiltshire, A., and Zaehle, S., (2014) Global carbon budget 2013. *Earth System Science Data*, 6(1), 235–263.

Lechowicz, M. J. (1984). Why do temperate deciduous trees leaf-on at different times? Adaptation and ecology of forest communities. *The American Naturalist*, 124(6), 821-842.

Leduc, M., Matthews, H. D., & de Elía, R. (2015). Quantifying the limits of a linear temperature response to cumulative CO_2 emissions. *Journal of Climate*, 28(24), 9955-9968.

Leduc, M., Matthews, H. D., & de Elía, R. (2016). Regional estimates of the transient climate response to cumulative CO_2 emissions. *Nature Climate Change*, 6(5), 474-478.

Lei, Z., Westerband, A. C., Wright, I. J., He, Y., Zhang, W., Cai, X., & Zhang, Y. (2022). Leaf trait covariation and controls on leaf mass per area (LMA) following cotton domestication. *Annals of Botany*, 130(2), 231-243.

Levine, J. M. (2016). Ecology: a trail map for trait-based studies. Nat. 529, 163.

Li, D., Cheng, T., Jia, M., Zhou, K., Lu, N., Yao, X., Tian, Y., Zhu, Y., & Cao, W. (2018). PROCWT: Coupling PROSPECT with continuous wavelet transform to improve the retrieval of foliar chemistry from leaf bidirectional reflectance spectra. *Remote Sensing of Environment*, 206, 1–14.

Li, D., Cheng, T., Yao, X., Zhang, Z., Tian, Y., Zhu, Y., & Cao, W. (2016). Wavelet-based PROSPECT inversion for retrieving leaf mass per area (LMA) and equivalent water thickness (EWT) from leaf reflectance. *2016 IEEE International Geoscience and Remote Sensing Symposium (IGARSS)*. 6910–6913.

Li, D., Tian, L., Wan, Z., Jia, M., Yao, X., Tian, Y., Zhu, Y., Cao, W., & Cheng, T. (2019). Assessment of unified models for estimating leaf chlorophyll content across directional-hemispherical reflectance and bidirectional reflectance spectra. *Remote Sensing of Environment*, 111240.

Li, H., Yang, W., Lei, J., She, J., & Zhou, X. (2021). Estimation of leaf water content from hyperspectral data of different plant species by using three new spectral absorption indices. *PloS One*, 16(3), e0249351.

Li, D., Tian, L., Wan, Z., Jia, M., Yao, X., Tian, Y., & Cheng, T. (2019a). Assessment of unified models for estimating leaf chlorophyll content across directional-hemispherical reflectance and bidirectional reflectance spectra. *Remote Sensing of Environment*, 231, 111240.

Li, W., Zhang, Y., Shi, X., Zhou, W., Huang, A., Mu, M., Qiu, B., and Ji, J. (2019b). Development of land surface model BCC_AVIM2. 0 and its preliminary performance in LS3MIP/CMIP6. *Journal of Meteorological Research*, *33*(5), 851-869.

Liang, J., Qi, X., Souza, L., and Luo, Y. (2016). Processes regulating progressive nitrogen limitation under elevated carbon dioxide: a meta-analysis. *Biogeosciences*, *13*(9), 2689-2699.

Lichtenthaler, H. (1987). Chlorophyll and carotenoids: pigments of photosynthetic biomembranes. *Methods in Enzymology*. 148, 331–382.

Liddicoat, S. K., Booth, B. B. B., & Joshi, M. M. (2016). An investigation into linearity with cumulative emissions of the climate and carbon cycle response in HadCM3LC. *Environmental Research Letters*, 11(6), 065003.

Lieth, H. (1974). Phenology and Seasonality Modeling. *Springer-Verlag, New York.*

Lieth, H. (1974). Phenology and Seasonality Modeling. *Springer-Verlag*, New York.

Ling, Y., Teng, S., Liu, C., Dash, J., Morris, H., & Pastor-Guzman, J. (2022). Assessing the Accuracy of Forest Phenological Extraction from Sentinel-1 C-Band Backscatter Measurements in Deciduous and Coniferous Forests. *Remote Sensing*, 14(3), 674.

Linnaeus, C. (1751). Philosophia botanica. *Stockholmiae [Stockholm]: apud Godofr*. Kiesewetter.

Liu, G., Chuine, I., Denéchère, R., Jean, F., Dufrêne, E., Vincent, G., & Delpierre, N. (2021). Higher sample sizes and observer inter-calibration are needed for reliable scoring of leaf phenology in trees. *Journal of Ecology*, 109(6), 2461-2474.

Liu, N., Garcia, M., Singh, A., Clare, J. D., Stenglein, J. L., Zuckerberg, B., Kruger, E. L., & Townsend, P. A. (2021). Trail camera networks provide insights into satellite-derived phenology for ecological studies. *International Journal of Applied Earth Observation and Geoinformation*, 97, 102291.

Liu, Q., Piao, S., Campioli, M., Gao, M., Fu, Y. H., Wang, K., He, Y., Li, X., & Janssens, I. A. (2020). Modeling leaf senescence of deciduous tree species in Europe. *Global Change Biology*, 26(7), 4104-4118.

Liu, S., Zheng, Y., Ma, R., Yu, K., Han, Z., Xiao, S., & Zou, J. (2020). Increased soil release of greenhouse gases shrinks terrestrial carbon uptake enhancement under warming. *Global Change Biology*, 26(8), 4601-4613.

Liu, Y. Y., Van Dijk, A. I., De Jeu, R. A., Canadell, J. G., McCabe, M. F., Evans, J. P., and Wang, G. (2015). Recent reversal in loss of global terrestrial biomass. *Nature Climate Change*, *5*(5), 470-474.

Liu, Y., Xiao, J., Ju, W., Zhu, G., Wu, X., Fan, W., and Zhou, Y. (2018). Satellite-derived LAI products exhibit large discrepancies and can lead to substantial uncertainty in simulated carbon and water fluxes. *Remote Sensing of Environment*, *206*, 174-188.

Liu, Z., Jiang, F., Li, F., & Jin, G. (2019). Coordination of intra and inter-species leaf traits according to leaf phenology and plant age for three temperate broadleaf species with different shade tolerances. *Forest ecology and management*, 434, 63-75.

Lopes, A. P., Nelson, B. W., Wu, J., de Alencastro Graça, P. M. L., Tavares, J. V., Prohaska, N., Martins, G.A., & Saleska, S. R. (2016). Leaf flush drives dry season green-up of the Central Amazon. *Remote Sensing of Environment*, 182, 90-98.

Loveland, T. R., Reed, B. C., Brown, J. F., Ohlen, D. O., Zhu, Z., Yang, L. W. M. J., and Merchant, J. W. (2000). Development of a global land cover characteristics database and IGBP DISCover from 1 km AVHRR data. *International Journal of Remote Sensing*, *21*(6-7), 1303-1330.

Lovenduski, N. S., & Bonan, G. B. (2017). Reducing uncertainty in projections of terrestrial carbon uptake. *Environmental Research Letters*, 12(4), 044020.

Lovenduski, N. S., and Bonan, G. B. (2017). Reducing uncertainty in projections of terrestrial carbon uptake. *Environmental Research Letters*, *12*(4), 044020.

Lovett, G. M., Cole, J. J., and Pace, M. L. (2006). Is net ecosystem production equal to ecosystem carbon accumulation?. *Ecosystems*, *9*(1), 152-155.

Löw, M., & Koukal, T. (2020). Phenology Modelling and Forest Disturbance Mapping with Sentinel-2 Time Series in Austria. *Remote Sensing*, 12(24), 4191.

Lu, X., & Keenan, T. F. (2022). No evidence for a negative effect of growing season photosynthesis on leaf senescence timing. *Global Change Biology*, 28(9), 3083-3093.

Lu, S., Lu, F., You, W., Wang, Z., Liu, Y., & Omasa, K. (2018). A robust vegetation index for remotely assessing chlorophyll content of dorsiventral leaves across several species in different seasons. Plant methods. 14(1), 15.

Lukasová, V., Vido, J., Škvareninová, J., Bičárová, S., Hlavatá, H., Borsányi, P., & Škvarenina, J. (2020). Autumn phenological response of European Beech to summer drought and heat. *Water*, 12(9), 2610.

Luyssaert, S., Inglima, I., Jung, M., Richardson, A. D., Reichstein, M., Papale, D., Piao, S.L., Schulze, E.D., Wingate, L., Matteucci, G. & Aragao, L.E.O.C. (2007). CO_2 balance of boreal, temperate, and tropical forests derived from a global database. *Global Change Biology*. 13, 2509–2537.

MacDougall, A. H. (2015). The transient response to cumulative CO_2 emissions: a review. *Current Climate Change Reports*, 2(1), 39-47.

MacDougall, A. H. (2017). The oceanic origin of path-independent carbon budgets. *Scientific Reports*, 7(1), 1-12.

MacDougall, A. H. (2019). Limitations of the 1% experiment as the benchmark idealized experiment for carbon cycle intercomparison in C^4MIP. *Geoscientific Model Development*, 12(2), 597-611.

MacDougall, A. H., & Friedlingstein, P. (2015). The origin and limits of the near proportionality between climate warming and cumulative CO_2 emissions. *Journal of Climate*, 28(10), 4217-4230.

MacDougall, A. H., Swart, N. C., & Knutti, R. (2017). The uncertainty in the transient climate response to cumulative CO_2 emissions arising from the uncertainty in physical climate parameters. *Journal of Climate*, 30(2), 813-827.

MacDougall, A. H., Zickfeld, K., Knutti, R., & Matthews, H. D. (2015). Sensitivity of carbon budgets to permafrost carbon feedbacks and non-CO_2 forcings. *Environmental Research Letters*, 10(12), 125003.

Mack, P. E. (1990). *Viewing the Earth: The social construction of the Landsat satellite system*. MIT Press.

MacKay, A. H. (1903). Phenological observations in Nova Scotia and Canada, 1901. *Proceedings of the Nova Scotian Institute of Science*, 10, 1898-1902.

MacLean, D. A., Taylor, A. R., Neily, P. D., Steenberg, J. W., Basquill, S. P., Quigley, E., Boone, C.K., Oikle, M., Bush, P., & Stewart, B. (2022). Natural disturbance regimes for implementation of ecological forestry: a review and case study from Nova Scotia, Canada. *Environmental Reviews*, 30(1), 128-158.

Maire, V., Wright, I. J., Prentice, I. C., Batjes, N. H., Bhaskar, R., van Bodegom, P. M., Cornwell, W.K., Ellsworth, D., Niinemets, Ü., Ordonez, A. & Reich, P.B. (2015). Global effects of soil and climate on leaf photosynthetic traits and rates. Global Ecology and Biogeography. 24, 706–717.

Maki, T., Ikegami, M., Fujita, T., Hirahara, T., Yamada, K., Mori, K., Takeuchi, A., Tsutsumi, Y., Suda, K., and Conway, T. J. (2010). New technique to analyse global distributions of CO_2 concentrations and fluxes from non-processed observational data. *Tellus B*, 62, 797–

809.

Malhi, Y., Aragao, L. E. O., Metcalfe, D. B., Paiva, R., Quesada, C. A., Almeida, S., Anderson, L., Brando, P., Chamber, J. Q., and da Costa, A. C. L. (2009). Comprehensive assessment of carbon productivity, allocation and storage in three Amazonian forests. *Global Change Biology*, *15*(5), 1255-1274.

Marchand, L. J., Dox, I., Gričar, J., Prislan, P., Van den Bulcke, J., Fonti, P., & Campioli, M. (2021). Timing of spring xylogenesis in temperate deciduous tree species relates to tree growth characteristics and previous autumn phenology. *Tree Physiology*, 41(7), 1161-1170.

Maréchaux, I., Bartlett, M. K., Gaucher, P., Sack, L., Chave, J. (2016). Causes of variation in leaf-level drought tolerance within an Amazonian forest. Journal of Plant Hydraulics. 3, e004.

Marquis, B., Bergeron, Y., Houle, D., Leduc, M., & Rossi, S. (2022). Variability in frost occurrence under climate change and consequent risk of damage to trees of western Quebec, Canada. *Scientific Reports*, 12(1), 1-15.

Marquis, B., Bergeron, Y., Simard, M., & Tremblay, F. (2020). Probability of spring frosts, not growing degree-days, drives onset of spruce bud burst in plantations at the boreal-temperate forest ecotone. *Frontiers in Plant Science*, 11, 1031.

Martin, A. R. Isaac, M. E. (2015). Plant functional traits in agroecosystems: a blueprint for research. Journal of Applied Ecology. 52, 1425–1435.

Martin, M., Gavazov, K., Koerner, C., Haettenschwiler, S., & Rixen, C. (2010). Reduced early growing season freezing resistance in alpine treeline plants under elevated atmospheric CO2. *Global Change Biology*, *16*(3), 1057-1070.

Martin, R., Chadwick, K., Brodrick, P., Carranza-Jimenez, L., Vaughn, N., Asner, G. (2018). An approach for foliar trait retrieval from airborne imaging spectroscopy of tropical forests. Remote Sensing, 10, 199.

Matiu, M., Bothmann, L., Steinbrecher, R., & Menzel, A. (2017). Monitoring succession after a non-cleared windthrow in a Norway spruce mountain forest using webcam, satellite vegetation indices and turbulent CO2 exchange. *Agricultural and Forest Meteorology*, 244, 72-81.

Matsumoto, K., Ohta, T., Irasawa, M., & Nakamura, T. (2003). Climate change and extension of the Ginkgo biloba L. growing season in Japan. *Global Change Biology*, 9(11), 1634-1642.

Matthews, H. D., Gillett, N. P., Stott, P. A., & Zickfeld, K. (2009). The proportionality of global warming to cumulative carbon emissions. *Nature*, 459(7248), 829-832.

Matthews, H. D., Graham, T. L., Keverian, S., Lamontagne, C., Seto, D., & Smith, T. J. (2014). National contributions to observed global warming. *Environmental Research Letters*, 9(1), 014010.

Matthews, H. D., Landry, J. S., Partanen, A. I., Allen, M., Eby, M., Forster, P. M., & Zickfeld, K. (2017). Estimating carbon budgets for ambitious climate targets. *Current Climate Change Reports*, 3(1), 69-77.

Matthews, H. D., Landry, J. S., Partanen, A. I., Allen, M., Eby, M., Forster, P. M., Friedlingstein, P., & Zickfeld, K. (2017). Estimating carbon budgets for ambitious climate targets. *Current Climate Change Reports*, 3(1), 69-77.

Matthews, H. D., Solomon, S., & Pierrehumbert, R. (2012). Cumulative carbon as a policy framework for achieving climate stabilization. *Philosophical Transactions of the Royal Society A: Mathematical, Physical and Engineering Sciences*, 370(1974), 4365-4379.

Matthews, H. D., Zickfeld, K., Knutti, R., & Allen, M. R. (2018). Focus on cumulative emissions, global carbon budgets and the implications for climate mitigation targets. *Environmental Research Letters*, 13(1), 010201.

Matyas, C. J. (2017). Comparing the spatial patterns of rainfall and atmospheric moisture among tropical cyclones having a track similar to Hurricane Irene (2011). *Atmosphere*, 8(9), 165.

Mauritsen, T., Bader, J., Becker, T., Behrens, J., Bittner, M., Brokopf, R., Brovkin, V., Claussen, M., Crueger, T., Esch, M., Fast, I., Fiedler, S., Fläschner, D., Gayler, V., Giorgetta, M., Goll, D. S., Haak, H., Hagemann, S., Hedemann, C., Hohenegger, C., Ilyina, T., Jahns, T., Jimenéz-de-la-Cuesta, D., Jungclaus, J., Kleinen, T., Kloster, S., Kracher, D., Kinne, S., Kleberg, D., Lasslop, G., Kornblueh, L., Marotzke, J., Matei, D., Meraner, K., Mikolajewicz, U., Modali, K., Möbis, B., Müller, W. A., Nabel, J. E. M. S., Nam, C. C. W., Notz, D., Nyawira, S.-S., Paulsen, H., Peters, K., Pincus, R., Pohlmann, H., Pongratz, J., Popp, M., Raddatz, T. J., Rast, S., Redler, R., Reick, C. H., Rohrschneider, T., Schemann, V., Schmidt, H., Schnur, R., Schulzweida, U., Six, K. D., Stein, L., Stemmler, I., Stevens, B., von Storch, J.-S., Tian, F., Voigt, A., Vrese, P., Wieners, K.-H., Wilkenskjeld, S., Winkler, A., and Roeckner, E. (2019). Developments in the MPI-M Earth System Model version 1.2 (MPI-ESM1. 2) and its response to increasing CO2. *Journal of Advances in Modeling Earth Systems*, *11*(4), 998-1038.

Mayorga, E., Seitzinger, S. P., Harrison, J. A., Dumont, E., Beusen, A. H. W., Bouwman, A. F., Fekete, B. M., Kroeze, C., and Van Drecht, G. (2010). Global nutrient export from WaterSheds 2 (NEWS 2): model development and implementation. *Environmental Modelling and Software*, *25*(7), 837-853.

McGroddy, M. E., Daufresne, T., and Hedin, L. O. (2004). Scaling of C: N: P stoichiometry in forests worldwide: Implications of terrestrial redfield-type ratios. *Ecology*, *85*(9), 2390-2401.

McKenney, D. W., Hutchinson, M. F., Papadopol, P., Lawrence, K., Pedlar, J., Campbell, K., Milewska, E., Hopkinson, R. F., & Price, D. (2013). Spatial climate models for Canada's forestry community. *The Forestry Chronicle*, 89, 659-663.

McKenney, D. W., Pedlar, J. H., Lawrence, K., Campbell, K., & Hutchinson, M. F. (2007). Potential impacts of climate change on the distribution of North American trees. *BioScience*, 57(11), 939-948.

Mckenney, D. W., Pedlar, J. H., Lawrence, K., Papadopol, P., Campbell, K., & Hutchinson, M. F. (2014). Change and evolution in the plant hardiness zones of Canada. *BioScience*, 64(4), 341-350.

McKenney, D. W., Pedlar, J. H., Rood, R. B., & Price, D. (2011). Revisiting projected shifts in the climate envelopes of North American trees using updated general circulation models. *Global Change Biology*, 17(8), 2720-2730.

McLennan, D., & Zorn, P. (2005). Monitoring for ecological integrity and state of the parks reporting. *Monitoring in Ontario's Parks and Protected Areas*, 35.

Medvigy, D., Jeong, S. J., Clark, K. L., Skowronski, N. S., & Schäfer, K. V. (2013). Effects of seasonal variation of photosynthetic capacity on the carbon fluxes of a temperate deciduous forest. *Journal of Geophysical Research: Biogeosciences*, 118(4), 1703-1714.

Meier, M., Vitasse, Y., Bugmann, H., & Bigler, C. (2021). Phenological shifts induced by climate change amplify drought for broad-leaved trees at low elevations in Switzerland. *Agricultural and Forest Meteorology*, *307*, 108485.

Meinshausen, M., Meinshausen, N., Hare, W., Raper, S. C., Frieler, K., Knutti, R., Frame, D.J., & Allen, M. R. (2009). Greenhouse-gas emission targets for limiting global warming to 2°C. *Nature*, 458(7242), 1158-1162.

Melaas, E. K., Friedl, M. A., & Richardson, A. D. (2016). Multiscale modeling of spring phenology across Deciduous Forests in the Eastern United States. *Global Change Biology*, 22(2), 792-805.

Mengis, N., Partanen, A. I., Jalbert, J., & Matthews, H. D. (2018). 1.5°C carbon budget dependent on carbon cycle uncertainty and future non-CO_2 forcing. *Scientific Reports*, 8(1), 1-7.

Menzel, A., & Fabian, P. (1999). Growing season extended in Europe. *Nature*, 397(6721), 659.

Menzel, A., Helm, R., & Zang, C. (2015). Patterns of late spring frost leaf damage and recovery in a European beech (Fagus sylvatica L.) stand in south-eastern Germany based on repeated digital photographs. *Frontiers in Plant Science,* 6, 110.

Menzel, A., Sparks, T. H., Estrella, N., Koch, E., Aasa, A., Ahas, R., Alm-Kübler, K., Bissolli, P., Braslavská, O.G., Briede, A., & Chmielewski, F. M. (2006). European phenological response to climate change matches the warming pattern. *Global Change Biology*, 12(10), 1969-1976.

Merzlyak, M. N., Chivkunova, O. B., Solovchenko, A. E., & Naqvi, K. R. (2008). Light absorption by anthocyanins in juvenile, stressed, and senescing leaves. Journal of Experimental Botany. 59, 3903–3911.

Merzlyak, M. N., Melø, T., & Naqvi, K. R. (2004). Estimation of leaf transmittance in the near infrared region through reflectance measurements. Journal of Photochemistry and Photobiology B: Biology. 74, 1011–1344. https://doi.org/10.1016/j.jphotobiol.2004.03.003.

Messner, D., Schellnhuber, J., Rahmstorf, S., & Klingenfield, J. (2013) The budget approach framework for a global transformation towards a low carbon economy Climate Change and Environmental Hazards Related to Shipping: An International Legal Framework. *Leiden: Brill Nijhoff*, 9-33.

Migliavacca, M., Sonnentag, O., Keenan, T. F., Cescatti, A., O'Keefe, J., & Richardson, A. D. (2012). On the uncertainty of phenological responses to climate change, and implications for a terrestrial biosphere model. *Biogeosciences*, 9(6), 2063-2083.

Millar, R. J., & Friedlingstein, P. (2018). The utility of the historical record for assessing the transient climate response to cumulative emissions. *Philosophical Transactions of the Royal Society A: Mathematical, Physical and Engineering Sciences*, 376(2119), 20160449.

Millar, R. J., Fuglestvedt, J. S., Friedlingstein, P., Rogelj, J., Grubb, M. J., Matthews, H. D., Skeie, R.B., Forster, P.M., Frame, D.J., & Allen, M. R. (2017a). Emission budgets and pathways consistent with limiting warming to 1.5°C. *Nature Geoscience*, 10(10), 741-747.

Millar, R. J., Nicholls, Z. R., Friedlingstein, P., & Allen, M. R. (2017b). A modified impulse-response representation of the global near-surface air temperature and atmospheric concentration response to carbon dioxide emissions. *Atmospheric Chemistry and Physics*, 17(11), 7213-7228.

Misra, G., Buras, A., Heurich, M., Asam, S., & Menzel, A. (2018). LiDAR derived topography and forest stand characteristics largely explain the spatial variability observed in MODIS land surface phenology. *Remote Sensing of Environment*, *218*, 231-244.

Mitchell, T. D., and Jones, P. D. (2005). An improved method of constructing a database of monthly climate observations and associated high-resolution grids. *International Journal of Climatology: A Journal of the Royal Meteorological Society*, *25*(6), 693-712.

Mizunuma, T., Wilkinson, M., L. Eaton, E., Mencuccini, M., IL Morison, J., & Grace, J. (2013). The relationship between carbon dioxide uptake and canopy color from two camera systems in a deciduous forest in southern England. *Functional Ecology*, 27(1), 196-207.

Monfreda, C., Ramankutty, N., and Foley, J. A. (2008). Farming the planet. Part 2: Geographic distribution of crop areas, yields, physiological types, and net primary production in the year 2000. *Global Biogeochemical Cycles*, GB1022.

Montgomery, R. A., Rice, K. E., Stefanski, A., Rich, R. L., & Reich, P. B. (2020). Phenological responses of temperate and boreal trees to warming depend on ambient spring temperatures, leaf habit, and geographic range. *Proceedings of the National Academy of Sciences*, 117(19), 10397-10405.

Moon, M., Richardson, A. D., & Friedl, M. A. (2021b). Multiscale assessment of land surface phenology from harmonized Landsat 8 and Sentinel-2, PlanetScope, and PhenoCam imagery. *Remote Sensing of Environment*, 266, 112716.

Moon, M., Seyednasrollah, B., Richardson, A. D., & Friedl, M. A. (2021a). Using time series of MODIS land surface phenology to model temperature and photoperiod controls on spring greenup in North American deciduous forests. *Remote Sensing of Environment*, *260*, 112466.

Moreno-Martínez, Á., Camps-Valls, G., Kattge, J., Robinson, N., Reichstein, M., van Bodegom, P., Kramer, K., Cornelissen, J.H.C., Reich, P., Bahn, M. & Niinemets, Ü. (2018). A methodology to derive global maps of leaf traits using remote sensing and climate data. Remote Sensing of Environment, 218, 69–88.

Morin, X., Lechowicz, M. J., Augspurger, C., O'Keefe, J. O. H. N., Viner, D., & Chuine, I. (2009). Leaf phenology in 22 North American tree species during the 21st century. *Global Change Biology*, 15(4), 961-975.

Morisette, J. T., Richardson, A. D., Knapp, A. K., Fisher, J. I., Graham, E. A., Abatzoglou, J., Wilson, B.E., Breshears, D.D., Henebry, G.M., Hanes, J.M., & Liang, L. (2009). Tracking the rhythm of the seasons in the face of global change: phenological research in the 21st century. *Frontiers in Ecology and the Environment*, 7(5), 253-260.

Mouillot, F., and Field, C. B. (2005). Fire history and the global carbon budget: A 1° × 1° fire history reconstruction for the 20th century. *Global Change Biology*, 11(3), 398– 420.

Murray, B. R., Hardstaff, L. K., & Phillips, M. L. (2013). Differences in leaf flammability, leaf traits and flammability-trait relationships between native and exotic plant species of dry sclerophyll forest. *PLoS One*. 8, e79 205.

Murray, M. B., Cannell, M. G. R., & Smith, R. I. (1989). Date of budburst of fifteen tree species in Britain following climatic warming. *Journal of Applied Ecology*, 693-700.

Myhre, G., Highwood, E. J., Shine, K. P., & Stordal, F. (1998). New estimates of radiative forcing due to well mixed greenhouse gases. *Geophysical Research Letters*, 25(14), 2715-2718.

Myneni, R. B., Ramakrishna, R., Nemani, R., and Running, S. W. (1997). Estimation of global leaf area index and absorbed PAR using radiative transfer models. *IEEE Transactions on Geoscience and remote sensing*, *35*(6), 1380-1393.

Nagler, P. L., Pearlstein, S., Glenn, E. P., Brown, T. B., Bateman, H. L., Bean, D. W., & Hultine, K. R. (2014). Rapid dispersal of saltcedar (Tamarix spp.) biocontrol beetles (Diorhabda carinulata) on a desert river detected by phenocams, MODIS imagery and ground observations. *Remote Sensing of Environment*, *140*, 206-219.

Nakaji, T., Oguma, H., & Hiura, T. (2011). Ground-based monitoring of the leaf phenology of deciduous broad-leaved trees using high resolution NDVI camera images. *Journal of Agricultural Meteorology*, *67*(2), 65-74.

NASA LP DAAC. (2017). MOD17A3 Terra/MODIS net primary production yearly L4 global 1 km. NASA EOSDIS Land Processes DAAC, USGS Earth Resources Observation and Science (EROS) Center, Sioux Falls, South Dakota (https://lpdaac.usgs.gov), at https://doi.org/10.5067/ASTER/AST_L1T.003.

Neily, P., Keys, K., Quigley, E., Basquill, S., & Stewart, B. (2013). *Forest ecosystem classification for Nova Scotia*. Truro, NS: Nova Scotia Department of Natural Resources.

Niinemets, Ü. (2010). Responses of forest trees to single and multiple environmental stresses from seedlings to mature plants: past stress history, stress interactions, tolerance and acclimation. *Forest Ecology and management*, 260(10), 1623-1639.

Nijsse, F. J., Cox, P. M., & Williamson, M. S. (2020). Emergent constraints on transient climate response (TCR) and equilibrium climate sensitivity (ECS) from historical warming in CMIP5 and CMIP6 models. *Earth System Dynamics*, 11(3), 737-750.

Nohara, D., Tsutsui, J., Watanabe, S., Tachiiri, K., Hajima, T., Okajima, H., & Matsuno, T. (2015). Examination of a climate stabilization pathway via zero-emissions using Earth system models. *Environmental Research Letters*, 10(9), 095005.

Nölte, A., Yousefpour, R., & Hanewinkel, M. (2020). Changes in sessile oak (Quercus petraea) productivity under climate change by improved leaf phenology in the 3-PG model. *Ecological Modelling*, 438, 109285.

Norby, R. J., DeLucia, E. H., Gielen, B., Calfapietra, C., Giardina, C. P., King, J. S., and Oren, R. (2005). Forest response to elevated CO2 is conserved across a broad range of productivity. *Proceedings of the National Academy of Sciences*, *102*(50), 18052-18056.

Norby, R. J., Hartz-Rubin, J. S., & Verbrugge, M. J. (2003). Phenological responses in maple to experimental atmospheric warming and CO2 enrichment. *Global Change Biology*, 9(12), 1792-1801.

Noseworthy, J., & Beckley, T. M. (2020). Borealization of the New England–Acadian Forest: a review of the evidence. *Environmental Reviews*, 28(3), 284-293.

Nouvellon, Y., Laclau, J.-P., Epron, D., Kinana, A., Mabiala, A., Roupsard, O., Bonnefond, J.M., Le Maire, G., Marsden, C., Bontemps, J.D. & Saint-Andre, L. (2010). Within-stand and seasonal variations of specific leaf area in a clonal Eucalyptus plantation in the Republic of Congo. Forest ecology and management. 259, 1796–1807.

Nowak, R. S., Ellsworth, D. S., and Smith, S. D. (2004). Functional responses of plants to elevated atmospheric CO_2–do photosynthetic and productivity data from FACE experiments support early predictions?. *New phytologist*, *162*(2), 253-280.

Nunes, M. H., Davey, M. P., & Coomes, D. A. (2017). On the challenges of using field spectroscopy to measure the impact of soil type on leaf traits. Biogeosciences. 14, 3371–3385.

Oliveira, J., Féret, J. B., Ponzoni, F. J., Nouvellon, Y., Gastellu-Etchegorry, J. P., Campoe, O. C., Stape, J.L., Rodriguez, L.C.E. & Le Maire, G. (2017). Simulating the canopy reflectance of different eucalypt genotypes with the DART 3-D model. IEEE Journal of Selected Topics in Applied Earth Observations and Remote Sensing. 10(11), 4844-4852.

Olson, D. M., Dinerstein, E., Wikramanayake, E. D., Burgess, N. D., Powell, G. V. N., Underwood, E. C., D'amico, J. A., Itoua, I., Strand, H. E., Morrison, J. C., Loucks, C. J., Allnutt, T. F., Ricketts, T. H., Kura, Y., Lamoreux, J. F., Wettengel, W. W., Hedao, P., and Kassem, K. R. (2006). Terrestrial Ecoregions of the World: A New Map of Life on Earth. *BioScience*, *51*(11), 933-938.

Olson, R., Sriver, R., Goes, M., Urban, N. M., Matthews, H. D., Haran, M., & Keller, K. (2012). A climate sensitivity estimate using Bayesian fusion of instrumental observations and an Earth System model. *Journal of Geophysical Research: Atmospheres*, 117(D4).

Ordóñez, C., & Duinker, P. N. (2012). Ecological integrity in urban forests. *Urban Ecosystems*, 15(4), 863-877.

Orth, R., Dutra, E., Trigo, I. F., and Balsamo, G. (2017). Advancing land surface model development with satellite-based Earth observations. *Hydrology and Earth System Sciences*, *21*(5), 2483-2495.

Pappas, C., Fatichi, S., & Burlando, P. (2016). Modeling terrestrial carbon and water dynamics across climatic gradients: does plant trait diversity matter?. *New Phytologist*, 209(1), 137-151.

Parks Canada Agency. (2011). Consolidated Guidelines for Ecological Integrity Monitoring in Canada's National Parks. Protected Areas Establishment and Conservation Branch, Parks Canada.

Parmentier, F. J. W., Nilsen, L., Tømmervik, H., & Cooper, E. J. (2021). A distributed time-lapse camera network to track vegetation phenology with high temporal detail and at varying scales. *Earth System Science Data*, 13(7), 3593-3606.

Partanen, A. I., Leduc, M., & Matthews, H. D. (2017). Seasonal climate change patterns due to cumulative CO_2 emissions. *Environmental Research Letters*, 12(7), 075002.

Pasquarella, V. J., Elkinton, J. S., & Bradley, B. A. (2018). Extensive gypsy moth defoliation in Southern New England characterized using Landsat satellite observations. *Biological Invasions*, 20(11), 3047-3053.

Pastorello, G., Trotta, C., Canfora, E., Chu, H., Christianson, D., Cheah, Y. W., Li, Y. (2020). The Fluxnet2015 dataset and the ONEFlux processing pipeline for eddy covariance data. *Scientific data*, *7*(1), 1-27.

Patarasuk, R., Gurney, K. R., O'Keeffe, D., Song, Y., Huang, J., Rao, P., Buchert, M., Lin, J.C., Mendoza, D., & Ehleringer, J. R. (2016). Urban high-resolution fossil fuel CO_2 emissions quantification and exploration of emission drivers for potential policy applications. *Urban Ecosystems*, 19(3), 1013-1039.

Paynter, D., & Frölicher, T. L. (2015). Sensitivity of radiative forcing, ocean heat uptake, and climate feedback to changes in anthropogenic greenhouse gases and aerosols. *Journal of Geophysical Research: Atmospheres*, 120(19), 9837-9854.

Pearson, E., & D'Orangeville, L. (2022). Relating the Growth Phenology and Biomass Allocation in Seedlings of 13 Acadian Tree Species With Their Drought Tolerance. *Frontiers in Forests and Global Change*, 16.

Peltoniemi, M., Aurela, M., Böttcher, K., Kolari, P., Loehr, J., Hokkanen, T., Karhu, J., Linkosalmi, M., Tanis, C.M., Metsämäki, S., Tuovinen, J.P., & Arslan, A. N. (2018). Networked web-cameras monitor congruent seasonal development of birches with phenological field observations. *Agricultural and Forest Meteorology*, 249, 335-347.

Peñuelas, J., & Filella, I. (2001). Responses to a warming world. *Science*, 294(5543), 793-795.

Peñuelas, J., & Filella, I. (2009). Phenology feedbacks on climate change. *Science*, 324(5929), 887-888.

Peñuelas, J., Filella, I., & Comas, P. (2002). Changed plant and animal life cycles from 1952 to 2000 in the Mediterranean region. *Global Change Biology*, 8(6), 531-544.

Peters, G. P. (2018). Beyond carbon budgets. *Nature Geoscience*, 11(6), 378-380.

Phillips, L. B., Hansen, A. J., and Flather, C. H. (2008). Evaluating the species energy relationship with the newest measures of ecosystem energy: NDVI versus MODIS primary production. *Remote Sensing of Environment*, *112*(12), 4381-4392.

Piao, S., Ciais, P., Friedlingstein, P., Peylin, P., Reichstein, M., Luyssaert, S., & Vesala, T. (2008). Net carbon dioxide losses of northern ecosystems in response to autumn warming. *Nature*, 451(7174), 49-52.

Piao, S., Friedlingstein, P., Ciais, P., Viovy, N., & Demarty, J. (2007). Growing season extension and its impact on terrestrial carbon cycle in the Northern Hemisphere over the past 2 decades. *Global Biogeochemical Cycles*, 21(3).

Piao, S., Liu, Q., Chen, A., Janssens, I. A., Fu, Y., Dai, J., Liu, L., Lian, X.U., Shen, M., & Zhu, X. (2019). Plant phenology and global climate change: Current progresses and challenges. *Global Change Biology*, 25(6), 1922-1940.

Piao, S., Liu, Q., Chen, A., Janssens, I. A., Fu, Y., Dai, J., Zhu, X. (2019). Plant phenology and global climate change: Current progresses and challenges. *Global change biology*, *25*(6), 1922-1940.

Polgar, C. A., & Primack, R. B. (2011). Leaf-out phenology of temperate woody plants: from trees to ecosystems. *New phytologist*, *191*(4), 926-941.

Poulter, B., MacBean, N., Hartley, A., Khlystova, I., Arino, O., Betts, R., Bontemps, S., Boettcher, M., Brockmann, C., Defourny, P., Hagemann, S., Herold, M., Kirches, G., Lamarche, C., Lederer, D., Ottlé, C., Peters, M., and Peylin, P. (2015). Plant functional type classification for earth system models: results from the European Space Agency's Land Cover Climate Change Initiative. *Geoscientific Model Development*, *8*(7), 2315-2328.

Price, D. T., Alfaro, R. I., Brown, K. J., Flannigan, M. D., Fleming, R. A., Hogg, E. H., Girardin, M.P., Lakusta, T., Johnston, M., McKenney, D.W., Pedlar, J.H., & Venier, L. A. (2013). Anticipating the consequences of climate change for Canada’s boreal forest ecosystems. *Environmental Reviews*, 21(4), 322-365.

Price, D. T., McKenney, D. W., Joyce, L. A., Siltanen, R. M., Papadopol, P., & Lawrence, K. (2011). *High-resolution interpolation of climate scenarios for Canada derived from general circulation model simulations*. Edmonton, AB: Canadian Forest Service, Northern Forestry Centre.

Pueyo, S. (2012). Solution to the paradox of climate sensitivity. *Climatic Change*, 113(2), 163-179.

Pureswaran, D. S., Neau, M., Marchand, M., De Grandpré, L., & Kneeshaw, D. (2019). Phenological synchrony between eastern spruce budworm and its host trees increases with warmer temperatures in the boreal forest. *Ecology and Evolution*, 9(1), 576-586.

Purkey, S. G., & Johnson, G. C. (2013). Antarctic Bottom Water warming and freshening: Contributions to sea level rise, ocean freshwater budgets, and global heat gain. *Journal of Climate*, 26(16), 6105-6122.

Python Software Foundation. (2022). Selenium 4.5.0 Available at: https://pypi.org/project/selenium/.

Qi, Y., Dennison, P. E., Jolly, W. M., Kropp, R. C., & Brewer, S. C. (2014). Spectroscopic analysis of seasonal changes in live fuel moisture content and leaf dry mass. Remote Sensing of Environment, 150, 198–206.

Qiu, F., Chen, J. M., Croft, H., Li, J., Zhang, Q., Zhang, Y., & Ju, W. (2019). Retrieving Leaf Chlorophyll Content by Incorporating Variable Leaf Surface Reflectance in the PROSPECT Model. Remote Sensing, 11, 1572.

Qiu, F., Chen, J. M., Ju, W., Wang, J., Zhang, Q., & Fang, M. (2018). Improving the PROSPECT Model to Consider Anisotropic Scattering of Leaf Internal Materials and Its Use for Retrieving Leaf Biomass in Fresh Leaves. IEEE TRANSACTIONS ON GEOSCIENCE AND REMOTE SENSING. 56, 3119–3136. https://doi.org/10.1109/TGRS.2018.2791930.

R Core Team (2022). R: A language and environment for statistical computing. *R Foundation for Statistical Computing, Vienna, Austria*. https://www.R-project.org/.

Randerson, J. T., Lindsay, K., Munoz, E., Fu, W., Moore, J. K., Hoffman, F. M., Mahowald, N.M., & Doney, S. C. (2015). Multicentury changes in ocean and land contributions to the climate-carbon feedback. *Global Biogeochemical Cycles*, 29(6), 744-759.

Randerson, J.T., G.R. van der Werf, L. Giglio, G.J. Collatz, and P.S. Kasibhatla. (2017). Global fire emissions database, version 4.1 (GFEDv4). ORNL DAAC, Oak Ridge, Tennessee, USA.

Raupach, M. R., Canadell, J. G., Ciais, P., Friedlingstein, P., Rayner, P. J., & Trudinger, C. M. (2011). The relationship between peak warming and cumulative CO_2 emissions, and its use to quantify vulnerabilities in the carbon-climate-human system. *Tellus B: Chemical and Physical Meteorology*, 63(2), 145-164.

Reich, P. B., Walters, M. B., & Ellsworth, D. S. (1992). Leaf life-span in relation to leaf, plant, and stand characteristics among diverse ecosystems. *Ecological monographs*, 62(3), 365-392.

Reich, P. B., Walters, M. B., Ellsworth, D. S. (1997). From tropics to tundra: global convergence in plant functioning. Proceedings of the National Academy of Sciences. 94, 13 730–13 734.

Reichler, T., and Kim, J. (2008). How well do coupled models simulate today's climate?. *Bulletin of the American Meteorological Society*, *89*(3), 303-312.

Réjou-Méchain, M., Tymen, B., Blanc, L., Fauset, S., Feldpausch, T. R., Monteagudo, A., Phillips, O.L., Richard, H., & Chave, J. (2015). Using repeated small-footprint LiDAR acquisitions to infer spatial and temporal variations of a high-biomass Neotropical forest. Remote Sensing of Environment, 169, 93-101.

Renner, S. S., & Zohner, C. M. (2018). Climate change and phenological mismatch in trophic interactions among plants, insects, and vertebrates. *Annual Review of Ecology, Evolution, and Systematics*, 49, 165-182.

Riano, D., Vaughan, P., Chuvieco, E., Zarco-Tejada, P. J., & Ustin, S. L. (2005). Estimation of fuel moisture content by inversion of radiative transfer models to simulate equivalent water thickness and dry matter content: analysis at leaf and canopy level. IEEE Transactions on Geoscience and Remote Sensing. 43, 819–826. https://doi.org/10.1109/TGRS.2005.843316.

Richardson, A. D. (2019). Tracking seasonal rhythms of plants in diverse ecosystems with digital camera imagery. *New Phytologist*, 222(4), 1742-1750.

Richardson, A. D., Hufkens, K., Milliman, T., Aubrecht, D., Chen, M., Gray, J. M., & Thom, J. E. (2017). PhenoCam Dataset v1. 0: Vegetation phenology from digital camera imagery, 2000–2015. *ORNL Distributed Active Archive Center*.

Richardson, A. D., Hufkens, K., Milliman, T., & Frolking, S. (2018b). Intercomparison of phenological transition dates derived from the PhenoCam Dataset V1. 0 and MODIS satellite remote sensing. *Scientific Reports*, 8(1), 1-12.

Richardson, A. D., Hufkens, K., Milliman, T., Aubrecht, D. M., Chen, M., Gray, J. M., Johnston, M.R., Keenan, T.F., Klosterman, S.T., Kosmala, M., Melaas, E.K., Friedl, M. A., & Frolking, S. (2018a). Tracking vegetation phenology across diverse North American biomes using PhenoCam imagery. *Scientific Data*, *5*(1), 1-24.

Richardson, A. D., Hufkens, K., Milliman, T., Aubrecht, D. M., Furze, M. E., Seyednasrollah, B., Krassovski, M.B., Latimer, J.M., Nettles, W.R., Heiderman, R.R., Warren, J.M., & Hanson, P. J. (2018c). Ecosystem warming extends vegetation activity but heightens vulnerability to cold temperatures. *Nature*, 560(7718), 368-371.

Richardson, A. D., Jenkins, J. P., Braswell, B. H., Hollinger, D. Y., Ollinger, S. V., & Smith, M. L. (2007). Use of digital webcam images to track spring green-up in a deciduous broadleaf forest. *Oecologia*, 152(2), 323-334.

Richardson, A. D., Keenan, T. F., Migliavacca, M., Ryu, Y., Sonnentag, O., and Toomey, M. (2013). Climate change, phenology, and phenological control of vegetation feedbacks to the climate system. *Agricultural and Forest Meteorology*, *169*, 156-173.

Richardson, A. D., Keenan, T. F., Migliavacca, M., Ryu, Y., Sonnentag, O., & Toomey, M. (2013). Climate change, phenology, and phenological control of vegetation feedbacks to the climate system. *Agricultural and Forest Meteorology*, 169, 156-173.

Ridgwell, A., & Hargreaves, J. C. (2007). Regulation of atmospheric CO_2 by deep-sea sediments in an Earth system model. *Global Biogeochemical Cycles*, 21(2).

Righi, M., Andela, B., Eyring, V., Lauer, A., Predoi, V., Schlund, M., Vegas-Regidor, J., Bock, L., Brötz, B., de Mora, L., Diblen, F., Dreyer, L., Drost, N., Earnshaw, P., Hassler, B., Koldunov, N., Little, B., Loosveldt Tomas, S., and Zimmermann, K. (2020). Earth System Model Validation Tool (ESMValTool) v2. 0–technical overview. *Geoscientific Model Development*, *13*(3), 1179-1199.

Ringer, M. A., &rews, T., & Webb, M. J. (2014). Global-mean radiative feedbacks and forcing in atmosphere-only and coupled atmosphere-ocean climate change experiments. *Geophysical Research Letters*, 41(11), 4035-4042.

Rodda, S. R., Thumaty, K. C., Praveen, M. S. S., Jha, C. S., and Dadhwal, V. K. (2021). Multi-year eddy covariance measurements of net ecosystem exchange in tropical dry deciduous forest of India. *Agricultural and Forest Meteorology*, *301*, 108351.

Rogelj, J., Den Elzen, M., Höhne, N., Fransen, T., Fekete, H., Winkler, H., Schaeffer, R., Sha, F., Riahi, K., & Meinshausen, M. (2016). Paris Agreement climate proposals need a boost to keep warming well below 2°C. *Nature*, 534(7609), 631-639.

Rogelj, J., Forster, P. M., Kriegler, E., Smith, C. J., & Séférian, R. (2019). Estimating and tracking the remaining carbon budget for stringent climate targets. *Nature*, 571(7765), 335-342.

Rogelj, J., Meinshausen, M., & Knutti, R. (2012). Global warming under old and new scenarios using IPCC climate sensitivity range estimates. *Nature climate change*, 2(4), 248-253.

Rogelj, J., Shindell, D., Jiang, K., Fifita, S., Forster, P., Ginzburg, V., Handa, C., Kheshgi, H., Kobayashi, S., Kriegler, E., Mundaca, L., & Zickfeld, K. (2018). Mitigation pathways compatible with 1.5°C in the context of sustainable development. *In Global warming of 1.5°C* (pp. 93-174). Intergovernmental Panel on Climate Change.

Rohling, E. J., Rohling, E. J., Sluijs, A., Dijkstra, H. A., Köhler, P., van de Wal, R. S. W., von der Heydt, A. S., Beerling, D. J., Berger, A., Bijl, P. K., Crucifix, M., DeConto, R., Drijfhout, S. S., Fedorov, A., Foster, G. L., Ganopolski, A., Hansen, J., Hönisch, B., Hooghiemstra, H., Huber, M., Huybers, P., Knutti, R., Lea, D. W., Lourens, L. J., Lunt, D., Masson-Delmotte, V., Medina-Elizalde, M., Otto-Bliesner, B., Pagani, M., Pälike, H., Renssen, H., Royer, D. L., Siddall, M., Valdes, P., Zachos J. C., & Zeebe, R. E. (2012). Making sense of paleoclimate sensitivity. *Nature*, 491(7426), 683-691.

Rowe, J.S. (1972). Forest regions of Canada. *Natural Resources Canada*, *Canadian Forest Service*, Ottawa, Canada.

Saatchi, S. S., Harris, N. L., Brown, S., Lefsky, M., Mitchard, E. T., Salas, W., Zutta, B.R., Buermann, W., Lewis, S.L., Hagen, S., and Morel, A. (2011). Benchmark map of forest carbon stocks in tropical regions across three continents. *Proceedings of the national academy of sciences*, *108*(24), 9899-9904.

Sakalli, A., Cescatti, A., Dosio, A., & Gücel, M. U. (2017). Impacts of 2°C global warming on primary production and soil carbon storage capacity at pan-European level. *Climate Services*, 7, 64-77.

Salmela, M. J., Cavers, S., Cottrell, J. E., Iason, G. R., & Ennos, R. A. (2013). Spring phenology shows genetic variation among and within populations in seedlings of Scots pine (Pinus sylvestris L.) in the Scottish Highlands. *Plant Ecology & Diversity*, 6(3-4), 523-536.

Sánchez-Pinillos, M., D'Orangeville, L., Boulanger, Y., Comeau, P., Wang, J., Taylor, A. R., & Kneeshaw, D. (2022). Sequential droughts: A silent trigger of boreal forest mortality. *Global Change Biology*, 28(2), 542-556.

Sangüesa-Barreda, G., Di Filippo, A., Piovesan, G., Rozas, V., Di Fiore, L., García-Hidalgo, M., García-Cervigón, A.I., Muñoz-Garachana, D., Baliva, M., & Olano, J. M. (2021). Warmer springs have increased the frequency and extension of late-frost defoliations in southern European beech forests. *Science of the Total Environment*, 775, 145860.

Santoro, M., Beaudoin, A., Beer, C., Cartus, O., Fransson, J. B. S., Hall, R. J., Pathe, C., Schmullius, C., Schepaschenko, D., Shvidenko, A., Thurner, M., and Wegmüller, U. (2015). Forest growing stock volume of the northern hemisphere: Spatially explicit estimates for 2010 derived from Envisat ASAR. *Remote Sensing of Environment*, *168*, 316-334.

Sardans, J., & Peñuelas, J. (2015). Potassium: a neglected nutrient in global change. *Global Ecology and Biogeography*. 24, 261–275.

Saugier, B., and Roy, J. (2001). Estimations of global terrestrial productivity: Converging towards a single number?. *Global Terrestrial Productivity: Past, Present and Future*, 573.

Schaepman-Strub, G., Schaepman, M.E., Painter, T.H., Dangel, S., & Martonchik, J.V. (2006). Reflectance quantities in optical remote sensing—definitions and case studies. *Remote Sensing of Environment*, 103, 27–42. https://doi.org/10.1016/j.rse.2006.03.002.

Scheffer, M., Bascompte, J., Brock, W. A., Brovkin, V., Carpenter, S. R., Dakos, V., Held, H., Van Nes, E.H., Rietkerk, M., & Sugihara, G. (2009). Early-warning signals for critical transitions. *Nature*, 461(7260), 53-59.

Scheifinger, H., Menzel, A., Koch, E., & Peter, C. (2003). Trends of spring time frost events and phenological dates in Central Europe. *Theoretical and Applied Climatology*, 74(1), 41-51.

Schlesinger, W. H. (1997). *Biogeochemistry: An analysis of global change* (2nd ed.). Oxford: Academic.

Schurgers, G., Ahlström, A., Arneth, A., Pugh, T. A., & Smith, B. (2018). Climate sensitivity controls uncertainty in future terrestrial carbon sink. *Geophysical Research Letters*, 45(9), 4329-4336.

Schwartz, M. D., Ahas, R., & Aasa, A. (2006). Onset of spring starting earlier across the Northern Hemisphere. *Global change biology*, *12*(2), 343-351.

Séférian, R., Nabat, P., Michou, M., Saint-Martin, D., Voldoire, A., Colin, J., Madec, G. (2019). Evaluation of CNRM Earth System Model, CNRM-ESM2-1: Role of Earth System Processes in Present-Day and Future Climate. *Journal of Advances in Modeling Earth Systems*, *11*(12), 4182-4227.

Seland, Ø., Bentsen, M., Seland Graff, L., Olivié, D., Toniazzo, T., Gjermundsen, A., Debernard, J. B., Gupta, A. K., He, Y., Kirkevåg, A., Schwinger, J., Tjiputra, J., Schancke Aas, K., Bethke, I., Fan, Y., Griesfeller, J., Grini, A., Guo, C., Ilicak, M., Hafsahl Karset, I. H., Landgren, O., Liakka, J., Onsum Moseid, K., Nummelin, A., Spensberger, C., Tang, H., Zhang, Z., Heinze, C., Iverson, T., and Schulz, M. (2020). Overview of the Norwegian Earth System Model (NorESM2) and key climate response of CMIP6 DECK, historical, and scenario simulations. *Geoscientific Model Development*, *13*(12), 6165-6200.

Sellar, A. A., Jones, C. G., Mulcahy, J. P., Tang, Y., Yool, A., Wiltshire, A., Zerroukat, M. (2019). UKESM1: Description and evaluation of the UK Earth System Model. *Journal of Advances in Modeling Earth Systems*, *11*(12), 4513-4558.

Serbin, S. P., Wu, J., Ely, K. S., Kruger, E. L., Townsend, P. A., Meng, R., & Rogers, A. (2019). From the Arctic to the tropics: multibiome prediction of leaf mass per area using leaf reflectance. *New Phytologist*, 224(4), 1557-1568.

Seyednasrollah, B., A.M. Young, K. Hufkens, T. Milliman, M.A. Friedl, S. Frolking, A.D. Richardson, M. Abraha, D.W. Allen, M. Apple, M.A. Arain, J. Baker, J.M. Baker, D. Baldocchi, C.J. Bernacchi, J. Bhattacharjee, P. Blanken, D.D. Bosch, R. Boughton, E.H. Boughton, R.F. Brown, D.M. Browning, N. Brunsell, S.P. Burns, M. Cavagna, H. Chu, P.E. Clark, B.J. Conrad, E. Cremonese, D. Debinski, A.R. Desai, R. Diaz-Delgado, L. Duchesne, A.L. Dunn, D.M. Eissenstat, T. El-Madany, D.S.S. Ellum, S.M. Ernest, A. Esposito, L. Fenstermaker, L.B. Flanagan, B. Forsythe, J. Gallagher, D. Gianelle, T. Griffis, P. Groffman, L. Gu, J. Guillemot, M. Halpin, P.J. Hanson, D. Hemming, A.A. Hove, E.R. Humphreys, A. Jaimes-Hernandez, A.A. Jaradat, J. Johnson, E. Keel, V.R.

Kelly, J.W. Kirchner, P.B. Kirchner, M. Knapp, M. Krassovski, O. Langvall, G. Lanthier, G.l. Maire, E. Magliulo, T.A. Martin, B. McNeil, G.A. Meyer, M. Migliavacca, B.P. Mohanty, C.E. Moore, R. Mudd, J.W. Munger, Z.E. Murrell, Z. Nesic, H.S. Neufeld, T.L. O'Halloran, W. Oechel, A.C. Oishi, W.W. Oswald, T.D. Perkins, M.L. Reba, B. Rundquist, B.R. Runkle, E.S. Russell, E.J. Sadler, A. Saha, N.Z. Saliendra, L. Schmalbeck, M.D. Schwartz, R.L. Scott, E.M. Smith, O. Sonnentag, P. Stoy, S. Strachan, K. Suvocarev, J.E. Thom, R.Q. Thomas, A.K. Van den berg, R. Vargas, J. Verfaillie, C.S. Vogel, J.J. Walker, N. Webb, P. Wetzel, S. Weyers, A.V. Whipple, T.G. Whitham, G. Wohlfahrt, J.D. Wood, S. Wolf, J. Yang, X. Yang, G. Yenni, Y. Zhang, Q. Zhang, and D. Zona. (2019a). PhenoCam Dataset v2.0: Vegetation Phenology from Digital Camera Imagery, 2000-2018. ORNL DAAC, Oak Ridge, Tennessee, USA. https://doi.org/10.3334/ORNLDAAC/1674.

Seyednasrollah, B., Bowling, D. R., Cheng, R., Logan, B. A., Magney, T. S., Frankenberg, C., Yang, J.C., Young, A.M., Hufkens, K., Arain, M.A., Black, T.A., & Richardson, A. D. (2021). Seasonal variation in the canopy colour of temperate evergreen conifer forests. *New Phytologist*, 229(5), 2586-2600.

Seyednasrollah, B., Young, A. M., Hufkens, K., Milliman, T., Friedl, M. A., Frolking, S., Richardson, A.D., Abraha, M., Allen, D.W., Apple, M., Arain, M.A., & Zona, D. (2019a). PhenoCam Dataset v2.0: Vegetation Phenology from Digital Camera Imagery, 2000-2018. *ORNL DAAC*.

Seyednasrollah, B., Young, A. M., Hufkens, K., Milliman, T., Friedl, M. A., Frolking, S., & Richardson, A. D. (2019b). Tracking vegetation phenology across diverse biomes using Version 2.0 of the PhenoCam Dataset. Scientific Data, 6(1), 1-11.

Seyednasrollah, B., Young, A. M., Hufkens, K., Milliman, T., Friedl, M. A., Frolking, S., & Richardson, A. D. (2019b). Tracking vegetation phenology across diverse biomes using Version 2.0 of the PhenoCam Dataset. *Scientific Data*, 6(1), 1-11.

Sheffield, J., Goteti, G., and Wood, E. F. (2006). Development of a 50-year high-resolution global dataset of meteorological forcings for land surface modeling. *Journal of climate*, *19*(13), 3088-3111.

Shevliakova, E., Malyshev, S., Martinez-Cano, I., Milly, P. C. D., Pacala, S. W., Ginoux, P., Dunne, K. A., Dunne, J. P., Dupius, C., Findell, K., Ghannam, K., Horowitz, L. W., John,

J. G., Knutson, T. R., Krasting, J. P., Naik, V., Zadeh, N., Zeng, F., and Zeng, Y. (2020). The land component LM4. 1 of the GFDL Earth System Model ESM4. 1: biophysical and biogeochemical processes and interactions with climate. *J. Adv. Model. Earth Syst., 2019MS002040, in review*.

Shevliakova, E., Stouffer, R. J., Malyshev, S., Krasting, J. P., Hurtt, G. C., & Pacala, S. W. (2013). Historical warming reduced due to enhanced land carbon uptake. *Proceedings of the National Academy of Sciences*, 110(42), 16730-16735.

Shiklomanov, A. N., Dietze, M. C., Viskari, T., Townsend, P. A., & Serbin, S. P. (2016). Quantifying the influences of spectral resolution on uncertainty in leaf trait estimates through a Bayesian approach to RTM inversion. Remote Sensing of Environment, 183, 226-238.

Shipley, B., De Bello, F., Cornelissen, J. H. C., Laliberté, E., Laughlin, D. C., & Reich, P. B. (2016). Reinforcing loose foundation stones in trait-based plant ecology. Oecologia, 180, 923–931.

Simard, M., Pinto, N., Fisher, J. B., and Baccini, A. (2011). Mapping forest canopy height globally with spaceborne lidar. *Journal of Geophysical Research: Biogeosciences*, *116*(G4).

Simmons, C. T., & Matthews, H. D. (2016). Assessing the implications of human land-use change for the transient climate response to cumulative carbon emissions. *Environmental Research Letters*, 11(3), 035001.

Simmons, M., Davis, D. S., Griffiths, L., & Muecke, A. (1984). Natural History of Nova Scotia. Vol. 1. *Nova Scotia Museum of Natural History, Halifax, NS*.

Smith, C. J., Forster, P. M., Allen, M., Leach, N., Millar, R. J., Passerello, G. A., & Regayre, L. A. (2018). FAIR v1. 3: a simple emissions-based impulse response and carbon cycle model. *Geoscientific Model Development*, 11(6), 2273-2297.

Smith, C., Beazley, K. F., Duinker, P., & Harper, K. A. (2010). The impact of moose (Alces alces andersoni) on forest regeneration following a severe spruce budworm outbreak in the Cape Breton Highlands, Nova Scotia, Canada. *Alces: A Journal Devoted to the Biology and Management of Moose,* 46, 135-150.

Smith, T., Traxl, D., & Boers, N. (2022). Empirical evidence for recent global shifts in vegetation resilience. *Nature Climate Change*, 1-8.

Snyder, K. A., Wehan, B. L., Filippa, G., Huntington, J. L., Stringham, T. K., & Snyder, D. K. (2016). Extracting plant phenology metrics in a great basin watershed: Methods and considerations for quantifying phenophases in a cold desert. *Sensors*, 16(11), 1948.

Sonnentag, O., Hufkens, K., Teshera-Sterne, C., Young, A. M., Friedl, M., Braswell, B. H., Milliman, T., O'Keefe, J., & Richardson, A. D. (2012). Digital repeat photography for phenological research in forest ecosystems. *Agricultural and Forest Meteorology*, 152, 159-177.

Sonobe, R., Miura, Y., Sano, T., & Horie, H. (2017). Estimating leaf carotenoid contents of shade-grown tea using hyperspectral indices and PROSPECT–D inversion. International Journal of Remote Sensing. 39(5), 1306-1320.

Sonobe, R., Sano, T., & Horie, H. (2018). Using spectral reflectance to estimate leaf chlorophyll content of tea with shading treatments. Biosystems engineering. 175, 168–182.

Spafford, L., & MacDougall, A. H. (2021). Validation of terrestrial biogeochemistry in CMIP6 Earth system models: a review. *Geoscientific Model Development*, 14(9), 5863-5889.

Spanner, M. A., Pierce, L. L., Peterson, D. L., & Running, S. W. (1990). Remote sensing of temperate coniferous forest leaf area index: The influence of canopy closure, understory vegetation and background reflectance. *Remote Sensing*, 11(1), 95-111.

Sparks, T. H., & Carey, P. D. (1995). The responses of species to climate over two centuries: an analysis of the Marsham phenological record, 1736-1947. *Journal of Ecology*, 321-329.

Spencer, D. M., & Holecek, D. F. (2007). A profile of the fall foliage tourism market. *Journal of Vacation Marketing*, 13(4), 339-358.

Spring, A., Ilyina, T., & Marotzke, J. (2020). Inherent uncertainty disguises attribution of reduced atmospheric CO_2 growth to CO_2 emission reductions for up to a decade. *Environmental Research Letters*, 15(11), 114058.

Steenberg, J. W., Duinker, P. N., & Bush, P. G. (2013). Modelling the effects of climate change and timber harvest on the forests of central Nova Scotia, Canada. *Annals of Forest Science*, *70*(1), 61-73.

Steenweg, R., Hebblewhite, M., Kays, R., Ahumada, J., Fisher, J. T., Burton, C., Townsend, S.E., Carbone, C., Rowcliffe, J.M., Whittington, J., & Brodie, J. (2017). Scaling-up camera traps: Monitoring the planet's biodiversity with networks of remote sensors. Frontiers in Ecology and the Environment. 15(1), 26-34.

Steinacher, M., & Joos, F. (2016). Transient Earth system responses to cumulative carbon dioxide emissions: linearities, uncertainties, and probabilities in an observation-constrained model ensemble. *Biogeosciences*, 13(4), 1071-1103.

Stephens, J. J., Black, T. A., Jassal, R. S., Nesic, Z., Grant, N. J., Barr, A. G., Helgason, W.D., Richardson, A.D., Johnson, M.S., & Christen, A. (2018). Effects of forest tent caterpillar defoliation on carbon and water fluxes in a boreal aspen stand. *Agricultural and Forest Meteorology*, 253, 176-189.

Stephenson, N. L., Das, A. J., Ampersee, N. J., Cahill, K. G., Caprio, A. C., Sanders, J. E., & Williams, A. P. (2018). Patterns and correlates of giant sequoia foliage dieback during California's 2012–2016 hotter drought. *Forest Ecology and Management*, 419, 268-278.

Stocker, T. (Ed.). (2014). *Climate change 2013: the physical science basis: Working Group I contribution to the Fifth assessment report of the Intergovernmental Panel on Climate Change. Cambridge university press*.

Stokes, G. G., (1862). IV. On the intensity of the light reflected from or transmitted through a pile of plates. Proceedings of the Royal Society of London. 545–556.

Sun, J., Shi, S., Yang, J., Du, L., Gong, W., Chen, B., & Song, S. (2018). Analyzing the performance of PROSPECT model inversion based on different spectral information for leaf biochemical properties retrieval. ISPRS Journal of Photogrammetry and Remote Sensing. 135, 74–83. https://doi.org/10.1016/j.isprsjprs.2017.11.010.

Sun, J., Shi, S., Yang, J., Gong, W., Qiu, F., Wang, L., & Chen, B. (2019). Wavelength selection of the multispectral lidar system for estimating leaf chlorophyll and water contents through the PROSPECT model. Agricultural and forest meteorology. 266, 43-52.

Swart, N. C., Cole, J. N. S., Kharin, V. V., Lazare, M., Scinocca, J. F., Gillett, N. P., Anstey, J., Arora, V., Christian, J. R., Hanna, S., Jiao, Y., Lee, W. G., Majaess, F., Saenko, O. A., Seiler, C., Seinen, C., Shao, A., Solheim, L., von Salzen, K., Yang, D. and Winter, B. (2019). The Canadian Earth System Model version 5 (CanESM5. 0.3). *Geoscientific Model Development*, *12*(11), 4823-4873.

Tachiiri, K., Hajima, T., & Kawamiya, M. (2015). Increase of uncertainty in transient climate response to cumulative carbon emissions after stabilization of atmospheric CO_2 concentration. *Environmental Research Letters*, 10(12), 125018.

Tachiiri, K., Hajima, T., & Kawamiya, M. (2019). Increase of the transient climate response to cumulative carbon emissions with decreasing CO_2 concentration scenarios. Environmental *Research Letters*, 14(12), 124067.

Taylor, A. R., Boulanger, Y., Price, D. T., Cyr, D., McGarrigle, E., Rammer, W., & Kershaw Jr, J. A. (2017). Rapid 21st century climate change projected to shift composition and growth of Canada's Acadian Forest Region. *Forest Ecology and Management*, 405, 284-294.

Taylor, A. R., Dracup, E., MacLean, D. A., Boulanger, Y., & Endicott, S. (2019). Forest structure more important than topography in determining windthrow during Hurricane Juan in Canada's Acadian Forest Region. *Forest Ecology and Management*, 434, 255-263.

Taylor, A. R., MacLean, D. A., Neily, P. D., Stewart, B., Quigley, E., Basquill, S. P., Boone, C.K., Gilby, D., & Pulsifer, M. (2020). A review of natural disturbances to inform implementation of ecological forestry in Nova Scotia, Canada. *Environmental Reviews*, *28*(4), 387-414.

Taylor, A. R., MacLean, D. A., Neily, P. D., Stewart, B., Quigley, E., Basquill, S. P., Boone, C.K., Gilby, D., & Pulsifer, M. (2020). A review of natural disturbances to inform implementation of ecological forestry in Nova Scotia, Canada. *Environmental Reviews*, 28(4), 387-414.

Taylor, K. E. (2001). Summarizing multiple aspects of model performance in a single diagram. *Journal of Geophysical Research: Atmospheres*, *106*(D7), 7183-7192.

The Canadian Press. (2022). Post-tropical storm Fiona most costly weather event to ever hit Atlantic Canada, new estimate says. *CBC News Nova Scotia*. Retrieved from: https://www.cbc.ca/news/79iona79/nova-scotia/79iona-atlantic-canada-insured-damages-660-million-1.6621583#:~:text=CBC%20News%20Loaded-,Post%2Dtropical%20storm%20Fiona%20most%20costly%20weather%20event%20to%20ever,%24660%20million%20in%20insured%20damage.

Thornton, M. M., Shrestha, R., Thornton, P. E., Kao, S., Wei, Y., & Wilson, B. E. (2021). Daymet Version 4 Monthly Latency: Daily Surface Weather Data. *ORNL DAAC*, Oak Ridge, Tennessee, USA. https://doi.org/10.3334/ORNLDAAC/1904.

Thornton, M. M., Shrestha, R., Wei, Y., Thornton, P. E., Kao, S., & Wilson, B. E. (2022). Daymet: Monthly Climate Summaries on a 1-km Grid for North America, Version 4 R1. *ORNL DAAC*, Oak Ridge, Tennessee, USA. https://doi.org/10.3334/ORNLDAAC/2129.

Thurner, M., Beer, C., Santoro, M., Carvalhais, N., Wutzler, T., Schepaschenko, D., Shvidenko, A., Kompter, E., Ahrens, B., Levick, S. R., and Schmullius, C. (2014). Carbon stock and density of northern boreal and temperate forests. *Global Ecology and Biogeography*, *23*(3), 297-310.

Tian, F., Cai, Z., Jin, H., Hufkens, K., Scheifinger, H., Tagesson, T., & Eklundh, L. (2021). Calibrating vegetation phenology from Sentinel-2 using eddy covariance, PhenoCam, and PEP725 networks across Europe. *Remote Sensing of Environment*, 260, 112456.

Tian, H., Yang, J., Lu, C., Xu, R., Canadell, J. G., Jackson, R. B., Arneth, A., Chang, J., Chen, G., Ciais, P., Gerber, S., Ito, A., Huang, Y., Joos, F., Lienert, S., Messina, P., Olin, S., Pan, S., Peng, C., Saikawa, E., Thompson, R. L., Vuichard, N., Winiwarter, W., Zaehle, S., Zhang, B., Zhang, K., and Zhu, Q. (2018). The global N_2O model intercomparison project. *Bulletin of the American Meteorological Society*, *99*(6), 1231-1251.

Todd-Brown, K. E. O., Randerson, J. T., Post, W. M., Hoffman, F. M., Tarnocai, C., Schuur, E. A. G., and Allison, S. D. (2013). Causes of variation in soil carbon simulations from CMIP5 Earth system models and comparison with observations. *Biogeosciences*, *10*(3), 1717-1736.

Tokarska, K. B., Gillett, N. P., Arora, V. K., Lee, W. G., & Zickfeld, K. (2018). The influence of non-CO_2 forcings on cumulative carbon emissions budgets. *Environmental Research Letters*, 13(3), 034039.

Tokarska, K. B., Gillett, N. P., Weaver, A. J., Arora, V. K., & Eby, M. (2016). The climate response to five trillion tonnes of carbon. *Nature Climate Change*, 6(9), 851-855.

Toomey, M., Friedl, M. A., Frolking, S., Hufkens, K., Klosterman, S., Sonnentag, O., Baldocchi, D.D., Bernacchi, C.J., Biraud, S.C., Bohrer, G., & Richardson, A. D. (2015). Greenness indices from digital cameras predict the timing and seasonal dynamics of canopy-scale photosynthesis. *Ecological Applications*, 25(1), 99-115.

Toomey, M., Friedl, M.A., Frolking, S., Hufkens, K., Klosterman, S., Sonnentag, O., Baldocchi, D.D., Bernacchi, C.J., Biraud, S.C., Bohrer, G., & Brzostek, E. (2015). Greenness indices from digital cameras predict the timing and seasonal dynamics of canopy-scale photosynthesis. *Ecological Applications*, 25(1), 99-115.

Tramontana, G., Jung, M., Schwalm, C. R., Ichii, K., Camps-Valls, G., Ráduly, B., Reichstein, M., Arain, M. A., Cescatti, A., Kiely, G., Merbold, L., Serrano-Ortiz, P., Sickert, S., Wolf, S., and Papale, D. (2016). Predicting carbon dioxide and energy fluxes across global Fluxnet sites with regression algorithms. *Biogeosciences*, 13, 4291– 4313.

Tsallis, C., & Stariolo, D. (1996). Generalized Simulated Annealing. *Physica A*, 233, 395-406. https://doi.org/10.1016/S0378-4371(96)00271-3.

Tucker, C. J., & Sellers, P. J. (1986). Satellite remote sensing of primary production. International journal of remote sensing. 7(11), 1395-1416.

Tucker, C. J., Fung, I. Y., Keeling, C. D., Gammon, R. H. (1986). Relationship between atmospheric CO_2 variations and a satellite-derived vegetation index. *Nature*, *319*(6050), 195-199.

Twine, T. E., Kustas, W. P., Norman, J. M., Cook, D. R., Houser, P., Meyers, T. P., and Wesely, M. L. (2000). Correcting eddy-covariance flux underestimates over a grassland. *Agricultural and forest meteorology*, *103*(3), 279-300.

Two Countries, One Forest. (2014). Ecoregion Boundary. Northern Appalachian/ Acadian Ecoregion Conservation Atlas. Available from: https://2c1forest.databasin.org/maps/new/#datasets=425508ee1f55464aacc2a2d4be4d0d69.

Umair, M., Kim, D., Ray, R. L., and Choi, M. (2018). Estimating land surface variables and sensitivity analysis for CLM and VIC simulations using remote sensing products. *Science of the Total Environment*, *633*, 470-483.

US Department of Commerce, N.O.A.A. (2020). May 3, 2020 derecho. *National Weather Service*. Retrieved June 6, 2022, from https://www.weather.gov/ohx/20200503.

Usha Rani, P., & Jyothsna, Y. (2010). Biochemical and enzymatic changes in rice plants as a mechanism of defense. *Acta Physiologiae Plantarum*, 32, 695-701.

Vaduva, C., Georgescu, F. A., Griparis, A., Neagoe, I., Grivei, A. C., & Datcu, M. (2019). Exploratory search methodology for sentinel 2 data: a prospect of both visual and latent characteristics. In IGARSS 2019-2019 IEEE International Geoscience and Remote Sensing Symposium. 10067-10070.

Vafaei, S., Soosani, J., Adeli, K., Fadaei, H., Naghavi, H., Pham, T. D., and Tien Bui, D. (2018). Improving accuracy estimation of Forest Aboveground Biomass based on incorporation of ALOS-2 PALSAR-2 and Sentinel-2A imagery and machine learning: A case study of the Hyrcanian forest area (Iran). *Remote Sensing*, *10*(2), 172.

van der Heijden, G. M., Powers, J. S., & Schnitzer, S. A. (2015). Lianas reduce carbon accumulation and storage in tropical forests. *Proceedings of the National Academy of Sciences*, 112(43), 13267-13271.

van den Hurk, B., Kim, H., Krinner, G., Seneviratne, S. I., Derksen, C., Oki, T., and Sheffield, J. (2016). LS3MIP (v1. 0) contribution to CMIP6: the Land Surface, Snow and Soil moisture Model Intercomparison Project–aims, setup and expected outcome. *Geoscientific Model Development*, *9*(8), 2809-2832.

van der Werf, G. R., Randerson, J. T., Giglio, L., van Leeuwen, T. T., Chen, Y., Rogers, B. M., Mu, M., van Marle, M. J. E., Morton, D. C., Collatz, G. J., Yokelson, R. J., and Kasibhatla, P. S. (2017). Global fire emissions estimates during 1997–2016. *Earth System Science Data*, 9, 697– 720.

Vaughn, W. R., Taylor, A. R., MacLean, D. A., D'Orangeville, L., & Lavigne, M. B. (2021). Climate change experiment suggests divergent responses of tree seedlings in eastern North America's Acadian Forest Region over the 21st century. *Canadian Journal of Forest Research*, 51(12), 1888-1902.

Verger, A., Filella, I., Baret, F., and Peñuelas, J. (2016). Vegetation baseline phenology from kilometric global LAI satellite products. *Remote sensing of environment*, *178*, 1-14.

Verhoef, W., & Bach, H. (2007). Coupled soil–leaf-canopy and atmosphere radiative transfer modeling to simulate hyperspectral multi-angular surface reflectance and TOA radiance data. *Remote Sensing of Environment*, 109(2), 166-182.

Verrelst, J., Camps-Valls, G., Muñoz-Marí, J., Rivera, J. P., Veroustraete, F., Clevers, J. G., & Moreno, J. (2015). Optical remote sensing and the retrieval of terrestrial vegetation bio-geophysical properties–a review. *ISPRS Journal of Photogrammetry and Remote Sensing,* 108, 273-290.

Verrelst, J., Muñoz, J., Alonso, L., Delegido, J., Rivera, J. P., Camps-Valls, G., & Moreno, J. (2012). Machine learning regression algorithms for biophysical parameter retrieval: Opportunities for Sentinel-2 and-3. *Remote Sensing of Environment*, 118, 127-139.

Vial, J., Dufresne, J. L., & Bony, S. (2013). On the interpretation of inter-model spread in CMIP5 climate sensitivity estimates. *Climate Dynamics*, 41(11), 3339-3362.

Vitasse, Y., & Basler, D. (2014). Is the use of cuttings a good proxy to explore phenological responses of temperate forests in warming and photoperiod experiments?. *Tree Physiology*, 34(2), 174-183.

Vitasse, Y., Baumgarten, F., Zohner, C. M., Kaewthongrach, R., Fu, Y. H., Walde, M. G., & Moser, B. (2021). Impact of microclimatic conditions and resource availability on spring and autumn phenology of temperate tree seedlings. *New Phytologist*, *232*(2), 537-550.

Vitasse, Y., Baumgarten, F., Zohner, C. M., Rutishauser, T., Pietragalla, B., Gehrig, R., Dai, J., Wang, H., Aono, Y., & Sparks, T. H. (2022). The great acceleration of plant phenological shifts. *Nature Climate Change*, 12(4), 300-302.

Vitasse, Y., François, C., Delpierre, N., Dufrêne, E., Kremer, A., Chuine, I., & Delzon, S. (2011). Assessing the effects of climate change on the phenology of European temperate trees. *Agricultural and Forest Meteorology*, 151(7), 969-980.

Vitasse, Y., Hoch, G., Randin, C. F., Lenz, A., Kollas, C., Scheepens, J. F., & Körner, C. (2013). Elevational adaptation and plasticity in seedling phenology of temperate deciduous tree species. *Oecologia*, 171(3), 663-678.

Vitasse, Y., Lenz, A., & Körner, C. (2014). The interaction between freezing tolerance and phenology in temperate deciduous trees. *Frontiers in Plant Science*, 5, 541.

Vitasse, Y., Porté, A. J., Kremer, A., Michalet, R., & Delzon, S. (2009). Responses of canopy duration to temperature changes in four temperate tree species: relative contributions of spring and autumn leaf phenology. *Oecologia*, 161(1), 187-198.

Vitasse, Y., Signarbieux, C., & Fu, Y. H. (2018). Global warming leads to more uniform spring phenology across elevations. *Proceedings of the National Academy of Sciences*, *115*(5), 1004-1008.

Vitousek, P. M., Menge, D. N., Reed, S. C., and Cleveland, C. C. (2013). Biological nitrogen fixation: rates, patterns and ecological controls in terrestrial ecosystems. *Philosophical Transactions of the Royal Society B: Biological Sciences*, *368*(1621), 20130119.

Vuichard, N., Messina, P., Luyssaert, S., Guenet, B., Zaehle, S., Ghattas, J., Peylin, P. (2019). Accounting for carbon and nitrogen interactions in the global terrestrial ecosystem model ORCHIDEE (trunk version, rev 4999): multi-scale validation of gross primary production. *Geoscientific Model Development*, *12*(11), 4751-4779.

Vuolo, F., Żółtak, M., Pipitone, C., Zappa, L., Wenng, H., Immitzer, M., Weiss, M., Baret, F., & Atzberger, C. (2016). Data service platform for Sentinel-2 surface reflectance and value-added products: System use and examples. *Remote Sensing*, 8(11), 938.

Waliser, D., Gleckler, P. J., Ferraro, R., Taylor, K. E., Ames, S., Biard, J., Bosilovich, M. G., Brown, O., Chepfer, H., Cinquini, L., Durack, P., Eyring, V., Mathieu, P.-P., Lee, T., Pinnock, S., Potter, G. L., Rixen, M., Saunders, R., Shulz, J., Thepaut, J.-N., and Tuma, M. (2020). Observations for model Intercomparison project (Obs4MIPs): Status for CMIP6. *Geoscientific Model Development*, *13*(7), 2945-2958.

Wang, F., Tokarska, K. B., Zhang, J., Ge, Q., Hao, Z., Zhang, X., & Wu, M. (2018). Climate warming in response to emission reductions consistent with the Paris Agreement. *Advances in Meteorology*, 2018.

Wang, J. R., Hawkins, C. D. B., & Letchford, T. (1998). Photosynthesis, water and nitrogen use efficiencies of four paper birch (Betula papyrifera) populations grown under different soil moisture and nutrient regimes. *Forest Ecology and Management*, 112(3), 233-244.

Wang, J. Y. (1960). A critique of the heat unit approach to plant response studies. *Ecology*, 41(4), 785-790.

Wang, S. W., He, X. F., Chen, J. G., Sun, H., Körner, C., & Yang, Y. (2021). Elevation-specific responses of phenology in evergreen oaks from their low-dry to their extreme high-cold range limits in the SE Himalaya. *Alpine Botany*, 131(1), 89-102.

Wang, Z., Skidmore, A. K., Wang, T., Darvishzadeh, R., & Hearne, J. (2015). Applicability of the PROSPECT model for estimating protein and cellulose + lignin in fresh leaves. *Remote Sensing of Environment,* 168, 205–218.

Wang, Z., Townsend, P. A., & Kruger, E. L. (2022). Leaf spectroscopy reveals divergent inter- and intra-species foliar trait covariation and trait–environment relationships across NEON domains. *New Phytologist*, 235(3), 923-938.

Watt, M. S., Leonardo, E. M. C., Estarija, H. J. C., Massam, P., de Silva, D., O'Neill, R., & Zarco-Tejada, P. J. (2021). Long-term effects of water stress on hyperspectral remote sensing indicators in young radiata pine. *Forest Ecology and Management*, 502, 119707.

Watts, J. D., Natali, S. M., Minions, C., Risk, D., Arndt, K., Zona, D., Euskirchen, E.S., Rocha, A.V., Sonnentag, O., Helbig, M., Kalhori, A., & Edgar, C. (2021). Soil respiration strongly offsets carbon uptake in Alaska and Northwest Canada. *Environmental Research Letters*, 16(8), 084051.

WCRP. (2020). CMIP Phase 6 (CMIP6). Retrieved January 23, 2021, from https://www.wcrp-climate.org/wgcm-cmip/wgcm-cmip6.

Wei, J., Dirmeyer, P. A., Yang, Z. L., and Chen, H. (2018). Effect of land model ensemble versus coupled model ensemble on the simulation of precipitation climatology and variability. *Theoretical and Applied Climatology*, *134*(3), 793-800.

White, M. A., Thornton, P. E., & Running, S. W. (1997). A continental phenology model for monitoring vegetation responses to interannual climatic variability. *Global Biogeochemical Cycles*, 11(2), 217-234.

Wieder, W. (2014). Regridded Harmonized World Soil Database v1.2, ORNL DAAC, Oak Ridge, Tennessee, USA, https://doi.org/10.3334/ORNLDAAC/1247.

Wieder, W. R., Cleveland, C. C., Smith, W. K., and Todd-Brown, K. (2015). Future productivity and carbon storage limited by terrestrial nutrient availability. *Nature Geoscience*, *8*(6), 441-444.

Wigley, T. M., & Schlesinger, M. E. (1985). Analytical solution for the effect of increasing CO_2 on global mean temperature. *Nature*, 315(6021), 649-652.

Williams, K. E., Harper, A. B., Huntingford, C., Mercado, L. M., Mathison, C. T., Falloon, P. D., & Kim, J. (2019). How can the First ISLSCP Field Experiment contribute to present-day efforts to evaluate water stress in JULESv5. 0?. *Geoscientific Model Development*, 12(7), 3207-3240.

Williams, R. G., Ceppi, P., & Katavouta, A. (2020). Controls of the transient climate response to emissions by physical feedbacks, heat uptake and carbon cycling. *Environmental Research Letters*, 15(9), 0940c1.

Williams, R. G., Goodwin, P., Ridgwell, A., & Woodworth, P. L. (2012). How warming and steric sea level rise relate to cumulative carbon emissions. *Geophysical Research Letters*, 39(19).

Williams, R. G., Goodwin, P., Roussenov, V. M., & Bopp, L. (2016). A framework to understand the transient climate response to emissions. *Environmental Research Letters*, 11(1), 015003.

Williams, R. G., Roussenov, V., Goodwin, P., Resplandy, L., & Bopp, L. (2017). Sensitivity of global warming to carbon emissions: Effects of heat and carbon uptake in a suite of Earth system models. *Journal of Climate*, 30(23), 9343-9363.

Wingate, L., Ogée, J., Cremonese, E., Filippa, G., Mizunuma, T., Migliavacca, M., Moisy, C., Wilkinson, M., Moureaux, C., Wohlfahrt, G., & Grace, J. (2015). Interpreting canopy development and physiology using a European phenology camera network at flux sites. *Biogeosciences*, 12(20), 5995-6015.

Wolkovich, E. M., & Cleland, E. E. (2011). The phenology of plant invasions: a community ecology perspective. *Frontiers in Ecology and the Environment*, 9(5), 287-294.

Wolkovich, E. M., Cook, B. I., Allen, J. M., Crimmins, T. M., Betancourt, J. L., Travers, S. E., Pau, S., Regetz, J., Davies, T.J., Kraft, N.J., Ault, T.R., & Cleland, E. E. (2012). Warming experiments underpredict plant phenological responses to climate change. *Nature*, 485(7399), 494-497.

Wright, I. J., Reich, P. B., Westoby, M., Ackerly, D. D., Baruch, Z., Bongers, F., Cavender-Bares, J., Chapin, T., Cornelissen, J.H., Diemer, M., & Flexas, J. (2004). The worldwide leaf economics spectrum. *Nature*, 428, 821.

Wu, C., Gough, C. M., Chen, J. M., & Gonsamo, A. (2013). Evidence of autumn phenology control on annual net ecosystem productivity in two temperate deciduous forests. *Ecological Engineering*, 60, 88-95.

Wu, C., Peng, J., Ciais, P., Peñuelas, J., Wang, H., Beguería, S., &rew Black, T., Jassal, R.S., Zhang, X., Yuan, W., Liang, E., & Ge, Q. (2022). Increased drought effects on the phenology of autumn leaf senescence. *Nature Climate Change*, 12(10), 943-949.

Wu, J., Chavana-Bryant, C., Prohaska, N., Serbin, S. P., Guan, K., Albert, L. P., Yang, X., van Leeuwen, W.J., Garnello, A.J., Martins, G., & Malhi, Y. (2016). Convergence in relationships between leaf traits, spectra and age across diverse canopy environments and two contrasting tropical forests. *New Phytologist*, 214(3), 1033-1048.

Wu, T., Lu, Y., Fang, Y., Xin, X., Li, L., Li, W., Jie, W., Zhang, J., Liu, Y., Zhang, L., Zhang, F., Zhang, Y., Wu, F., Li, J., Chu, M., Wang, Z., Shi, X., Liu, X., Wei, M., Huang, A., Zhang, Y., and Liu, X. (2019). The Beijing Climate Center climate system model (BCC-CSM): The main progress from CMIP5 to CMIP6. *Geoscientific Model Development*, *12*(4), 1573-1600.

Xiang, Y., Gubain, S., Suomela, B., & Hoeng, J. (2013). Generalized Simulated Annealing for Efficient Global Optimization: the GenSA Package for R. *The R Journal, Volume 5/1, June 2013*. https://journal.r-project.org/archive/2013/RJ-2013-002/index.html.

Xiao, J., Chevallier, F., Gomez, C., Guanter, L., Hicke, J. A., Huete, A. R., and Zhang, X. (2019). Remote sensing of the terrestrial carbon cycle: A review of advances over 50 years. Remote Sensing of Environment, 233, 111383.

Xie, X., Li, A., Tan, J., Lei, G., Jin, H., and Zhang, Z. (2020). Uncertainty analysis of multiple global GPP datasets in characterizing the lagged effect of drought on photosynthesis. *Ecological Indicators*, *113*, 106224.

Xie, Y., Civco, D. L., & Silander Jr, J. A. (2018a). Species-specific spring and autumn leaf phenology captured by time-lapse digital cameras. *Ecosphere*, 9(1), e02089.

Xie, Y., Wang, X., & Silander, J. A. (2015). Deciduous forest responses to temperature, precipitation, and drought imply complex climate change impacts. *Proceedings of the National Academy of Sciences*, 112(44), 13585-13590.

Xie, Y., Wang, X., Wilson, A. M., & Silander Jr, J. A. (2018b). Predicting autumn phenology: how deciduous tree species respond to weather stressors. *Agricultural and forest meteorology*, 250, 127-137.

Xu, Z., Jiang, Y., Jia, B., and Zhou, G. (2016). Elevated-CO_2 response of stomata and its dependence on environmental factors. *Frontiers in plant science*, *7*, 657.

Yadav, S., & Shukla, S. (2016). Analysis of k-fold cross-validation over hold-out validation on colossal datasets for quality classification. *In 2016 IEEE 6th International conference on advanced computing* (IACC) (pp. 78-83). IEEE.

Yan, Y., Zhou, X., Jiang, L., and Luo, Y. (2017). Effects of carbon turnover time on terrestrial ecosystem carbon storage. *Biogeosciences*, *14*(23), 5441-5454.

Yang, X., Tang, J., & Mustard, J. F. (2014). Beyond leaf color: Comparing camera-based phenological metrics with leaf biochemical, biophysical, and spectral properties throughout the growing season of a temperate deciduous forest. *Journal of Geophysical Research: Biogeosciences*, 119(3), 181-191.

Yang, X., Tang, J., Mustard, J. F., Wu, J., Zhao, K., Serbin, S., & Lee, J. E. (2016). Seasonal variability of multiple leaf traits captured by leaf spectroscopy at two temperate deciduous forests. *Remote Sensing of Environment*, 179, 1-12.

Yebra, M., Chuvieco, E., & Riaño, D. (2008). Estimation of live fuel moisture content from MODIS images for fire risk assessment. *Agricultural and Forest Meteorology*, 148, 523–536.

Yoshikawa, C., Kawamiya, M., Kato, T., Yamanaka, Y., and Matsuno, T. (2008). Geographical distribution of the feedback between future climate change and the carbon cycle. *Journal of Geophysical Research: Biogeosciences*, *113*(G3).

Yuan, Z., & Chen, H. Y. (2015). Decoupling of nitrogen and phosphorus in terrestrial plants associated with global changes. *Nature Climate Change*, 5, 465.

Zaehle, S., and Dalmonech, D. (2011). Carbon–nitrogen interactions on land at global scales: current understanding in modelling climate biosphere feedbacks. *Current Opinion in Environmental Sustainability*, *3*(5), 311-320.

Zakharova, L., Meyer, K. M., & Seifan, M. (2019). Trait-based modelling in ecology: A review of two decades of research. *Ecological Modelling*, 407, 108703.

Zandalinas, S. I., Mittler, R., Balfagón, D., Arbona, V., & Gómez-Cadenas, A. (2018). Plant adaptations to the combination of drought and high temperatures. *Physiologia plantarum*, 162, 2–12.

Zani, D., Crowther, T. W., Mo, L., Renner, S. S., & Zohner, C. M. (2020). Increased growing-season productivity drives earlier autumn leaf senescence in temperate trees. *Science*, 370(6520), 1066-1071.

Zanne, A. E., Pearse, W. D., Cornwell, W. K., McGlinn, D. J., Wright, I. J., & Uyeda, J. C. (2018). Functional biogeography of angiosperms: life at the extremes. *New Phytologist*, 218(4), 1697-1709.

Zarco-Tejada, P., Guillén-Climent, M., Hernández-Clemente, R., Catalina, A., González, M., & Martín, P. (2013). Estimating leaf carotenoid content in vineyards using high resolution hyperspectral imagery acquired from an unmanned aerial vehicle (UAV). *Agricultural and Forest Meteorology*. 171-172, 281–294. https://doi.org/10.1016/j.agrformet.2012.12.013.

Zhang, H.-M., Huang, B., Lawrimore, J., Menne, M., & Smith, T.M. (2019). NOAA Global Surface Temperature Dataset (NOAAGlobalTemp), Version 5.1. *NOAA National Centers for Environmental Information.* doi:10.25921/9qth-2p70.

Zhang, M., & Huang, Y. (2014). Radiative forcing of quadrupling CO_2. *Journal of Climate*, 27(7), 2496-2508.

Zhang, S., Buttò, V., Khare, S., Deslauriers, A., Morin, H., Huang, J. G., Ren, H., & Rossi, S. (2020). Calibrating PhenoCam data with phenological observations of a black spruce stand. *Canadian Journal of Remote Sensing*, 46(2), 154-165.

Zhang, Y. J., Yu, G. R., Yang, J., Wimberly, M. C., Zhang, X. Z., Tao, J., Jiang, Y. B., and Zhu, J. T. (2014). Climate-driven global changes in carbon use efficiency. *Global Ecology and Biogeography*, 23, 144– 155.

Zhang, Z., Zhang, Y., Zhang, Y., Gobron, N., Frankenberg, C., Wang, S., and Li, Z. (2020). The potential of satellite FPAR product for GPP estimation: An indirect evaluation using solar-induced chlorophyll fluorescence. *Remote Sensing of Environment*, *240*, 111686.

Zhao, M., Heinsch, F. A., Nemani, R. R., and Running, S. W. (2005). Improvements of the MODIS terrestrial gross and net primary production global data set. *Remote Sensing of Environment*, *95*(2), 164-176.

Zhu, Q., Castellano, M. J., and Yang, G. (2018). Coupling soil water processes and the nitrogen cycle across spatial scales: Potentials, bottlenecks and solutions. *Earth-Science Reviews*, *187*, 248-258.

Zhu, W., Sun, Z., Yang, T., Li, J., Peng, J., Zhu, K., & Liao, X. (2020). Estimating leaf chlorophyll content of crops via optimal unmanned aerial vehicle hyperspectral data at multi-scales. *Computers and Electronics in Agriculture*, 178, 105786.

Zhu, X., Helmer, E. H., Gwenzi, D., Collin, M., Fleming, S., Tian, J., Marcano-Vega, H., Meléndez-Ackerman, E.J., & Zimmerman, J. K. (2021). Characterization of Dry-Season Phenology in Tropical Forests by Reconstructing Cloud-Free Landsat Time Series. *Remote Sensing*, 13(23), 4736.

Zhu, Z., Bi, J., Pan, Y., Ganguly, S., Anav, A., Xu, L., Samanta, A., Piao, S., Nemani, R.R., and Myneni, R. B. (2013). Global data sets of vegetation leaf area index (LAI) 3g and fraction of photosynthetically active radiation (FPAR) 3g derived from global inventory modeling and mapping studies (GIMMS) normalized difference vegetation index (NDVI3g) for the period 1981 to 2011. *Remote sensing*, *5*(2), 927-948.

Zickfeld, K., Arora, V. K., & Gillett, N. P. (2012). Is the climate response to CO_2 emissions path dependent?. *Geophysical Research Letters*, 39(5).

Zickfeld, K., Eby, M., Matthews, H. D., & Weaver, A. J. (2009). Setting cumulative emissions targets to reduce the risk of dangerous climate change. *Proceedings of the National Academy of Sciences*, 106(38), 16129-16134.

Zickfeld, K., Eby, M., Weaver, A. J., Alexander, K., Crespin, E., Edwards, N. R., Eliseev, A.V., Feulner, G., Fichefet, T., Forest, C.E., Friedlingstein, P., & Zhao, F. (2013). Long-term climate change commitment and reversibility: an EMIC intercomparison. *Journal of Climate*, 26(16), 5782-5809.

Zickfeld, K., MacDougall, A. H., & Matthews, H. D. (2016). On the proportionality between global temperature change and cumulative CO_2 emissions during periods of net negative CO_2 emissions. *Environmental Research Letters*, 11(5), 055006.

Ziehn, T., Chamberlain, M. A., Law, R. M., Lenton, A., Bodman, R. W., Dix, M., Stevens, L., Wang, Y.P., Srbinovsky, J., (2020). The Australian Earth System Model: ACCESS-ESM1. 5. *Journal of Southern Hemisphere Earth Systems Science*, *70*(1), 193-214.

Ziehn, T., Kattge, J., Knorr, W., and Scholze, M. (2011). Improving the predictability of global CO2 assimilation rates under climate change. *Geophysical Research Letters*, *38*(10).

Zohner, C. M., & Renner, S. S. (2019). Ongoing seasonally uneven climate warming leads to earlier autumn growth cessation in deciduous trees. *Oecologia*, *189*(2), 549-561.

Zohner, C. M., Mo, L., Renner, S. S., Svenning, J. C., Vitasse, Y., Benito, B. M., Ordonez, A., Baumgarten, F., Bastin, J.F., Sebald, V., Reich, P., & Crowther, T. W. (2020). Late-spring frost risk between 1959 and 2017 decreased in North America but increased in Europe and Asia. *Proceedings of the National Academy of Sciences*, 117(22), 12192-12200.

Zohner, C. M., Rockinger, A., & Renner, S. S. (2019). Increased autumn productivity permits temperate trees to compensate for spring frost damage. *New Phytologist*, 221(2), 789-795.

Appendix I: Validation of Terrestrial Biogeochemistry in CMIP6 Earth System Models: A Review

This paper was published in Geoscientific Model Development, 14(9), 5863-5889, https://doi.org/10.5194/gmd-14-5863-2021.

Lynsay Spafford[1,2], Andrew H. MacDougall[1]

[1] Climate and Environment, Saint Francis Xavier University, Antigonish, Canada

[2] Environmental Sciences, Memorial University, St. John's, Canada

Abstract. The vital role of terrestrial biogeochemical cycles in influencing global climate change is explored by modelling groups internationally through Land Surface Models (LSMs) coupled to atmospheric and oceanic components within Earth System Models (ESMs). The sixth phase of the Coupled Model Intercomparison Project (CMIP6) provided an opportunity to compare ESM output by providing common forcings and experimental protocols. Despite these common experimental protocols, a variety of terrestrial biogeochemical cycle validation approaches were adopted by CMIP6 participants, leading to ambiguous model performance assessment and uncertainty attribution across ESMs. In this review we summarize current methods of terrestrial biogeochemical cycle validation utilized by CMIP6 participants and concurrent community model comparison studies. We focus on variables including: the dimensions of evaluations, observation-based reference datasets, and metrics of model performance. To ensure objective and thorough validations for the seventh phase of CMIP (CMIP7) we recommend the use of a standard validation protocol employing a broad suite of certainty-weighted observation-based reference datasets, targeted model performance metrics, and comparisons across a range of spatiotemporal scales.

A1.1 Introduction

The terrestrial biosphere is presently responsible for sequestering about one quarter of anthropogenic carbon emissions, substantially reducing the severity of ongoing climate change (Friedlingstein et al., 2020). The future capacity of the terrestrial biosphere to sequester CO_2 emissions is uncertain due to non-linear feedbacks such as CO_2 fertilization, growing season extension in cold-limited regions, enhanced heterotrophic respiration, and potentially other feedbacks, as well as environmental and physiological constraints such as moisture availability, nutrient limitations and stomatal closure (Fleischer et al., 2019; Green et al., 2019; Xu et al., 2016; Wieder et al., 2015). Earth system models (ESMs) are a means to simulate past, present, and future terrestrial biogeochemical cycles, examine the influence of changes in climate and atmospheric CO_2 concentration on CO_2 uptake, explore feedbacks and limitations, and estimate anthropogenic carbon emissions compatible with avoiding a given threshold in global temperature change. ESMs simulate global exchanges of matter and energy through the coupling of land, atmospheric, and oceanic components. Through concerted efforts, successive generations of ESMs have improved in terms of spatiotemporal resolution, complexity, and process representation (Anderson et al., 2016). Despite this progress, terrestrial biogeochemical cycles remain a major source of uncertainty in future climate projections (Arora et al., 2020; Lovenduski and Bonan, 2017). This uncertainty stems from limited process understanding, lacking observational constraints, inherent cycle variability, temporal discrepancy between forcings and responses (Sellar et al., 2019; Ciais et al., 2013), and uncertain stock quantifications (Ito et al., 2020; Wieder et al., 2015) which together compound uncertainty within models. Among models, this uncertainty is amplified by artefacts in the form of inconsistent model structure, boundary conditions, forcing datasets, experimental protocols, and benchmarking observational datasets, which is magnified by the increasing number, diversity, and complexity of ESMs (Eyring et al., 2020). Subsequently, a study on uncertainty in projected terrestrial carbon uptake based upon 12 Coupled Model Intercomparison Project phase 5 (CMIP5) ESMs indicated that uncertainty stemming from model structure may be four times greater than uncertainty from different emission scenarios and internal variability (Lovenduski and Bonan, 2017). Some progress has been made in addressing the large uncertainty associated with the terrestrial biogeochemistry in ESMs, as comparison of the carbon-climate and carbon-concentration feedback among ESMs participating in the sixth phase of CMIP (CMIP6) by Arora et al. (2020) shows a reduced model spread amongst models which included a nitrogen cycle, which provided a realistic constraint on photosynthesis in the context of elevated atmospheric CO_2 concentration. However, the spread in estimated feedback parameters across ESMs overall has not been significantly reduced from CMIP6 relative to CMIP5 (Arora et al., 2020; 2013).

To answer scientific questions regarding climate change, the CMIP was initiated in 1995 by the World Climate Research Programme’s (WCRP) Working Group of Coupled Modelling (WCRP, 2020). The CMIP designates standard experimental protocols, model output formats, and model forcings to diagnose climate change variability, predictability, and uncertainty following various scenarios within a multi-model framework. CMIP6 began in 2013 with three years of planning and community consultation to address knowledge gaps, prior to the conduction of simulations and analyses in 2016 and onwards. Model validation in the context of CMIP consists of demonstrating sufficient agreement between model output data and historical observation-based reference data following model development and is a crucial process in model advancement. Such comparison facilitates model improvement by identifying model limitations in performance or sources of model-data uncertainty (Lovenduski and Bonan, 2017), and informs the weighting of different ESMs in influencing climate projections and policy (Eyring et al., 2019). CMIP6 specified detailed experimental protocols for modelling group participants to facilitate objective comparisons of the output of different models with common forcings (Eyring et al., 2016a).

Here we focus on validations of the stocks and biological fluxes of fully coupled ESMs and associated LSM releases from 2017 onwards with explicit terrestrial biogeochemical cycle representation contributed by CMIP6 participating modelling groups (hereafter participants; Table A1-1; Arora et al., 2020). Validations are analyzed in terms of variables included, spatiotemporal scales, reference datasets, and metrics of performance. Section A1.2 compares the methods of historical terrestrial biogeochemical cycle validation used by participants, Section A1.3 summarizes the methods used in community analyses of CMIP5 era models, and Section A1.4 provides a critique of these methods. A future outlook is also presented in Section A1.4.

Table A1-1. *Modelling group contributions to C^4MIP of CMIP6 from Arora et al. (2020).*

Modelling Group	**ESM**	**Land Surface Model Biogeochemistry Component**	**Explicit N Cycle**	**Dynamic Vegetation**	**Prognostic LAI**	**Prognostic Leaf Phenology**	**Reference**
CSIRO	ACCESS-ESM1.5	CABLE2.4	Yes	No	Yes	No	Ziehn et al., 2020
BCC	BCC-CSM2-MR	BCC-AVIM2	No	No	Yes	Yes (for deciduous)	Wu et al., 2019; Li et al., 2019b
CCCma	CanESM5	CLASS-CTEM	No	No	Yes	Yes	Swart et al., 2019
CESM	CESM2	CLM5	Yes	No	Yes	Yes	Danabasoglu et al., 2020; Lawrence et al., 2019
CNRM	CNRM-ESM2-1	ISBA-CTRIP	No	No	Yes	Yes (from leaf carbon balance)	Séférian et al., 2019; Delire et al., 2020
GFDL	GFDL-ESM4	LM4.1	No	Yes	-	-	Dunne et al., 2020
IPSL	IPSL-CM6A-LR	ORCHIDEE, version 2.0	No	No	Yes	Yes	Boucher et al., 2020; Vuichard et al., 2019
JAMSTEC	MIROC-ES2L	VISIT-e	Yes	No	Yes	Yes	Hajima et al., 2020
MPI	MPI-ESM1.2-LR	JSBACH3.2	Yes	Yes	Yes	Yes	Mauritsen et al., 2019; Goll et al., 2017
NCC	NorESM2-LM	CLM5	Yes	No	Yes	Yes	Seland et al., 2020
UK	UKESM1-0-LL	JULES-ES-1.0	Yes	Yes	Yes	Yes	Sellar et al., 2019

A1.2 Participant Methods of Validating Terrestrial Biogeochemical Cycles

To participate in CMIP6, participants had to submit four Diagnosis, Validation, and Characterization of Klima (DECK) experimental simulations which included a control simulation with prescribed idealized pre-industrial (1850) forcing for at least 500 years to demonstrate stability in global climate and biogeochemical exchanges. Additionally, participants had to conduct historical simulations from 1850-2014 using designated CMIP6 forcings (available at https://esgf-node.llnl.gov/search/input4MIPs/, last access: February 8th, 2021) as well as initialization from the pre-industrial forcing control run (Eyring et al., 2016a). Each modelling group demonstrated stability in the global carbon cycle, with global net carbon exchange below the suggested limit of 0.1 PgC year^{-1} by Jones et al. (2016), while no suitable pre-industrial simulation global nitrogen or phosphorus flux was specified for CMIP6 though these were generally below 2.0 Pg year^{-1} (Ziehn et al., 2020). Each modelling group validated terrestrial biogeochemical cycle components for the historical simulation in a unique fashion, which is summarized below and detailed in Section A1.6.

A1.2.1 Variables Included in Validations

The number of terrestrial biogeochemical cycle variables evaluated against observation-based estimates by participants varied considerably from 0 to 21, with a total of 38 unique variables evaluated by all participants combined. The variable validated most often was Gross Primary Production (GPP), which was validated by all but one participant. The next nine most validated variables in descending order were soil carbon, the global land carbon sink, leaf area index (LAI), vegetation carbon, ecosystem respiration, global land-atmosphere CO_2 flux, surface CO_2 concentrations, total biomass, and burned area (Figure A1-1). For a list of variable definitions, see Table A1-2.

Table A1-2. *Terms associated with terrestrial biogeochemical cycles and their definitions as used by participants.*

Term	**CMIP6 Definition**
Gross Primary Production (GPP)	The quantity of CO_2 removed from the atmosphere by vegetation.
Net Primary Productivity (NPP)	The quantity of CO_2 removed from the atmosphere by vegetation minus the quantity of CO_2 from autotrophic respiration.
Autotrophic Respiration (AR)	The quantity of CO_2 from cellular respiration in plants.
Ecosystem Respiration (ER)	The quantity of CO_2 from autotrophic respiration and heterotrophic respiration.
Heterotrophic Respiration (HR)	The quantity of CO_2 from cellular respiration by heterotrophs.
Net Ecosystem Production (NEP)	The quantity of CO_2 removed from the atmosphere by vegetation minus the quantity of CO_2 from autotrophic and heterotrophic respiration.
Net Biome Production (NBP)	The net rate of organic carbon accumulation minus autotrophic and heterotrophic respiration as well as non-respiratory losses from disturbance.
Net Ecosystem Carbon Balance (NECB)	The net rate of organic carbon accumulation in an ecosystem, independent of scale.

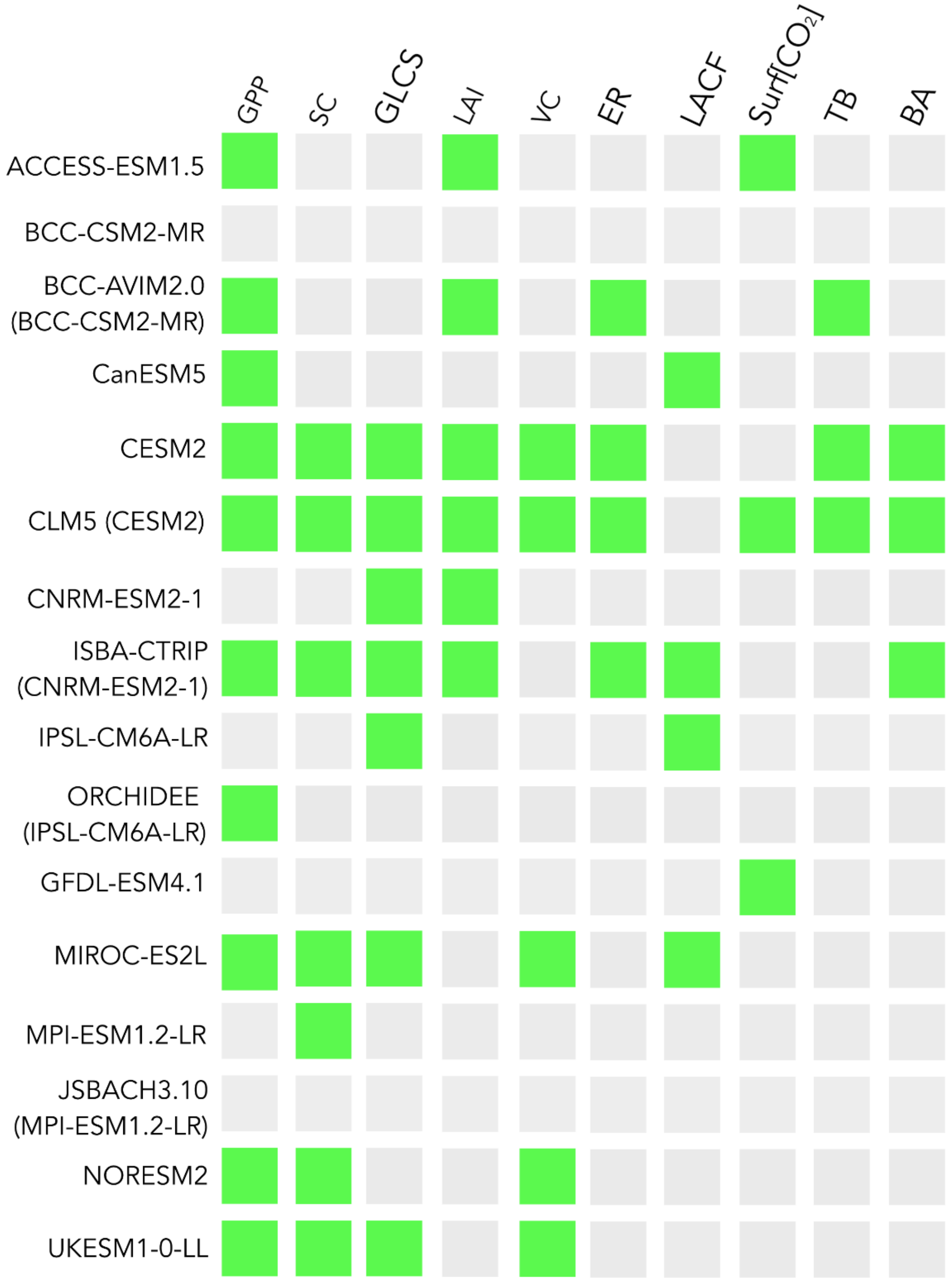

	GPP	SC	GLCS	LAI	VC	ER	LACF	Surf[CO$_2$]	TB	BA
ACCESS-ESM1.5	🟩	⬜	⬜	🟩	⬜	⬜	⬜	🟩	⬜	⬜
BCC-CSM2-MR	⬜	⬜	⬜	⬜	⬜	⬜	⬜	⬜	⬜	⬜
BCC-AVIM2.0 (BCC-CSM2-MR)	🟩	⬜	⬜	🟩	⬜	🟩	⬜	⬜	🟩	⬜
CanESM5	🟩	⬜	⬜	⬜	⬜	⬜	🟩	⬜	⬜	⬜
CESM2	🟩	🟩	🟩	🟩	🟩	🟩	⬜	⬜	🟩	🟩
CLM5 (CESM2)	🟩	🟩	🟩	🟩	🟩	🟩	⬜	🟩	🟩	🟩
CNRM-ESM2-1	⬜	⬜	🟩	🟩	⬜	⬜	⬜	⬜	⬜	⬜
ISBA-CTRIP (CNRM-ESM2-1)	🟩	🟩	🟩	🟩	⬜	🟩	🟩	⬜	⬜	🟩
IPSL-CM6A-LR	⬜	⬜	🟩	⬜	⬜	⬜	🟩	⬜	⬜	⬜
ORCHIDEE (IPSL-CM6A-LR)	🟩	⬜	⬜	⬜	⬜	⬜	⬜	⬜	⬜	⬜
GFDL-ESM4.1	⬜	⬜	⬜	⬜	⬜	⬜	⬜	🟩	⬜	⬜
MIROC-ES2L	🟩	🟩	🟩	⬜	🟩	⬜	🟩	⬜	⬜	⬜
MPI-ESM1.2-LR	⬜	🟩	⬜	⬜	⬜	⬜	⬜	⬜	⬜	⬜
JSBACH3.10 (MPI-ESM1.2-LR)	⬜	⬜	⬜	⬜	⬜	⬜	⬜	⬜	⬜	⬜
NORESM2	🟩	🟩	⬜	⬜	🟩	⬜	⬜	⬜	⬜	⬜
UKESM1-0-LL	🟩	🟩	🟩	⬜	🟩	⬜	⬜	⬜	⬜	⬜

Figure A1-1*. Validation (green) or omission (grey) of the ten most frequently validated variables by participants (treating ESMs and LSMs separately), including Gross Primary Productivity (GPP), Soil Carbon (SC), Global Land Carbon Sink (GLCS), Leaf Area Index (LAI), Vegetation Carbon (VC), Ecosystem Respiration (ER), Land-Atmosphere CO2 Flux (LACF), Surface CO2 concentrations (Surf[CO2]), Total Biomass (TB), and Burned Area (BA).*

The majority of variables were validated by just one or two participants (Figure A1-2).

Danabasoglu et al. (2020) and Lawrence et al. (2019) validated a relatively extensive suite of variables with the International Land Model Benchmarking (ILAMB) package version 2.1 (ILAMBv2.1; Collier et al., 2018, Figure A1-3), including an explicit uncertainty analysis of the influences of interannual variability, forcing datasets, and model structure in the form of prescribed versus prognostic vegetation phenology. While no nitrogen cycle variable was validated by more than one group, soil N_2O flux and total N_2O emissions were evaluated by Hajima et al. (2020) and Lawrence et al. (2019), respectively.

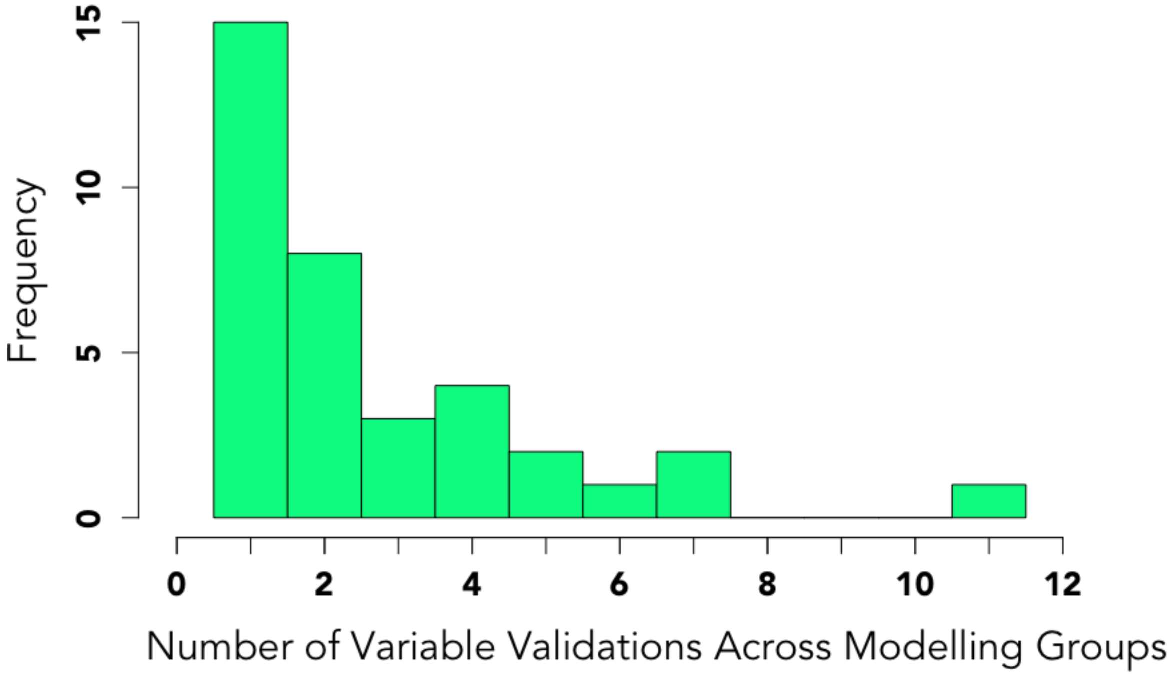

Figure A1-2. *Frequency of a given variable being validated across participants (treating ESMs and LSMs separately). Most variables were validated only once across participants (leftmost x-axis), while GPP was validated by 11 participants (rightmost bar).*

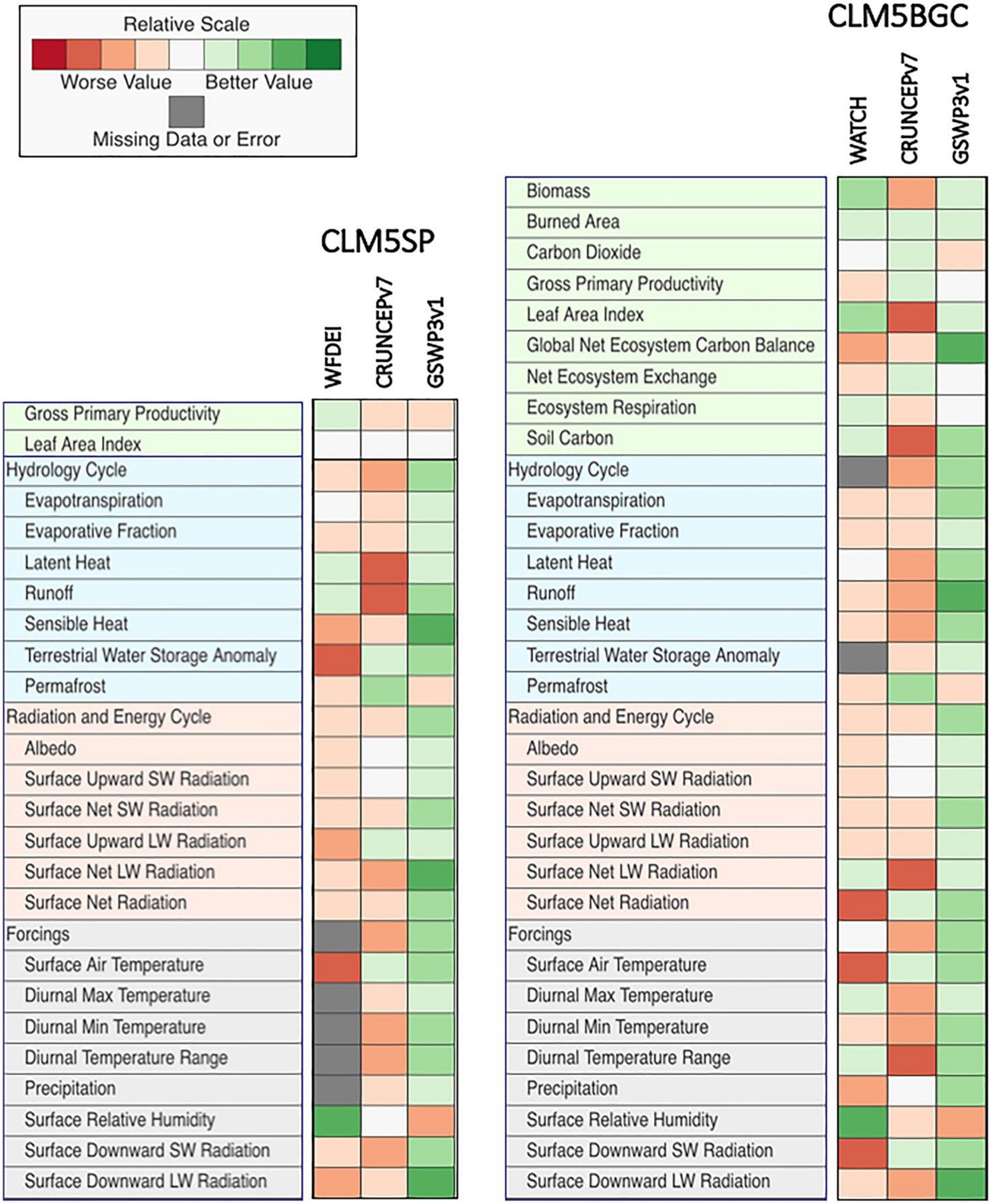

Figure A1-3. *Validation results for terrestrial variables within the CLM5 by Lawrence et al. (2019) using ILAMB analysis (Collier et al., 2018) including three different climate forcing data products (individual columns) and two forms of model structure (column groups). CLM5SP denotes MODIS (Zhao et al., 2005) prescribed vegetation phenology, while CLM5GBC denotes* *prognostic phenology. Climate forcing data products include WATCH/WFDEI from Mitchell and Jones, (2005), CRUNCEPv7, the default forcing dataset used by the Global Carbon Project (Le Quéré et al., 2018), and GSWP3v1, the default forcing dataset used in the Land Surface, Snow and Soil Moisture MIP (van den Hurk et al., 2016). This figure was made available under a Creative Commons Attribution License (CC BY).*

A variety of spatiotemporal scales of these variables were considered in validations both within and among participants. Spatial scales consisted of site-level, model grid cell, degree of latitude, region, and global, with the latter being the most common across participants. Temporal scales included daily, seasonal, annual, decadal, select periods, and long-term trends, accumulations, or averages over the whole historical simulation period from 1850-2014. For more detail on the spatiotemporal scales of validation used by each participant, readers should refer to section A.6. Dynamic variables such as LAI were subject to a detailed assessment, including annual maximum and minimum magnitude (Séférian et al., 2019) and month (Li et al., 2019b), seasonality (Ziehn et al., 2020), and seasonal average, as well as global averages. GPP was also evaluated across a variety of scales, including in terms of the daily, seasonal, and annual magnitude on a plant functional type (PFT), spatial, and global basis against site-level observations (Vuichard et al., 2019), as well as globally in terms of functional relationships with temperature and precipitation (Swart et al., 2019) and the relative contribution of drivers of variation (Vuichard et al., 2019). Biomass and carbon stock variables were evaluated in terms of spatial distributions or global averages over chosen time periods, often on a decadal scale (Li et al., 2019b). Global vegetation and soil carbon turnover times were also evaluated for selected time periods (Delire et al., 2020; Lawrence et al., 2019).

A1.2.2 Reference Datasets

For variables which were validated by more than one modelling group, such as GPP, a variety of observation-based reference datasets were utilized. For example, across participants, several different GPP reference datasets were used (Table A1-3), though most participants utilized model tree ensemble (MTE) machine-learning upscaled ground eddy-covariance, meteorological, and satellite observation-based estimates of GPP from Jung et al. (2011). Interestingly one group, Centre National de Recherches Météorologiques (CNRM; Delire et al., 2020) used a more recent Fluxnet-based GPP dataset (FluxComv1; Jung et al., 2016; Tramontana et al., 2016), and further used the mean of 12 products therein. CNRM along with the Institut Pierre Simon Laplace (IPSL, Vuichard et al., 2019) were the only groups to include a comparison to site-level GPP observations. A variety of reference datasets were also utilized for the second most frequently validated variable, soil carbon (Table A1-4), spanning a 12-year publication range (Batjes, 2016; Global Soil Data Task Group, 2002). Several participants used more than one reference dataset for evaluation of soil carbon depending upon regional or global focus, such as the Northern Circumpolar Soil Carbon Database provided by Hugelius et al. (2013) for mid-high latitudes, while global soil carbon estimates were obtained from Batjes (2016), Carvalhais et al. (2014), Todd-Brown et al. (2013), and FAO (2012). While biomass and carbon stocks were predominantly compared to present day observations, Delire et al. (2020) used records from the Global Database of Litterfall Mass and Litter Pool Carbon and Nutrients database which extends from 1827-1997 (Holland et al., 2015).

Table A1-3. *The source for Gross Primary Production (GPP) data referenced by each modelling group for ESM or LSM simulations. Adjacent contributions from the same modelling group are banded in a common fashion for readability. LSM-focused validations by each modelling group are presented with the associated ESM in brackets.*

Model Validation	GPP Reference Data
ACCESS-ESM1.5	Jung et al., 2011; Ziehn et al., 2011; Beer et al., 2010
BCC-CSM2-MR	-
BCC-AVIM2.0 (BCC-CSM2-MR)	Jung et al., 2011
CanESM5	Jung et al., 2009
CESM2	Jung et al., 2011
CLM5 (CESM2)	Jung et al., 2011
CNRM-ESM2-1	-
ISBA-CTRIP (CNRM-ESM2-1)	Jung et al., 2016; Tramontana et al., 2016; Joetzjer et al., 2015
IPSL-CM6A-LR	-
ORCHIDEE (IPSL-CM6A-LR)	Jung et al., 2011
GFDL-ESM4.1	-
MIROC-ES2L	Jung et al., 2011
MPI-ESM1.2-LR	-
JSBACH3.10 (MPI-ESM1.2-LR)	-
NORESM2	Jung et al., 2011
UKESM1-0-LL	Jung et al., 2011

Table A1-4. *The source for soil carbon data referenced by each modelling group for ESM or LSM simulations. Adjacent contributions from the same modelling group are banded in a common fashion for readability. LSM-focused validations by each modelling group are presented with the associated ESM in brackets.*

Model Validation	Soil Carbon Reference Data
ACCESS-ESM1.5	-
BCC-CSM2-MR	-
BCC-AVIM2.0 (BCC-CSM2-MR)	-
CanESM5	-
CESM2	Hugelius et al., 2013; Todd-Brown et al., 2013
CLM5 (CESM2)	FAO, 2012
CNRM-ESM2-1	-
ISBA-CTRIP (CNRM-ESM2-1)	FAO, 2012
IPSL-CM6A-LR	-
ORCHIDEE (IPSL-CM6A-LR)	-
GFDL-ESM4.1	-
MIROC-ES2L	Batjes, 2016; Hugelius et al., 2013; Todd-Brown et al., 2013
MPI-ESM1.2-LR	Goll et al., 2015
JSBACH3.10 (MPI-ESM1.2-LR)	-
NORESM2	FAO, 2012
UKESM1-0-LL	Batjes, 2016; Carvalhais et al., 2014; Global Soil Data Task Group, 2002

A1.2.3 Statistical Metrics of Model Performance

A variety of statistical metrics were used to quantify model performance in simulating historical variables in comparison to observations, though chosen metrics were more consistent than selected variables. The comparison of simulated and observation-based averages calculated over space and time was the most common metric used by all but two participants (Table A1-5). The next most commonly used metric was root mean squared error (RMSE), followed by bias (simulated – observed) on a spatial or global basis. Evaluations of global accumulations, seasonal phase, seasonal maximum and or minimum, as well as global totals were also used. The

Taylor diagram, which geometrically combines spatiotemporal correlation, standard deviations, and root mean square (RMS) difference (Taylor, 2001) was used to summarize model performance by three participants (Li et al., 2019b; Collier et al., 2018; Goll et al., 2017). The correlation coefficient (r) was also used by three participants (Swart et al., 2019; Mauritsen et al., 2019; Goll et al., 2017). RMSE normalized by the standard deviation of observations (NRMSE) was only used by Swart et al. (2019), while the coefficient of determination (r^2) was only used by Mauritsen et al. (2019). A targeted metric in the form of dissected mean squared deviation (Kobayashi and Salam, 2000), the sum of squared bias, squared difference between standard deviations, and lack of correlation weighted by standard deviation, was used to distinguish model sources of error by Vuichard et al. (2019). In addition to quantitative metrics, the qualitative aspects of simulations were compared to observational reference data, such as in demonstrating source or sink behaviour over time (Danabasoglu et al., 2020), or in visual comparison of spatial distribution maps.

Table A1-5. *Model performance metrics used by each modelling group for ESM or LSM simulations. Adjacent contributions from the same modelling group are banded in a common fashion for readability. LSM-focused validations by each modelling group are presented with the associated ESM in brackets.*

Model Validation	**Presented Model Performance Assessment Metrics**
ACCESS-ESM1.5	Space-time averages, seasonal amplitude, timing and magnitude of annual maximums and minimums
BCC-CSM2-MR	-
BCC-AVIM2.0 (BCC-CSM2-MR)	Average annual cycle phase, global mean bias, RMSE, Taylor score
CanESM5	Space-time averages, geographic distribution of time averages and bias, latitudinal averages, correlation coefficient (r), RMSE, NRMSE (RMSE ÷ standard deviation of observations), change in NRMSE
CESM2	Space-time averages, seasonal cycles, spatial distributions, time series, interannual variability, global accumulations, functional relationships, relative bias, RMSE, ILAMB relative scale
CLM5 (CESM2)	Space-time averages, seasonal cycles, annual monthly maximum, spatial distributions, global totals, turnover time, time series, interannual variability, functional relationships, bias, relative bias, RMSE, ILAMB relative scale
CNRM-ESM2-1	Average annual maximums and minimums, spatial distribution, bias, RMSE, model correlation between spatial pattern of error
ISBA-CTRIP (CNRM-ESM2-1)	Geographic distribution of time averages and bias, latitudinal averages, global accumulations, bias, spatial correlation, turnover time, average annual maximums, seasonal cycle amplitude and phase
IPSL-CM6A-LR	Global annual averages and accumulations over time
ORCHIDEE (IPSL-CM6A-LR)	Daily, seasonal, annual averages, spatial distribution, regional averages, global averages, RMSE, NRMSE, dissected mean squared deviation (squared bias, squared difference between standard deviations, lack of correlation weighted by standard deviations from Kobayashi and Salam (2000)), relative drivers of variation
GFDL-ESM4.1	Spatial distribution of seasonal amplitude, interannual variability, RMSE, correlation coefficient (r), coefficient of determination (r^2)
MIROC-ES2L	Space-time averages, latitudinal averages, spatial distribution, gradient, seasonality, density, global accumulations
MPI-ESM1.2-LR	Spatial variability, latitudinal average density, global accumulations
JSBACH3.10 (MPI-ESM1.2-LR)	Space-time averages, spatial variability, frequency distribution, response ratio, correlation coefficient (r), RMSE, Taylor score
NORESM2	Global averages and totals
UKESM1-0-LL	Space-time averages, spatial distribution, latitudinal averages, global accumulations and totals

A1.3 Community Methods of Validating Terrestrial Biogeochemical Cycles

A variety of software and projects have been dedicated to the communal evaluation of ESM (Gleckler et al., 2016) and LSM performance (Kumar et al., 2012; Gulden et al., 2008), with CMIP6-era collaborative efforts including the Earth System Model Evaluation Tool version 2 (ESMValToolv2.0; Eyring et al., 2016b) and ILAMBv2.1 (Danabasoglu et al., 2020; Lawrence et al., 2019; Collier et al., 2018). Both ESMValToolv2.0 and ILAMBv2.1 are openly available tools for the evaluation of a variety of model output against re-processed observations (cmip-esmvaltool.dkrz.de; https://pypi.org/project/ILAMB/; Eyring et al., 2020; 2016b; Collier et al., 2018). The observation-based reference datasets for each are displayed in Table A1-6. For ESMValToolv2.0 dataset re-processing for compatible comparison in space as well as masking of missing observations is detailed in Righi et al. (2020). The analysis of the land carbon cycle in ESMValToolv2.0 (Eyring et al., 2020) is based upon the approach of Anav et al. (2013) in considering long-term trends, interannual variability, and seasonal cycles. A variety of model performance tailored metrics are available with ESMValToolv2.0 (Eyring et al., 2020). The relative space-time root-mean square deviation (RMSD) indicates model success relative to the multi-model median in simulating the seasonal cycle of key variables, originally from Flato et al. (2013), and allows simultaneous comparison to more than one observational reference for each simulated variable, where available. ESMValTool2.0's AutoAssess function provides a highly resolved model performance evaluation for 300 individual variables, originally developed by the UK Met Office. Further, land cover can be comprehensively evaluated with ESMValToolv2.0 in terms of areas, mean fractions, and biases on a regional and global basis, accommodating different model representations of land cover. ILAMBv2.1 was used to validate terrestrial biogeochemical cycle components in CESM2 (Danabasoglu et al., 2020) and CLM5 (Figure A1-

3; Lawrence et al., 2019). ILAMBv2.1 was also used to demonstrate the absolute and relative performance of DGVMs within several iterations of the Global Carbon Project (Friedlingstein et al., 2020; 2019; Le Quéré et al., 2018). In addition to variables presented in Table A1-6, functional relationships between these variables and temperature and precipitation are provided for validation purposes in ILAMBv2.1. ILAMBv2.1 employs a weighting system to assign scores to observation-based datasets, which encompasses certainty measures, spatiotemporal scale appropriateness, and process implications. In computing statistical model performance scores, ILAMBv2.1 acknowledges how reference observations represent discontinuous constants in time and space. For example, if a reference dataset contains average information across a span of years, the annual cycle of such a dataset is assumed to be undefined and is therefore not used as a reference. The calculation of averages over time in ILAMBv2.1 addresses spatiotemporally discontinuous data by performing calculations over specific intervals for which data are considered valid. For each variable evaluation, ILAMBv2.1 generates a series of graphical diagnostics, including spatial contour maps, time series plots, and Taylor diagrams (Taylor, 2001), as well as statistical model performance scores including period mean, bias, RMSE, spatial distribution, interannual coefficient of variation, seasonal cycle, and long-term trend. These scores are then scaled based upon the weighting of reference observation-based datasets, and for multi-model comparisons are presented across metrics and datasets to provide a single score.

Table A1-6. *Select observation-based reference dataset sources for ESMValToolv2.0 (Eyring et al., 2020) and ILAMBv2.1 (Collier et al., 2018), including Net Biome Production (NBP), Leaf Area Index (LAI), Land Cover (LC), Gross Primary Production (GPP), Net Ecosystem Exchange (NEE), Soil Carbon (SC), Vegetation Carbon (VC), Ecosystem Carbon Turnover (ECT), Vegetation Biomass (VB), and Burned Area (BA). Note that vegetation carbon is dependent upon vegetation biomass.*

Variables	ESMValToolv2.0	ILAMBv2.1
NBP	Le Quéré et al., 2018; Maki et al., 2010	Le Quéré et al., 2016; Hoffman et al., 2014
LAI	Zhu et al., 2013; Baret et al., 2007	De Kauwe et al., 2011; Myneni et al., 1997
LC	Defourny et al., 2016	
GPP, NEE	Jung et al., 2019; 2011	Lasslop et al., 2010; Jung et al., 2010
SC	Wieder, 2014	Todd-Brown et al., 2013; Hugelius et al., 2013
VC	Gibbs, 2006	-
ECT	Carvalhais et al., 2014	-
VB	-	Saatchi et al., 2011; Kellndorfer et al., 2013; Blackard et al., 2008
BA	-	Giglio et al., 2010

A1.4 Critique of Validation Approaches

While standard protocols were used by participants for historical simulations in CMIP6, no standard protocol in terms of variables evaluated, reference data, performance metrics, or acceptable performance threshold was adopted for terrestrial biogeochemical cycle validation. The validation of particular variables by different participants occasionally employed the same datasets, though in many cases inconsistent reference datasets were used for the same variable, and the spatial and temporal dimension of validations was often distinct. This contrasts with other works employing multiple models such as the Global Carbon Project (Friedlingstein et al., 2020; 2019; Le Quéré et al., 2018) which provide explicit validation criteria, such as simulating recent historical net land-atmosphere carbon flux within a particular range and being within the 90% confidence interval of specified observations. The stringency of such criteria must be carefully chosen to acknowledge the role of observational uncertainty as well as uncertainty stemming from potential model tuning to forcing datasets. The use of different validation approaches impedes the comparison of performance across models, however it also provides a diverse collection of example methods.

A1.4.1 Variable Choice

A comprehensive validation of a process-based model should include all simulated interacting variables for which a reliable empirical reference is available. Improvement in the simulation of one variable through altered parameters, structure, or algorithms may translate into degradation for other variables, which would be otherwise obscured in a restricted variable analysis (Deser et al., 2020; Ziehn et al., 2020; Lawrence et al., 2019). Given the scope of CMIP6 publications in demonstrating model improvements relative to previous versions as well as the results of CMIP6 experiments, it is understandable that most participants validated a few select variables, and more extensive validations may be in preparation. Essential Climate Variables (ECVs) prioritized for land evaluation in the ESMValToolv2.0 included GPP, LAI, and NBP (Eyring et al., 2020; 2016b), as these variables intersect with other ESM components in matter and energy exchanges (Reichler and Kim, 2008). Contrarily, LAI and NBP were not as frequently validated as GPP by CMIP6 participants (Figure A1-1), though the third most validated variable, the global land carbon sink, is equivalent to NBP minus land use emissions. The most common variable chosen for validation by participants was GPP, which is advantageous as it represents a crucial carbon cycle flux. GPP designates the quantity of CO_2 removed from the atmosphere and assimilated into structural and non-structural carbohydrates during photosynthesis by vegetation, part of which is later respired back to the atmosphere. This quantity is limited by nutrient availability, light, soil moisture, stomatal response to atmospheric CO_2 concentration, and other environmental factors (Davies-Barnard et al., 2020), and is the largest carbon flux between the land biosphere and atmosphere (Xiao et al., 2019). Over-or under-estimations of GPP can lead to biases in carbon stocks, which are exacerbated through time (Carvalhais et al., 2014).

An emergent ecosystem property which integrates a variety of influential model processes is carbon turnover time calculated as the ratio of a long-term average total carbon stock compared to GPP or NPP (Eyring et al., 2020; Yan et al., 2017; Carvalhais et al., 2014). Carbon turnover times can be the source of pervasive uncertainty within ESMs, and their misrepresentation can lead to long-term drifts in carbon stocks, fluxes, and feedbacks (Koven et al., 2017). The evaluation capacity of turnover times was seldom utilized by CMIP6 participants, despite soil carbon being a relatively commonly validated variable. Many CMIP5 models were found to underestimate turnover times both globally and on a latitudinal basis (Eyring et al., 2020; Fan et al., 2020), while two participants here reported overestimated carbon turnover times, Delire et al. (2020) and Lawrence et al. (2019), though demonstrate improvement from previous models.

Another approach to validation which combines high-level variables and re-parameterization efforts is the assessment of functional relationships or emergent constraints, such as the relationship between GPP or turnover times and temperature, moisture, growing season length, and nutrient stoichiometry (Danabasoglu et al., 2020; Swart et al., 2019; Anav et al., 2015; McGroddy et al., 2004). Physically interpretable emergent constraints can aid in identifying model components which are particularly influential to climate projections (Eyring et al., 2019), such as the temperature control on carbon turnover in the top metre of soil in cold climates (Koven et al., 2017), GPP responses to soil moisture availability (Green et al., 2019), or regional carbon-climate feedbacks (Yoshikawa et al., 2008). With the goal of realistically simulating Earth system processes to develop informed predictions of future climate, large scope variables which inherit uncertainty from an amalgamation of processes are often prioritized for validation. Several participants focused on comparing simulated long-term trends or accumulations in global land carbon fluxes to observation-based estimates from the Global Carbon Project (Friedlingstein et al., 2019; Le Quéré et al., 2018; 2016). While this summation approach can signal a large bias (Eyring et al., 2020; 2016b; Reichler and Kim, 2008) and reduce the effect of sub-scale noise, it does not identify sources of model error or may even obscure model error. For example, if simulated land-atmosphere carbon flux from the pre-industrial era to the 2010s is found to concur with observation-based estimates, this could be due in part to compounding underlying biases which neutralize one another over time (Fisher et al., 2019; Yoshikawa et al., 2008), or alternatively suitable global averages may be susceptible to antagonistic regional biases, such as between the tropics and northern high latitudes. Plant functional type-level evaluations, such as that of the maximum rate of rubisco carboxylation and canopy height by Lawrence et al. (2019) demonstrate the performance of underlying variables in influencing large-scale carbon fluxes and stocks. Several participants included latitudinal-scale evaluations (Delire et al., 2020; Hajima et al., 2020; Mauritsen et al., 2019), which are both informative and readily comparable to observations. A comprehensive validation should therefore encompass a range of scales and a variety of variables to demonstrate model performance in not only producing suitable averages or accumulations, though also in representing processes.

A1.4.2 Reference Datasets

Satellite-based remote sensing of terrestrial biogeochemical components has been conducted for almost 50 years, with the launch of the Landsat satellite in 1972 (Xiao et al., 2019; Mack, 1990), while field-based experimental and observational data has been available since at least the early 19th century (Holland et al., 2015). In terms of just satellite-based observational data products there are currently thousands available (Waliser et al., 2020). Despite this seeming wealth in observational data and observation-based data products, the implementation of a variety of observation-based references for validation of terrestrial biogeochemical cycles within ESMs and LSMs is challenging for several reasons. These include the specifications required for direct model output comparison, inconsistent spatial and temporal domains, missing observations, logistical biases, and large uncertainty in global scale data products (Delire et al., 2020; Collier et al., 2018; Lovenduski and Bonan, 2017). The incomplete coverage of observational datasets in space-time dimensions has led to significant bias in comparisons of model data and observation data previously (de Mora et al., 2013), though was not generally discussed in validation exercises by CMIP6 participants. Observational discontinuity has been addressed previously in a LSM validation by Orth et al. (2017) which excluded daily observation reference averages when more than one hour of data from a 24-hr period was missing, and through exclusion criteria in Collier et al. (2018). For example, the compilation of satellite observations to develop a LAI data product with one observation-based estimate every 15 days by Zhu et al. (2013) for monthly average or seasonal extrema comparison would require careful consideration for comparison to model averages computed from more resolved output. In an analysis of how sparse historical measurements compare to continuous model output, de Mora et al. (2013) demonstrate that where data are lacking in time or space, the discrete comparison of model output to records from site-level measurements may provide a strategic assessment of model performance over time, especially in producing interannual variability. Site-level comparisons of GPP and or CO_2 concentrations were performed by Delire et al. (2020), Dunne et al. (2020), and Vuichard et al. (2019), while Collier et al. (2018) caution against the use of spatially sparse data, though indicate that inclusion of site level evaluations is a key future focus for the ILAMB project.

Another approach to overcome spatial discontinuity may be to compare broad gradients or trends in a given variable with reference datasets, such as regional and functional type trends in forest carbon stocks rather than a global summation or average (Thurner et al., 2014), to investigate whether or not the model captures enduring spatial patterns. In addition, some observational methods may invoke inherent bias, such as satellite-based observation estimates of LAI in mid to high latitudes seasonally underestimating LAI due to snow cover, leading to ambiguous model performance assessment (Ziehn et al., 2020; Liu et al., 2018). Observational uncertainty can be addressed by applying a weighting to reference datasets as in ILAMBv2.1, as well as by using more than one observational reference when available (Eyring et al., 2020; Sellar et al., 2019; Collier et al., 2018). Careful consideration of spatiotemporal discontinuity in observations and inherent bias is warranted in future validations, which can be achieved through filtered exclusions, site-level comparisons, pattern comparison, certainty weighting of datasets, and the use of more than one reference dataset.

The globally gridded 1982-2008 GPP data product frequently used for GPP validation by CMIP6 participants was developed from machine learning upscaling of site-level eddy-covariance Fluxnet observations with model tree ensembles based on remote sensing vegetation indices, meteorological data, and land use (Jung et al., 2011). Observation-based estimates of

GPP can be obtained through satellite-derived vegetation indices such as the normalized difference vegetation index (NDVI; Phillips et al., 2008) and solar induced chlorophyll fluorescence (Zhang et al., 2020), in addition to ground-based monitoring of turbulent CO_2 fluxes with the eddy covariance technique (Jung et al., 2009). Logistical challenges with eddy covariance-based techniques of estimating GPP can result in potentially extensive data gaps and systematic omission of diel cycle observations (Rodda et al., 2021; Erkkilä et al., 2017; Jung et al., 2011; Lasslop et al., 2010; 2008; Desai et al., 2008). For example, in a study of eddy-covariance monitoring of CO_2 flux, Jonsson et al. (2008) report only 34% data coverage of a growing season period, of which 54% was discarded as it did not demonstrate energy balance closure. To address these challenges Jung et al. (2011) employ Bowen ratio corrections of energy imbalance (Twine et al., 2000), quality control criteria to exclude sites with more than 20% missing observations, and monthly averages to alleviate noise. Where NEE observations are missing in space over time driver relationships can be utilized for multi-decadal extrapolation, though only 38% and 60% of Fluxnet sites with less than 15 years of observations capture mean conditions and interannual variability of drivers sufficiently well for this extrapolation as of 2015, and most have been operating for less than five years (Chu et al., 2017). While the site-level observations from Jung et al. (2011) originate from 212 sites, presenting a globally extensive network, regions with an important contribution to overall carbon stocks and fluxes are underrepresented (Jung et al., 2020), and even the recent global Fluxnet GPP data product by Jung and Tramontana et al. (2016) has just 14 tropical and 5 Arctic sites. GPP observations from Fluxnet products currently do not account for fire and waterbody emissions, which prompts regional and interannual bias (Jung et al., 2020). Despite these caveats, such global-scale data products provide a critical resource to the CMIP community in conducting model validation

(Collier et al., 2018), and the relatively common use of Jung et al. (2011) for validations by CMIP6 participants coincidentally reduces the influence of observational contradiction (Xie et al., 2020; Anav et al., 2015). Site-level GPP evaluation with observations from the tropics by Delire et al. (2020) and Vuichard et al. (2019) demonstrates a strategic approach to addressing the representation bias in GPP validations. Site-level evaluations often benefit from a wealth of available information including spatially consistent meteorological forcing, and avoid the influence of spatial extrapolation error. While Jung et al. (2011) do not provide uncertainty measures, several forms of uncertainty are explicitly presented for the Fluxnet2015 dataset by Pastorello et al. (2020). Therefore the utility of Fluxnet GPP data products could be improved with standardized use by participants in junction with other independent data products, select site-level evaluations, explicit uncertainty quantifications, and improved ecological representation in underlying site-level data.

A1.4.3 Statistical Metrics and Validation Approaches

Several participants relied primarily on residual-based metrics such as bias (simulated-observed) for validation of terrestrial biogeochemical cycle model components. On a spatial basis bias can identify significant regional over-or under-estimations of a given variable. However, the attribution of model error from global maps of bias can be ambiguous, as the displayed bias is the combined result of different forms of uncertainty, including model structural representations, unforced variability, and spatial disagreement (Deser et al., 2020; Lovenduski and Bonan, 2017; Koch et al., 2016). Such residual-based metrics may not indicate how well the model would perform in simulating future conditions beyond the current contextual envelope of observations (Gulden et al., 2008), and neglect the contribution of uncertainty from observations. These limitations are considerable in the context of ESMs and LSMs as tools for predicting terrestrial biogeochemical function. A more contextualized bias assessment is the Wilcoxon test as applied by Swart et al. (2019) to filter insignificant bias. In a LSM evaluation, Orth et al. (2017) provides an observationally robust bias assessment by subtracting mean seasonal cycles from each grid cell and correlating the resulting anomalies between observation-based datasets and model output. In addition, RMSE normalized by the mean or standard deviation of the observed quantity, NRMSE, contextualizes the difference between simulated and observed variable quantities in terms of the magnitude or inherent variability of the variable of interest (Swart et al., 2019; Fan et al., 2018), which is advantageous for variables such as GPP with large interannual variability.

Beyond these, a variety of targeted model skill metrics have been published for process-based modelling which provide detailed assessments of different forms of model uncertainty (Collier et al., 2018; Orth et al., 2017; Eyring et al., 2016b; Koch et al., 2016; Law et al., 2015; Kumar et al., 2012; Taylor, 2001; Kobayashi and Salam, 2000). Mean squared deviation, the sum of squared bias, squared difference between standard deviations, and lack of correlation weighted by standard deviations, presented by Kobayashi and Salam, (2000), was used by Vuichard et al. (2019). This metric is readily applicable to the objective validation and improvement of mechanistic models, as its dissection allows for the accurate attribution of different sources of model errors. Additionally, a Taylor diagram (Figure A1-4, Taylor, 2001) conveys several dimensions of model error and allows for the concise simultaneous display of variables and models and was utilized in the evaluation of BCC-AVIM2 (Li et al., 2019b), and NORESM2 (Seland et al., 2020), as well as several LSMs and ESMs by Anav et al. (2015) and is incorporated into ILAMBv2.1 (Collier et al., 2018). The Taylor diagram was designed for simultaneous performance comparison of several simulated variables and serves as a concise and informative validation tool. Caution is warranted however in the evaluation of fully coupled model output due to the inability of fully coupled models to reproduce the timing of internal climate variability phenomena such as El Niño-Southern Oscillation (ENSO; Flato et al., 2013). While the magnitude of observed and simulated internal climate variability may be statistically consistent, bias, RMSE, and NRMSE assessments of fully coupled model output should encompass decadal or longer periods to address the influence of temporal mismatches in simulated internal climate variability relative to observational records. Alternatively, as offline simulations can be directly forced with historical observation data, the output of offline simulations can be validated on a finer temporal scale.

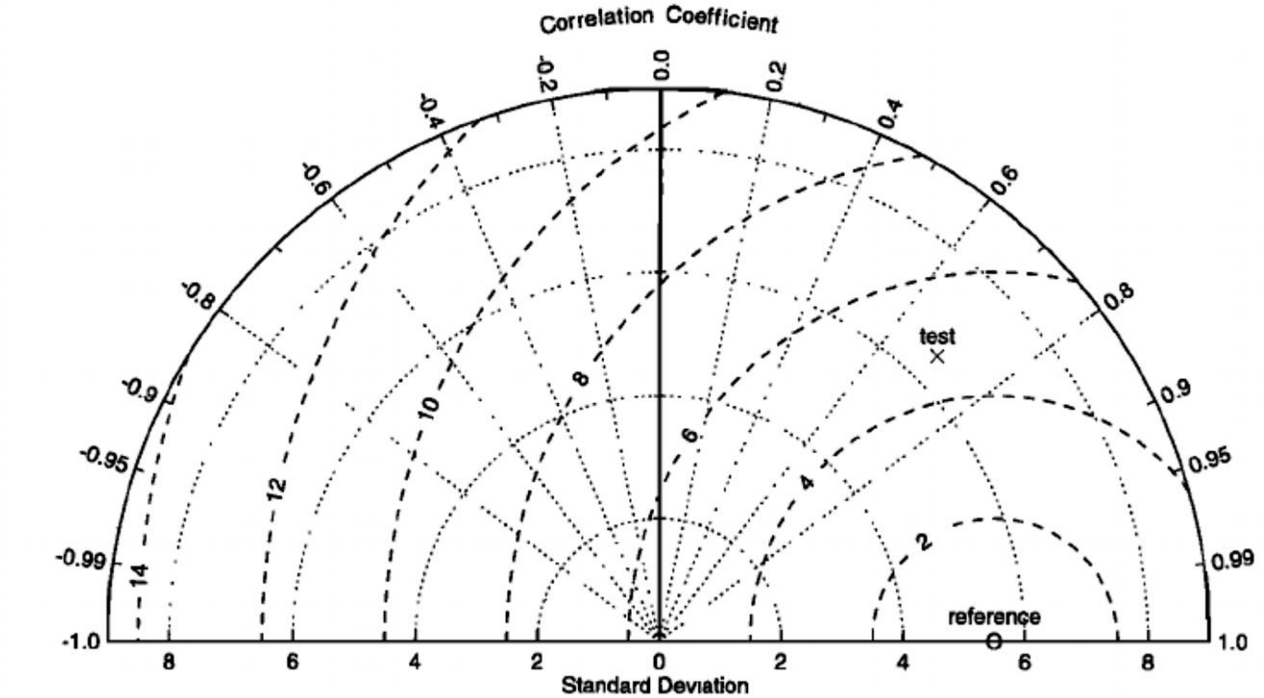

Figure A1-4. *Taylor diagram from Taylor, (2001). The standard deviation of model fields is displayed as the radial distance from the origin and can be visually compared to the observed (reference) point, which is indicated by a circle on the abscissa. The correlation between the model and observed fields decreases with azimuthal angle (dotted lines), and the root-mean-square difference between the model and observed fields is proportional to the distance from the reference point (quantified by dashed contours).*

For example, Taylor diagrams of global and regional NPP by Anav et al. (2015) demonstrated consistent low correlation and high standard deviation for model estimates in the tropics which is substantially reduced in the extratopics and globally, warranting focus on tropical NPP. The validation process of terrestrial biogeochemical cycles and dissection of model uncertainty may also be enhanced through offline simulations or models with intermediate complexity as these allow for a greater replication of simulations with different initializations, forcing datasets, and model configurations, due to their computational affordability (Bonan et al., 2019; Umair et al., 2018; Orth et al., 2017). Offline simulations also reduce the potential for incidental compounding error from coupling components, though this leads to an underestimation in uncertainty for equivalent fully coupled simulations. Replicate simulations with different initial conditions allow for the attribution of uncertainty from unforced variability, such as performed by Danabasoglu et al. (2020), which accounted for half of the inter-model spread in key variables previously (Deser et al., 2020; Eyring et al., 2019). In addition, replicate simulations with different forcing datasets can indicate the role of forcing uncertainty (Wei et al., 2018), which Lawrence et al. (2019) found to be significant. Further, sensitivity analyses or perturbed parameter analyses involving replicated simulations with one or more variables fixed as performed by Hajima et al. (2020) and Lawrence et al. (2019) illuminate structural uncertainty. The use of well-established statistical and model performance metrics in addition to strategic simulations facilitates a detailed analysis of model uncertainty.

A1.4.4 Moving Forward

A model can only be expected to perform well in simulating past, present, and future conditions if provided with high quality observational constraints. Lovenduski and Bonan (2017) suggest that obtaining accurate observations and improving process understanding should take precedence over reducing model spread, as constraining models to uncertain observations does not improve their predictive capacity, and even models which agree well with observations can prompt divergent projections. Several of the challenges inherent in implementing observations in model validation and development are now a key focus of the Observations for Model Intercomparison Project (obs4MIPs; Waliser et al., 2020) which strives to deliver long-term, high-quality observations from international efforts. An obs4MIPs meeting held in preparation for CMIP6 with more than 50 satellite data and global climate modelling experts identified underutilized observation products and recommended new efforts to address knowledge gaps, including an expanded inventory of datasets, higher-frequency datasets and model output, more reliable uncertainty measures, more datasets tailored to offline simulations, and more explicit metadata for modellers (Waliser et al., 2020). Further, recent satellite missions such as the Sentinel2A twin satellite launched in 2015 have unprecedented spectral, spatial, and temporal resolution combinations, which can be used alone or in combination with other satellite-based observations to provide higher fidelity references for validation (Vafaei et al., 2018). Field experimental data provide unique insight as to the functional responses of vegetation to elevated CO_2 concentration (Goll et al., 2017), temperature change (Richardson et al., 2018), moisture availability (Williams et al., 2019; Hovenden and Newton, 2018), and nutrient limitations (Fleischer et al., 2019), outside the current context of observations. The integration of experimental findings in evaluations is challenging given the environmentally rapid application of treatments and limited ecological representation (Nowak et al., 2004), though sophisticated relationship-based techniques such as used by Goll et al. (2017) alleviate some of these issues. Increased collaboration between field and model researchers in designing experiments could improve the applicability of future experiments. In addition, enhanced field and remote sensing collaboration would allow for higher fidelity calibrated global data products (Orth et al., 2017; Verger et al., 2016). Thus future CMIPs will benefit from forthcoming collaborations and reference data products tailored for validation.

A standard protocol for the validation of terrestrial biogeochemical variables would facilitate a thorough and objective assessment of model performance within and among participants. Further, the collective merits and limitations of the current variety of approaches utilized by participants could be consolidated and addressed in a comprehensive protocol. In the interest of model improvement and weighting for predictions, validation with an exhaustive assessment of variables across a range of spatiotemporal scales against all available peer-recommended observation-based references is optimal. Dataset-specific expertise is also warranted to correctly implement reference datasets in these evaluations (Waliser et al., 2020; Liu et al., 2018). The procurement and application of reference datasets within validations is demanding for participants, considering their presiding obligation to continuously refine model components and participate in CMIP with computationally expensive ESM simulations. Additionally, the universal inclusion of often overlooked processes such as moisture limitation, nitrogen and phosphorus cycles, dynamic vegetation, prognostic leaf phenology, and natural disturbance regimes should be a priority focus for participants in developing diagnostic models as these processes are highly influential on terrestrial biogeochemistry and physics (Eyring et al., 2020; Fleisher et al., 2019; Piao et al., 2019; Wieder et al., 2015; Achard et al., 2014; Richardson et al., 2013; Heimann and Reichstein, 2008; Tucker et al., 1986), and their omission contributes to widespread bias (Green et al., 2019; Anav et al., 2015). While outside the focus of this review, equal attention should be applied to the physical components of terrestrial biogeochemical cycles, including explicit representation of permafrost and riverine carbon transport dynamics. In fact, a study including four CMIP5 ESMs found that soil moisture variability prompted variability in terrestrial NBP on the order of gigatonnes, with non-linear responses to both moisture scarcity and excess (Green et al., 2019). Further, many of the merits and limitations of the validation approaches discussed herein apply to the validation of these physical components as well.

The communal use of software packages such as ESMValToolv2.0 and ILAMBv2.1 (Eyring et al., 2020; Collier et al., 2018) could liberate time and computational resources for modellers. In addition, this would standardize validation protocols, address long-overlooked model uncertainty distinctions (Deser et al., 2020), and avoid terminology confusion (Lovett et al., 2006). While these packages include extensive suites of peer-verified observational reference datasets and performance metrics, these packages do not yet include evaluation of nitrogen and phosphorus cycles, which may be due to the combined scarcity of observations, upscaling approaches, and model representations (Lawrence et al., 2019; Zhu et al., 2018; Wieder et al., 2015; Zaehle and Dalmonech, 2011). The strategic situation of nitrogen, phosphorus, and soil moisture monitoring which coincides with current Fluxnet sites (Jung et al., 2020) could provide high fidelity insight as to nutrient and environmental limitations on GPP, coherent turnover time assessments, and broadly applicable functional relationships to facilitate upscaling. The co-situation of multiple observational monitoring objectives at Fluxnet sites would enhance the utility of each site-level dataset and alleviate errors due to spatiotemporal inconsistencies between datasets in both performing evaluations and developing large scale data products. Following increased collaboration between empirical and modelling communities to strategically expand observations, and their inclusion in a comprehensive evaluation software, the CMIP-designated use of such software would standardize, conserve, and augment validation efforts.

A1.5 Conclusion

The current generation of ESMs which participated in the sixth phase of the Coupled Model Intercomparison Project adopted a broad assortment of approaches to validate historically simulated terrestrial biogeochemical cycles. Validations which encompassed a large suite of variables over a range of spatiotemporal scales in conjunction with informative model performance metrics demonstrated relatively comprehensive assessments of model performance. Across CMIP6 participants, the variety of variables, reference datasets, evaluation dimensions, and statistical metrics utilized make general assessments of model performance in simulating terrestrial biogeochemistry challenging. To address this inconsistency and alleviate the immense responsibilities of participants, we recommend the designation of a standard validation protocol for CMIP participants, which is consolidated in an open-source software (such as the Earth System Model Evaluation Tool version 2 (ESMValToolv2.0) or the International Land Model Benchmarking version 2.1 (ILAMBv2.1)). This protocol should utilize a comprehensive suite of certainty-weighted observational reference datasets, targeted model performance metrics, and comparisons across a range of spatiotemporal dimensions. The insights from a universally adopted validation protocol would precisely attribute model uncertainty and aid in directing future observational efforts to improve crucial process understanding within terrestrial biogeochemical cycles.

Author contributions

LS and AHMD both initiated the research and significantly contributed to the writing of the paper. LS conducted the analysis and wrote the original draft. AHMD provided supervisory support.

A1.6 Technical Summary of Validation Activities by Participants

A1.6.1 CSIRO

The Australian Community Climate and Earth System Simulator (ACCESS-ESM1.5) was developed by the Australian modelling group Commonwealth Scientific and Industrial Research Organization (CSIRO) for participation in CMIP6 (Ziehn et al., 2020). The land surface model used in ACCESS-ESM1.5 is the Community Atmosphere Biosphere Land Exchange (CABLE) model (Kowalczyk et al., 2013; 2006) version 2.4. Ziehn et al. (2020) compared ACCESS-ESM1.5 simulated land carbon cycle variables against observation-based estimates for the 1986-2005 period. The spatial distribution of simulated average annual GPP was compared to upscaled Fluxnet observations from Jung et al. (2011), while average annual global GPP was compared to observation-based estimates from Beer et al. (2010) and Ziehn et al. (2011). Simulated LAI magnitude and seasonality was compared to global and regional estimates based on Moderate Resolution Imaging Spectroradiometer (MODIS) and Advanced Very High-Resolution Radiometer (AVHRR) data from Zhu et al. (2013). Simulated surface CO_2 concentrations in terms of mean seasonal cycle amplitude and timing were compared to four NOAA/Earth System Research Laboratory station flask samples provided in the GLOBAL VIEW data product (GLOBAL VIEW-CO_2 2013).

A1.6.2 BCC

The Beijing Climate Centre (BCC) participated in CMIP6 with the BCC Climate System Model version 2 with medium resolution (BCC-CSM2-MR; Wu et al., 2019). Land biogeochemistry in BCC-CSM2-MR was simulated through the BCC Atmosphere and Vegetation Interactive Model version 2.0 (BCC-AVIM2; Li et al., 2019b). While Wu et al. (2019) did not provide validation results for terrestrial biogeochemistry from BCC-CSM2-MR, a detailed validation with offline simulations of BCC-AVIM2 was provided by Li et al. (2019b) using the Princeton global forcing dataset (Sheffield et al., 2006). Li et al. compared the annual peak month, seasonal average, and global average of LAI to satellite observations from 1982-2010 by the AVHRR (Myneni et al., 1997). Surface carbon fluxes including GPP and ER were compared to upscaled Fluxnet observations from Jung et al. (2011). Above ground biomass was compared to Avitabile et al. (2016), while global total biomass carbon from 1990-2010 was compared to Saatchi et al. (2011). The performance of BCC-AVIM2 in estimating each of these variables was assessed through bias, RMSE, and Taylor diagram metrics (Taylor, 2001).

A1.6.3 CCCma

The Canadian Centre for Climate Modelling and Analysis (CCCma) participated in CMIP6 with the CCCma fifth generation Earth System model (CanESM5; Swart et al., 2019). The land biogeochemistry component of CanESM5 is the Canadian Terrestrial Ecosystem Model (CTEM; Arora and Boer, 2010; 2005). Swart et al. (2019) compared CanESM5 simulated GPP from 1982-2009 with observation-based estimates from Jung et al. (2009) in terms of geographical distribution, zonal averages, as well as functional relationships with air temperature and precipitation. Several metrics were used to illustrate CanESM5's performance in simulating GPP, including the correlation coefficient (r) between simulated and observed spatial patterns in GPP, bias (simulated – observed), as well as root mean squared error (RMSE) normalized (NRMSE) by observed spatial standard deviation. Global average decadal land-atmosphere CO_2 flux as well as net cumulative atmosphere-land CO_2 flux from 1850-2014 were compared to observation-based estimates from the Global Carbon Project (GCP; Le Quéré et al., 2018), the latter by subtracting cumulative land use emissions from cumulative land carbon uptake.

A1.6.4 Climate and Global Dynamics Laboratory NCAR

The Community Earth System Model version 2 (CESM2) was developed by the Climate and Global Dynamics Laboratory at the American National Centre for Atmospheric Research (NCAR) for participation in CMIP6 (Danabasoglu et al., 2020). The land component of CESM2 is the Community Land Model Version 5 (CLM5; Lawrence et al., 2019). Danabasoglu et al. (2019) and Lawrence et al. (2019) comprehensively assessed terrestrial biogeochemical cycle variable outputs from simulations of CESM2 and CLM5, respectively, with the International Land Model Benchmarking package (ILAMBv2.1; Collier et al., 2018), including an explicit analysis of interannual variability with a three member ensemble from different pre-industrial control initialization years (CESM2), the influence of forcing through the use of three forcing datasets (CLM5), and the influence of prescribed versus prognostic vegetation phenology (CLM5). ILAMBv2.1 utilizes a suite of data products weighted by certainty. These included vegetation biomass (tropical: Saatchi et al., 2011; global: Kellndorfer et al., 2013; Blackard et al., 2008), burned area (Giglio et al., 2010), CO_2 concentrations, GPP (Fluxnet: Lasslop et al., 2010; Global biosphere-atmosphere flux: Jung et al., 2010), LAI (AVHRR: Myneni et al., 1997; MODIS: de Kauwe et al., 2011), global net ecosystem carbon balance (GCP: Le Quéré et al., 2014; Hoffman et al., 2014), net ecosystem exchange (Fluxnet: Lasslop et al., 2010; GBAF: Jung et al., 2010), NBP, ER, NEP (equivalent to GPP-ER), soil carbon (Harmonized World Soil Database (HWSD): Todd-Brown et al., 2013; Northern Circumpolar Soil Carbon Database (NCSCDV22): Hugelius et al., 2013), as well as 10 functional relationships. Lawrence et al. (2019) also compared the relationship between apparent soil carbon turnover times versus air temperature to observation-based estimates developed from HWSD, NCSDV22, and MODIS. Lawrence et al. (2019) additionally compared maximum monthly LAI and average V_{cmax25}

(maximum rubisco carboxylation rate at 25°C and high irradiance per unit leaf area in $\mu\text{mol}\cdot\text{m}^{-2}\cdot\text{s}^{-1}$) at the PFT-level for the year 2010 to Zhao et al. (2005) and Kattge et al. (2009), respectively, as well as canopy height for the year 2005 for tree PFTs to Simard et al. (2011). Nitrogen cycle variables evaluated by Lawrence et al. (2019) with observational references included nitrogen deposition (Fowler et al., 2013), symbiotic fixed nitrogen (Vitousek et al., 2013), soy fixed nitrogen (Herridge et al., 2008), crop nitrogen fertilization (Fowler et al., 2013), denitrification (Fowler et al., 2013), hydrologic nitrogen losses (Fowler et al., 2013), fire losses (Lamarque et al., 2010), and N_2O flux (Fowler et al., 2013). Different climate forcing datasets and anthropogenic forcings were utilized to examine the effect of climate, CO_2 emissions, land use change, and nitrogen additions on carbon cycle variables as well as three CLM model versions to partition total uncertainty into forcing and model contributions using fixed-effect analysis of variance, with additional PFT-level analysis and prognostic versus prescribed vegetation and carbon cycling for CLM5. In addition to the ILAMB validation, Danabasoglu et al. (2019) and Lawrence et al. (2019) compared simulated global net biome production (NBP) and cumulative land carbon sink to observation-based estimates from 1850-2014 from the GCP for 1959-2014 (Le Quéré et al., 2016), and from Hoffman et al. (2014) for 1850-2010. Observation-based GPP, ER, and NEP (equivalent to GPP-ER), comparison data were obtained from Jung et al. (2011; 2010). Vegetation carbon was evaluated relative to observations for the tropics from Saatchi et al. (2011), as well as GEOCARBON and GlobalCarbon datasets (Collier et al., 2018; Avitabile et al., 2016; Santoro et al., 2015). ILAMBv2.1 results from these investigations comprised a collection of statistical metrics for annual mean, bias, relative bias, RMSE, seasonal cycle phase, spatial distribution, and interannual variability, in addition to functional relationships. Bonan et al. (2019) provides a detailed analysis on the role of climate forcing uncertainty in influencing CLM5 output.

A1.6.5 CNRM and CERFACS

The Centre National de Recherches Météorologiques (CNRM) and Centre Européen de Recherche et de Formation Avancée en Calcul Scientifique (CERFACS) contributed the CNRM-ESM2-1 to CMIP6 (Séférian et al., 2019). The land component in CNRM-ESM2-1 is the Interaction Soil-Biosphere-Atmosphere with Total Runoff Integrating Pathways with carbon cycling (ISBA-CTRIP; Delire et al., 2020). Séférian et al. (2019) compared CNRM-ESM2-1 simulated annual minimum and maximum LAI to AVHRR observations from 1998-2011 (Zhu et al., 2013). The simulated land carbon sink from 1982-2010 was compared to a multi-model estimate by Huntzinger et al. (2013). These validations included spatial bias, global mean bias, RMSE, as well as spatial error correlation between CNRM ESM versions to distinguish model sources of error. Delire et al. (2020) validated offline ISBA-CTRIP simulated GPP, NPP, autotrophic respiration, and ER from 1980-2010 with estimates with the mean of 12 products from the FluxComv1 dataset (Jung et al., 2017; 2016; Tramontana et al., 2016), and a satellite product from the Numerical Terradynamic Simulation Group: MODIS17A3 (NASA LP DAAC, 2017; Zhao et al., 2005), with reference autotrophic respiration calculated as the mean of FLUXCOM GPP products minus MODIS17A3 NPP. Simulated crop NPP for the 2000s was compared to the Harvested Area and Yield dataset (Monfreda et al., 2008). Carbon use efficiency (CUE), calculated as the ratio of NPP to GPP, was evaluated with observation and model-based estimates for tropical evergreen forest from Malhi et al. (2009), and tropical deciduous, temperate, and boreal forests from He et al. (2018), Zhang et al. (2014), and theoretical derivations by Amthor, (2000). Simulated heterotrophic respiration was evaluated with a data product from Hashimoto et al. (2015) which combines global and Amazonian in situ observations from the Soil Respiration database (Bond-Lamberty et al., 2018) and Malhi et al. (2009), respectively, and global gridded climate data. The simulated burned area and fire CO_2 emissions were compared to Mouillot and Field (2005) and the Global Fire Emissions Database version 4.1 (Randerson et al., 2017; van der Werf et al., 2017). Simulated dissolved organic carbon yield leached from soil was compared to model results of Mayorga et al. (2010), and observations by Dai et al. (2012). Simulated global aboveground biomass carbon was validated with observation-based estimates from 1993-2012 from Liu et al. (2015), regional datasets for mid-high northern latitudes from Thurner et al. (2014), and tropical datasets from Saatchi et al. (2011) and Baccini et al. (2012). Simulated above ground litter carbon was compared to site measurements from 1827-1997 from the Global Database of Litterfall Mass and Litter Pool Carbon and Nutrients (Holland et al., 2015). Simulated belowground organic carbon was validated with the HWSDv1.2 (FAO, 2012). Vegetation turnover time calculated as biomass divided by NPP and soil turnover time calculated as the combination of litter and soil carbon divided by NPP for 1984-2014 were also computed for validation. Delire et al. (2020) also used local scale Fluxnet data from Joetzjer et al. (2015) to assess ISBA-CTRIP performance. Each variable was validated through comparison of the distribution of simulated and observation-based estimates of annual averages, as well as zonal averages, and the spatial distribution of the bias (simulated minus observed). Average simulated carbon fluxes from 2006-2015 and the trend from 1960-2015 were also compared to observation-based estimates from the GCP (Le Quéré et al., 2018) and Ciais et al. (2019).

A1.6.6 IPSL

The Institut Pierre Simon Laplace (IPSL) participated in CMIP6 with IPSL-CM6A-LR, the land component of which was the ORCHIDEE land surface model version 2.0 (Boucher et al., 2020; Hourdin et al., 2020). Boucher et al. (2020) evaluated IPSL-CM6A-LR simulated average annual carbon fluxes from 1990-1999 and 2009-2018 resulting from land cover change, fossil fuel emissions, the terrestrial sink, and total net land fluxes (the terrestrial sink minus land cover change) with observation-based estimates from the 2019 GCP (Friedlingstein et al., 2019). Vuichard et al. (2019) validated ORCHIDEE simulated GPP in terms of the mean annual, seasonal, and daily simulated GPP on a PFT, spatial, and global basis against observations from 78 Fluxnet sites (Vuichard and Paple, 2015) and the global-scale MTE-GPP product based upon upscaled Fluxnet observations for 1982-2008 (Jung et al., 2011). RMSE as well as dissected mean squared deviation (MSE; which is the sum of squared bias, squared difference between standard deviations, and lack of correlation weighted by standard deviations; based on Kobayashi and Salam, (2000)), metrics were used to attribute different sources of uncertainty. The relative contribution of drivers of variation in present-day GPP were also assessed, including seasonal variability in NO_x and NH_x deposition as well as leaf carbon: nitrogen ratio. The sensitivity of ORCHIDEE output to model structure in terms of MSE was also analyzed on a global and PFT-level basis, including fixed and dynamic fully coupled carbon-nitrogen cycles.

A1.6.7 GFDL

The American National Oceanic and Atmospheric Administration Geophysical Fluid Dynamics Laboratory (GFDL) participated in CMIP6 with GFDL-ESM4.1 (Dunne et al., 2020), in which land biogeochemistry is simulated with the GFDL Land Model version 4.1 (LM4.1; Shevliakova et al., 2020). Dunne et al. (2020) validated GFDL-ESM4.1’s simulated spatial distribution of seasonal amplitude in CO_2 concentrations and interannual variability of CO_2 concentrations compared to NOAA Global Monitoring Division sites with at least 15-year long records (Global Monitoring Laboratory, 2005) using RMSE and the coefficient of determination (r^2), as well as the correlation coefficient (r) for individual sites.

A1.6.8 JAMSTEC, University of Tokyo, and National Institute for Environmental Studies

The Japanese Agency for Marine-Earth Science and Technology (JAMSTEC), University of Tokyo, and National Institute for Environmental Studies participated in CMIP6 with the Model for Interdisciplinary Research on Climate Earth System version 2 for Long-term simulations (MIROC-ES2L; Hajima et al., 2020). The land biogeochemical component in MIROC-ES2L is Vegetation Integrative Simulator for Trace gases model (VISIT-e; Ito and Inatomi, 2012). Hajima et al. (2020) evaluated MIROC-ES2L simulated terrestrial carbon gain with and without land use, as well as land use emissions from 1850-2014 in comparison to multi-model estimates from the GCP (Le Quéré et al., 2018). Observational-based data products used for other comparisons included 1) the spatial pattern, gradient across biomes, magnitude, seasonality, and length of growing season of global gridded GPP from 1986-2005 from Fluxnet (Jung et al., 2011), 2) the magnitude and density of forest carbon stock (Kindermann et al., 2008) and 3) global and regional soil organic carbon from the harmonized soil property values for broad-scale modelling (WISE30Sec; Batjes, 2016), the northern high latitudes from the Northern Circumpolar Soil Carbon Database version 2 (NCSCDv2; Hugelius et al., 2013), and an estimate from Todd-Brown et al. (2013) developed from the HWSD version 1.3 (FAO, 2012). Hajima et al. (2020) also compared simulated and observation-based estimates of annual biological nitrogen fixation (BNF) from 1850-2014 (Gruber and Galloway, 2008), present-day BNF (Galloway et al., 2008; Herridge et al., 2008), annual unperturbed state terrestrial N_2 flux

(Gruber and Galloway, 2008), and change in annual soil nitrous oxide emissions from 1850-2014 relative to a model comparison study by Tian et al. (2018).

A1.6.9 MPI

The Max Planck Institute for Meteorology (MPI) Earth System Model version 1.2 Low Resolution (MPI-ESM1.2-LR) was developed for participation in CMIP6 (Mauritsen et al., 2019) by the MPI, the land component of which is JSBACH3.2 (Goll et al., 2017). Mauritsen et al. (2019) compared the spatial variability and zonally averaged density of MPI-ESM1.2-LR simulated soil and litter carbon stocks to estimates by Goll et al. (2015) developed from the Harmonized World Soil Database. The simulated evolution in global total land carbon from 1850-2013 was compared to estimates provided by Ciais et al. (2013). Additionally, simulated land use change carbon emissions from 1860-2013 were compared to estimates provided by Ciais et al. (2013). In a model description paper of JSBACH version 3.10, which was set to be used in CMIP6, Goll et al. (2017) compare JSBACH3.1 simulated present-day NPP to Ito (2011), while simulated present-day biomass carbon was compared to Saugier and Roy, (2001) and Ciais et al. (2013). The simulated response of NPP and GPP to increases in atmospheric CO_2 were compared to experimentally observed estimates from four free-air CO_2 enrichment (FACE) experiments (Norby et al., 2005) and an intramolecular isotope distribution examination of plant metabolic shifts (Ehlers et al., 2015). Simulated present-day biomass nitrogen was compared to Schlesinger (1997) while simulated present-day total nitrogen was compared to Galloway et al. (2013). Simulated values of pre-industrial (1850) and present-day leaching and BNF were compared to Galloway et al. (2013; 2004), Vitousek et al. (2013), and short-term experimental results from a meta-analysis by Liang et al. (2016), while simulated present-day denitrification was compared to Galloway et al. (2013). Goll et al. (2017) also verified the simulated spatial variability in reactive nitrogen-loss pathways using a compilation of nitrogen-15 isotopic data (Houlton et al., 2015) with the statistical metrics r, RMSE, and Taylor score (Taylor 2001).

A1.6.10 NCC

The Norwegian Earth System Model (NORESM2) was developed for participation in CMIP6 (Seland et al., 2020) by the Norwegian Climate Consortium (NCC) and is based on CESM2. As in CESM2, the land model in NORESM2 is CLM5 (Lawrence et al., 2019). The performance of NORESM2 was validated through a three-member ensemble of historical simulations from 1850-2014 with slightly varying initial conditions. Simulated carbon cycle variables which were compared to observation variables included GPP, soil carbon, and vegetation carbon, from Jung et al. (2011), FAO, (2012), and Avitabile et al. (2016) and Santoro et al. (2015), respectively. Seland et al. (2020) NORESM2 results in terms of carbon stocks and fluxes broadly agree with those of Lawrence et al. (2019) while conducting land-only simulations of CLM5.

A1.6.11 NERC and Met Office

The United Kingdom Community Earth System Model (UKESM1-0-LL) was developed for participation in CMIP6 by the United Kingdom Natural Environmental Research Council (NERC) and National Meteorological Service (Met Office; Sellar et al., 2019). The land component in UKESM1-0-LL is an updated version of the Joint UK Land Environment Simulator (JULES; Clark et al., 2011) with an additional PFT updated competition scheme (Harper et al., 2018). Sellar et al. (2019) evaluated UKESM1-0-LL simulated global GPP magnitude and evolution in time through comparisons to recent decadal GPP from the Fluxnet model tree ensemble data product (Jung et al., 2011). The areal land cover of aggregated plant functional types (PFTs) was validated with satellite observation-based datasets from the

European Space Agency Climate Change Initiative Land Cover data (Poulter et al., 2015) as well as the International Geosphere-Biosphere Programme (IGBP) Land Use and Cover Change project (Loveland et al., 2000) using the model year 2005. The coverage of PFTs were validated using these observation-based datasets as references both spatially and as a fraction of biomes based upon regions defined by Olson et al. (2006). The simulated vegetation carbon distribution was validated on a latitudinal basis with observation-based estimates from GEOCAROBON (Avitabile et al., 2016) and Saatchi et al. (2011), while the spatial distribution of soil carbon was validated with observation-based estimates WISE30sec (Batjes, 2016), IGBP-DIS (Global Soil Data Task Group, 2002), and Carvalhais et al. (2014). The magnitude of simulated global total soil carbon was compared to whole soil profile observation-based estimates from Carvalhais et al. (2014) and upper 2 m observation-based estimates from Batjes, (2016). Cumulative carbon uptake and land use emissions from 1850-2014 was compared to observation-based estimates from the GCP (Le Quéré et al., 2018).

Appendix II: Supplementary Information for Chapter 2

To evaluate the sensitivity of our simulation to the assumed prior distributions of the input parameters, we conducted a number of sensitivity analyses. Assuming a normal distribution for all of the input variables (Figure A2-1) had a negligible influence upon the form and statistics of the calculated TCRE probability distribution function (PDF) (Figure A2-2). With normally distributed input parameters, the calculated TCRE PDF had a log-normal distribution, with a mean of 1.8 K EgC^{-1}, and a median of 1.7 K EgC^{-1}.

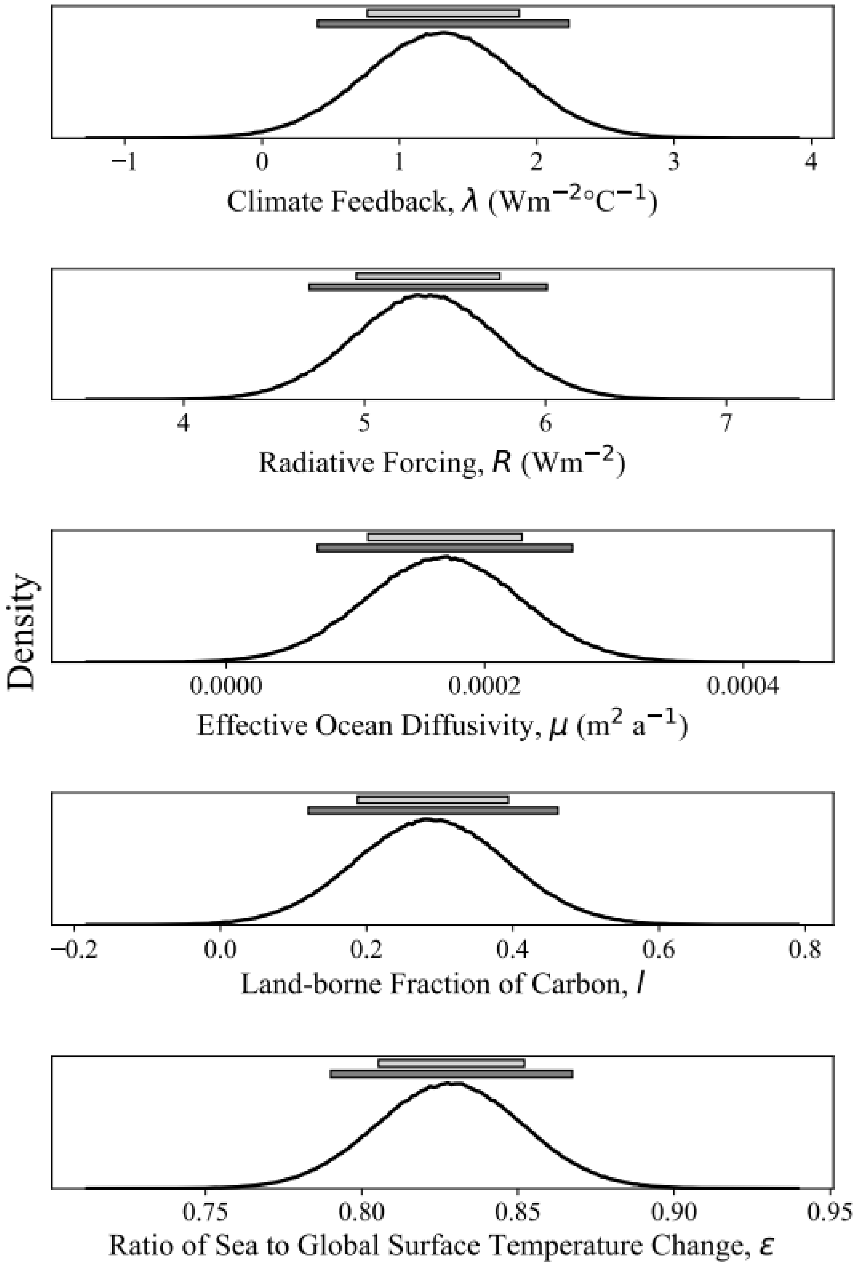

Figure A2-1. *Probability density functions (PDFs) of parameters used in the sensitivity analysis of the TCRE assuming normal parameter distributions. The light grey bar designates a 16-84% confidence interval, and the dark grey bar designates a 5-95% confidence interval.*

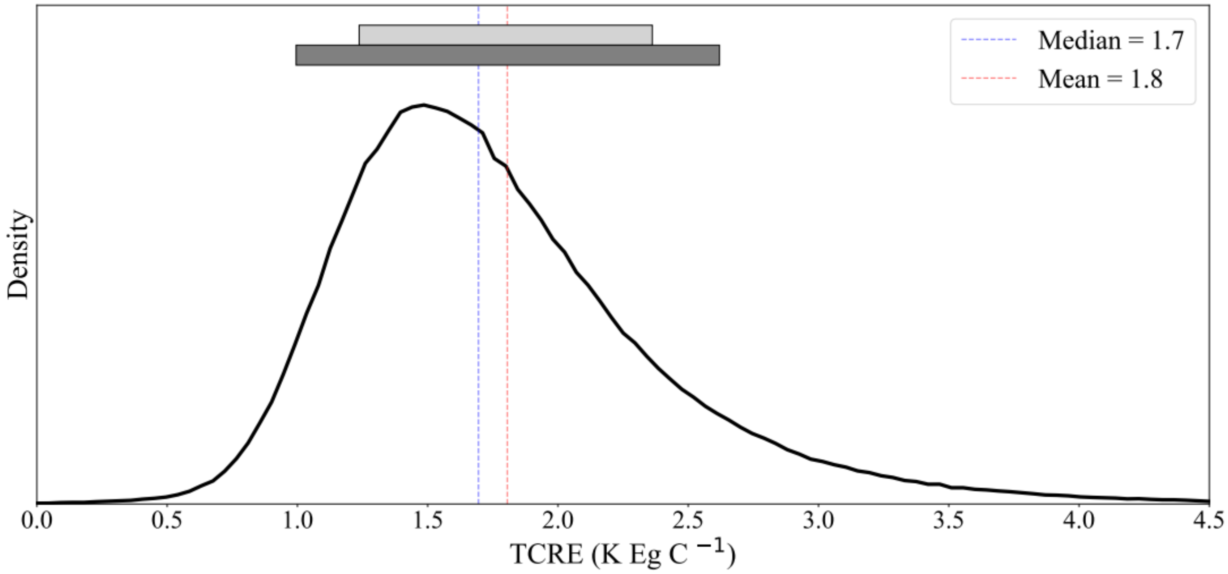

Figure A2-2. *Probability density function of calculated TCRE values resulting from assumed normal parameter distributions. The light grey bar designates a 16-84% confidence interval, and the dark grey bar designates a 5-95% confidence interval.*

Table A2-1 displays the range in TCRE values resulting from a uniform prior PDF for each of the input parameters while holding all other parameters at the best estimate value. The TCRE was most sensitive to the climate feedback parameter, followed by the fraction of landborne carbon emissions, effective ocean diffusivity, radiative forcing from an e-fold increase in atmospheric CO2, and least sensitive to the ratio of sea to global surface temperature change.

Table A2-1. *The TCRE range resulting from assuming a uniform probability distribution function for each input parameter of interest while maintaining all other parameters at a best estimate value.*

Parameter from Uniform Resultant TCRE Distribution (n=1,000,000)	**Resultant TCRE Range (K EgC−1)**
Effective Ocean Diffusivity (μ) (m^2a^{-1})	1.04 -3.09
Climate Feedback (λ) (Wm^{-2} ◦C^{-1})	0.64 -3.65
Radiative Forcing from an e-fold Increase in atmospheric CO2 (R) (Wm^{-2})	1.08 -2.41
Ratio of Sea to Global Surface Temperature Change (ε)	1.64 -1.87
Land-borne Fraction of Carbon (l)	0.07 -3.05

We conducted an analysis to examine the effect of assuming independent rather than linked probabilities between the climate feedback and radiative forcing from an e-fold increase in atmospheric CO_2 parameters. Assuming that these two parameters had linked probabilities had a negligible influence on the shape and statistics of the resultant TCRE PDF (Figure A2-3), which had a log-normal distribution, with a mean of 1.9 $KEgC^{-1}$, and a median of 1.8 K EgC^{-1}.

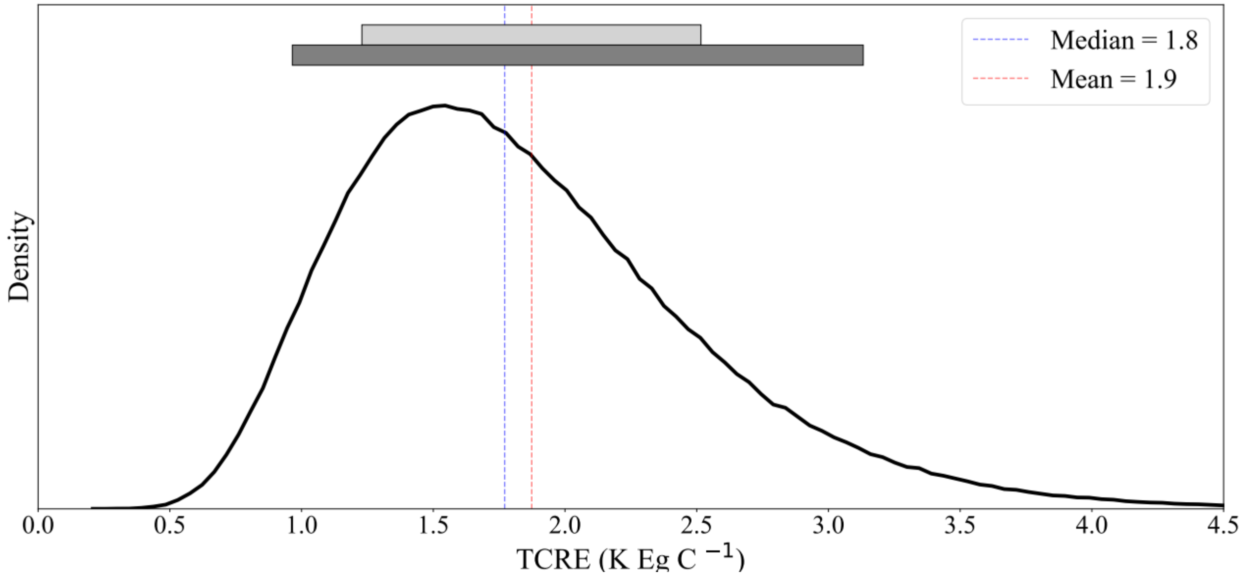

Figure A2-3. *Probability density function of calculated TCRE values resulting from assuming linked probabilities between radiative forcing from an e-fold increase in CO2 and climate feedback parameters. The light grey bar designates a 16-84% confidence interval, and the dark grey bar designates a 5-95% confidence interval.*

We examined the influence of utilizing an alternative estimate for Earth's Energy Imbalance (EEI) from Trenberth et al. (2016; 0.9 ± 0.3 W m^{-2}, from 2005-2014) rather than Johnson et al. (2016; 0.71 ± 0.11 W m^{-2}, from 2005.5-2015.5) in constructing the effective ocean diffusivity PDF and calculating the PDF of the TCRE. Using the estimate of EEI by Trenberth et al. (2016) had negligible impact on the shape and statistics of the resultant TCRE PDF (Figure A2-4), which had a log-normal distribution, with a mean of 1.8 K EgC^{-1} , and a median of 1.7 K EgC^{-1}.

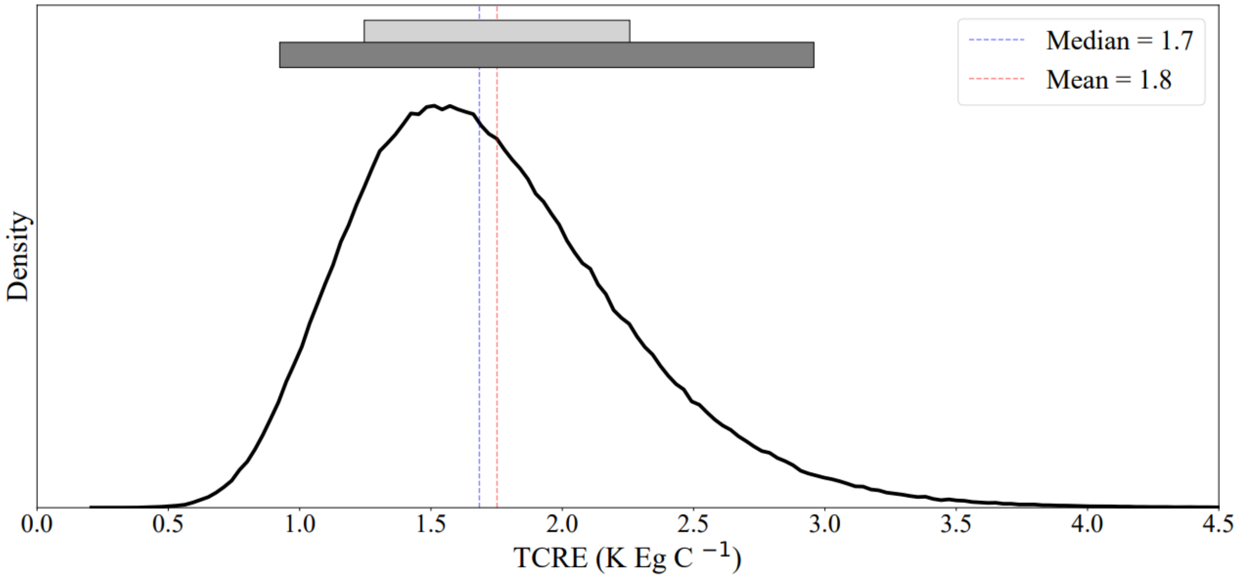

Figure A2-4. *Probability density function of calculated TCRE values resulting from using the Earth Energy Imbalance estimate (0.9 ± 0.3 W m−2, from 2005-2014) provided by Trenberth et al. (2016). The light grey bar designates a 16-84% confidence interval, and the dark grey bar designates a 5-95% confidence interval.*

We examined the implications of calculating the PDF for climate feedback with and without varying the forcing associated with a doubling of atmospheric CO2, 3.71 W m^{-2} (Myhre et al., 1998). The effect of varying forcing from a doubling of atmospheric CO2 was negligible in terms of both the resultant climate feedback PDF and the TCRE PDF (Figure A2-5). The resultant climate feedback PDFs in both cases had a mean of 1.3 W m^{-2}°C^{-1} and a median of 1.2 W m^{-2}°C^{-1}, while the resultant TCRE PDFs were both log-normal with a mean of 1.9 K EgC^{-1}, and a median of 1.8 K EgC^{-1}.

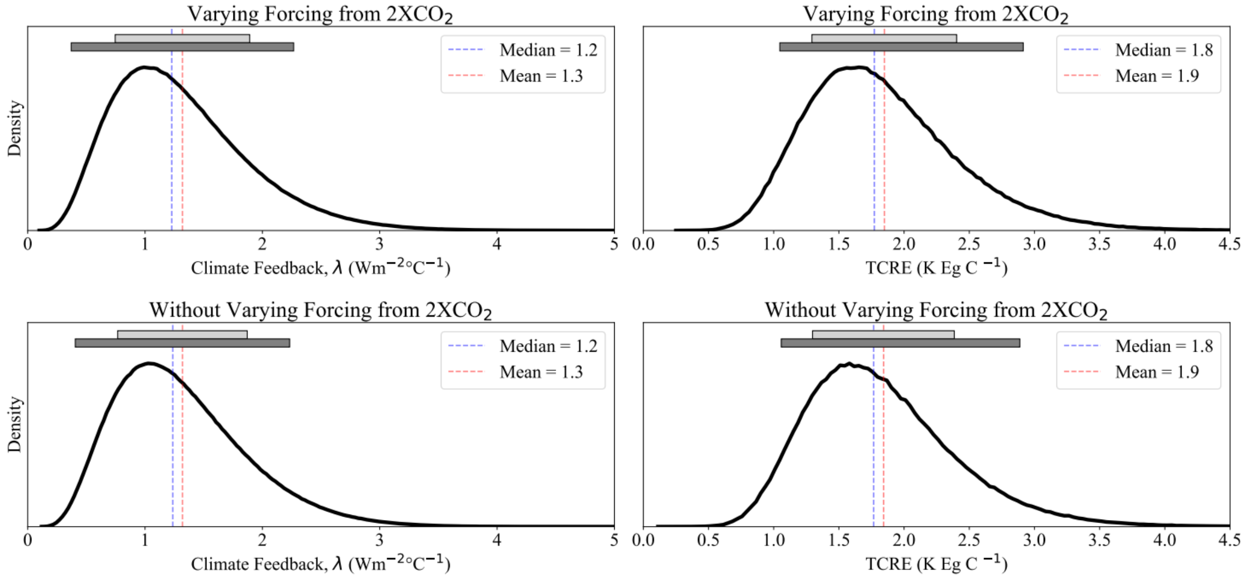

Figure A2-5. *Climate feedback (left) and Transient Climate Response to Cumulative CO2 Emissions (right) probability distribution functions resulting from Monte-Carlo simulations (n=1,000,000) wherein climate feedback is calculated with a varying radiative forcing from a doubling of CO2 (top) and wherein climate feedback is calculated with a fixed radiative forcing from a doubling of CO2 (bottom). The light grey bar designates a 16-84% confidence interval, and the dark grey bar designates a 5-95% confidence interval.*

Appendix III: Supplementary Information for Chapter 4

Table A3-1. *Leaf emergence process models included in this study for estimating the timing of the start of season (SOS) or leaf emergence. Note that each leaf emergence site-year runs from September 1st to August 31st such that a starting date of January 1st corresponds to a* t_0 *of 103.* R_{frc} *and* R_{chl} *denote the rate of forcing and chilling, respectively.* S_{frc} *and* S_{chl} *denote the accumulated state of forcing and chilling, respectively.* DR_t *and* DR_p *denote the rate of dormancy induction based on temperature and photoperiod, respectively.* S_{DR} *denotes the state of dormancy induction accumulation.*

Model	Variables, Parameters, & Release Process(es) Included	Equation	Reference
Null	-mean date from all observations $\overline{SOS_o}$ **None**	$SOS = \overline{SOS_o}$	-
Thermal Time (TT)	-starting date t_0 -daily mean temperature T_i -base temperature for accumulation T_b -critical threshold for leaf emergence F_{crit} **Ecodormancy**	$R_{frc}(i) = \begin{cases} T_i > T_b: T_i - T_b \\ T_i \leq T_b: 0 \end{cases}$ $S_{frc} = \sum_{i=t_0}^{n} R_{frc}$ $S_{frc} \geq F_{crit}$	Hufkens et al., 2018; Basler, 2016; Wang 1960; Réaumur, 1735
Thermal Time with Sigmoidal Temperature Response (TTs)	-starting date t_0 -daily mean temperature T_i -response parameter *b* -response parameter *c* -critical threshold for leaf emergence F_{crit} **Ecodormancy**	$R_{frc}(i) = \frac{1}{1 + e^{-b(T_i - c)}}$ $S_{frc} = \sum_{i=t_0}^{n} R_{frc}$ $S_{frc} \geq F_{crit}$	Hufkens et al., 2018; Basler, 2016; Kramer, 1994; Hänninen, 1990

Photo-Thermal Time (PTT)	-starting date t_0 -daily mean temperature T_i -base temperature for accumulation T_b -daylength L_i -critical threshold for leaf emergence F_{crit} **Ecodormancy**	$R_{frc}(i) = \frac{L_i}{24} * \begin{cases} T_i > T_b: T_i - T_b \\ T_i \le T_b: 0 \end{cases}$ $S_{frc} = \sum_{i=t_0}^{n} R_{frc}$ $S_{frc} \ge F_{crit}$	Hufkens et al., 2018; Basler, 2016; Črepinšek et al., 2006; Masle, 1989
Photo-Thermal Time with Sigmoidal Temperature Response (PTTs)	-starting date t_0 -daily mean temperature T_i -response parameter b -response parameter c -daylength L_i -critical threshold for leaf emergence F_{crit} **Ecodormancy**	$R_{frc}(i) = \frac{L_i}{24} * \frac{1}{1+ e^{-b(T_i - c)}}$ $S_{frc} = \sum_{i=t_0}^{n} R_{frc}$ $S_{frc} \ge F_{crit}$	Hufkens et al., 2018; Basler, 2016; Črepinšek et al., 2006; Kramer, 1994; Hänninen, 1990; Masle, 1989
M1	-starting date t_0 -daily mean temperature T_i -base temperature for accumulation T_b -daylength L_i -response parameter k -critical threshold for leaf emergence F_{crit} **Ecodormancy**	$R_{frc}(i) = \left(\frac{L_i}{10}\right)^k * \begin{cases} T_i > T_b: T_i - T_b \\ T_i \le T_b: 0 \end{cases}$ $S_{frc} = \sum_{i=t_0}^{n} R_{frc}$ $S_{frc} \ge F_{crit}$	Hufkens et al., 2018; Basler, 2016; Blümel and Chmielewski, 2012
Alternating (AT)	-starting date t_0 -daily mean temperature T_i -base	$R_{chl}(i) = \begin{cases} T_i < T_b: 0 \\ T_i \ge T_b: 1 \end{cases}$	Hufkens et al., 2018; Basler, 2016; Murray et al.,

	temperature for accumulation T_b -response parameter a -response parameter b -response parameter c **Endodormancy & Ecodormancy**	$S_{chl} = \sum_{i=t_0}^{n} R_{chl}$ $R_{frc}(i) = \begin{cases} T_i > T_b: T_i - T_b \\ T_i \leq T_b: 0 \end{cases}$ $S_{frc} = \sum_{i=t_0}^{n} R_{frc}$ $F_{crit} = a + b * e^{c * S_{chl}}$ $S_{frc} \geq F_{crit}$	1989; Cannel and Smith 1983
Sequential (SQ)	-chilling starting date t_{0c} -forcing starting date t_{0f} -daily mean temperature T_i -minimum temperature for chilling accumulation T_{min} -optimal temperature for chilling accumulation T_{opt} -maximum temperature for chilling accumulation T_{max} -threshold for forcing accumulation	$R_{tchl}(i) = \begin{cases} T_{min} \leq T_i < T_{opt} : \frac{T_i - T_{min}}{T_{opt} - T_{min}} \\ T_{opt} \leq T_i < T_{max} : 1 - \frac{T_i - T_{opt}}{T_{max} - T_{opt}} \\ T_i < T_{min} : 0 \\ T_i > T_{max} : 0 \end{cases}$ $S_{chl} = \sum_{i=t_{0c}}^{n} R_{tchl}$ $k = \begin{cases} S_{chl} < C_{req} : 0 \\ S_{chl} \geq C_{req} : 1 \end{cases}$ $R_{frc}(i) = k * \begin{cases} T_i > T_b: T_i - T_b \\ T_i \leq T_b: 0 \end{cases}$ $S_{frc} = \sum_{i=t_{0f}}^{n} R_{frc}$ $S_{frc} \geq F_{crit}$	Hufkens et al., 2018; Basler, 2016; Kramer, 1994; Hänninen, 1990

	C_{req} -base temperature for forcing accumulation T_b -critical threshold for leaf emergence F_{crit} **Endodormancy & Ecodormancy**		
Dormphot (DP)	-dormancy induction sensitivity parameter a -daily mean temperature T_i -response parameter for dormancy induction accumulation b -daylength L_i -threshold daylength for dormancy induction accumulation L_{crit} -threshold for dormancy induction D_{crit} -chilling sensitivity parameter c -rate of chilling accumulation parameter d -forcing sensitivity	$DR_t(i) = \frac{1}{1 + e^{a(T_i - b)}}$ $DR_p(i) = \frac{1}{1 + e^{10(L_i - L_{crit})}}$ $S_{DR} = \sum_{i=t_0}^{n} DR_t * DR_p$ $R_{chl}(i) = \begin{cases} S_{DR} < D_{crit}: 0 \\ S_{DR} \geq D_{crit}: \frac{1}{1 + e^{c(T_i - d)^2 + (T_i - d)}} \end{cases}$ $S_{chl} = \sum_{i=t_0}^{n} R_{chl}$ $dl_{50}(i) = \frac{24}{1 + e^{h_L(S_{chl}(i) - C_{req})}}$ $T_{50}(i) = \frac{60}{1 + e^{gT(L_i - dl_{50})}}$ $R_{frc}(i) = \begin{cases} S_{DR} < D_{crit}: 0 \\ S_{DR} \geq D_{crit}: \frac{1}{1 + e^{df(T_i - T_{50}(i))}} \end{cases}$	Hufkens et al., 2018; Basler, 2016; Caffarra et al., 2011

	parameter h_L -chilling threshold parameter for forcing accumulation C_{req} -daylength sensitivity parameter gT -forcing accumulation parameter df -critical threshold for leaf emergence F_{crit} **Dormancy Induction, Endodormancy, & Ecodormancy**	$$S_{frc} = \sum_{i=t_0}^{n} R_{frc}$$ $$S_{frc} \geq F_{crit}$$	

Table A3-2. *Optimal parameters and initial parameter range in square brackets for or each leaf emergence model using general simulated annealing. Note that each leaf emergence site-year runs from September 1st to August 31st such that a starting date of January 1st corresponds to a* t_0 *of 103.*

Model	**Parameters**	***Acer rubrum***	***Betula papyrifera***	***Abies balsamea***
Thermal Time (TT)	-starting date t_0 -base temperature for accumulation T_b -critical threshold for leaf emergence F_{crit}	t_0: 192 [1-365] T_b: 4.062 [-5 - +10] F_{crit}: 212.5 [0 -2000]	t_0: 181 [1-365] T_b: 4.804 [-5 - +10] F_{crit}: 157.6 [0 -2000]	t_0: 175 [1-365] T_b: 9.989 [-5 - +10] F_{crit}: 6.584 [0 -2000]
Thermal Time with Sigmoidal Temperature Response (TTs)	-starting date t_0 -response parameter b -response parameter c -critical threshold for leaf emergence F_{crit}	t_0: 185 [1-365] b: 0.1443 [0 - 100] c: 30.74 [0 - 100] F_{crit}: 2.188 [0 -350]	t_0: 193 [1-365] b: 0.1778 [0 - 100] c: 20.33 [0 - 100] F_{crit}: 5.147 [0 -350]	t_0: 177 [1-365] b: 2.1472 [0 - 100] c: 12.99 [0 - 100] F_{crit}: 0.9415 [0 -350]
Photo-Thermal Time (PTT)	-starting date t_0 -base temperature for accumulation T_b -critical threshold for leaf emergence F_{crit}	t_0: 191 [1-365] T_b: 4.888 [-5 - +10] F_{crit}: 103.7 [0 -2000]	t_0: 181 [1-365] T_b: 4.319 [-5 - +10] F_{crit}: 101.8 [0 -2000]	t_0: 173 [1-365] T_b: 9.918 [-5 - +10] F_{crit}: 3.876 [0 -2000]
Photo-Thermal Time with Sigmoidal Temperature Response (PTTs)	-starting date t_0 -response parameter b -response parameter c -critical threshold for leaf emergence F_{crit}	t_0: 185 [1-365] b: 0.1696 [0 - 100] c: 30.36 [0 - 100] F_{crit}: 0.8392 [0 -350]	t_0: 177 [1-365] b: 0.2260 [0 - 100] c: 16.94 [0 - 100] F_{crit}: 4.019 [0 -350]	t_0: 178 [1-365] b: 2.552 [0 - 100] c: 12.79 [0 - 100] F_{crit}: 0.6102 [0 -350]
M1	-starting date t_0 -base temperature	t_0: 151 [1-365] T_b: 6.708 [-5 -	t_0: 174 [1-365] T_b: 4.753 [-5 -	t_0: 174 [1-365] T_b: 9.996 [-5 -

	for accumulation T_b -response parameter k -critical threshold for leaf emergence F_{crit}	+10] k: 4.991 [0 -5] F_{crit}: 710.7 [0 -2000]	+10] k: 3.079 [0 -5] F_{crit}: 470.1 [0 -2000]	+10] k: 4.392 [0 -5] F_{crit}: 31.98 [0 -2000]
Alternating (AT)	-starting date t_0 -base temperature for accumulation T_b -response parameter a -response parameter b -response parameter c	t_0: 193 [1-365] T_b: 3.425 [-5 - +10] a: 226.2 [0 - 500] b: 2.549 [0 - 1000] c: 4.774 [0 -5]	t_0: 182 [1-365] T_b: 4.023 [-5 - +10] a: 36.65 [0 - 500] b: 148.1 [0 - 1000] c: 0.7998 [0 - 5]	t_0: 175 [1-365] T_b: 9.999 [-5 - +10] a: 0.8163 [0 - 500] b: 5.783 [0 - 1000] c: 2.780 [0 -5]
Sequential (SQ)	-chilling starting date t_{0c} -forcing starting date t_{0f} -minimum temperature for chilling accumulation T_{min} -optimal temperature for chilling accumulation T_{opt} -maximum temperature for chilling accumulation T_{max} -threshold for forcing accumulation C_{req} -base temperature for forcing accumulation T_b	t_{0c}: 30 [1-365] t_{0f}: 192 [1-365] T_{min}: -3.191 [-5 -+10] T_{opt}: 7.873 [-5 -+10] T_{max}: 14.56 [-5 -+10] C_{req}: 12.82 [0 -350] T_b: 3.009 [-5 - +10] F_{crit}: 246.8 [0 -2000]	t_{0c}: 14 [1-365] t_{0f}: 181 [1-365] T_{min}: -3.882 [-5 -+10] T_{opt}: 0.3103 [-5 -+10] T_{max}: 1.314 [-5 -+10] C_{req}: 2.801 [0 -350] T_b: 4.816 [-5 - +10] F_{crit}: 157.2 [0 -2000]	t_{0c}: 19 [1-365] t_{0f}: 177 [1-365] T_{min}: -4.331 [-5 -+10] T_{opt}: 5.636 [-5 -+10] T_{max}: 12.01 [-5 -+10] C_{req}: 3.838 [0 -350] T_b: 9.984 [-5 - +10] F_{crit}: 6.641 [0 -2000]

	-critical threshold for leaf emergence F_{crit}			
Dormphot (DP)	-dormancy induction sensitivity parameter a -response parameter for dormancy induction accumulation b -threshold daylength for dormancy induction accumulation L_{crit} -threshold for dormancy induction D_{crit} -chilling sensitivity parameter c -rate of chilling accumulation parameter d -forcing sensitivity parameter h_L -chilling threshold parameter for forcing accumulation C_{req} -daylength sensitivity parameter gT -forcing accumulation parameter df -critical threshold	a: 4.351 [-5 - +5] b: 13.95 [0 - 100] L_{crit}: 11.11 [8 -14] D_{crit}: 35.89 [0 -100] c: 0.3875 [0 - 5] d: 17.88 [0 - 100] h_L: 0.0383 [0 - 20] C_{req}: 0.7199 [0 -100] gT: 0.6398 [0 -10] df: -0.3400 [-1000 -0] F_{crit}: 10.34 [0 -100]	a: 2.775 [-5 - +5] b: 18.25 [0 - 100] L_{crit}: 12.54 [8 -14] D_{crit}: 21.89 [0 -100] c: 0.01198 [0 - 5] d: 79.89 [0 - 100] h_L: 16.14 [0 - 20] C_{req}: 27.51 [0 -100] gT: 0.1176 [0 -10] df: -0.5319 [-1000 -0] F_{crit}: 16.04 [0 -100]	a: 1.807 [-5 - +5] b: 3.461 [0 - 100] L_{crit}: 13.16 [8 -14] D_{crit}: 10.42 [0 -100] c: 0.6685 [0 - 5] d: 16.39 [0 - 100] h_L: 2.321 [0 - 20] C_{req}: 0.2033 [0 -100] gT: 4.6868 [0 -10] df: -386.4 [-1000 -0] F_{crit}: 4.005 [0 -100]

	for leaf emergence F_{crit}			

Table A3-3. *Leaf senescence process models included in this study. Note that each leaf senescence site-year runs from January 1st to December 31st such that a starting date of January 1st corresponds to a* t_0 *of 1.* R_{tp}, R_t, *and* R_p *denote the rate of temperature cooling and photoperiod reducing, the rate of temperature cooling, and the rate of photoperiod reducing, respectively.* S_{tp}, S_t, *and* S_p *denote the accumulated state of temperature cooling and photoperiod reducing, the accumulated state of temperature cooling, and the accumulated state of photoperiod reducing, respectively.*

Model	**Variables, Parameters, and Process(es) Included**	**Equation**	**Reference**
Null	-mean date from all observations $\overline{EOS_o}$ **None**	$EOS = \overline{EOS_o}$	-
White (WM)	-starting date fixed to July 1st -daily mean temperature T_i -temperature for combined temperature daylength senescence trigger T_{b1} -daylength L_i -daylength for combined temperature daylength senescence trigger L_{crit} -temperature for singular temperature senescence	$R_{tp}(i) = \begin{cases} T_i < T_{b1} \wedge L_i < L_{crit} : 1 \\ T_i \geq T_{b1} \vee L_i \geq L_{crit} : 0 \end{cases}$ $R_t(i) = \begin{cases} T_i < T_{b2} : 1 \\ T_i \geq T_{b2} : 0 \end{cases}$ $R_{tp} > 0$ $R_t > 0$	Liu et al., 2020; White et al., 1997

	trigger T_{b2} -criteria for senescence: first day of either R_{tp} or R_t not equal to 0 **Dormancy Induction**		
Delpierre (DM)	-starting date fixed to July 1st -daily mean temperature T_i -daylength L_i -temperature threshold and parameter for accumulation T_b -daylength threshold and parameter for accumulation L_{crit} -exponential weight parameter for temperature importance x -exponential weight parameter for daylength importance y -critical threshold for leaf senescence	$R_{tp}(i) = \begin{cases} T_i < T_b \wedge L_i < L_{crit} : (T_b - T_i)^x * \left(\frac{L_i}{L_{crit}}\right)^y \\ T_i \geq T_b \vee L_i \geq L_{crit} : 0 \end{cases}$ $S_{tp} = \sum_{i=182}^{n} R_{tp}$ $S_{tp} \geq F_{crit}$	Liu et al., 2020; Delpierre et al., 2009

	F_{crit} **Dormancy Induction**		
Jeong (JM)	-starting date fixed to July 1st -daily mean temperature T_i -daylength L_i -temperature threshold and parameter for accumulation T_b -daylength threshold for accumulation L_{crit} -critical threshold for leaf senescence F_{crit} **Dormancy Induction**	$R_{tp}(i) = \begin{cases} T_i < T_b \wedge L_i < L_{crit} : T_b - T_i \\ T_i \geq T_b \vee L_i \geq L_{crit} : 0 \end{cases}$ $S_{tp} = \sum_{i=182}^{n} R_{tp}$ $S_{tp} \geq F_{crit}$	Liu et al., 2020; Jeong et al., 2014
Dormphot with just Dormancy Induction (DPDI)	-dormancy induction sensitivity parameter a -daily mean temperature T_i -response parameter for dormancy induction accumulation b -daylength L_i	$R_t(i) = \frac{1}{1 + e^{a(T_i - b)}}$ $R_p(i) = \frac{1}{1 + e^{10(L_i - L_{crit})}}$ $S_{tp} = \sum_{i=182}^{n} R_t * R_p$ $S_{tp} \geq D_{crit}$	Liu et al., 2020; Hufkens et al., 2018; Caffarra et al., 2011

	-threshold daylength for dormancy induction accumulation L_{crit} -critical threshold for senescence D_{crit} **Dormancy Induction**		
Delpierre's with Preceding Spring Leaf Emergence (DMs)	-starting date fixed to July 1st -daily mean temperature T_i -daylength L_i -temperature threshold and parameter for accumulation T_b -daylength threshold and parameter for accumulation L_{crit} -exponential weight parameter for temperature importance x -exponential weight parameter for daylength importance y -threshold	$R_{tp}(i) = \begin{cases} T_i < T_b \wedge L_i < L_{crit} : (T_b - T_i)^x * \left(\frac{L_i}{L_{crit}}\right)^y \\ T_i \geq T_b \vee L_i \geq L_{crit} : 0 \end{cases}$ $S_{tp} = \sum_{i=182}^{n} R_{tp}$ $S_a = SOSy - \overline{SOS}_{30y}$ $F_{crit} = a + b * S_a$ $S_{tp} \geq F_{crit}$	Liu et al., 2020; Delpierre et al., 2009

	modification parameter of anomaly in leaf emergence in the preceding spring relative to the 30-year average estimated with the PTTs model S_a -threshold modification parameter a -threshold modification parameter b -critical threshold for leaf senescence F_{crit} **Preceding Ecodormancy Release & Dormancy Induction**		
Dormphot Dormancy Induction with Preceding Spring Leaf Emergence (DPDIs)	-dormancy induction sensitivity parameter $a1$ -daily mean temperature T_i -response parameter for dormancy induction accumulation	$R_t(i) = \frac{1}{1 + e^{a1(T_i - b1)}}$ $R_p(i) = \frac{1}{1 + e^{10(L_i - L_{crit})}}$ $S_{tp} = \sum_{i=182}^{n} R_t * R_p$ $S_a = SOSy - \overline{SOS}_{30y}$	Liu et al., 2020; Caffarra et al., 2011

	$b1$ -daylength L_i -threshold daylength for dormancy induction accumulation L_{crit} -threshold modification parameter of anomaly in leaf emergence in the preceding spring relative to the 30-year average estimated with the PTTs model S_a -threshold modification parameter $a2$ -threshold modification parameter $b2$ -critical threshold for leaf senescence D_{crit} **Preceding Ecodormancy Release & Dormancy Induction**	$D_{crit} = a2 + b2 * S_a$ $S_{tp} \geq D_{crit}$	

Table A3-4. *Optimal parameters and initial parameter range in square brackets for or each leaf senescence model using general simulated annealing. Note that each leaf senescence site-year runs from January 1st to December 31st such that a starting date of January 1st corresponds to a t_0 of 1.*

Model	**Parameters**	***Acer rubrum***	***Betula papyrifera***	***Abies balsamea***
White (WM)	-temperature for combined temperature daylength senescence trigger T_{b1} -daylength for combined temperature daylength senescence trigger L_{crit} -temperature for singular temperature senescence trigger T_{b2}	T_{b1}: 28.52 [0 - 30] L_{crit}: 11.55 [6-18] T_{b2}: 7.170 [-20 -+20]	T_{b1}: 16.39 [0 - 30] L_{crit}: 12.14 [6-18] T_{b2}: 3.281 [-20 -+20]	T_{b1}: 10.73 [0 - 30] L_{crit}: 11.47 [6-18] T_{b2}: -1.388 [-20 -+20]
Delpierre (DM)	-temperature threshold and parameter for accumulation T_b -daylength threshold and parameter for accumulation L_{crit} -exponential weight parameter for temperature importance x -exponential weight parameter for daylength importance y	T_b: 39.76 [0 - 40] L_{crit}: 12. 92 [6 -18] x: 2 {0,1,2} y: 0 {0,1,2} F_{crit}: 16192 [0 – 100,000]	T_b: 33.06 [0 - 40] L_{crit}: 15.33 [6 -18] x: 1 {0,1,2} y: 2 {0,1,2} F_{crit}: 981.9 [0 – 100,000]	T_b: 22.57 [0 - 40] L_{crit}: 15.48 [6 -18] x: 0 {0,1,2} y: 2 {0,1,2} F_{crit}: 69.73 [0 – 100,000]

	-critical threshold for leaf senescence F_{crit}			
Jeong (JM)	-temperature threshold and parameter for accumulation T_b -daylength threshold for accumulation L_{crit} -critical threshold for leaf senescence F_{crit}	T_b: 34.63 [0 - 50] L_{crit}: 13.15 [6 -18] F_{crit}: 613.1 [0 – 2000]	T_b: 30.60 [0 - 50] L_{crit}: 15.31 [6 -18] F_{crit}: 1003 [0 – 2000]	T_b: 35.69 [0 - 50] L_{crit}: 15.48 [6 -18] F_{crit}: 1911 [0 – 2000]
Dormphot with just Dormancy Induction (DPDI)	-sensitivity parameter a -response parameter for accumulation b -threshold daylength for dormancy induction accumulation L_{crit} -threshold for dormancy induction D_{crit}	a: 0.1432 [-5 - +5] b: 2.120 [0 - 100] L_{crit}: 12.83 [8 -18] D_{crit}: 44.42 [0 – 100]	a: 3.141 [-5 - +5] b: 16.31 [0 - 100] L_{crit}: 12.93 [8 -18] D_{crit}: 98.61 [0 – 100]	a: 4.885 [-5 - +5] b: 12.02 [0 - 100] L_{crit}: 11.56 [8 -18] D_{crit}: 33.87 [0 – 100]
Delpierre's with Preceding Spring Leaf Emergence (DMs)	-temperature threshold and parameter for accumulation T_b -daylength threshold and parameter for accumulation L_{crit} -exponential weight parameter for temperature	T_b: 39.63 [0 - 40] L_{crit}: 12.88 [6 -18] x: 2 {0,1,2} y: 0 {0,1,2} a: 15754 [0 - 100000] b: 0.07018 [0 - 1000]	T_b: 39.44 [0 - 40] L_{crit}: 15.33 [6 -18] x: 2 {0,1,2} y: 1 {0,1,2} a: 34388 [0 - 100000] b: 92.98 [0 - 1000]	T_b: 39.59 [0 - 40] L_{crit}: 15.48 [6 -18] x: 1 {0,1,2} y: 2 {0,1,2} a: 1723 [0 - 100000] b: 0.05690 [0 - 1000]

	importance x -exponential weight parameter for daylength importance y -threshold modification parameter a -threshold modification parameter b			
Dormphot Dormancy Induction with Preceding Spring Leaf Emergence (DPDIs)	-dormancy induction sensitivity parameter $a1$ -response parameter for dormancy induction accumulation $b1$ -threshold daylength for dormancy induction accumulation L_{crit} -threshold modification parameter $a2$ -threshold modification parameter $b2$	$a1$: 0.1573 [-5 -+5] $b1$: 6.478 [0 - 100] L_{crit}: 12.79 [8 -18] $a2$: 63.93 [0 - 100] $b2$: 0.003743 [0 -10]	$a1$: 4.537 [-5 - +5] $b1$: 16.75 [0 - 100] L_{crit}: 12.86 [8 -18] $a2$: 99.78 [0 - 100] $b2$: 0.01281 [0 -10]	$a1$: 4.701 [-5 - +5] $b1$: 12.03 [0 - 100] L_{crit}: 11.59 [8 -18] $a2$: 34.37 [0 - 100] $b2$: 0.001405 [0 -10]

Table A3-5. *Leaf emergence observations at sites across the Acadian Phenocam Network used in this study. Day of year (DOY) is the calendar day of year from December 31st of the previous year.*

Site	**Year**	**Species**	**Emergence (DOY)**
NE1	2019	*Acer rubrum*	161
NE3	2019	*Acer rubrum*	165
NE4	2019	*Acer rubrum*	162
NE6	2019	*Acer rubrum*	159
SW1	2019	*Acer rubrum*	159
SW2	2019	*Acer rubrum*	164
SW4	2019	*Acer rubrum*	163
SW5	2019	*Acer rubrum*	160
NE4	2020	*Acer rubrum*	156
NE6	2020	*Acer rubrum*	151
SW4	2020	*Acer rubrum*	152
SW5	2020	*Acer rubrum*	150
NE1	2021	*Acer rubrum*	152
NE2	2021	*Acer rubrum*	152
NE3	2021	*Acer rubrum*	151
NE4	2021	*Acer rubrum*	153
NE5	2021	*Acer rubrum*	152
NE6	2021	*Acer rubrum*	145
SW1	2021	*Acer rubrum*	146
SW2	2021	*Acer rubrum*	150
SW3	2021	*Acer rubrum*	147
SW4	2021	*Acer rubrum*	146
SW6	2021	*Acer rubrum*	150
NE1	2022	*Acer rubrum*	152
NE2	2022	*Acer rubrum*	157
NE3	2022	*Acer rubrum*	149
NE4	2022	*Acer rubrum*	160
NE5	2022	*Acer rubrum*	156
NE6	2022	*Acer rubrum*	146
SW1	2022	*Acer rubrum*	145
SW2	2022	*Acer rubrum*	152
SW3	2022	*Acer rubrum*	150
SW4	2022	*Acer rubrum*	147
SW6	2022	*Acer rubrum*	152
NE1	2019	*Betula papyrifera*	158

SW3	2019	*Betula papyrifera*	154
SW4	2019	*Betula papyrifera*	158
SW5	2019	*Betula papyrifera*	155
NE4	2020	*Betula papyrifera*	155
SW4	2020	*Betula papyrifera*	155
SW5	2020	*Betula papyrifera*	145
NE1	2021	*Betula papyrifera*	145
NE2	2021	*Betula papyrifera*	149
NE4	2021	*Betula papyrifera*	148
SW2	2021	*Betula papyrifera*	158
SW4	2021	*Betula papyrifera*	144
SW5	2021	*Betula papyrifera*	142
NE1	2022	*Betula papyrifera*	145
NE2	2022	*Betula papyrifera*	154
NE4	2022	*Betula papyrifera*	153
SW2	2022	*Betula papyrifera*	153
SW3	2022	*Betula papyrifera*	141
SW4	2022	*Betula papyrifera*	147
SW5	2022	*Betula papyrifera*	141
NE1	2019	*Abies balsamea*	160
NE3	2019	*Abies balsamea*	155
NE4	2019	*Abies balsamea*	163
NE6	2019	*Abies balsamea*	158
SW3	2019	*Abies balsamea*	154
SW4	2019	*Abies balsamea*	157
SW6	2019	*Abies balsamea*	147
NE4	2020	*Abies balsamea*	154
NE6	2020	*Abies balsamea*	148
SW4	2020	*Abies balsamea*	147
NE1	2021	*Abies balsamea*	149
NE2	2021	*Abies balsamea*	158
NE3	2021	*Abies balsamea*	144
NE4	2021	*Abies balsamea*	150
NE5	2021	*Abies balsamea*	152
NE6	2021	*Abies balsamea*	146
SW3	2021	*Abies balsamea*	143
SW4	2021	*Abies balsamea*	146
SW6	2021	*Abies balsamea*	158
NE1	2022	*Abies balsamea*	144

NE2	2022	*Abies balsamea*	155
NE3	2022	*Abies balsamea*	142
NE4	2022	*Abies balsamea*	154
NE5	2022	*Abies balsamea*	159
NE6	2022	*Abies balsamea*	144
SW3	2022	*Abies balsamea*	148
SW4	2022	*Abies balsamea*	147
SW6	2022	*Abies balsamea*	158

Table A3-6. *Leaf senescence observations at sites across the Acadian Phenocam Network used in this study. Day of year (DOY) is the calendar day of year from December 31st of the previous year.*

Site	Year	Species	Senescence (DOY)
NE1	2019	*Acer rubrum*	241
NE3	2019	*Acer rubrum*	244
NE4	2019	*Acer rubrum*	298
NE5	2019	*Acer rubrum*	253
NE6	2019	*Acer rubrum*	258
SW1	2019	*Acer rubrum*	263
SW2	2019	*Acer rubrum*	270
SW4	2019	*Acer rubrum*	266
SW5	2019	*Acer rubrum*	256
SW5	2020	*Acer rubrum*	281
SW6	2020	*Acer rubrum*	268
NE1	2021	*Acer rubrum*	270
NE2	2021	*Acer rubrum*	252
NE3	2021	*Acer rubrum*	258
NE4	2021	*Acer rubrum*	243
NE5	2021	*Acer rubrum*	279
NE6	2021	*Acer rubrum*	256
SW1	2021	*Acer rubrum*	271
SW2	2021	*Acer rubrum*	270
SW3	2021	*Acer rubrum*	242
SW4	2021	*Acer rubrum*	237
SW6	2021	*Acer rubrum*	253
NE1	2019	*Betula papyrifera*	241
SW3	2019	*Betula papyrifera*	233
SW4	2019	*Betula papyrifera*	259
SW5	2019	*Betula papyrifera*	275
SW5	2020	*Betula papyrifera*	277
SW6	2020	*Betula papyrifera*	278
NE1	2021	*Betula papyrifera*	224
NE2	2021	*Betula papyrifera*	245
NE4	2021	*Betula papyrifera*	268
SW2	2021	*Betula papyrifera*	248
SW3	2021	*Betula papyrifera*	224
SW4	2021	*Betula papyrifera*	224
SW5	2021	*Betula papyrifera*	286

SW6	2021	*Betula papyrifera*	246
NE1	2019	*Abies balsamea*	249
NE3	2019	*Abies balsamea*	289
NE5	2019	*Abies balsamea*	249
NE6	2019	*Abies balsamea*	259
SW3	2019	*Abies balsamea*	285
SW4	2019	*Abies balsamea*	254
NE1	2021	*Abies balsamea*	264
NE2	2021	*Abies balsamea*	251
NE3	2021	*Abies balsamea*	244
NE4	2021	*Abies balsamea*	273
NE5	2021	*Abies balsamea*	302
NE6	2021	*Abies balsamea*	247
SW3	2021	*Abies balsamea*	286
SW4	2021	*Abies balsamea*	219
SW6	2021	*Abies balsamea*	288